UNIVERSIDADE TÉCNICA DE LISBOA

INSTITUTO SUPERIOR TÉCNICO

Use of Geostatistical Models to Improve Reservoir Description and Flow Simulation in Heterogeneous Oil Fields

José António de Almeida

(Mestre)

Dissertação para obtenção do Grau de Doutor em Engenharia de Minas

Orientador:	Doutor Amílcar de Oliveira Soares
Júri:	
Presidente:	Reitor da Universidade Técnica de Lisboa
Vogais:	Doutor John Archer
	Doutor António José da Costa e Silva
	Engenheiro Luís António Aires de Barros
	Doutor António Diogo Pinto
	Doutor Rogério Eduardo Bordalo da Rocha
	Doutor Amílcar de Oliveira Soares

Julho de 1999

Abstract

This work presents a set of techniques able to describe the internal morphology and spatial distribution of petrophysical properties within a highly heterogeneous reservoir based on data from a small number of wells. The techniques used show that it is possible to present a coherent description of highly complex and heterogeneous reservoirs, by imposing the spatial continuity models extractable from the experimental data. In the present work, reservoir characterisation focuses in the following main topics:

i) Stochastic simulation of the internal morphology of the reservoir (spatial distribution of lithoclasses) encompassing a comparative study between three simulation algorithms for categorical variables: truncated Gaussian field with posterior conditioning, sequential indicator simulation with correction for local probabilities, and simulated annealing.

ii) Zonal control estimation of porosity and permeability conditioned to the simulated images of lithoclasses. Estimation of water saturation based on a coordinate transformation to the referential of the free water level to cope with the problem of the non-stationarity displayed by this variable.

iii) Stochastic simulation of permeability – an undersampled property presenting high variability and heterogeneity that significantly affect all fluid flow scenarios.

iv) Screening of realisations following a ranking selection based on the volume of geobodies of high and low permeability.

v) Upscaling of properties from the stochastic block model to the fluid flow simulator block model based on a pressure solver technique.

Key words

Reservoir, Multi-phase set, Stochastic simulation, Simulated annealing, Zonal control estimation, Upscaling

Resumo

Este trabalho tem como objectivo a caracterização da morfologia interna e das propriedades petrofísicas de um reservatório de petróleo heterogéneo tendo por base um conjunto de amostras de um número reduzido de poços. As técnicas utilizadas mostraram que é possível efectuar a descrição coerente de reservatórios deste tipo, ao impor nos cenários obtidos as características de continuidade evidenciadas pelas amostras. Este estudo de caracterização resume-se à seguinte sequência de etapas:

i) Simulação morfológica da arquitectura interna do reservatório (distribuição espacial de litoclasses). Efectuou-se um estudo comparativo de três algoritmos de simulação estocástica de variáveis categóricas: *truncated Gaussian field* com condicionamento posterior, simulação sequencial da indicatriz com correcção das probabilidades locais e *simulated annealing*.

ii) Estimação por krigagem com controlo zonal da porosidade e permeabilidade condicionadas aos mapas de litoclasses. Estimação da saturação em água, recorrendo a uma transformação de coordenadas por forma a contornar o problema da não estacionaridade desta variável.

iii) Simulação estocástica da permeabilidade – propriedade petrofísica, regra geral sub-amostrada, de elevada variabilidade e heterogeneidade.

iv) Classificação e selecção das imagens simuladas, baseada em critérios de volumes de corpos de alta e baixa permeabilidade.

v) Mudança de escala – *upscaling* - dos blocos do modelo estocástico para os blocos do modelo de simulação de fluidos, com uma abordagem nova baseada no método de “pressure solver”.

Palavras chave

Reservatório petróleo, Conjunto multifásico, Simulação estocástica, *Simulated annealing*, Estimação com controlo zonal, *Upscaling*

Agradecimentos

Este trabalho aqui apresentado é o resultado da actividade de investigação sobre métodos geoestatísticos e a sua aplicação à caracterização de reservatórios de petróleo. É pois com a maior satisfação que tenho de agradecer às pessoas, que de uma maneira ou de outra contribuíram para o desenvolvimento e aplicação das técnicas compiladas nesta tese.

Quero começar por agradecer ao meu orientador científico, o Prof. Amílcar Soares pelo seu extraordinário rigor científico e simultaneamente pela sua capacidade imaginativa e prática, o que me incentivou a utilização deste tema como trabalho de tese. Agradeço-lhe a sua colaboração e dedicação a este ramo de aplicação da geoestatística, assim como a oportunidade que me deu de ter partilhado este percurso com uma equipa de nível excepcional e de valor reconhecido internacionalmente, que é da sua coordenação.

Ao Prof. Costa e Silva, agradeço a sua disponibilidade em todas as fases deste trabalho, concretamente na discussão de aspectos ligados à aplicabilidade dos métodos estocásticos a reservatórios e na fase final na revisão do texto e da apresentação.

Ao Prof. Sezgin Daltaban agradeço-lhe a oportunidade que me deu de efectuar dois estágios no *Reservoir Modelling Division* (RMD) do Imperial College, que foram fundamentais para a evolução dos trabalhos na área de simulação dinâmica e *upscaling* da permeabilidade. Agradeço-lhe também todo o apoio prestado na divulgação desse trabalho.

Queria também fazer um agradecimento muito especial aos restantes professores e funcionários da secção de Mineralurgia e Planeamento Mineiro, Prof. Henrique Garcia Pereira, Prof. Jorge de Sousa, Prof. Fernando Durão, D. Inês, D. Delminda, João Albernaz e o Paulo pelo seu apoio e camaradagem incondicionais ao longo de todos estes anos.

À Maria João Pereira agradeço-lhe a sua boa disposição e camaradagem assim como as suas opiniões em trabalhos conjuntos, que são sempre importantes no desenvolvimento e consolidação das metodologias científicas.

Ao José João Luís, Carla Nunes e Alexandre Rodrigues agradeço-lhes a sua disponibilidade e a sua particular boa disposição e camaradagem em todos os momentos.

A todos os colegas de trabalho na área de estudos de reservatórios, Eng. Victor Alcobia, Luís Guerreiro, Justino Carvalho, Luís Ramos, Luís Costa, Pedro Soares, Pedro Matos, Edna e outros que ao longo destes anos se tem cruzado comigo em diferentes projectos de caracterização de reservatórios.

A todos os restantes colegas dos centros de investigação da secção de Mineralurgia e Planeamento Mineiro, em especial Domingas, Miguel Lince e Barbara Rodrigues, agradeço-lhes a camaradagem e boa disposição que tem proporcionado, factor sempre indispensável ao equilíbrio.

Ao Paul Covill, agradeço-lhe a sua cuidadosa revisão do texto em língua inglesa.

Agradeço à Junta Nacional de Investigação Científica (Programa Ciência e *Praxis* XXI) a concessão de uma bolsa de Doutoramento e o consequente financiamento do trabalho de tese, assim como o financiamento indispensável à participação nalgumas conferências internacionais, cuja participação é fundamental para manter uma actualização constante em todas as metodologias de ponta.

Agradeço também ao Centro de Modelização de Reservatórios Petrolíferos do Instituto Superior Técnico a sua comparticipação em algumas despesas e a utilização do equipamento e *software*, indispensáveis para a execução deste trabalho.

Contents

List of figures

List of tables

1 INTRODUCTION

1.1 METHODOLOGICAL ORIENTATION

The characterisation of oil reservoirs is one of the most important strategic areas in the process of studying a reservoir. Indeed, the great challenge we face nowadays is that production from increasingly depleted and heterogeneous reservoirs is generally a result of previous strategies which were not always the most appropriate to ensure the maximisation of oil recovery. The new strategies for reservoir characterisation based on geostatistical models are the outcome of a close inter-relation between reservoir knowledge and its complexity. The result is the need to increase knowledge based on greater intervention during characterisation and bearing in mind the strategic guideline of maintaining a market balance between oil recovery and required reservoir knowledge.

Stochastic characterisation of reservoirs is a relatively recent application in the history of geostatistics (Journel and Huijbregts, 1978, Da Costa e Silva, 1984, 1992, Isaaks and Srivastava, 1989, Pereira *et al*, 1990, Daly and Verly, 1994, Deutsch, 1996). Geostatistical models were first applied in the mining industry. The oil industry's considerable initial reluctance to use these techniques was due to a number of different factors, the most important of which were the following:

- Lack of available information, which made it difficult to create reliable models of spatial continuity which are at the basis of their design and application;

- Geostatistical estimation techniques are not particularly appropriate in terms of results when applied to large areas generally recognised as having relatively little information. In such cases, the result consists of vague and smooth images showing the spatial distribution of the properties, and is therefore not very realistic;

- There is little objective and methodological parallelism between a calculation of mining reserves and applications for the oil industry. In the case of mines, what is required is a calculation of most probable reserves using available concrete information. In the oil industry, as the reserves are a dynamic concept, what is required is a range of possible scenarios based on a set of descriptive models in line with a limited number of premises imposed by the scarcity of information. Most of the uncertainly comes from poor knowledge of the surrounding geology: the oil industry is exploiting a resource where there is no way of making close contact with associated surrounding geological formations.

To cope with this situation, several techniques suitable for dealing with poorly sampled oil fields based on stochastic simulations have been applied with success. Conceptual models with deterministic characteristics have proved not to be the most appropriate methods to describe the internal geometry of complex fields. The output of these models consists of just one smooth image of spatial variability, precisely because its background does not include any type of uncertainty model and spatial continuity structure. The history match using the data from these deterministic models is certainly simplistic, and performing further studies forecasts of production or injection has serious drawbacks that could led to calamitous results. Questions answered by dynamic flow simulation studies, like the proper location of newly developed wells, horizontal wells, injection of water and steam, flow pattern channels and preferential location of dead areas, can not be properly answered using deterministic models, which are also unable to provide extreme scenarios and uncertainty in forecasting studies.

The use of geostatistical techniques in oil fields may produce an average image or a set of equiprobable images of the spatial distribution of petrophysical variables, highlighting lithologies or rock types, permeability, porosity and saturation. Each of these images comprises a two or three-dimensional regular grid, usually with millions of nodes representing the internal architecture of the field (morphology and petrophysical values) (Journel 1989, Deutsch and Journel, 1992, Srivastava, 1994). They are used in flow simulation studies to characterise the fluid flow between adjacent blocks.

Stochastic models act as tools in oil field characterisation, and the modelling process has a multidisciplinary nature. The stages of characterisation involve niches of methodologies designed to satisfy each area of the model. These working areas may develop independently and are interrelated so as to come together to form a strategic action aimed at the same objectives. The contribution of each of these areas is updated with the developments taking place in the others, to update the capacity of the models in such a way as to involve new sources of information and to ensure coherent development in interaction with the other areas, always bearing in mind that innovation should be associated with coherence and the validation of many different disciplines.

This study is therefore very much along the lines outlined above, a contribution showing the current state of the application of geostatistical models to the characterisation of oil reservoirs. Following this study, the development and explanation of each methodological sequence always appears alongside the correspondent characterisation step, leading to the development of a complete stochastic model of the reservoir.

1.2 OBJECTIVES AND PRESENTATION OF THE WORK

This research work was developed with the main aim of describing the internal morphology and properties within oil fields. The objective is accordingly to apply geostatistical techniques to under-sampled and particularly heterogeneous reservoirs. The under-sampled reservoir treated in this study is characterised by few wells; also few cores and no seismic data are available. In fact, in the studied reservoir the number of wells is relatively low: 19 for a field surface area around 160 km^2 and a thickness varying from 100 to 1000 feet.

In this study, the characterisation of oil fields is proposed in a step-by-step process, focused on the following main topics:

i) Morphological simulation of the internal architecture of the reservoir using categorical or indicator algorithms (the field is previously classified by rock types or lithoclasses);

ii) Characterisation of the petrophysical properties by estimation, conditioned to the morphological model of geological categories;

iii) Geostatistical simulation of the properties showing more spatial variability and heterogeneity (usually permeability and in some cases porosity), followed by a spatial uncertainty evaluation based on these output images;

iv) Data preparation for the dynamic fluid flow simulator: screening of realisations using geobody analysis and flow sensibility tests and upscaling of the detailed stochastic model to be a suitable input for a fluid flow simulator. The scale-up of the detailed stochastic model in a small number of coarse grid blocks to be inputted into the simulator of fluids is the final but not least important step of this study given the need to preserve heterogeneities observed in the detailed pattern of the fine grid blocks.

The stochastic reservoir model developed agrees with the major features present in the conceptual geological model, honours the known data from wells and matches the available core and log data and continuity models. It provides an internal representation of the reservoir heterogeneities between wells, taking into account the morphology of the defined facies. The result is a 3D model of geology (lithoclasses) and petrophysical variables (porosity, permeability and saturations) with several million small blocks. Each stochastic realisation is a lithological reservoir image, which reproduces the spatial variability of, for instance of permeable and impermeable formations. Multiple generation of such equally probable images allows visualisation of different geometry scenarios. Although this model is

reduced in number of blocks (scale-up) the detailed geostatistical model provides insight into reservoir connectivity and vertical and lateral distribution of properties.

In the particular oil field studied, four main sources of heterogeneity were found (the same sources that can be found in other similar heterogeneous oil fields) (Da Costa e Silva and Soares, 1994, Da Costa e Silva *et al*, 1997): vertical heterogeneity (between layers), lithological changes within each layer, geometric arrangements of lithoclasses and some petrophysical variability inside lithoclasses. The modelling approach should deal with the complexity deriving from the high degree of variability in petrophysical properties, mostly between lithoclasses. With this in mind, a geostatistical or stochastic simulation model of the geology is proposed first, and the sources of heterogeneity are incorporated in the final model as follows:

- The vertical zoning effect is taken into account if the spatial continuity analysis and the conditioning procedure and imposed statistics are done within a layer and independently layer by layer;

- Geometrical arrangements and the corresponding transitions between rock types are taken into account in the construction of individual or multi-phase covariances, and simultaneously by imposing the experimental proportions within each layer;

- The spatial variability of the properties observed within geological units and the actual variability of the geological units is taken into account following the two-step sequential methodological approach proposed. This two-step approach comprises simulation of the geological units and subsequent estimation or simulation of petrophysical properties conditioned to the simulated categorical images of the internal geology of the field.

Part of the morphological geostatistical methods described and implemented in the scope of this research work are based on the multi-phase concept introduced by Soares, 1992. When the number of categories is significant and the reservoir is highly heterogeneous, this concept and the correspondent multi-phase continuity measure tool have proved to be at present the most suitable to characterise the spatial continuity of categorical variables (for example, lithologies or rock types) compared to the usual methods of calculating individual covariances or more complex co-regionalization models. These methods are *a priori* more complex and detailed but are more demanding in terms of the number of samples and evidence of continuity. The usual methods in heterogeneous and under-sampled reservoirs

are implemented using simplifications and assumptions that are generally difficult to justify, except if the reason is simply to run the model.

In this research work, the main topics are presented in the following sequence:

Section one is an introduction explaining the main methodological orientations, guidelines and innovations. It also includes a summary of the geology and main field characteristics of the reservoir studied related to the construction of the stochastic model.

The second section is dedicated to an explanation of categorical simulation methods using the indicator formalism extended to multi-phase structures for the spatial description of lithoclasses or geological units. In the case study presented, results from three different algorithms of spatial simulation of categorical variables are compared. These methods are sequential indicator simulation with corrections of local probabilities, morphological simulation based on a truncated Gaussian field plus a subsequent conditioning step, and simulated annealing (used basically for post-processing the results provided by the two previous methods). The output images from both methods are validated based on the imposed premises: the global continuity model, basic statistics, and matching of experimental data. For each individual approach, a comparative evaluation of the variability between the resulting images is carried out, in order to rank these three methods by an entropy quality measure.

Section three deals with the spatial characterisation of petrophysical properties (porosity, permeability and water saturation) using estimation methods based on kriging. Estimation was sub-divided into two sections, corresponding respectively to variables extremely dependent on the internal morphology of the geological units and thus predominantly dependent on deterministic phenomena. The first encompasses porosity and permeability and the second is related to fluid saturation. For porosity and permeability, estimation follows the zoning control estimation technique, which consists of extending multi-phase morphological estimation to the domain of continuous variables. The objective consists of estimating the variable spread along a set of geological units. To accomplish this, just one multi-phase variogram is required, instead of individual variograms or covariances, in order to perform the estimation in a single step for all geological units. The same method is used to estimate the permeability previously classified in classes. Considering that permeability is a non-additive variable and the main interest is to map extreme values, and knowing that kriging is not an adequate estimator of extreme values, the multi-phase indicator formalism is more suitable for permeability estimation. Concerning estimation of fluid saturation, this research work proposes an approach based on a single coordinate transformation to the

referential of the free water level (FWL). This single transformation is able to cope with the problem of non-stationarity displayed by this variable in the oil fields.

Section four is dedicated to the characterisation of spatial uncertainty in permeability, provided by stochastic simulation. Due to the non-additive nature of permeability and the major importance of extreme values, the simulation follows a methodological sequence that combines sequential indicator simulation (SIS) and probability field simulation (*p*-field).

Section five deals with the interface between geostatistical models and the input to the fluid flow simulator. Two main aspects are reviewed in this section: the screening of realisations and the upscaling of permeability. As far as the screening of the realisations is concerned, the study proposes a single method using a ranking selection based on the volumes of geobodies of high and low permeability. Regarding the upscaling of permeability, this work proposes a technique derived from the traditional upscaling technique based on the pressure solver. The objective is to quantify and minimise the differences between fluid flows at small and corresponding large scales using a moving window that covers a set of neighbouring blocks of the current upscaling block. The upscaling of each block in each loop takes into account the neighbouring blocks and the values from previous iterations.

Finally, section six contains a final series of important remarks involving all methodologies described. The global set of techniques used in the framework of this research work is summarised in Table 1.1, which shows the main characteristics (variable name, data structure, input and outputs).

1.3 FIELD SELECTED: SUMMARY OF GEOLOGICAL CHARACTERISATION AND PETROPHYSICAL DATA

The studied reservoir is located in the Middle East. This reservoir is one of the most heterogeneous in the region, and for this reason has become a reference-framework for researchers associated with geology and reservoir engineering. The main geological structure of the field consists of a single lengthened anticline with a NE-SW orientation, measuring approximately 27 km along the major axis and 8 km at the perpendicular, corresponding to a surface area of about 160 km^2 (Craft and Hawkins, 1959; Gatlin, 1960, North, 1985). The geological structure of this reservoir is a carbonate rich sequence of *Maashtrichiana* age (Upper Cretaceous) deposited during an actively growing paleohigh in shallow marine subtidal to intertidal and supratidal conditions. Based on palaeontological information, this formation is sub-divided into two sub-units, Upper R1 and Lower (R2 plus R3), the Lower being sub-divided into two further sub-units (R2 and R3).

Table 1.1 List of proposed methodologies and main characteristics.

Variables	Methods	Sata structure	Inputs	Outputs	Group of methods	Section
Lithoclass	Sequential indicator simulation	Categorical	Samples location Marginal histograms Multi-phase variograms	Simulated images displaying the spatial variability of lithoclasses	Simulation	2
	Truncated Gaussian simulation plus subsequent conditioning					
	Simulated annealing					
Porosity	Zonal control estimation	Continuous	Samples location Multi-phase variograms Basic statistics Simulated images of lithoclasses	Estimated images of porosity conditioned to the images of lithoclasses	Estimation	3
Permeability	Zonal control estimation	Categorical (permeability classes)	Samples location Multi-phase variograms Basic statistics Simulated images of lithoclasses	Estimated images of permeability classes conditioned to the images of lithoclasses	Estimation	3
	Sequential indicator simulation plus p-field simulation	Continuous		Simulated images of permeability conditioned to the images of lithoclasses	Simulation	4
Water saturation	Ordinary kriging	Continuous	Samples location Water saturation variograms Depth and thickness of each layer	Estimated images of water saturation	Estimation	3
Permeability	Conditional upscaling	Continuous	Detailed images of permeability	Coarse grid images of permeability	Upscaling	5

The geological characterisation of the field involves interpretation of the intensive diagenetic alterations of the original carbonates (North, 1985). The interaction of the diagenetic cycles with tectonic activity led to the formation of a perceptibly layered sequence in the upper zones of the field named unit R1. This sequence is made up of porous and permeable carbonates alternating with clay beds. Each of these lithological units is relatively discontinuous. During the deposition of the Lower Units (R2 and R3), the interplay comprises dolomitization, sedimentation and tectonic activity, which led to overdolomitization and amalgamation at the crest, with thicknesses varying from 50 to 150 feet. These dolomites are impermeable, with a massive aspect, and the porosity occurs along cavities, particularly vugs and percolating fractures. These tight dolomites, located along the crest of the principal structure, are surrounded by porous dolomites (sucrosic dolomites) along the flanks.

In the Upper unit, the depositional conditions changed and, as a consequence, the beds are more clearly defined and observed. However, it is difficult to correlate the numerous beds identified in wells throughout the field, due to a sharp variation in thickness (between 5 and 20 feet). Thickness increases from crest to flanks along all the structure and in all directions, although more quickly in the longitudinal direction of the anticline (NW-SE). These variations, associated with the depositional process, justify the need for a transformation of coordinates. This transformation was carried out on all well data before running stochastic models. The only exception was the saturation model, where a different transformation method was applied due to a deterministic factor (capillary pressure) that conditions the vertical distribution of fluids.

Based on well data (logs and cores) a detailed classification of the rocks was established. Eight layers were identified in the Upper Unit of the field (R1 Unit) and initially six in the Lower Unit (R2 plus R3), making up the 14-layer model initially identified which forms the basis of the initial geological study. The above six layers were further redefined and finally 17 layers were identified, in addition to the 8 layers for the Upper Unit (see Figure 0.1). Additionally, a new unit was added to the basis, characterised by its accumulation of oil.

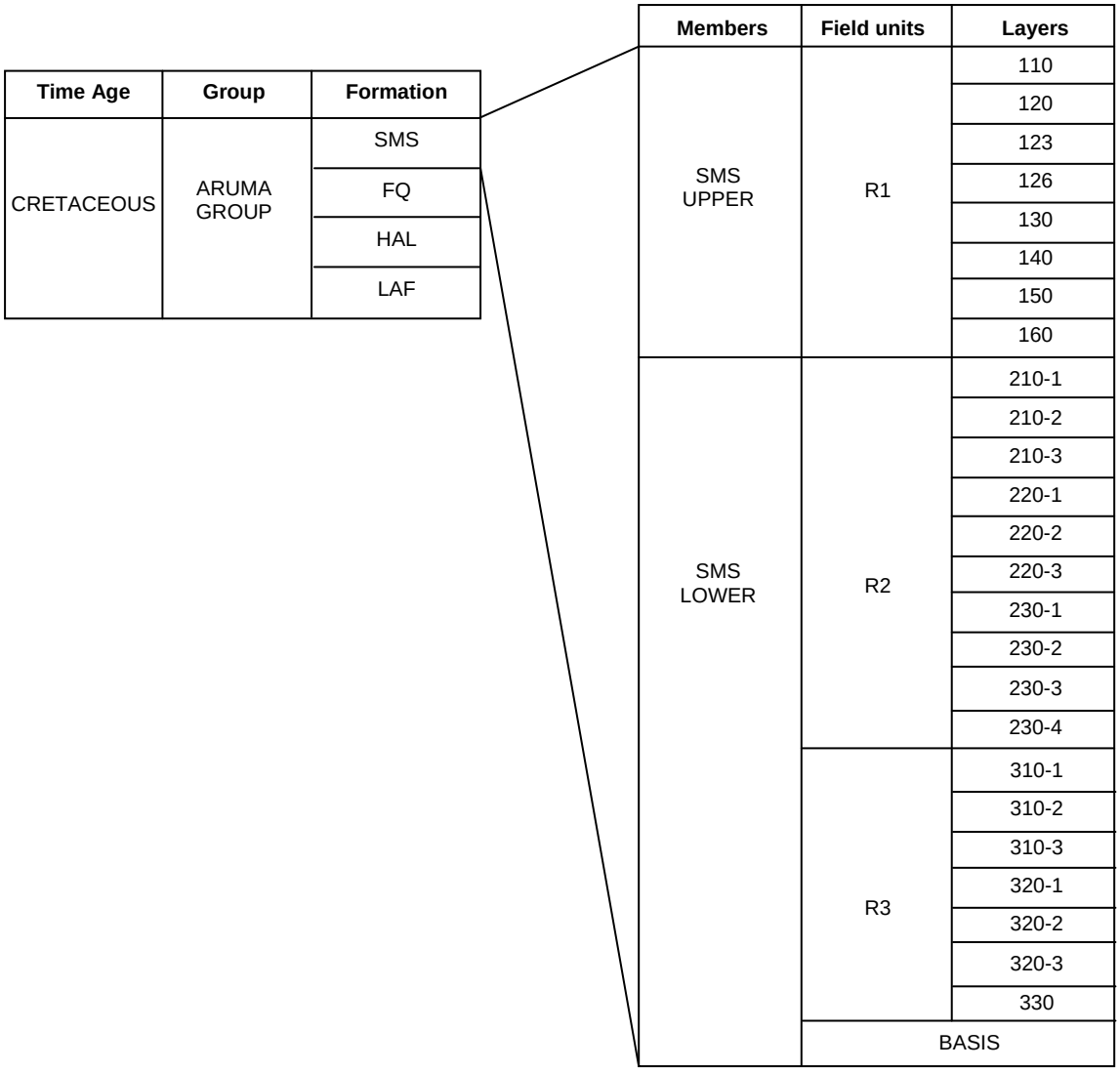

Figure 0.1 Stratigraphic representation and vertical zoning of the studied field: sequence of reservoir units: R1, R2 and R3.

From the first studies it was observed that this field is particularly complex, showing sharp variations in petrophysical properties for both vertical and horizontal directions. These variations are the result of the combination of a complex depositional scenario, influenced by syndepositional structural development, with an elevation followed by erosion due to meteoric waters and evaporites of diagenetic origin, associated with post-depositional diagenesis. For all these reasons, strong variations in the petrophysical attributes are clear throughout the field (porosity, permeability and, in addition, saturation) as well as the thickness of each layer or stratum.

Due to the wide range of values displayed by the petrophysical characteristics within each rock type and inside each layer, it was necessary to take into account an additional sub-

division of the lithologies, based on the following parameters: rock type, capillary pressure variations in the stratigraphic column and porosity and permeability. The concept of lithoclass was introduced in order to represent spatial areas with high homogeneity of porosity and permeability and represented by a typical capillary pressure curve, obtained in laboratories through core analysis procedures.

Due to the great heterogeneity in this particular oil field, it is difficult to perform a classification into lithoclasses that simultaneously lead to an internal small range variability concerning these variables, which are discordant most of the time. However, the classification into lithoclasses is considered a suitable basis for the implementation of a stochastic model, rather than using a few and more heterogeneous lithologies. The discordance involving these parameters and the high heterogeneity means that only around half of the lithoclasses present significant spatial continuity within each layer.

Well data came from 19 vertical wells (see geographical representation in Figure 0.2) that cross all identified units and allow the identification by geologists of the 20 lithoclasses. Table 0.1 lists all identified lithoclasses and displays the corresponding rock type and indicative values for porosity and permeability. One important point to note is that, in the same geological unit, the entire set of lithoclasses do not appear simultaneously (maximum observed is 17, but usually less than 10 occur), which contributes to the construction of a model showing a remarkable vertical zonation, as described by the geology and observed in the marginal histograms.

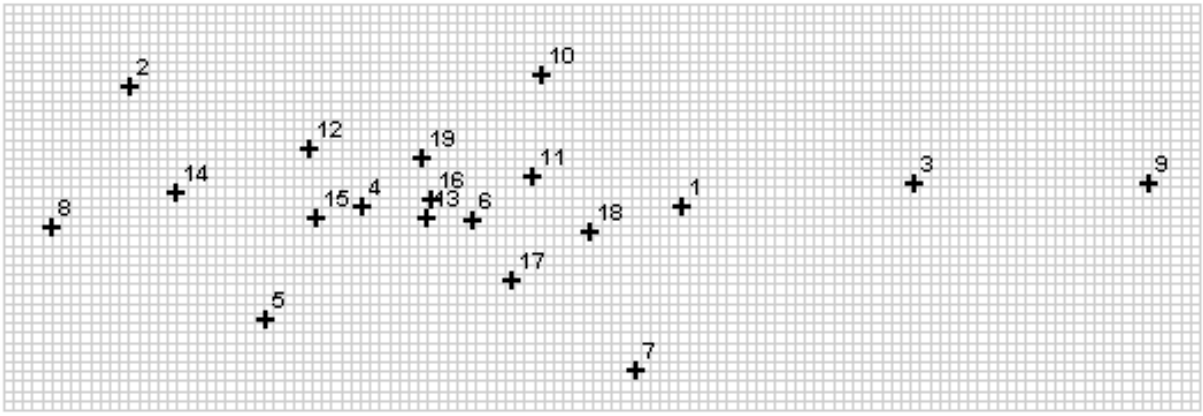

Figure 0.2 Aerial view of the entire field with superposition of the stochastic simulation grid and well locations.

Each well was sampled at intervals of 1 foot and is now represented by a categorical sequence of geological formations - lithoclasses. Lithoclass unit (LCU) or statigraphic unit

(S.U.) designates each one of these intervals. Each unit is described by a set of variables derived from core or log analysis, among which the most important are porosity, permeability (core permeability - horizontal and vertical - and log derived permeability by correlation with porosity) and fluid saturation. The proportion of wells with cores varies from 20 to 80 % approximately, depending on the layer.

Table 0.1 Lithoclasses identified in the present oil field: typical rock types and porosity and permeability average ranges.

Lithoclass	Rock type	Porosity[1] (%)	Permeability[1] (mD)
1	Shale	0.0	0.0
2*, 3	Mudstone	4.0	0.5
4,5*,6	Mudstones to wackestones	7.5	0.9
7*	Wackestones	15	1.5
8*,9*,10,15	Mouldic dolomites	25.5	29.5
11,12*,13,14*	Grain to packstones	25	68
20,21*,22*	Tight dolomites	15	4.2
23*,24*	Sucrosic dolomites	25.5	1250

* - Dominant lithoclass

The stochastic models presented in this study characterise the reservoir properties in a discrete grid of points, covering the volume, which bounds the entire reservoir. The unitary block in the grid selected for the stochastic model is 250 by 250 m in both X and Y directions and 1 foot in the vertical direction. Taking into account the dimensions of the reservoir, the total number of blocks is laterally 124 in the X direction and 42 in the Y direction. The number of blocks in the Z direction depends from the maximum thickness of each layer.

[1] Illustrative values

2 STOCHASTIC MODELLING OF LITHOCLASSES

2.1 DEFINITION OF LITHOCLASSES

One of the most critical steps in the construction of a reservoir flow simulation model is the description of the reservoir geology. To describe reservoirs characterised by high complexity, conceptual and deterministic geological models are, in most cases unable, to represent the internal geometry of the reservoir adequately. In fact, they ignore spatial zoning effects derived from the irregular distribution of the heterogeneities, and as a consequence they do not represent the actual connectivity and flow patterns. The concept of heterogeneity is very complex, but it has commonly been associated with predominant spatial random transitions and patterns evidenced by geological formations and/or petrophysical properties.

The stochastic simulations of geological units in this heterogeneous reservoir were based on an initial descriptive geological model of the reservoir. Core analysis available in a limited number of wells provided detailed information on the geological formations. Usually with this information it is possible to provide a first geological classification into rock types. However, in very heterogeneous reservoirs a wide range of porosity and permeability can be found for the same rock type, which constitutes a considerable challenge when mapping extreme values of the petrophysical properties. To cope with the geological complexity and to assist in understanding the internal distribution of properties, the concept of lithoclasses was introduced in this oil field. Lithoclasses were identified from cores based on their lithology, petrophysical properties and capillary pressure. The stochastic simulation of the geological units performed in the present work consists in the spatial simulation of this lithoclasses as categorical variables.

Four main sources of heterogeneity were found in the oil field studied (which are of course the same sources that can be found in similar heterogeneous oil fields) (Da Costa e Silva and Soares, 1994): heterogeneity between layers, lithological changes within each layer, geometric arrangement of lithoclasses, and some petrophysical variability inside lithoclasses. The high degree of variability in petrophysical properties, mostly between lithoclasses, suggests that this spectrum of variation covers a wide range and that the modelling approach should cope with this complexity. Bearing this goal in mind, the stochastic modelling of reservoir properties followed in this case study includes two main steps: the geometry of the lithoclasses is simulated first, and then the spatial characterisation of the petrophysical variables is performed within each simulated lithoclass.

Following this methodology, a geostatistical or stochastic simulation model for the geological characterisation of heterogeneous fields is proposed in the present section.

Once a set of simulated images of the distribution of lithoclasses is generated, the next critical step is to fill each one with the petrophysical properties (permeability, porosity and water saturation). Each stochastic image or realisation must honour the experimental data, the real proportions of each lithoclass, and the spatial continuity revealed by experimental variograms.

2.2 SPATIAL SIMULATION OF LITHOCLASSES

2.2.1. INTRODUCTION

Stochastic simulations consist of a set of methods able to generate numerical models or realisations of the spatial distribution of a categorical variable (for example, geological units, lithotypes, etc) or a numerical variable (porosity, permeability, water saturation, etc.). The set of outputs consists of equally probable images in the sense that they have the same probability of occurrence (Matheron *et al*, 1987, Journel and Alabert, 1988, Journel and Hernandez, 1989, Perez and Journel, 1990, Goovaerts, 1994, 1996).

As has been demonstrated in several case studies, these models are based on a probabilistic formalism and have proved to be the most suitable to describe spatial heterogeneity in oil fields. The use of stochastic models enables this intrinsic complexity to be modelled and equally probable scenarios of the internal architecture of the reservoirs to be predicted, mainly in inter-wells or low conditioned areas. In fact, these techniques allow a set of different equally probable images of the spatial distribution of the main petrophysical properties that describe the oil fields, namely lithologies, lithogroups, permeability and porosity, to be created based on a small amount of data extracted from an experimental data set.

All the steps involving the development of these models, mainly data preparation and interpretation, constitute a multidisciplinary task, which entails the cooperation of several teams, ranging from geology and seismic studies to reservoir engineering. These different spatial output images constitute the input of the fluid flow simulators (a transfer function), helping to develop dynamic simulation studies that can lead to a better management of fields over their productive life.

The methodological approach for the characterisation of an oil field using geostatistics can be sub-divided into two main sequential steps. The first step consists in simulation of the

morphology of geological units using categorical simulation algorithms. The second step consists in a subsequent estimation of petrophysical variables within each layer, using local conditioning to the previous simulated geological units. The result of the first step consists of a set of equally probable geological images representing the heterogeneity among lithoclasses.

The implementation and application of a geostatistical method (sequence) must take into account the existing heterogeneities and if possible their sources. The use of a two-step methodology as outlined above implies that the model will cope with the main sources of heterogeneity: heterogeneity among and within lithoclasses. The other two important sources of heterogeneity (heterogeneity between layers and geometric arrangement between lithoclasses) are achieved by these methods: independent simulations performed in several layers using spatial continuity analysis give rise to a measure of uncertainty (see section 4).

The practical application of these methodologies must comply with the Conceptual Geological Model that describes the internal architecture of the reservoir. This association of procedures (conceptual geological description and stochastic model) proved to be an advantage in most case studies. First of all, geostatistical models deal with continuity measures, which is their major advantage. The possibility of generation of multiple equally probable images and the integration of different sources of information are equally important advantages. On top of that there are other advantages, such as matching of experimental data, basic statistics and continuity measures. Given the lack of data and additional information in inter-well areas, the use of this type of model can also be justified by the need to generate multiple images, which constitute one practical way to characterise the uncertainty in oil fields.

2.2.2. GENERAL DESCRIPTION OF GEOSTATISTICAL SIMULATION ALGORITHMS FOR CATEGORICAL VARIABLES

Many algorithms to perform stochastic simulations of categorical variables have been described in the literature with different backgrounds. Examples of stochastic simulation algorithms used to create equally probable images of the internal architecture of a categorical set include Boolean models (object-based models) (Ripley, 1987, Haldorsen *et al*, 1988, Omre *et al*, 1990, Deutsch and Wang, 1996, Soares and Brusco, 1997), truncated Gaussian field plus subsequent conditioning (Deutsch and Journel, 1992, Journel and Huijbregts, 1978, Da Costa e Silva *et al*, 1991), sequential indicator simulation (Journel and Alabert, 1989) and the more recent simulated annealing (Deutsch and Journel, 1992). It is

also possible to combine these individual techniques to solve various questions in particular cases. Bearing in mind the diversity of methods, which is the most appropriate?

The answer to this fundamental question depends on each particular case study. Any method has advantages and drawbacks depending on the theoretical formulation and its suitability to the specific features of the case studied. In a general way any method can be used so long as it can integrate all the available information and ensure that (depending on the volume of work) (Deutsch, 1994):

- The simulation runs in a realistic period of time;
- Several aspects evidenced by the samples can be matched. These aspects are dependent on the available amount and diversity of information (geological information, seismic interpretations, production well data, etc.) and the major goals defined for the study;
- It puts a wide spread of uncertainty in the final images conditioned by the experimental data and quantifies that uncertainty.

All algorithms involved in a stochastic simulation study are designed to match a set of measures revealed by the experimental data. The final images should reproduce the variable statistics, the patterns revealed by the experimental samples, the geological conceptual trends, the information from the seismic images (soft data) and even some features of analogous fields and outcrops. The possibility of imposing some additional constraints depends on the way they can be numerically expressed.

Usually, with a geostatistical simulation model one intends to reproduce in the final images the spatial variability of the phenomena, by imposing the two following statistics: the probability distribution function and the variogram or multi-phase variogram. When dealing with a categorical set (multi-phase set), the final simulated images must honour the following aspects: i) the proportion of each phase $m_i = m_{S_i}$, (*i=1,…K* phases) as evidenced in the initial data set; ii) the spatial continuity as revealed by the individual or multi-phase variograms $\gamma_i(h) = \gamma_{S_i}(h)$; iii) at each experimental data location x_α, the simulated images have the same value $K_i(x_\alpha) = K_{S_i}(x_\alpha)$.

The set of resulting images is named equally probable in such a way that all images have the same probability of occurrence and reproduce the two main statistics - the probability distribution function and the variogram - and finally match the experimental data.

Basically two main groups of algorithms for stochastic simulation can be found in the literature: simulation with independent conditioning and sequential simulation. One additional group can be considered - simulated annealing - based on the background concept of “trial and error”. This generic classification can be applied both to categorical (single or multi-phase sets) and continuous variables. However, later in the present section, we assume dealing with categorical variables.

Independent conditioning simulation groups a set of techniques, which are based on a simulation process independent of the posterior conditioning process. Basically these methods have two main steps: non-conditional simulation and posterior conditioning. The non-conditional simulation can be any one since the result consists in a non-conditional categorical simulation that reproduces the two main statistics – the probability distribution function and the variogram. The conditioning step is based on a spatial estimation of errors, leading to the designation of ESE: estimation plus simulated errors. One method of this group, to deal with categorical or multi-phase sets, is named truncated Gaussian simulation plus subsequent conditioning approach or morphological simulation (Journel and Isaaks, 1984, Da Costa e Silva *et al*, 1994, 1997).

Sequential simulation methods belong to a relatively new family of simulation algorithms based on a sequential approach (Journel and Alabert, 1988). When dealing with categorical variables the method is sequential indicator simulation.

The use of methods based on simulation annealing algorithms to perform the simulation appears as an alternative way of simulation or as a post-processing in association with conventional processes. In a more general context, one can denote as simulated annealing a class of algorithms based on a solution of an optimisation problem (Aarts and Korst, 1989, Farmer, 1992, Sen *et al*, 1992, Almeida[a], 1996). This process is based on an evolution of the system towards the minimisation of an objective function that describes the final and appropriate state following a perturbation mechanism and evaluating the consequences in a “trial and error” iterative sequence.

2.2.3. GEOSTATISTICAL SIMULATION METHODOLOGY USING A MULTI-PHASE FORMALISM

The multi-phase concept represents the continuity and transitions of a set of phases using a global continuity model. Instead of assuming the probability of two points separated by *h* belonging to a particular phase *A* or *B*, the covariance assumes the probability of two points separated by *h* belonging to the same phase whatever it may be. From a spatial analysis

point of view, this average measure is conceptually weaker than individual covariances, but in most cases it is the only tool to properly model simultaneously heterogeneous and undersampled reservoirs, without assuming prior simplifications that may misrepresent the field characteristics. In the present section an experimental procedure is proposed involving a set of algorithms that can be chosen depending on the conditioning effect and computing time. Basically, two main simulation algorithms are proposed each of them encompassing two alternatives. A final post-processing is suggested to improve the variogram match and the conditioning effect.

The complete simulation approach is described below and comprises three main methodological steps (see flow chart in Figure 2.1):

- First, identification of the present phases and construction of a multi-phase variogram as a spatial continuity tool;
- Stochastic simulation of the set of lithoclasses;
- Finally, checking of the imposed statistics and the data conditioning process through visual validation of the output images.

Following the proposed flow chart in more detail, the first step involves the following sub-tasks:

1. Identification of lithoclasses and transformation of categorical variables into indicator multi-phase vectors;
2. Computation of individual indicator variograms for each lithoclass, along different preferential directions (major and minor directions of the reservoir, vertical direction);
3. Identification of groups of lithoclasses with similar characteristics in terms of continuity. In the present case study this implies the spatial simulation of the morphology of a multi-phase heterogeneous set, being identified by two groups with very distinct continuity measures along the horizontal direction within each layer. One clearly shows continuity greater that 2000 metres and the other is characterised by no evidence of any continuity;
4. Computation of experimental multi-phase variograms for the two groups along the preferential directions and fitting a theoretical model to the experimental values for both groups;
5. Stochastic simulation of categorical variables;

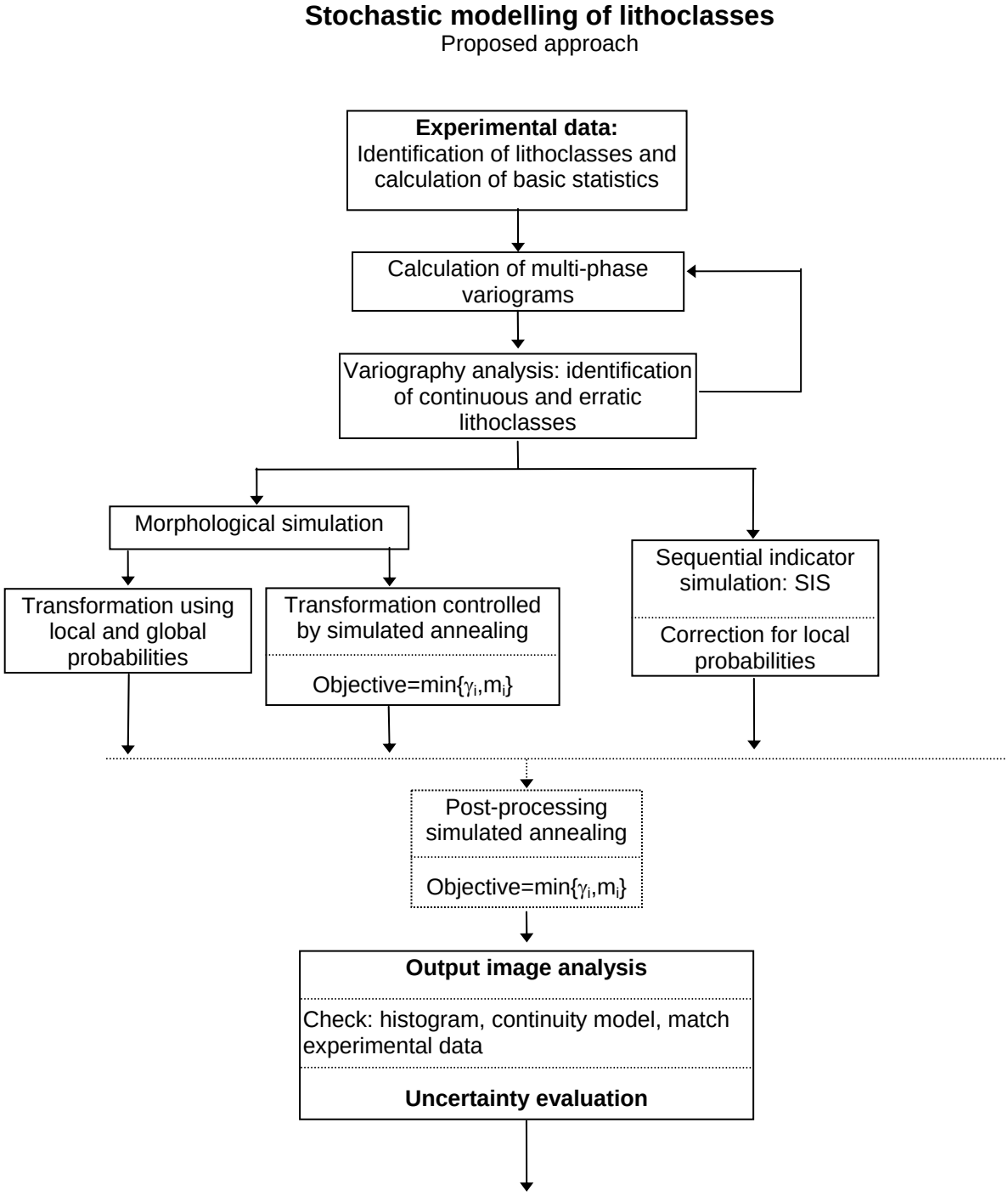

Figure 2.1 A flow chart illustrating the proposed experimental steps for the generation of stochastic images of lithoclasses.

The first method proposed, named morphological simulation, is based on the truncated Gaussian field model with posterior and independent conditioning to the experimental data. The output consists of maps representing the probability of each grid node belonging to each identified category or to each lithoclass (in the context of this particular case study). These values must be transformed into indicator values following one of the two proposed algorithms: i) morphological classification based on local and global probabilities; ii) one

alternative method that combines the conventional process based on local and global probabilities with the simulated annealing technique. This method performs a transformation controlled by one objective function that computes in each loop the bias between the continuity models (theoretical and experimental) and the proportions of each phase.

The second method proposed is based on sequential indicator simulation (SIS) extended to multi-phase structures. The basis of the algorithm includes the correction for local probabilities proposed by Soares, 1998. The objective is to minimise deviations between the objective probabilities and simulated proportions. These deviations occur at times, especially when long range variograms in phases evidencing small proportions were used. Outputs of this method consist of morphological multi-phase maps conditioned to the experimental data.

6. Post-processing using simulated annealing;

Any of the above categorical simulated maps could be post-processed using the simulated annealing algorithm in order to improve initial patterns or to incorporate additional constraints. It is possible to apply this algorithm to completely random images and the result will be one simulated image matching the required parameters. However, bearing in mind the particular background of this method (massive use of CPU due to intensive calculations) it is recommended to use one initial image partially matching the required parameters and use the simulated annealing in a post-processing step.

7. Analysis of the outputs.

This consists in checking of the parameters to be honoured: the proportions of each lithoclass and the continuity model and verifying if the simulated points match the experimental values. Other equally important aspects, like the shape uncertainty evidenced when performing several realisations, some zoning effects and contacts between lithoclasses and the extension of the continuity evidenced by each lithoclass, must also be analysed and validated, based on geological, geophysical and reservoir knowledge.

In order to rank outputs based on an entropy measure, 30 realisations were performed using the proposed methods: i) sequential indicator simulation with correction for local probabilities; ii) morphological simulation plus classification based on local and global probabilities; iii) morphological simulation plus classification using simulated annealing. All 30 images resulting from sequential indicator simulation were post-processed by simulated annealing and the entropy of all these images was calculated. In this test it is possible to evaluate the conditioning effect derived from simulated annealing.

2.3 MULTI-PHASE VECTOR VARIABLES

2.3.1. DEFINITION OF AN INDICATOR VECTOR VARIABLE

The basic idea of the proposed methods is to use the framework of indicator random functions to spatially describe the X_k, *(k = 1, K)* lithoclasses - where *K* denotes the number of categories or phases. At each spatial location *x* and according to the vertical sub-divisions in layers, all lithoclasses were coded as a non-ordered indicator vector X_k to all phases, *(k = 1, K)* (see Figure 2.2):

$$I_k(x) = \begin{cases} 1 & \text{if } x \text{ belongs to phase } X_k \\ 0 & \text{if } x \text{ belongs to phase } X_j \text{ with } j \neq k \text{ and } k = 1,K \end{cases} \qquad (2.1)$$

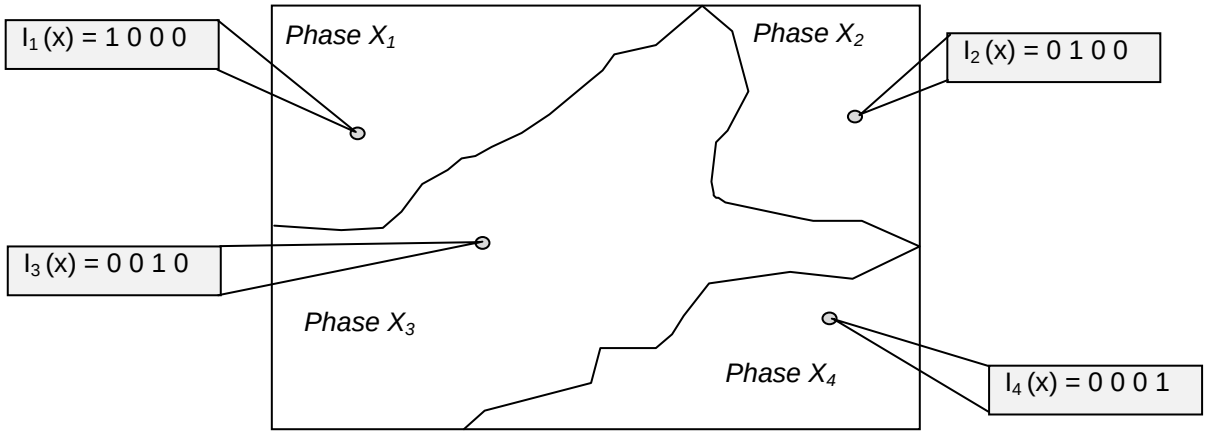

Figure 2.2 Codification into an indicator vector.

In the framework of a stochastic model, the indicator vector or variable at each point *x*: *{$I_1(x)$, $I_2(x)$, $I_3(x)$, ... $I_k(x)$}* can be interpreted as the probability of a point *x* belonging to one lithoclass X_k, *k = 1, K*, and can be used as a random variable located at *x*.

$$I_k(x) = prob\{ x \in phase\ k \}, \quad \forall\ k = 1, K \qquad (2.2)$$

The set of *N* samples in area *A* were coded in all possible combinations of "*1*" and "*0*" and can be interpreted as a realisation of a random function $I_k(x)$.

The realisation $I_k(x_i)$, $i = 1, N$ of the random function $I_k(x)$ has the two following moments:

a) Mean of each phase m_k : measure of the proportion of each phase X_k in all area A:

$$m_k = \frac{1}{N}\sum_{i=1}^{N} I_k(x_i) \tag{2.3}$$

b) Variance of each phase σ_k^2

$$\sigma_k^2 = \frac{1}{N}\sum_{i=1}^{N}(I_k(x_i) - m_k)^2 = m_k(1 - m_k) \tag{2.4}$$

Important remarks:

- The values of $I_k(x)$ are usually dichotomous, which means that each point x belongs only to one category or lithoclass. However, it is possible to include points with an associated uncertainty degree of belonging to a set of phases. In these cases, the meaning of probability is preserved and the same concepts can be applied;
- The terms of the indicator vector have no order relation between them.

2.3.2. SPATIAL CONTINUITY CHARACTERISATION

The spatial continuity of each phase in area A can be measured using bi-point statistics, namely the covariance $C_k(h)$ of phase k, with ($k = 1, K$) number of phases:

$$C_k(h) = E\{I_k(x).I_k(x+h)\} - m_k^2 \tag{2.5}$$

or the equivalent indicator variogram:

$$\gamma_k(h) = \frac{1}{2}E\{I_k(x) - I_k(x+h)\}^2 \tag{2.6}$$

with:

$$C_k(h) = \sigma_k^2 - \gamma_k(h) \quad \text{or} \quad C_k(0) - \gamma_k(h)$$

When dealing with multi-phase sets the amount of data is usually insufficient to estimate all individual covariances or variograms. In these cases or when it is not possible to calculate spatial continuity models for each phase (which is normal when dealing with a set of phases in undersampled oil fields), Soares (1992) proposed using a global model which synthesises the spatial continuity of all sets of lithoclasses - multi-phase covariance. This means the probability of two points separated by *h* belonging to the same phase. The multi-phase covariance can be calculated by:

$$C(h) = E\left\{\sum_{k=1}^{K}\left[I_k(x).I_k(x+h)\right]\right\} \tag{2.7}$$

and the equivalent multi-phase variogram:

$$\gamma(h) = \frac{1}{2}E\left\{\sum_{k=1}^{K}\left[I_k(x) - I_k(x+h)\right]^2\right\} \tag{2.8}$$

Obviously, the application of a unique model to a mixture of different structures should be avoided. In some case studies, depending on the number of samples and phases, it is not possible to join all calculated individual covariances or variograms into a unique model. In these cases (for example, when we have many lithoclasses in a heterogeneous field), the entire set of lithoclasses must be characterised by more than one multi-phase variogram, usually no more than two.

Denoting as *N(h)* the number of pairs of points separated by *h*, the multi-phase variogram can be directly estimated using *N* experimental indicator vectors ($I_k(x_i)$, $k = 1, K$; $i = 1, N$) using the following expression:

$$\gamma(h) = \frac{1}{2N(h)}\sum_{i=1}^{N(h)}\left\{\sum_{k=1}^{K}\left[I_k(x_i) - I_k(x_i+h)\right]^2\right\} \tag{2.9}$$

Both covariance and variogram can be decomposed by the sum of the individual covariances or variogram:

$$C(h) = \sum_{k=1}^{K}C_k(h) \quad \text{and} \quad \gamma(h) = \sum_{k=1}^{K}\gamma_k(h) \tag{2.10}$$

Once one or a set of experimental variograms have been calculated, the continuity modelling process follows the conventional sequence of steps:

- Find anisotropies between the different directions;
- Fit the experimental points with a theoretical model, usually a spherical or exponential function type.

In fact, multi-phase continuity can be modelled by the classic variogram parameters: range, nugget effect, main and minor directions and anisotropy relations. All these parameters have a different but determining influence on the simulated images. For instance, range gives an average of the lengths of the geobodies, and the relations of anisotropy reflect the variations of these measures along different major directions. The nugget effect is a measure of the transitions at a short scale and as a consequence reflects heterogeneity at very small distances. When the nugget effect is high, the consequences in the output images are remarkable and can be observed in the increasing number of transitions at a small scale and the irregularity of the contour-shape - the image appears more irregular or random.

2.4 SIMULATION OF MULTI-PHASE STRUCTURES

In the following sections, morphological simulation, multi-phase sequential indicator simulation and simulated annealing post-processing will be succinctly described, noting various improvements performed in each methodology to run this particular case study.

The practical implementation was performed using both routines provided by GSLIB software (Deutsch and Journel, 1992) with some modifications (for example SISIM and SGSIM) and geoMS (geostatistical modelling software developed by CMRP, Rodrigues *et al*, 1998) with modules developed in the scope of this study.

2.4.1. MORPHOLOGICAL SIMULATION

2.4.1.1. TRUNCATED GAUSSIAN SIMULATION PLUS POSTERIOR CONDITIONING APPROACH

Morphological simulation approach belongs to a set of methods that split the simulation in two distinct and consecutive steps: a non-conditional indicator simulation followed by a posterior conditioning. For a multi-phase set, it can be applied according to the following sequence of steps (see Figure 2.3):

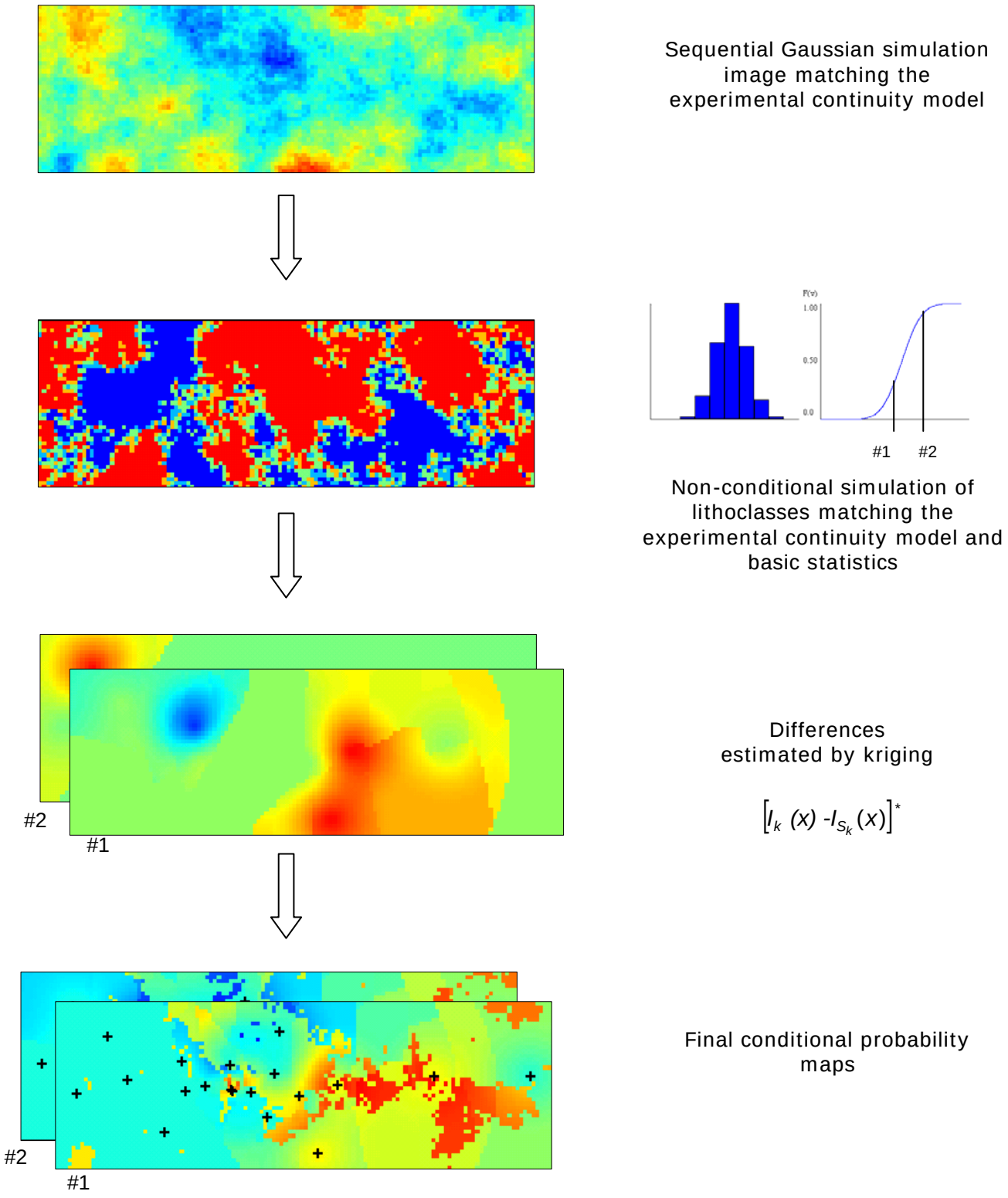

Figure 2.3 Sequence of steps to perform a non-conditional indicator simulation followed by a conditional step.

i) A non-conditional Gaussian simulation $Y_S(x)$ is performed covering the entire volume of the layer using the theoretical model fitted to the experimental multi-phase variogram, plus a transformation. Several algorithms provide a Gaussian simulation, including non-conditional sequential Gaussian simulation (Deutsch and Journel, 1992) and the turning bands method (Journel, 1977, Journel and Huijbregts, 1978, Dowd, 1979, Sousa, 1983).

During this non-conditional step, a Gaussian transformation of the experimental indicator data is not required. Indeed, this transformation is not possible when dealing with categorical variables (Gaussian transform of a non-continuous distribution). It is important to point out that only transformation of the indicator multi-phase variogram is required to accomplish this step.

Calculation of the variogram of $Y_S(x)$ can be achieved in several ways. For instance, Journel and Posa, 1990 propose a heuristic model for indicator variogram transformation.

Journel and Isaaks, 1984, propose the use of the following relation, which can be applied to multi-phase sets:

$$\gamma_{Y_S}(h) = L^{-1}\left[y, y, m_k - \gamma_k(h;y)\right] \text{ or } \gamma_{Y_S}(h) = 1 - L^{-1}\left[y, y, (1 - G(y)) - \gamma_k(h;y)\right] \quad (2.11)$$

where:

$\gamma_{Y_S}(h)$ - variogram of $Y_S(x)$

L - the standard bivariate normal distribution (tabulated in *e.g.* Abramovitz and Stegum, 1972)

y - the cut-off value in the Gaussian set of values: $y = G^{-1}(1 - m_k)$

G - is the distribution function of $Y(x)$ - Gaussian distribution function

m_k - proportion of phase k

Another approach is based on the hermitian polynomial development proposed by Matheron, 1987:

$$\rho_I(h) = (g(y))^2 \sum_{n=1}^{\infty} \left(\frac{H^2{}_{n-1}(y)}{n!}\right) \rho_Y{}^n(h) \quad (2.12)$$

with:

H_n - hermitian polynomial of order *n*

g(y) - the standard Gaussian density function

$\rho_I(h)$ - correlogram of the indicator variable for a distance *h*

$\rho_Y(h)$ - correlogram of the Gaussian values for a distance *h*

ii) Truncation of the Gaussian simulated variable $Y_S(x)$ in *K* classes, using (*K-1*) thresholds y_{c_k}, calculated according the experimental means of the phases:

$$y_{c_k} = G^{-1}(1 - m_i) \text{ with} \tag{2.13}$$

$$m_i = \sum_{k=1}^{i} m_k \tag{2.14}$$

In the above expression, *G(x)* denotes the Gaussian probability distribution function pdf and m_i and m_k respectively the cumulative and the experimental mean of each phase *k*.

These thresholds are obtained by calculation of the $G^{-1}(x)$ using polynomial approximations of the Gaussian pdf (Abramowitz and Stegun, 1972). Alternatively the $Y_S(x)$ simulated values can be ranked by decreasing order and the threshold value that correspond to the calculated one can be picked directly, using the experimental proportions.

Applying the above cut-offs with the $Y_S(x)$ leads to a non-conditional indicator simulation:

$$I_{S_k}(x) = \begin{cases} 1 & \text{if } y_{c_{k-1}} \le Y_S(x) < y_{c_k} \\ 0 & \text{otherwise} \end{cases} \tag{2.15}$$

The simulated values $I_{S_k}(x)$ reproduce the global multi-phase variogram model.

iii) Conditioning step

The final conditioning process aims to condition the simulated images to the experimental sample values and to reproduce the spatial patterns imposed by the experimental samples. In this regard, the conditioning step should not be performed with the Gaussian values since, as has been already, it requires the Gaussian transformation of indicator values, which in all

rigour is not possible. In the technique proposed the conditioning phase is performed with the indicator data.

In this critical step, the multi-phase kriging technique is applied for conditioning the simulated values to the experimental data. The simulated values $I_{S_k}(x)$ are conditioned to the experimental values $I_k(x_\alpha)$, $\alpha = 1, N$ via the classical relation where the final conditional map $I_{S_k}{}^c(x)$ is equal to the estimated map $I_k^*(x)$ plus a simulated error $e_S(x)$:

$$I_{S_k}{}^c(x) = I_k{}^*(x) + e_S(x) \tag{2.16}$$

with

$$e_S(x) = I_{S_k}(x) - I_{S_k}{}^*(x) \tag{2.17}$$

The two multi-phase kriging estimations $I_k{}^*(x)$ and $I_{S_k}{}^*(x)$ are calculated with the same global multi-phase covariance:

$$I_k{}^*(x) = \sum_\alpha \lambda_\alpha . I_k(x_\alpha) \tag{2.18}$$

$$I_{S_k}{}^*(x) = \sum_\alpha \lambda_\alpha . I_{S_k}(x_\alpha) \tag{2.19}$$

and can be summarised to the estimation of the difference:

$$\left[I_k(x) - I_{S_k}(x)\right]^* = \sum_\alpha \lambda_\alpha \left[I_k(x_\alpha) - I_{S_k}(x_\alpha)\right]$$

The values $I_{S_k}{}^c(x)$ have the meaning of the probability of a point x belonging to each phase X_k: for each simulated point x, the sum of $I_{S_k}{}^c(x)$ is equal to one, and the values are in the range 0 to 1.

iv) After the simulation of $I_{S_k}{}^c(x)$ the probability of a point x belonging to the phase k - for all points x_0 inside the area A, the final step consists in a classification of each point x_0 to the most probable phase - which means transforming each probability value $I_{S_k}{}^c(x)$ into an indicator value.

To perform this final step, two different methods based on the values of $I_{S_k}^{c}(x)$ were followed and the corresponding results are further compared:

- The first classification is based on the local and global probabilities belonging to phases X_k ($k = 1,K$) (Soares, 1992, Almeida *et al*, 1993);
- The second consists of using the simulated annealing technique to obtain the shape of each unit with spatial variability as revealed by the multi-phase variogram of $I_k(x)$.

2.4.1.2. TRANSFORMATION OF PROBABILITY MAPS INTO MORPHOLOGICAL MAPS USING LOCAL AND GLOBAL PROBABILITIES BELONGING TO PHASES X_K

The resulting simulated probability maps are transformed into morphological maps according to the twofold criteria: maximisation of local probabilities until the global probabilities are honoured. It can be summarised in the following sequence of steps:

i) For each phase, rank the total N local simulated probability values $I_{S_k}^{c}(x)$ in decreasing order. Hereafter, consider n_k, the number of grid nodes allocated to each phase in order to respect the required proportions:

$$n_1 = m_1 \, . \, N$$
$$n_2 = m_2 \, . \, N$$
$$\ldots$$
$$n_K = m_K \, . \, N$$

ii) Select and allocate to phase X_k the n_k highest values of $I_{S_k}^{c}(x)$ until the global proportion of phase X_k , (m_k) is reached, with $m_k = n_k / N$. The global proportion of each phase is expressed by the mean of the experimental indicator values. The transformation of the probability maps into morphological maps starts row by row: the highest value $I_{S_k}^{c}(x)$ of each phase: $I_{S_1}^{c}(x_\alpha)$, $I_{S_2}^{c}(x_\beta)$, ... $I_{S_k}^{c}(x_\gamma)$ is chosen and transformed until the absolute number of each phase n_k is reached.

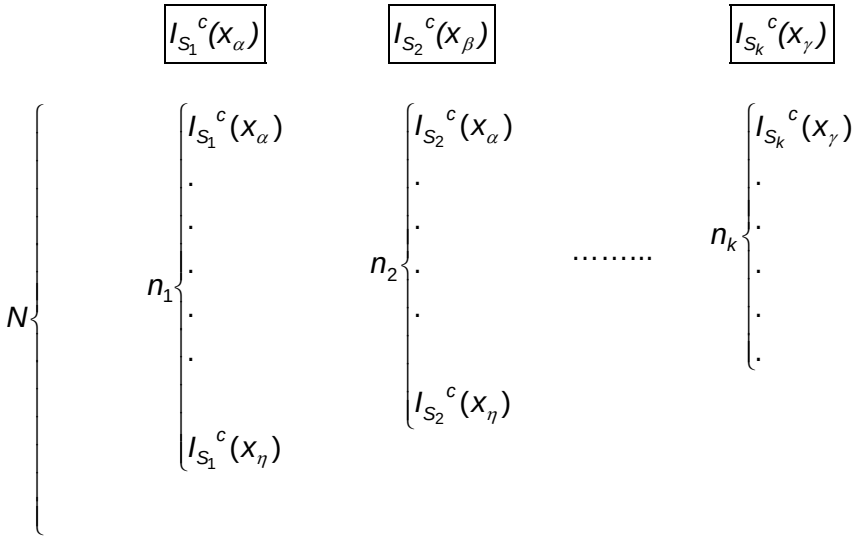

iii) When a point is spatially located in the transition zone of these phases (not conditioned inter-well areas) it can belong to more than one phase. The criterion to allocate the point is still based on the simulated highest probability of belonging to the phases. For example, the point x_η, spatially located in the transition zone between phases *1* and *2* can belong to both phases. Thus, if $I_{S_1}{}^c(x_\eta) > I_{S_2}{}^c(x_\eta)$ the point x_η is allocated to phase *1*; otherwise is allocated to phase *2*. Once x_η is allocated to phase *1*, the point is withdrawn from the ranked ordered vector of phase *2* and the next value corresponding to the $n_2 + 1$ position of rank ordered vector $I_{S_2}{}^c(x_j)$ is added to the phase *2*.

In this classification there is a balance between the maximisation of local probabilities and the global criteria of reproducing the estimated proportion of each phase X_k in area *A*. The main drawback of this approach is that during the transformation of probability maps into morphological maps the variogram of the output image can show some deviations from the theoretical model imposed, and as a consequence the final shapes of each phase X_k do not reproduce the spatial variability of the multi-phase variogram of $I_k(x)$. In order to overcome this important drawback, an additional criterion is proposed based on the definition of an objective function designed to minimise the deviations regarding the multi-phase indicator variograms and simultaneously to control the proportion of each phase.

2.4.1.3. USE OF SIMULATED ANNEALING TO CONTROL CLASSIFICATION

The basic idea of this class of algorithms is the analogy with certain thermodynamic processes, specifically how liquids or metals slowly cool and become solids. At high temperatures, the molecules that constitute these substances move freely. When cooling, molecules cease their free movement and begin to arrange themselves in crystals that correspond more appropriately to external conditions. This analogy can be completely transposed to the background of this class of algorithms. At the beginning - corresponding to high temperatures - every perturbation is usually accepted, although the objective function increases. With the evolution of the process - cooler temperatures - the probability of rejecting a perturbation that increases the objective function is higher.

The application of this technique firstly requires the choice of a property or set of properties that can be numerically expressed based on initial data or on training images derived from, for example, conceptual geological models or processed seismic data (Sen *et al*, 1992). An objective function is defined based on the weighted sum of the deviations between the set of statistics or a training image and the current state of the simulated image. The optimisation procedure consists in minimisation of the objective function in order that the simulated image will tend to reproduce the features included in the objective. It is always necessary to establish a perturbation mechanism in order to define an easier way to update the objective function. For example, in the particular context of the simulation of categorical variables, if one intends to impose the variogram as a statistical measure one must include this measure in the objective function.

In order to reproduce the spatial variability of the final shapes, an alternative way is proposed that uses the simulated annealing algorithm to perform and control the classification of probability maps.

In this simulated annealing procedure, the perturbation process starts from the highest local probability values of the phases X_k, $\max\left\{ I_{S_k}{}^{c}(x) \right\}$ and consists in transforming the simulated probability values into binary values. One perturbation consists in transformation of a probability value into one indicator value. In order to transform all values more quickly the usual perturbation based on swapping values was added. This method encompasses the following steps and matches the proportion of each phase and the multi-phase variograms (Deutsch and Journel, 1992, Deutsch and Cockerham, 1994).

i) definition of an objective function: in this particular case, the objective of the annealing process is a combination of two positive functions:

a) the square of the deviation between the theoretical variogram model (target) of $I_k(x)$ ($\gamma_{O_{i,k}}$) and the experimental variogram of simulated values ($\gamma_{i,k}$) after each perturbation;

b) the modulus of the deviation between the target estimated global proportion of each phase X_k and the equivalent statistic after each perturbation.

$$O = \sum_{k=1}^{K} \sum_{i=1}^{N_c} \lambda_i \ (\gamma_{i,k} - \gamma_{O_{i,k}})^2 + \sum_{k=1}^{K} (m_k - m_{S_k}) \qquad (2.20)$$

with:

O - objective function

K - number of phases

N_c - number of class distances

λ_i - weight of each class distance

γ - variogram function model

m_k *and* m_{S_k} - proportions of the phases in experimental data and simulated data

ii) Establishing a perturbation mechanism: following the highest values of probability, transition of a probability vector to a binary one (one phase equal to one and others equal to zero). The transition is selected by generating a random number p uniformly distributed between *0* and *1*: for example, for two phases X_1 and X_2, $I_{S_i}^{c}(x)$ is classified in X_1 if $p > I_{S_i}^{c}(x)$, otherwise it is classified in X_2. Following the decreasing sequence given by the probability values the process is much faster than the usual random perturbation;

iii) Re-calculation of the objective function after the perturbation;

iv) The perturbation will be accepted if the objective function decreases; otherwise the perturbation has a probability of acceptance given by the Gibbs distribution law. This process continues until the transformation of all estimated points, *i.e.*, the image is completely "cooled".

$$P\{accept.\} = \begin{cases} 1 \quad \text{if} \quad O_{new} \leq O_{old} \\ e^{1-\frac{-|O_{old}-O_{new}|}{c}} \quad \text{otherwise} \end{cases} \tag{2.21}$$

c - control parameter with analogy to temperature - During the evolution of the simulation *c* decreases slowly in order to avoid the cases leading to an increase of the objective function.

Important remarks:

- The speed of the cooling process increases if the sequence of points follows the decreasing order of the probability values, as a result of an initial ranking. This sequence is designed in such a way that the shape corresponding to each phase grows around several grid nodes (seeds), corresponding to the highest local probability values;

- In the case of a conditional simulation, the initial values of probability are naturally transformed into an indicator value; so, in these cases, the annealing process does not affect these points, which act as the main seeds for the growing of the shape of each phase.

2.4.2. SEQUENTIAL INDICATOR SIMULATION FOR MULTI-PHASE STRUCTURES

2.4.2.1. BACKGROUND DESCRIPTION

Based on the initial formulation of the sequential algorithm an extension for the sequential simulation of multi-phase structures is now explained. The background of the extended algorithm for multi-phase structures can be summarised as follows:

Consider the joint distribution of N random variables and n experimental and initial conditioning data: $F(N) = (Z_1, Z_2, Z_3, ...Z_N \mid n)$. The simulation of $F(N)$ can be performed through the Bayes relation in N consecutive steps and applying successive unitary increments to the conditioning data:

i) following a random path in area A, simulation of a value z_1 using the cumulative distribution function of Z_1. Once z_1 is simulated, this value is considered an additional conditioning data points and is added to the initial set of experimental data; the number of conditioning data points increases from n to $n+1$: $n + z_1$;

ii) simulation of a new value z_2 from the univariate cumulative distribution Z_2 based on the $(n+1)$ conditioning values. This new simulated value z_2 is added to the conditioning data, which increases from $n+1$ to $n+2$: $(n+1) + z_2$;

iii) repetition of this sequential process until the simulation of all N variables is performed.

If it is intended to simulate the same variable, the set of N dependent random variables $Z_1, Z_2, Z_3, ... Z_N$ can represent the same variable, spatially referenced in N regular grid nodes, over an area A. Considering the n initial and conditioning experimental data, the joint distribution of N random variables becomes:

$$F(N) = (Z(x_1), Z(x_2), Z(x_3),... Z(x_N) \mid (n)) \quad (2.22)$$

To perform the sequential simulation, it is necessary to know the N random cumulative and conditional functions:

$Prob \{Z(x_1) < z_1 \mid (n) \}$

$Prob \{Z(x_2) < z_2 \mid (n+1) \}$

$Prob \{Z(x_3) < z_3 \mid (n+2) \}$

...

$Prob \{Z(x_N) < z_N \mid (n+N-1) \}$

Lack of knowledge of these functions in practical cases is the main disadvantage in the implementation of this family of methods. Journel and Alabert, 1989, proposed the use of geostatistics to estimate these functions in spatial processes, particularly multi-Gaussian kriging for sequential Gaussian simulation and indicator kriging for sequential indicator simulation.

Initially, this method in the indicator form was developed for the simulation of binary structures. Let us examine in more detail the extension of the sequential indicator simulation algorithm for multi-phase structures. The practical implementation of this method can be performed using the following sequence of steps:

i) Select a random path that covers all non-simulated grid nodes;

ii) In any spatial location, the local probability of a point *x* belong to a different phase can be estimated by:

$$prob\left\{x_0 \in X_k \mid n\right\} = \sum_{\alpha} \lambda_\alpha I_k(x_\alpha) \qquad (2.23)$$

using a set of neighbouring samples of point *x*.

The weights are calculated according to the solution of the the multi-phase kriging system using the multi-phase variogram model or using individual models grouping, or not grouping, sets of phases.

iii) Select randomly a spatial grid node x_0 in area *A*. Using the previous estimator, calculate the probability of x_0 belonging to the different phases (X_k, $k=1,K$):

$$\left[prob\left\{x_0 \in X_k\right\}\right]^* = \left[I_k(x_0)\right]^* \qquad (2.24)$$

The use of just one structural model - for example a global multi-phase model - ensures that the sum of $\left[I_k(x_0)\right]^*$ is one. In other cases, when using more than one continuity model, a renormalisation or other type of correction must be performed to ensure that the probability definitions are preserved:

$$\sum_{k=1}^{K}\left[prob\left\{x_0 \in X_k\right\}\right]^* = 1 \qquad (2.25)$$

So, the effective estimator of probability in point x_0 is given by:

$$[I_k(x_0)]^* = \frac{[I_k(x_0)]^*}{\sum_{k=1}^{K}[I_k(x_0)]^*} \tag{2.26}$$

iv) Create one auxiliary variable $J_i(x_0)$ that is a cumulative sum of $[I_k(x_0)]^*$

$$J_i(x_0) = \sum_{j=1}^{i}[I_i(x_0)]^* \qquad \text{with } i = 1,K \tag{2.27}$$

Use the Monte Carlo method to draw a random number between 0 and 1 with uniform distribution. The simulated value $I_{S_i}(x_0)$ is equal to (see Figure 2.4):

$$I_{S_i}(x_0) = \begin{cases} 1 \text{ if } J_{i-1}(x_0) < p \le J_i(x_0) \\ 0 \quad \textit{otherwise} \end{cases} \tag{2.28}$$

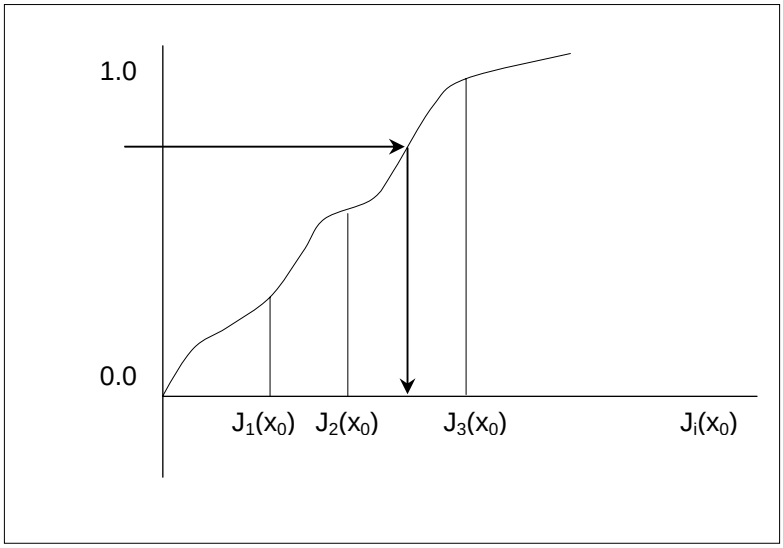

Figure 2.4 Simulation of categorical variables: draw a random number between 0 and 1 and transform it into a categorical value.

v) The simulated value $I_{S_i}(x_0)$ becomes a conditioning data for the next grid node simulation. The number of conditioning data increases by one: $(n+1)=(n)+\{I_S(x_0)\}$. This process loops until all the grid nodes have been simulated.

In the literature several advantages and drawbacks of this method are reported. One of the most often mentioned advantages is its easy practical implementation. Advantages of this method in comparison with morphological simulation are the ability to incorporate or include in the same simulation phases with different continuity models and preferential orientations,

as occur in some case studies, notably of fluvio-deltaic reservoirs. Furthermore, this method proves to be the most appropriate stochastic simulation procedure to deal with these situations (Soares, 1990, Luís *et al*, 1997).

However, some important disadvantages have been pointed out, basically related to the increase of conditioning data, which influences the estimation of $\left[I_k(x_0)\right]^*$. When the number of conditioning data increases (near the end of the simulation process), the estimation becomes difficult and the result is less precise. The result of a simulation can be an image with shapes similar to that obtained by a kriging estimation but different from the corresponding theoretical model of continuity. During the simulation it is thus important to control the selection of the set of neighbouring conditioning samples. For example, Journel (1989) proposes a random selection of *n* neighbouring samples of the simulated point x_0, in order to cover a wide range of distances in the neighbouring samples selected. Another drawback pointed out regards the difficulty of reproducing the proportions of each phase, which is one of the major objectives of the simulation.

2.4.2.2. SEQUENTIAL INDICATOR SIMULATION WITH CORRECTION FOR LOCAL PROBABILITIES

To minimise deviations between the experimental proportions of each phase and the final proportions of the simulated indicator values, Soares, 1998, proposed a correction for local probabilities. This effect is more significant in phases with smaller proportions and represented by variograms with relatively high ranges. During the simulation process, the random path can impose a dominant spatial pattern to the first simulated points that can seriously bias the experimental proportions of each phase. In this regard, a simple correction can be performed as described below, in order to minimise deviations between the simulated proportions and the corresponding objective.

After estimation of $\left[prob\left\{x_0 \in X_k\right\}\right]^* = \left[I_k(x_0)\right]^*$ $i=1,...N$, at each grid node x_0, the basic idea is to correct these local probabilities according to the global proportions (marginal probabilities) of each phase. Considering the global proportions m_k of phase k, it is possible to calculate one deviation e_k^s between this and the corresponding proportions at a given iteration step s of the simulation procedure:

$$e_k^{\,s} = m_k - p_k^{\,s} \tag{2.29}$$

where p_k^s denotes the marginal probability of lithoclass k in iteration s.

This calculated deviation e_k^s is added to the estimated local probabilities, even when normalised:

$$p_k^{\,s}(x_0) = \left[I_k(x_0)\right]^* + e_k^{\,s} \tag{2.30}$$

Considering the sum of the deviations to be null, the sum of the probabilities for all categorical variables is equal to one.

After this correction, the sequential simulation proceeds as usual, building a cumulative function of local probabilities and drawing a random number to simulate a value at point x_0. The simulated value is added to the conditioning data and the process loops until all grid nodes have been visited.

2.4.3. USE OF SIMULATED ANNEALING AS A POST-PROCESSING OR SIMULATION TECHNIQUE

The basis for the implementation of the numerical method of simulated annealing for categorical simulations is the definition of an objective function (key parameter). This objective function can combine any numerically quantified constraints, usually two-point statistics (individual or multi-phase variograms), marginal probabilities (histograms) or multi-point statistics. In the present case study, simulated annealing was used to match the multi-phase variograms and the histograms, the objective function being similar to the one described above. If the initial image matches the marginal proportions, the objective function includes only the deviations of the variograms.

The perturbation mechanism consists in swapping values from pairs of grid nodes selected randomly, excluding the experimental grid nodes (nearest grid nodes matching experimental data) if the prior image is simulated conditionally. Another possible perturbation mechanisms consists in randomly selecting a grid node and changing its value. This perturbation has the disadvantage of changing the marginal proportions, which must, in this particular case, be part of the objective function. It is important to emphasise that grid nodes corresponding to experimental data values never swap, which guarantees their match.

During the process of simulated annealing, recalculation of the objective function is the critical step in terms of CPU time. For this reason, it is a good idea to optimise the software in this sensitive section of the processing. For example, during recalculation of the deviations of the variograms, it is only necessary to use pairs of points that include at least one of the swapping grid nodes. The temperature is a parameter that controls the acceptance of perturbations that raise the objective function. When applied for post-processing steps, simulated annealing can not be started at a high temperature. If it were, the image would be randomised before the beginning of the convergence process. In these cases, the proper procedure begins with a relative low temperature and decreases quickly, imposing a reduction factor for cycles of loops.

This technique is extremely CPU time-consuming, unless the initial image partially matches the desired spatial features. Basically, the use of this method is limited to the final work on prior simulated images or small grid nodes. Just to give an idea of the CPU time required, for a grid with 124 x 42 x 21 (109368) nodes and 4 lithoclasses, it take about 2 hours on a Digital Alpha 600 to perform a complete simulation (transforming a random image of 4 lithoclasses, respecting the global proportions). This involves about 2.2 million loops (around 20 times the total number of grid nodes), which is enough to simulate and reproduce the required spatial features.

2.5 CASE STUDY OF LITHOCLASS SIMULATION

2.5.1. DATA PREPARATION

The data set used in this field study involves cores and logs from 19 wells drilled into the formation. As described in section 1.3, 20 different lithoclasses were identified, corresponding to different petrophysical characteristics. Despite the large number of lithoclasses, in these 25 layers no sets had more than 11 lithoclasses in each layer.

According to the methodologies outlined above, summarised in the flow chart displayed in Figure 2.1, all different simulation procedures for lithoclasses start with classification of the geological information (*K* lithoclasses) into indicator vectors, layer by layer. Final results consist of simulated images showing lithoclass distribution by layer. An extract from an indicator data file prepared for calculation of basic statistics and multi-phase variograms is displayed in Figure 2.5.

```
34291.328 80067.164     1.000   0 0 0 0 0 0 1
34291.328 80067.172     2.000   0 0 0 0 0 0 1
34291.332 80067.180     3.000   0 0 0 0 0 0 1
34291.332 80067.188     4.000   0 0 0 0 0 0 1
34291.336 80067.188     5.000   0 0 1 0 0 0 0
34291.336 80067.195     6.000   0 0 1 0 0 0 0
34291.336 80067.203     7.000   0 1 0 0 0 0 0
34291.340 80067.211     8.000   0 1 0 0 0 0 0
34291.340 80067.219     9.000   0 0 0 0 0 0 1
```

Figure 2.5 Extract from a indicator data file (X, Y, Z, I_1, I_2,... I_k).

In order to compute spatial variograms and perform stochastic simulations in the stratigraphical depositional referential, it was necessary to execute a geometrical transformation of the vertical component in the initial coordinates. This single transformation consists of recalculating the vertical component (Z) based on the top coordinate and the maximum thickness of the layer observed in the wells using the expression:

$$Z' = \frac{TOP(X,Y) - Z}{MAX\{THICK(X,Y)\}} \tag{2.31}$$

As a consequence of this transformation, the origin of the vertical component and the thickness became the same for all wells. Figure 2.6 shows a graphical sketch of the transformation applied to the entire set of wells in one intermediate layer. Regarding this transformation, it is important to emphasise the following points:

i) The goal of this transformation was to calculate horizontal variograms with homologous or stratigraphically correlated samples, assuming that the entire layer was regularly formed by deposition and the different thicknesses observed in the wells derive from secondary geological processes;

ii) All wells preserve the sequence of lithoclasses as observed and inside each well the proportions of lithoclasses were preserved;

iii) An inverse transformation is performed at the simulated image to restore the initial referential. Usually this inverse transformation is calculated directly in the flow simulation grid when the top and thickness of each grid node within each layer is defined.

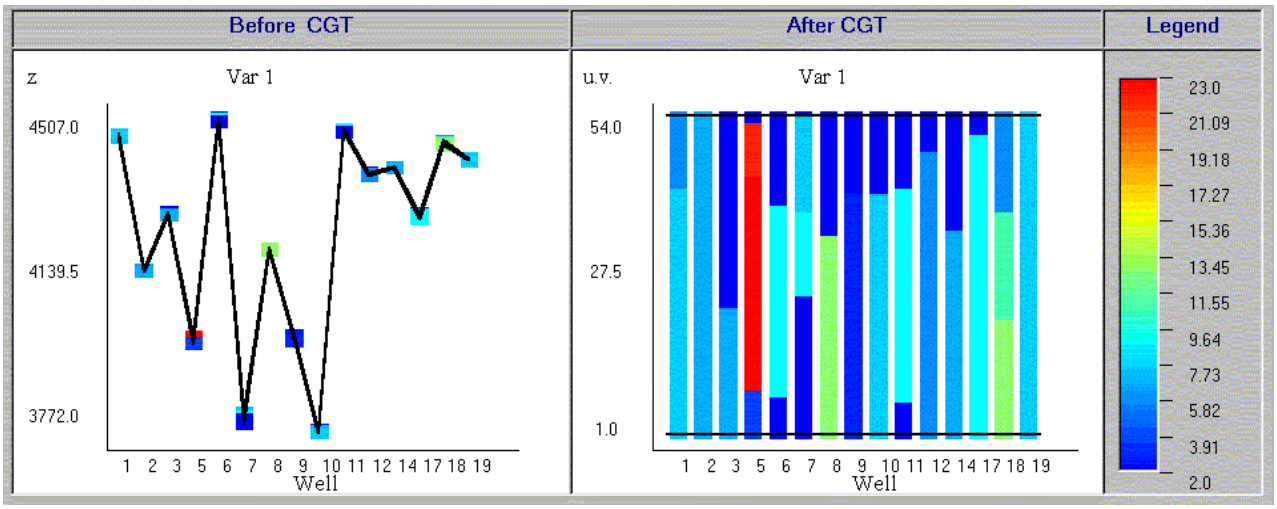

Figure 2.6 Location of lithoclasses in wells: a) initial coordinates; b) transformed coordinates.

2.5.2. SPATIAL ANALYSIS BY MULTI-PHASE VARIOGRAMS

In order to identify similar groups of lithoclasses (for the sake of continuity), individual variograms were calculated within each layer. Due to the similar continuity in the vertical direction observed in most of the lithoclasses in each layer, similarity of characteristics was taken into account in the selection of groups only for experimental variograms in the horizontal direction. Regarding this evidence, spatial analysis began with computation of individual variograms of lithoclasses only in the horizontal direction.

In the entire field, two distinct groups of lithoclasses were found within each layer: one exhibiting a clear continuity with ranges varying from 2000 metres to 8000 meters and a complementary group displaying very small ranges. The only exceptions are the first and last layer of the field, which exhibit a low spatial continuity in all lithoclasses, even the most representative ones. To illustrate the application of these simulation techniques to this particular field, an intermediate layer in the Upper Unit of the field (Unit R1, layer 150) was selected to detail results. In the selected layer, 124 by 42 by 21 points (total 109368) constitute the 3D grid. The spacing between grid nodes in the horizontal direction is 250 metres and 1 stratigraphical unit (S.U.)[1] in the vertical direction.

In the present layer R1-150, 9 distinct lithoclasses were found: 2, 3, 4, 5, 6, 7, 8, 9 and 15. The proportions of each lithoclass in this layer are shown in Table 2.1. Lithoclasses 2 and 9 are predominant and represent approximately 50% of the geological set.

[1] One stratigraphical unit is equivalent to 1.0 foot in the larger well.

Table 2.1..Proportions of each lithoclass in layer R1-150.

Lithoclass	Before coordinate transformation		After coordinate transformation	
	Samples (#)	Mean	Samples (#)	Mean
2	54	0.132	155	0.193
3	14	0.034	32	0.041
4	20	0.049	54	0.068
5	24	0.058	36	0.045
6	36	0.088	64	0.080
7	34	0.083	57	0.070
8	52	0.126	92	0.115
9	114	0.278	237	0.300
15	62	0.152	71	0.088

Figure 2.7 and Figure 2.8 display a typical representation of individual variograms for continuous lithoclasses (2, 4, 8 and 15) and erratic lithoclasses (3, 5, 6, 7 and 9) corresponding to this selected layer. Obviously “erratic” should be understood in a spatial distribution sense, for a given scale.

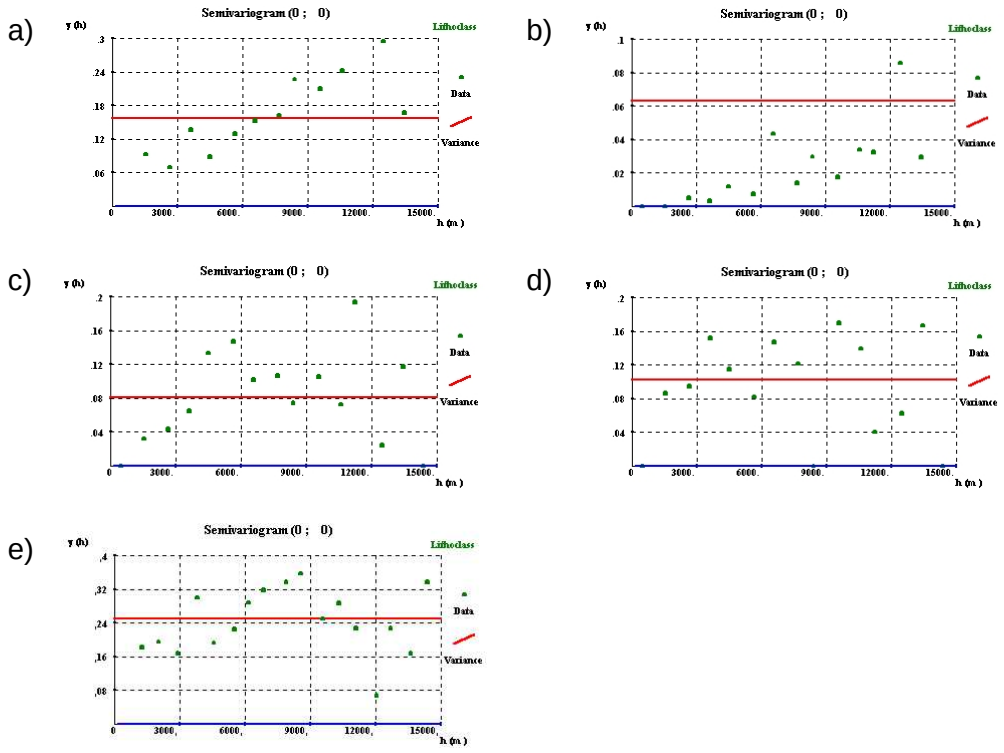

Figure 2.7 Experimental variograms corresponding to continuous lithoclasses within the selected layer: a) lithoclass 2; b) lithoclass 4; c) lithoclass 8; d) lithoclass 15; e) set of erratic lithoclasses.

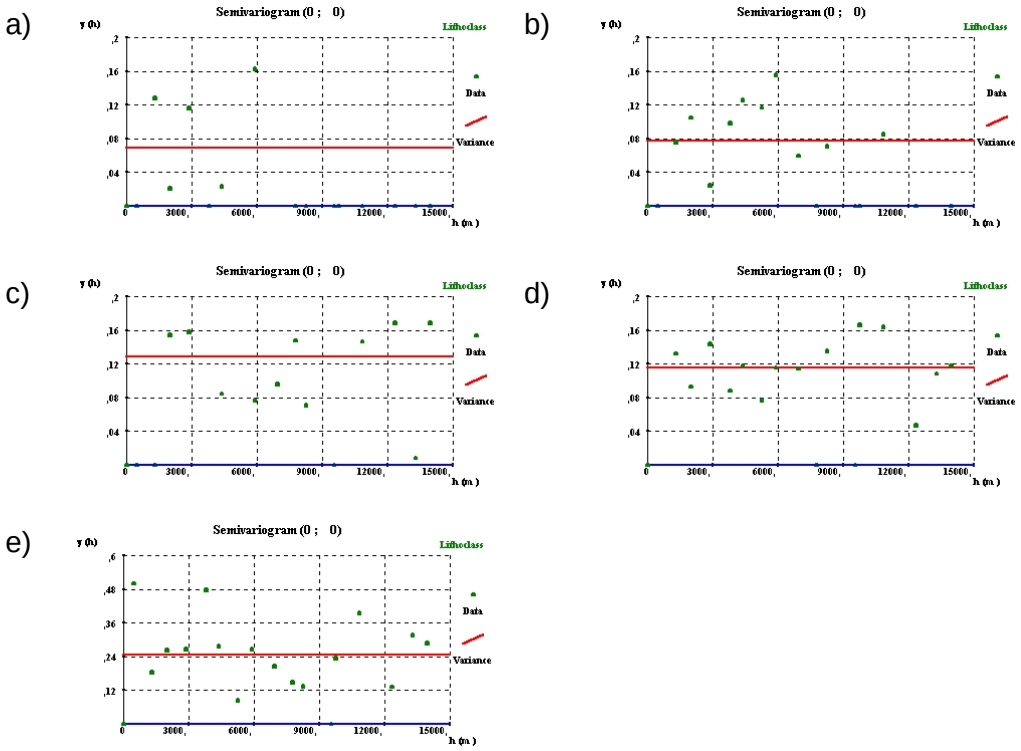

Figure 2.8 Experimental variograms corresponding to erratic lithoclasses within the selected layer: a) lithoclass 3; b) lithoclass 5; c) lithoclass 6; d) lithoclass 7; e) lithoclass 9.

Grouping the set of erratic lithoclasses into one new category (complementary to the continuous phases) and calculating the corresponding individual variogram, the results show that this "new" category exhibits a continuous variogram like the continuous lithoclasses 2, 4, 8 and 15 (see figure 2.7). Based on this evidence, a methodological sequence was established, starting with the calculation of individual variograms for all lithoclasses, followed by the selection of continuous and erratic lithoclasses, and finally grouping the set of erratic lithoclasses into one category worked out as a continuous category.

For each categorical group, multi-phase variograms in both horizontal and vertical directions were calculated within each layer. In the horizontal direction only one omni-horizontal variogram was inferred due to the small number of wells and of corresponding samples, which are not enough to infer directional variograms. The experimental multi-phase variograms of the continuous group was fitted using one exponential theoretical model with a range of 4000 metres in the horizontal direction and 45 S.U. in the vertical direction. For the experimental multi-phase variograms of the erratic group an exponential model was used with a range of 500 meters (length of each block in the final flow simulator model) in the horizontal direction and 45 S.U. in the vertical direction. In Figure 2.9 and Figure 2.10, the models fitting the experimental multi-phase variograms for both the continuous and the erratic group along horizontal and vertical directions are shown.

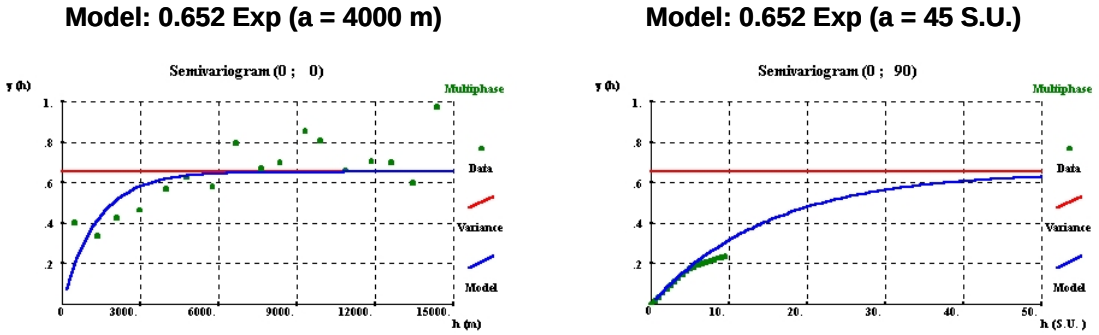

Figure 2.9 Experimental multi-phase variograms for the selected layer (continuous lithoclasses and set of erratic lithoclasses): left: horizontal direction; right: vertical direction.

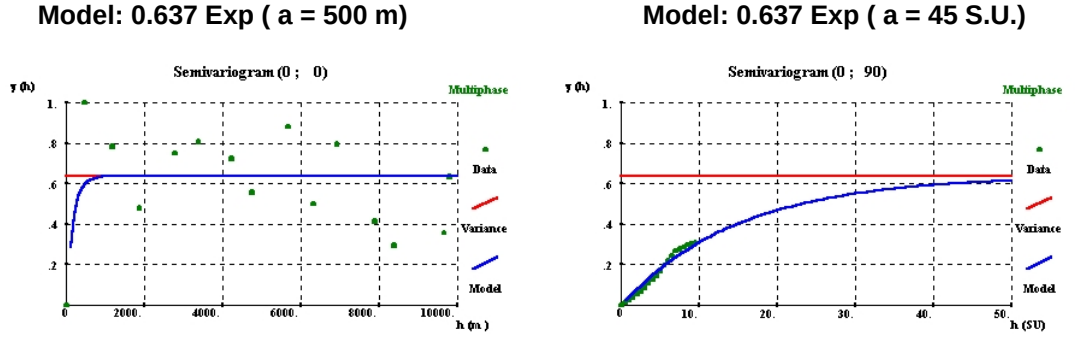

Figure 2.10 Experimental multi-phase variograms for the selected layer (erratic lithoclasses): left: horizontal direction; right: vertical direction.

2.5.3. SIMULATION OF LITHOCLASSES

According to the methodology described in the previous sections, a geological model of lithoclasses was built for the entire field, based on the theoretical continuity models fitted to each individual layer. Since we are dealing with two groups of lithoclasses, the simulations must be performed in two steps. The first step consists of simulation of the continuous group including one additional category corresponding to the set of erratic lithoclasses for the entire layer. The second step consists of simulation of the erratic lithoclasses for the entire layer. Finally the two images were merged according to the location of erratic lithoclasses simulated in the set of continuous lithoclasses (Figure 2.11).

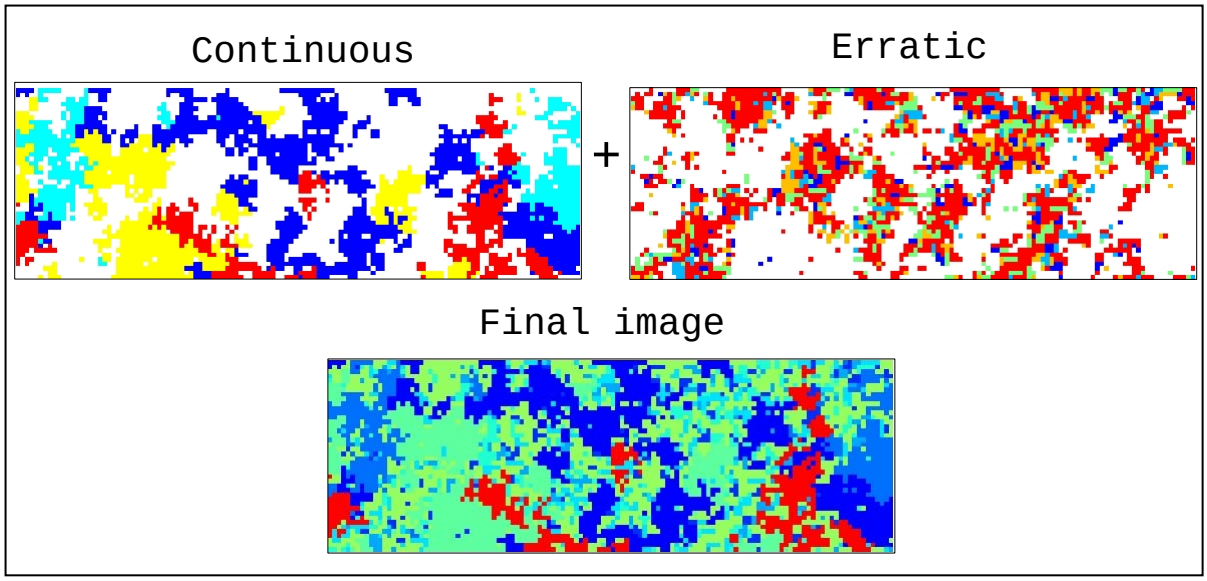

Figure 2.11 Joint simulated images corresponding to continuous and erratic lithoclasses.

In order to compare the different approaches described above, an entropy test was performed on a single layer for the continuous group. The main objective of this test is to evaluate the lateral conditioning effect in these methods. Thus, for the selected layer 30 realisations were performed using the following methods:

i) multi-phase sequential indicator simulation with correction for local probabilities;

ii) multi-phase morphological simulation: truncated Gaussian simulation with posterior conditioning and using the algorithm of classification based on local and global probabilities;

iii) multi-phase morphological simulation: truncated Gaussian simulation with posterior conditioning and using the simulated annealing algorithm to transform the probability values into indicator values;

iv) post-processing of an image created using the sequential indicator simulation algorithm with simulated annealing.

Lastly a set of simulated images of the lithoclasses with the validation checks corresponding to the different methods is displayed.

2.5.4. TRANSFORMATION OF SIMULATED PROBABILITY MAPS INTO MORPHOLOGICAL MAPS USING SIMULATED ANNEALING

Since the transformation method based on simulated annealing to classify the probability maps into morphological maps is a newly proposed method, a sequence of images showing partial results (5%, 10%, 25%, 50%, 75% and 100% of classification of the entire image) for one intermediate layer is presented below. In this sequence it is possible to compare intermediate variograms with the growth of geobodies. For this specific layer of the Upper Unit, the growth of the geobodies was followed during the sequence of transformation controlled by simulated annealing. During this process, probability values are transformed into indicator values following a decreasing order of probability as described in 2.4.1.3. The perturbation mechanism consists of both transformation of a probability value into one indicator value and a conventional swap of two position values. These two perturbation mechanisms, when associated, ensure a more accurate match of the variograms. In Figure 2.12 through Figure 2.17, one can see the growth of geobodies.

The corresponding multi-phase variograms and proportions are displayed for a single level of one layer. It is important to note that as the process starts, the grid nodes corresponding to data locations have probability values of one of belonging to a specific category and zero of belonging to the others. Since the beginning of the transformation process these points have already been transformed into indicator values, which guarantees the conditioning.

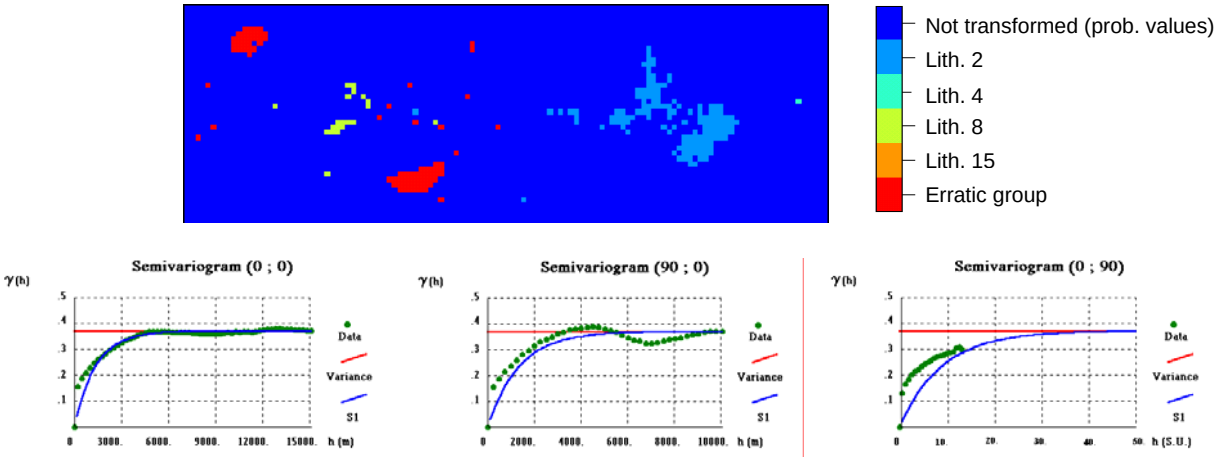

Figure 2.12 Use of simulated annealing as a classifier of simulated probability values into categorical values: after transformation of 5% of values.

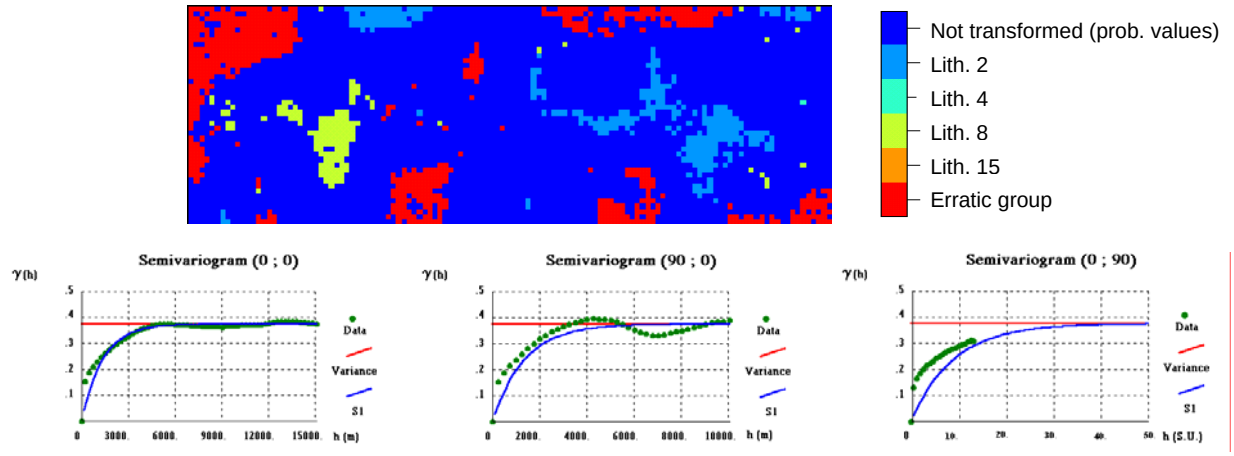

Figure 2.13 Use of simulated annealing as a classifier of simulated probability values into categorical values: after transformation of 10% of values.

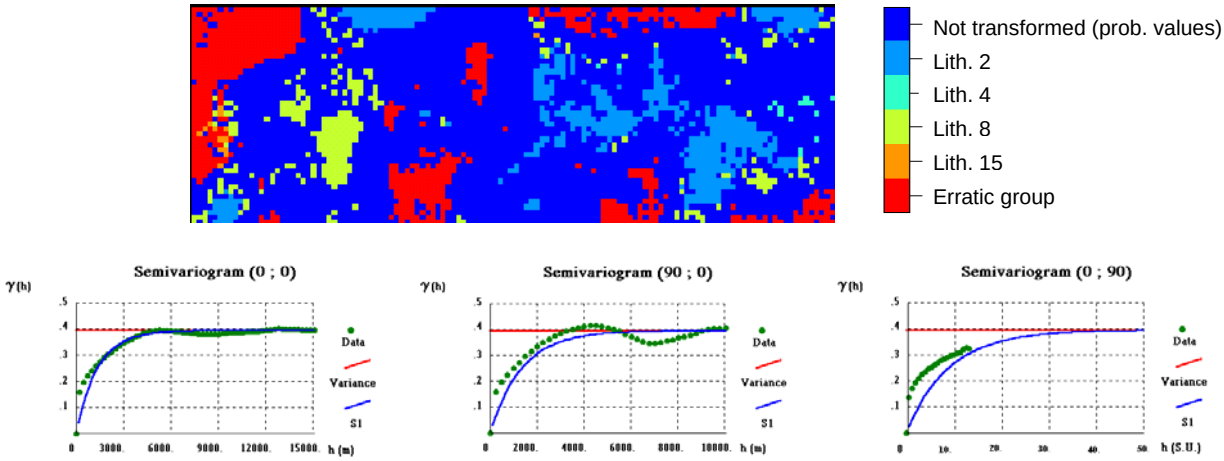

Figure 2.14 Use of simulated annealing as a classifier of simulated probability values into categorical values: after transformation of 10% of values.

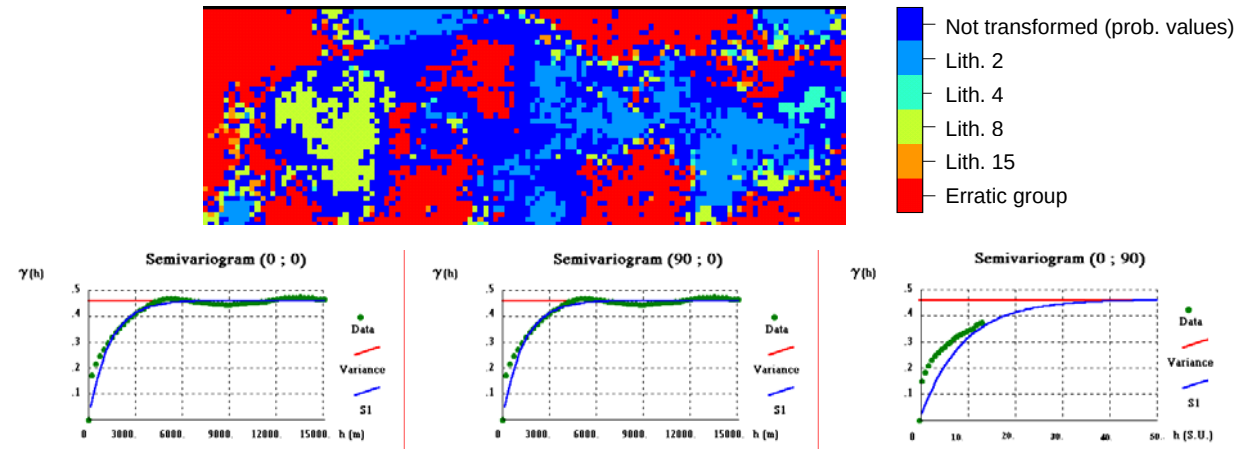

Figure 2.15 Use of simulated annealing as a classifier of simulated probability values into categorical values: after transformation of 50% of values.

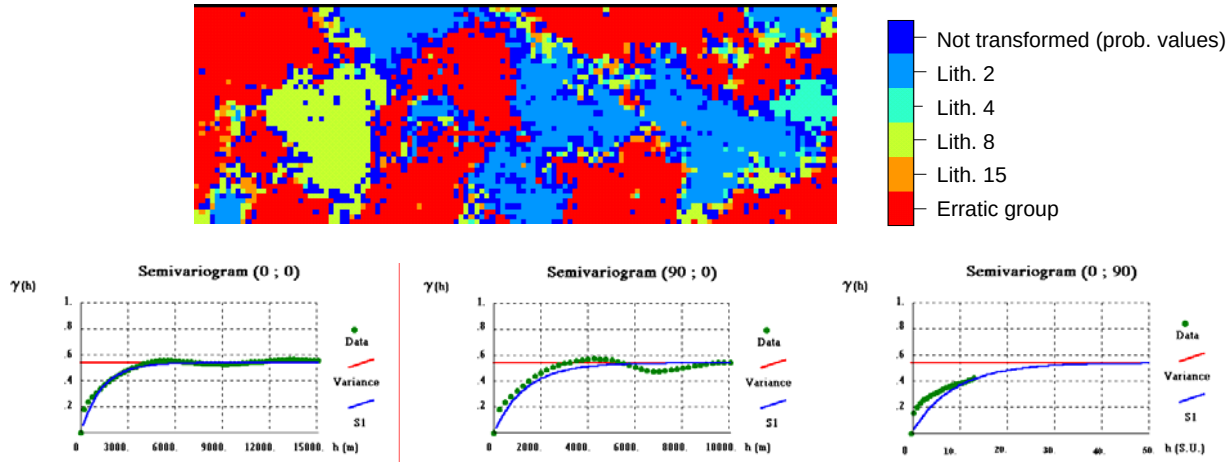

Figure 2.16 Use of simulated annealing as a classifier of simulated probability values into categorical values: after transformation of 75% of values.

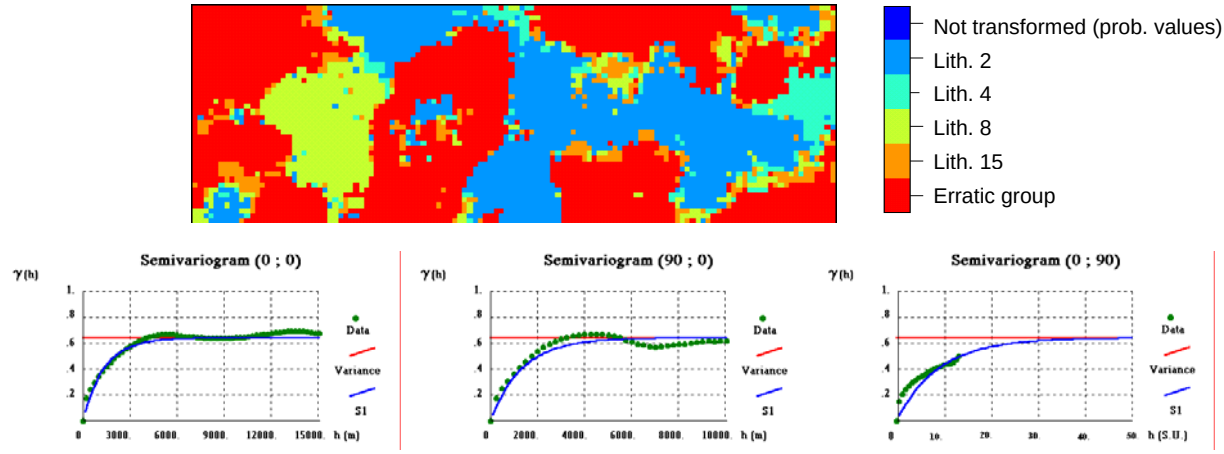

Figure 2.17 Use of simulated annealing as a classifier of simulated probability values into categorical values: final image.

The proportion of each lithoclass during the transformation process is presented in the following table (Table 2.2):

Table 2.2 Proportion of the transformed values using simulated annealing as a classifier of simulated probability values into categorical values.

Categories	5%	10%	25%	50%	75%	All values	Objective
2	0.161	0.162	0.162	0.162	0.164	0.193	0.193
4	0.087	0.086	0.084	0.076	0.067	0.069	0.068
8	0.211	0.210	0.207	0.192	0.175	0.121	0.115
15	0.065	0.064	0.064	0.060	0.064	0.088	0.088
Set of erratic lithoclasses	0.476	0.478	0.483	0.510	0.530	0.529	0.536

During the transformation, a reduction of the difference between the theoretical model and all experimental multi-phase variograms along different directions is observed. Again during the transformation, all proportions of all phases are very well matched, and the reported differences are very small. It is important to note that all geobodies tend to grow from isolated points of high probability (most of them data points) which leads to better conditioned images and generally homogeneous patterns.

In the present example, the transformation follows a decreasing order of probability and because the perturbation includes swapping of values, processing time is not a critical issue, compared with the traditional simulated annealing applied to post-processing images. In fact, to perform a complete transformation which includes about 10 x (total number of grid nodes) = 1093680 loops, takes around one hour on an Alpha Station 600 (Digital). In order to decrease the processing time only three directions (X, Y and Z) are included in the objective function, instead of including diagonal directions. The number of lag distances included in the objective functions was reduced to just five in all three directions (the number of grid nodes are 124, 42 and 21 in X, Y and Z directions respectively) and this small number of lags proved to be enough. Identical weights for all three directions and a decreasing weight based on the lag distance (equal to $(1/lag)^2$) within each direction were used. The temperature was low at first, decreasing very slowly during the process (it is reduced at each set of 109368 loops – total number of grid nodes). Just to give an idea of the initial value of the temperature, only around 5% of the perturbations that increase the objective function were accepted. This procedure proves to be effective and ensures that all probability points were transformed.

2.5.5. ENTROPY ANALYSIS OF THE DIFFERENT OUTPUT IMAGES.

To characterise the uncertainty reflected by the outputs of each simulation, a set of 30 realisations was performed using the methods described above: multi-phase sequential indicator simulation (using correction for local probabilities) and morphological simulation using the two transformed proposed approaches. Also, the images resulting from sequential indicator simulation were post-processed using simulated annealing. In this case, the objective is to illustrate the conditioning effect introduced by the annealing algorithm associated with the improvement in matching the variograms. During the application of the annealing algorithm, the temperature begins rise slightly in order to disturb the images while maintaining the main patterns. In the following loops the temperature decreases and the

system again tends to match the required parameters. During the whole process, 10 x (total number of grid nodes) = 1093680 loops were performed.

The uncertainty measure used is the entropy of the local probability distribution (Goovaerts,1997), which can be defined for a set of *K* phases (whereas $p_k^*(x)$ is the average of the 30 indicator simulated values in each grid node *x*):

$$H(x) = -\sum_{k=1}^{K} \left[\ln p_k^*(x)\right] p_k^*(x) \qquad (2.32)$$

The entropy is measured between *0* at the sample location (where there is no uncertainty) and *ln K* associated with the uniform distribution $p_k^*(x) = 1/k$. A standardised measure valued within interval [*0*; *1*] for this local entropy is given by:

$$H_R(x) = \frac{H(x)}{\ln K} \qquad (2.33)$$

For the four sets of 30 images, this standardised entropy measure was calculated. In Figure 2.18 through Figure 2.21 the distribution of entropy is illustrated for some levels associated with the location of wells.

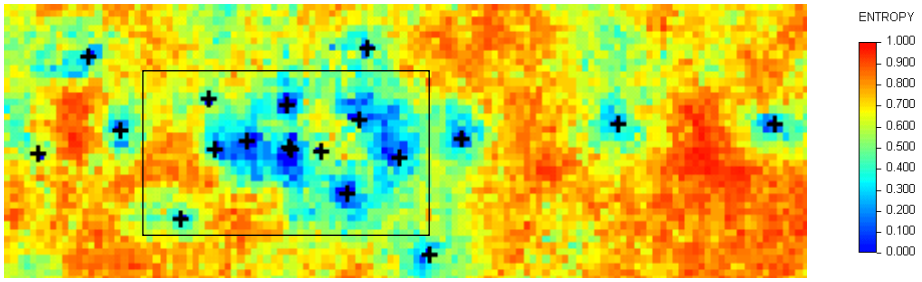

Figure 2.18 Entropy distribution on level 11 - multi-phase sequential indicator simulation with correction for local probabilities.

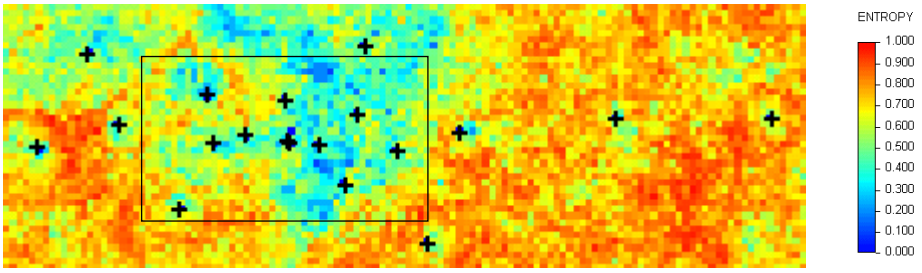

Figure 2.19 Entropy distribution on level 11 - morphological simulation plus classification using local and global probabilities to transform probability values into categorical values.

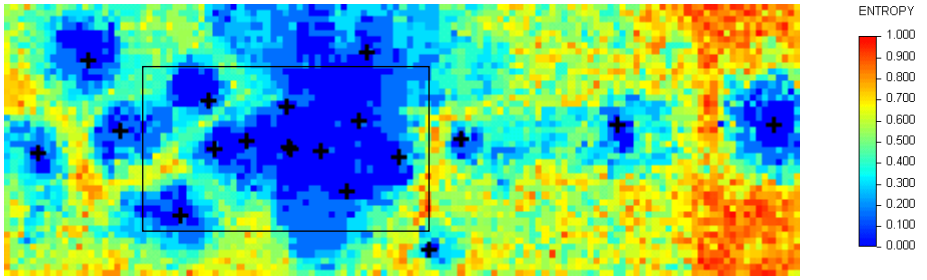

Figure 2.20 Entropy distribution on level 11 - morphological simulation plus classification using annealing algorithm to transform probability values into categorical values.

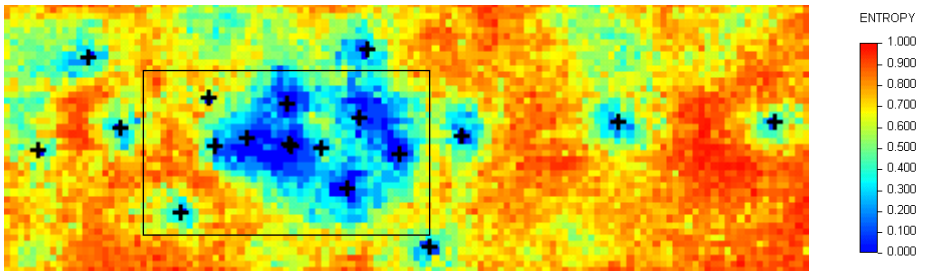

Figure 2.21 Entropy distribution on level 11 - post-processing images using annealing algorithm to a sequential indicator simulation set of images.

Based on these images it is possible to rank the four geostatistical simulation methods in decreasing order using the entropy as follows:

1) Morphological simulation using the morphological method to transformation probability values into morphological categories;

2) Multi-phase sequential indicator simulation with correction for local probabilities plus post-processing by simulated annealing;

3) Multi-phase sequential indicator simulation with correction for local probabilities;

4) Morphological simulation using annealing algorithm as transformation method.

Following this sequence, it is observed that the use of simulated annealing as a post-processing simulation method reduces the entropy, as observed by comparing the entropy Figure 2.18 and the corresponding post-processed image, Figure 2.21. To express these differences numerically, the sum of the entropy for the whole area (and the entire depth) and for a highly conditioned sub-area (nearby 11 wells) was calculated for each method; see Table 2.3.

Table 2.3 Sum of the entropy values for the entire layer and for a central area.

Method	Entire layer	Central area
Sequential indicator simulation with correction for local probabilities	61613	5021
Morphological simulation plus morphological classification	72507	6132
Morphological simulation plus annealing classification	47665	1785
Sequential indicator simulation with correction for local probabilities plus post-processing by simulated annealing	72050	4058

Results in this table confirm the rank. It is important to note the following points:

- Post-processing using simulated annealing has a strong conditioning effect comparing the sum of entropy in the highly conditioned sub-area. Considering the entire area, results were almost identical;
- Morphological simulation plus annealing transformation proved a highly conditioned method especially in conditioned areas, where this conditioning effect is noticeable;
- By contrast, morphological simulation plus transformation using local and global probabilities produces the most variable set of images. However, all realisations produced using these methods matched the required parameters (basic statistics and variograms) and the experimental data.

Figure 2.22 shows a set of 3 horizontal views from different layers comparing the four different simulations methods for categorical variables.

2.5.6. VALIDATION OF THE RESULTS

The validation of stochastic images was ensured through different levels of control, involving basically coherence analysis of the simulated images against the experimental data points and the conceptual model.

To illustrate the coherence of the simulated images using the above methods, a set of figures (horizontal views and cross sections) is presented. The figures were obtained using the three methods: sequential indicator simulation with correction for local probabilities, and morphological simulation using the two proposed transformation methods. In Figure 2.23 through Figure 2.25 a set of vertical cross-sections of the entire field and using the three different methods is illustrated.

The final check consists of the following:

- comparison between experimental and simulated proportions of each lithoclass;
- comparison of the continuity of the lithoclasses in the simulated images and in the experimental data;
- checking whether the simulations honoured the experimental values.

The comparison of proportions for each lithoclass is presented for one layer. Post-processing by annealing when using the iterative swap of values does not alter the initial proportions.

In Table 2.4, the final proportions for each lithoclass for the final simulated images are represented and compared with the initial values.

Table 2.4 Comparison of the lithoclass proportions in the simulated images for the selected layer.

Lithoclass	Experimental data	SIS	Morphological simulation with transformation using local and global probabilities	Morphological simulation with annealing transformation
2	0.193	0.196	0.193	0.193
4	0.068	0.068	0.068	0.070
8	0.115	0.127	0.115	0.121
15	0.088	0.090	0.088	0.069
3	0.041	0.039	0.040	0.041
5	0.045	0.040	0.045	0.046
6	0.080	0.074	0.083	0.086
7	0.070	0.071	0.071	0.072
9	0.300	0.295	0.297	0.302

Proportions from images resulting from morphological simulation using morphological transformation are matched exactly due to the background of the method. In the present case study, this exact match is observed in the continuous phases: 2, 4, 8 and 15. The resulting simulated image of the erratic set of lithoclasses also exactly matches the experimental proportions. After merging these images with those resulting from the continuous set simulation (and the additional phase that reproduces the entire set of erratic lithoclasses) the proportions may show some bias. However, due to the erratic nature of these images, which imposes local averages in small moving windows equal to the global proportions, the bias is reduced, as shown in Table 2.4. The proportions of the simulated images coming from sequential indicator simulation using correction for local probabilities are generally close to the experimental values, even in the small proportion phases. The major difference is observed in lithoclass 5, about 10%, but all the others are very small. The morphological simulation method with annealing transformation shows that these proportions are well matched. It is important to note that in this method the bias of the proportions is one term of the objective function.

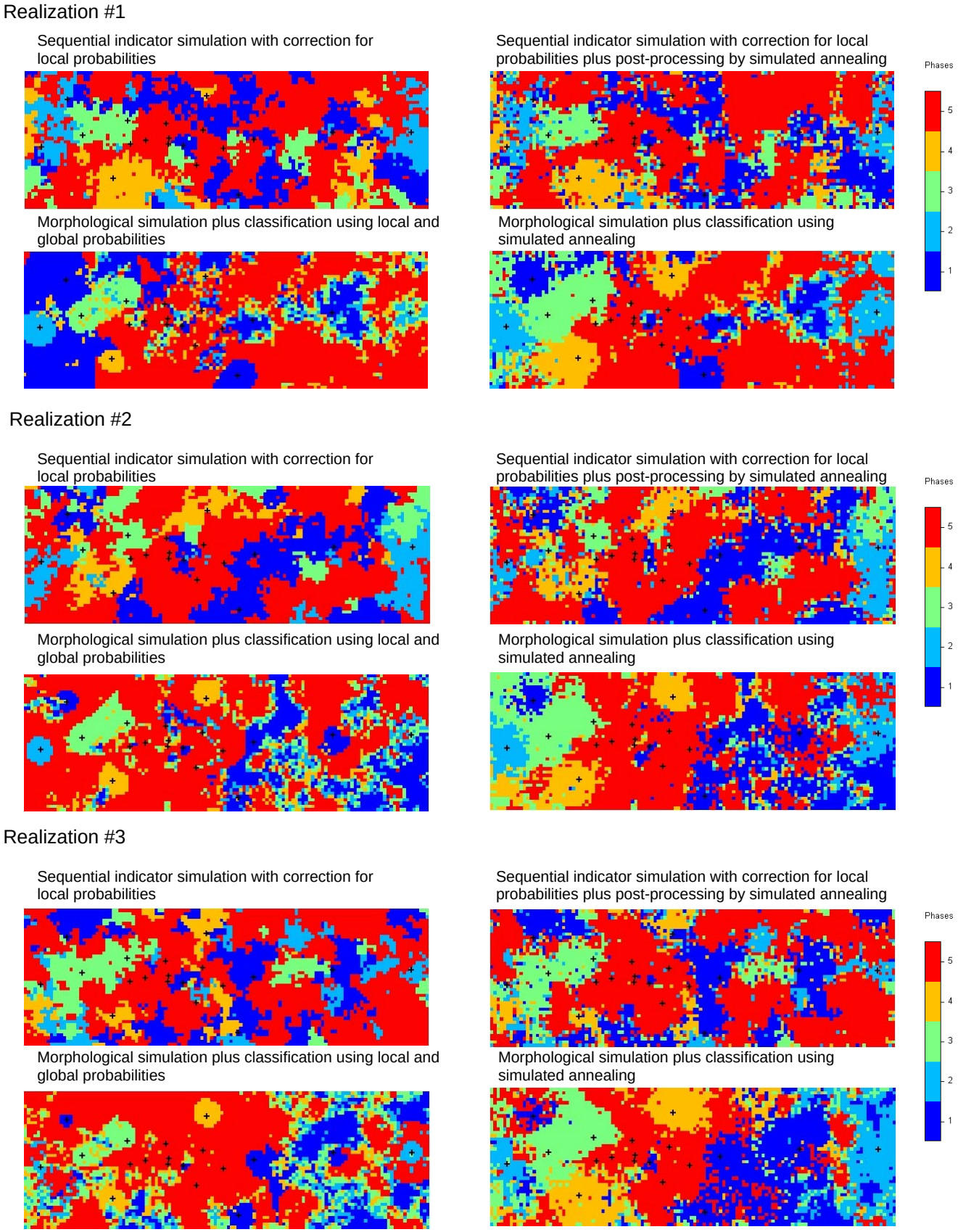

Figure 2.22 Illustration of 3 horizontal views from the generated stochastic images comparing the different methods.

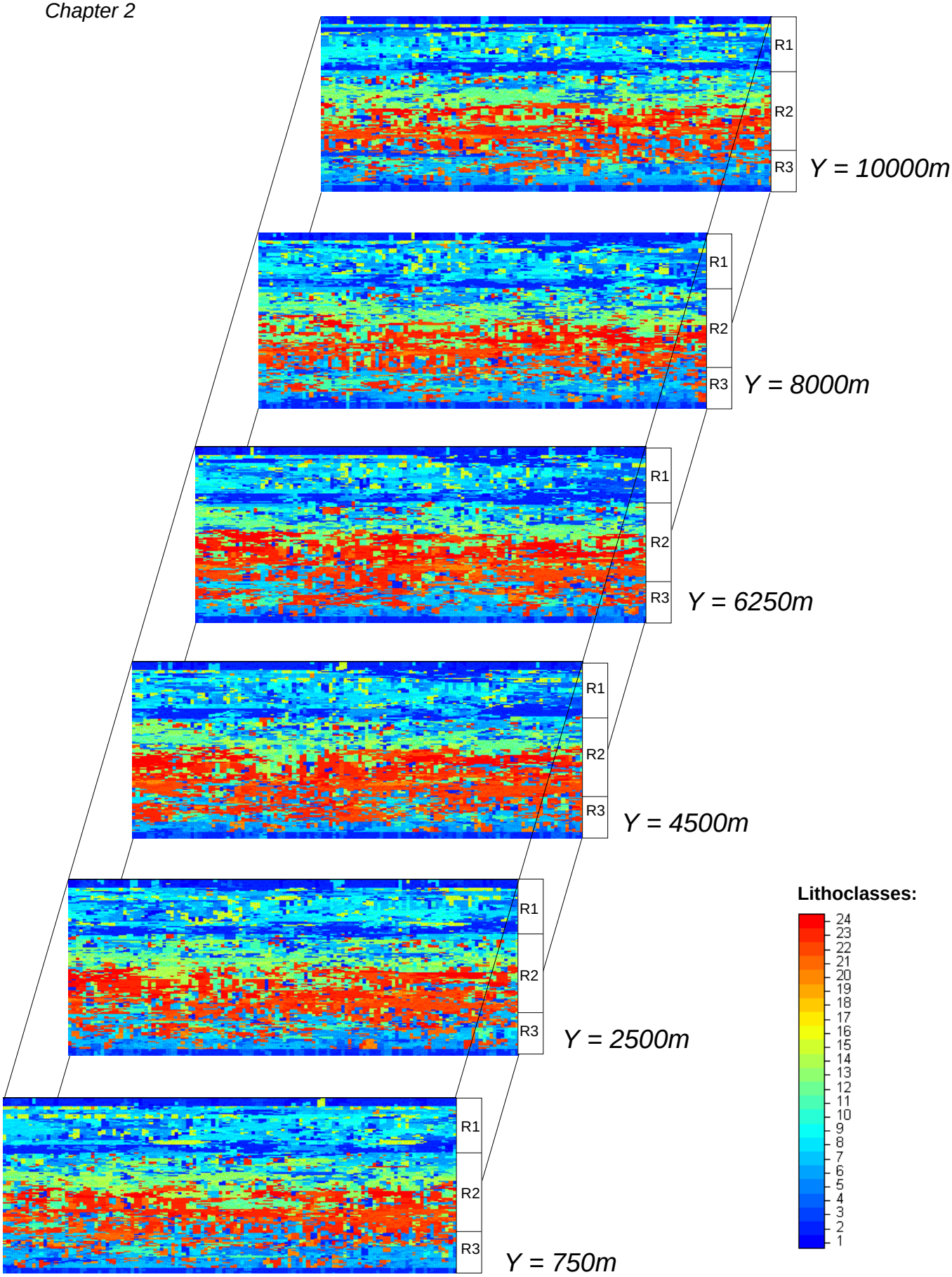

Figure 2.23 Cross-sections showing reservoir geological model - multi-phase sequential indicator simulation with correction for local probabilities.

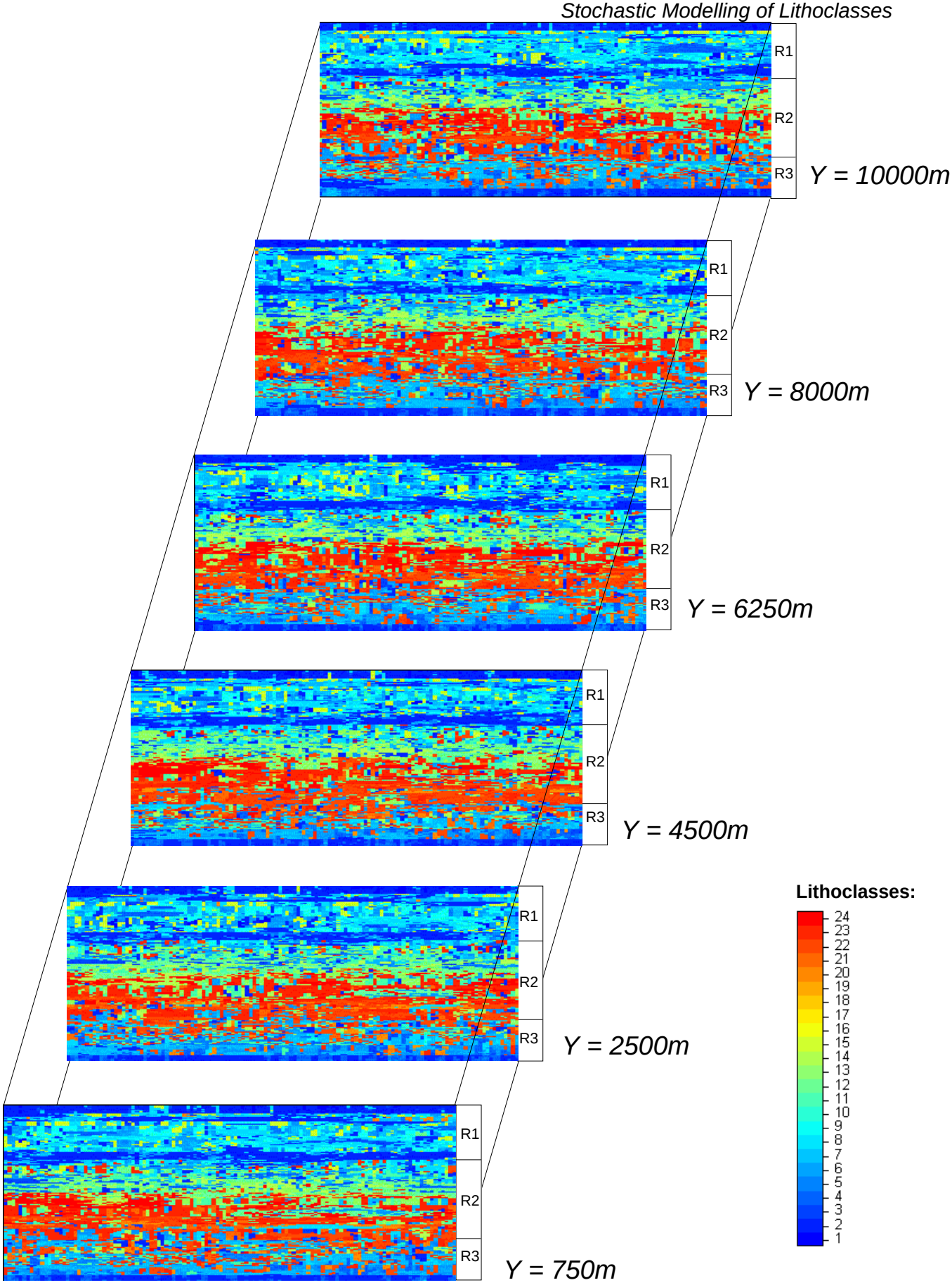

Figure 2.24 Cross-sections showing reservoir geological model - morphological simulation plus classification using local and global probabilities.

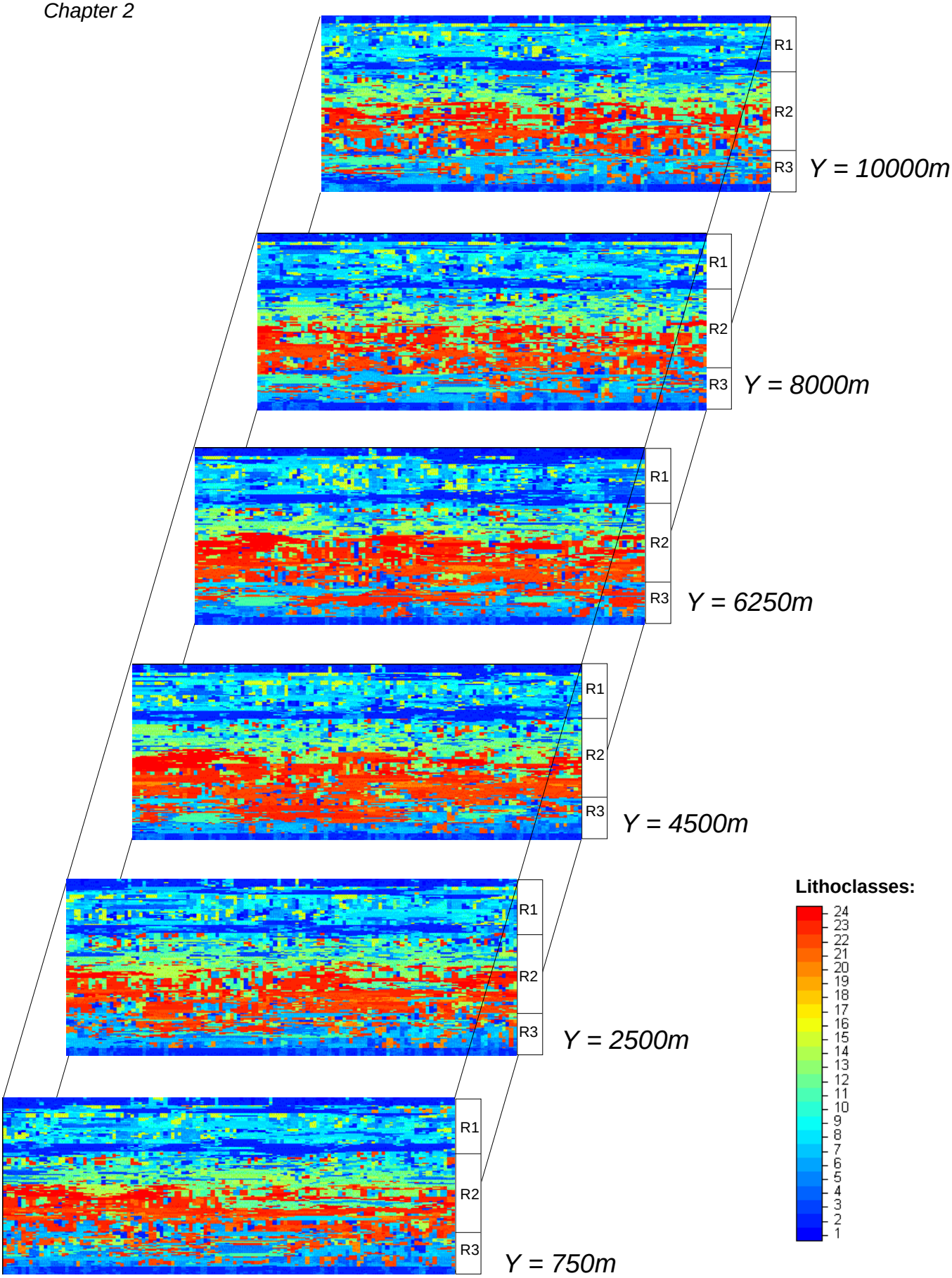

Figure 2.25 Cross-sections showing reservoir geological model - morphological simulation plus classification using simulated annealing algorithm.

Variograms of the simulated images are now presented to illustrate the reproduction of the continuity models. For the same layer, in Figure 2.26 through Figure 2.29, the experimental variograms and theoretical functions of the continuous simulation images are illustrated for the three methods plus post-processing by annealing in the three main orthogonal directions (X, Y and Z). In Figure 2.30 through Figure 2.32 the corresponding experimental variograms for the erratic group are illustrated, for the three methods described above. For the erratic group, post-processing by annealing was not applied because this group is already well characterised. From these variograms it is possible to conclude that all methods reproduce the theoretical models imposed well. However it is possible to observe more accurate reproduction in the annealing methods.

All these methods include in their backgrounds the assumption that the experimental data must be matched at sampled locations. The final check for the confirmation that the simulations honoured the experimental values is simply a test to verify that the experimental procedure was properly conducted. If the samples are translated to the near grid nodes, the final images exactly match data values in data locations. Otherwise, and particularly in oversampled areas, the nearest grid node could have a different simulated value from the corresponding experimental data.

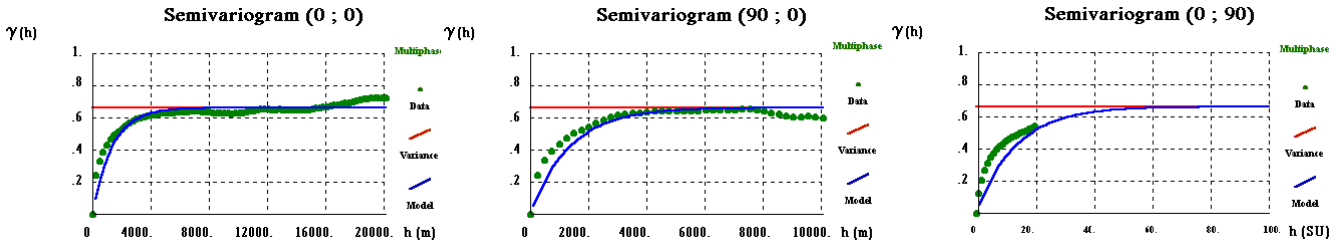

Figure 2.26 Variograms of the continuous group using multi-phase sequential indicator simulation with correction for local probabilities.

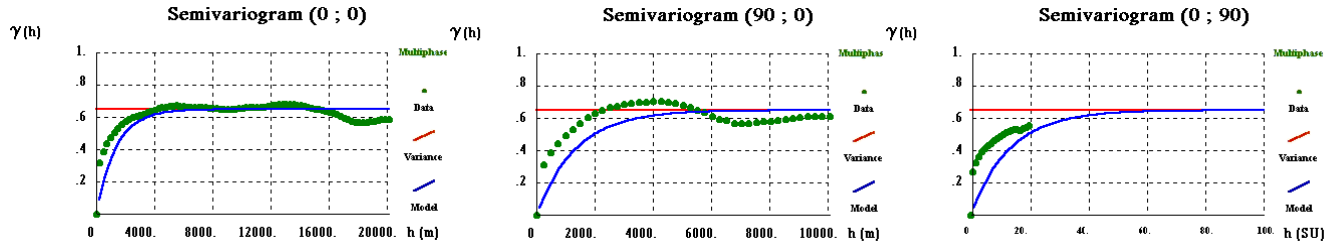

Figure 2.27 Variograms of the continuous group using morphological simulation plus classification using local and global probabilities.

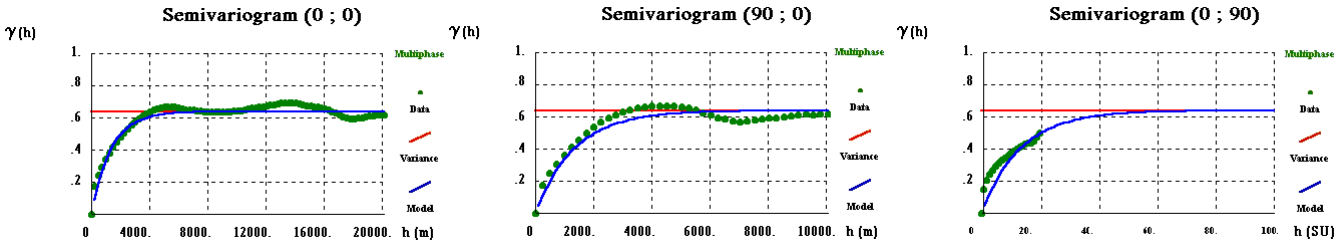

Figure 2.28 Variograms of the continuous group using morphological simulation plus classification with annealing algorithm.

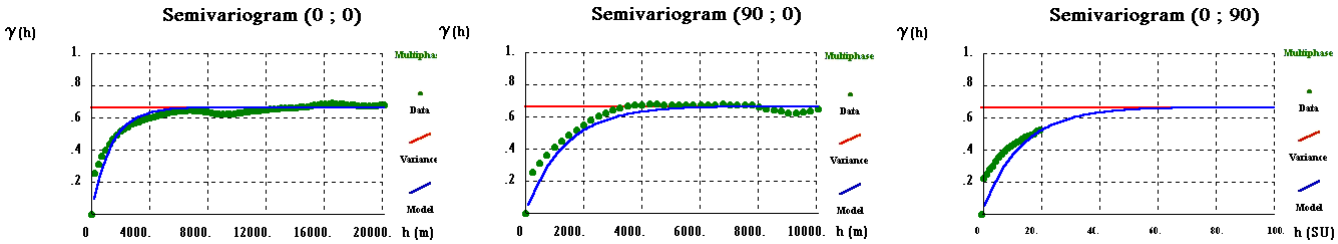

Figure 2.29 Variograms of the continuous group using post-processing by simulated annealing to a sequential indicator simulation image.

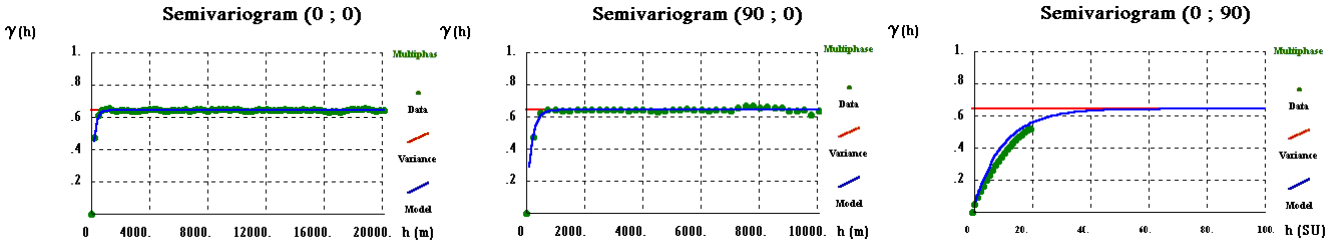

Figure 2.30 Variograms of the erratic group using multi-phase sequential indicator simulation with correction for local probabilities.

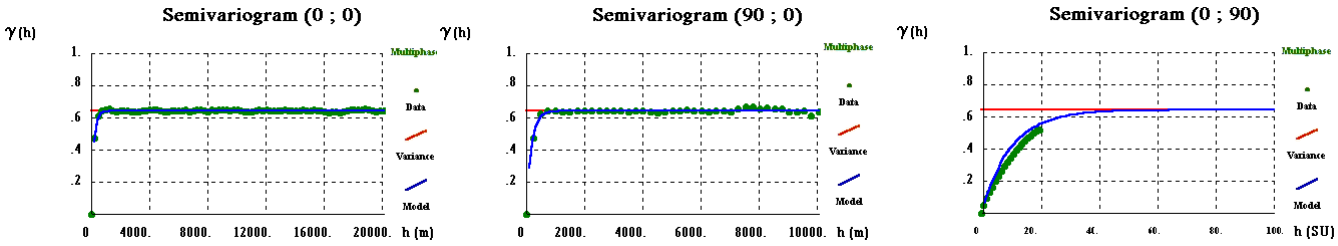

Figure 2.31 Variograms of the erratic group using morphological simulation plus classification using local and global probabilities.

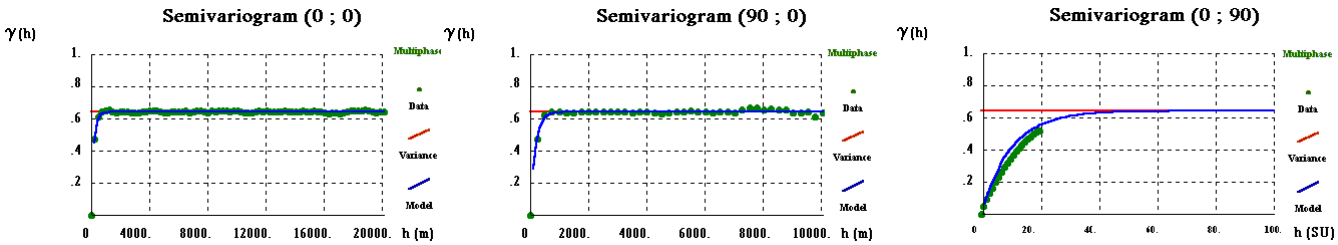

Figure 2.32 Variograms of the erratic group using morphological simulation plus classification with annealing algorithm.

2.6 FINAL REMARKS

The aim of this chapter is to compare 3 algorithms for the simulation of categorical variables and an algorithm for post-processing of images, which may be used together or separately to characterise the internal morphology of formations, based on a prior classification into lithoclasses or rock types. The main goal of stochastic simulation methods is to quantify uncertainties as expressed in the analysis of different realisations. The set of equally probable images of the geology can be conditioned to the available information for a posterior estimation or simulation of petrophysical properties, which are the input of a flow simulator (a transfer function). This transfer function produces a spread of production results based on extreme and most likely scenarios of flow patterns. Although all realisations have the same statistics they may yield different probable predictions in reservoir production and performance, which may affect selection of the optimal strategy for field development, although all the realisations are equally probable.

In the formation of this particular study, each layer has a set of lithoclasses, which for the sake of continuity are subdivided into continuous and erratic. In this study it was found that a lithoclass which is identified as being continuous in one layer is frequently identified as being erratic in another, and there appears to be no relation in the way in which the continuity of a given lithoclass varies in depth (from layer to layer). Similarly, no link was observed between the proportion of each lithoclass in a given layer and its continuity in that layer: there are lithoclasses with high proportions and which display erratic behaviour (when greater continuity might be expected) as well as other less frequent ones which are concentrated in particular areas, which leads them to display continuity.

After the results of lithoclass simulation involving three algorithms for simulation of categorical variables and a post-processing algorithm, some conclusions can be drawn about the methods used and the results obtained.

Any one of the algorithms imposes the following characteristics on the final images: experimental proportion of lithoclasses, model of continuity, and values at known points. This derives from the theoretical conception of the methods themselves.

Sequential indicator simulation with correction for local probabilities is an algorithm for the simulation of categorical variables, which generates images reproducing the averages of each of the phases and the variogram model. For the layer used in the comparative study, the total variability of the images obtained is high, the second highest of all the methods tested. The images have a fairly regular pattern of distribution of lithoclasses around the

wells, its influence being dependent on the continuity models used and the proportions of the lithoclasses. Use of this method at the outset makes it possible to use different variogram models for each lithoclass, which would suggest a single execution of this algorithm for the whole set of phases; continuous and erratic. However, it was seen that simulations involving lithoclasses with such different variograms (500 metres < to < 4000 metres) lead to images with intermediate variograms for all lithoclasses, which definitively rules out this possibility.

Morphological simulation (truncated Gaussian simulation plus posterior conditioning) is an algorithm which was developed in two versions. After the conditioning phase the result is a map of the probability of each point belonging to each simulated lithoclass. The final stage of this method is the transformation of probability maps into multi-phase lithoclass maps. This stage was implemented in accordance with two classification criteria (a classification based on local and global probability values and a classification process based on simulated annealing). These two methods of classification produce final results which are completely different in terms both of the standards of images and of the conditioning effect. Thus the images resulting from classification using the conventional transformation method have a weak conditioning effect compared with the results obtained by the other methods under study. As a consequence, in circumstances which are the same in terms of variogram model and disposition of samples, this is the method which generates simulated images with the greatest variability. This is not to be expected, bearing in mind that the conditioning factor is the last and should therefore prevail. When conditioning is carried out based on a non-conditional simulation, one of two things may happen with each sample: either by coincidence the non-conditional simulation obtained the correct value for the sample and there is no conditioning (no difference between real and simulated data), or it did not obtain the correct value and there is a contribution from this sample with a positive difference. These differences are estimated for the remaining areas, which means that their values gradually disappear as one moves away from the well. A consequence of this fact is the co-existence of a conditioning effect, which is strong in some cases (illustrated by circles around the wells) and very weak in others (different lithoclasses were simulated at a small distance from the samples). These two conditioning standards are evident in Figure 2.22. The predominance of a number of occurrences of the second conditioning standard means that, overall, the images show a high degree of variability. It should also be stressed that in non-conditioned areas there is a clear sequential zoning of lithoclasses resulting from the process of truncating Gaussian distribution values which, in examples like this in which categories have no order relation, introduces an artificial pattern.

The influence of the wells in classification using simulated annealing can be observed in the patterns of the images around the samples. In fact, simulated annealing, which simultaneously includes two types of perturbation - the transformation of probability values into categorical values and the spatial permutation of pairs of values - makes the conditioning effect the highest of all algorithms tested. The images obtained are fairly similar to each other, as can be seen in the measurement of the weak variability between the images for different realisations. The images present a standard of marked continuity around all wells, with practically no exceptions, with a few pixels showing erratic distribution.

Simulated annealing as a post-processing of simulated images (in this case, SIS) improves approximation to theoretical variogram models, which are reproduced with practically total faithfulness. The perturbation used (permutation of values) does not introduce any alteration in the proportions of each lithoclass, in the same way that the fact that the blocks containing wells are not used in these permutations means that the simulation remains conditional. These images also feature some pixels (rather more than in the algorithm referred to above) displaying erratic distribution. These pixels represent the visible face of local minima in which the objective function falls in its path towards minimisation. In any case, these local minima are already in a somewhat low value domain of the objective function. This image obtained by post-processing has an angular pattern, due to the fact that the objective function has contributions only from orthogonal directions of the variograms. This may be minimised by introducing new directions in the objective function. Finally, it was observed that it is sufficient to include in the objective function the difference in values of variograms for small distances (in the examples described, the objective function was optimised with 5 grid nodes in each orthogonal direction).

Finally, it should be remembered that the simulation took place in a new frame of reference, and that it has to be transformed once again to the frame of reference of the formation. One of the major disadvantages that may be pointed out in this transformation of coordinates is the fact that inverse transformation does not necessarily mean that the proportions of the lithoclasses will be respected in the original frame of reference. Indeed, when inverse transformation is carried out, the final proportions are variable and only by mere coincidence would they turn out to be the same as the original values. In any case, application of the transform is absolutely essential to find continuity models in the horizontal direction.

3 DESCRIPTION OF PETROPHYSICAL PROPERTIES USING ESTIMATION METHODS

3.1 ESTIMATION OF PROPERTIES

The basic objective of any reservoir description consists of the generation of a two- or three-dimensional grid with nodes that spatially characterise the required properties, particularly in inter-well areas. Specific features associated with each particular field are the key factor in selection of the most appropriate multi-step approach.

If the main objective is to achieve the uncertainty of the main characteristics of the reservoir, simulation methods (see section 2 and 4) are the most appropriate techniques. Once we have defined the lithoclasses as homogeneous geological bodies, with regard to their internal properties, and we have characterised their spatial dispersion with simulation methodologies, we are now able to map the average values of the internal properties inside each lithoclass.

For this purpose, in this section a set of techniques is proposed to achieve the estimation of the main descriptive properties in oil fields: porosity, permeability and water saturation. In this particular oil field, based on a relationship between petrophysical properties and lithoclasses, it is possible to identify two distinct situations:

- the porosity and permeability values are strongly dependent on the lithoclass classification;
- the water saturation is mainly dependent on physical conditions (capillary pressure) but usually shows a correlation with porosity, permeability and capillary pressure.

These two distinct situations led to the selection of two different approaches in order to perform an appropriate spatial characterisation of these properties.

Regarding porosity and permeability estimation, the proposed method (zonal control estimation with ordinary kriging) takes into account the generated images of lithoclasses and follows a conditional process of zonal control. Due to the small correlation between porosity and permeability, and since the classification into lithoclasses took into account the porosity and permeability values, the estimation of both could be independent. Thus, each stochastic realisation of lithoclasses produces one estimated map corresponding to each variable. Following this methodology, the goal consists in highlighting the heterogeneity between lithoclasses, based on the homogeneity inside each lithoclass.

By contrast, estimation of the water saturation must take into account the physical rules that condition its spatial distribution and variability. Water saturation is a non-stationary variable and the estimation methods must take into account this physical tendency. To estimate the spatial distribution of this variable, and due to the small correlation with porosity and permeability, a simple method is proposed based on a single geometrical transformation and using ordinary kriging as an interpolator method. The relation between porosity and permeability with saturation is derived by a J function, which consists of a correlation function between water saturation, capillary pressure, porosity, and permeability (Archer and Wall, 1986). Thus, the objective is to work on a new frame that more easily correlates the physics of the phenomena with the selection of neighbouring samples. The main drawback that could be associated with this method is that a unique average image of the distribution of water saturation is produced, completely independent of lithoclasses and petrophysical properties. However, during this study a different approach based on an external drift provided by the J function was also tried. Nevertheless, for this particular case study, given the small correlation that exists between the water saturation and the theoretical J function, the use of kriging with an external drift provided by a J function do not bring any advantage.

3.2 ESTIMATION USING ZONAL CONTROL TECHNIQUE

3.2.1. CONTEXT OF THE PROBLEM

Geostatistical estimation of the internal properties of a reservoir must account for the wide variations between geological units. Sometimes, internal properties change sharply between geological units and smooth transitions are unlikely to occur. Therefore, when this zoning effect occurs, as is the most common situation, estimation combining data from different geological units will produce an artificial smoothing effect across the geological boundaries and transitions. To cope with this, geostatistical estimators must be conditioned throughout a zonal control, in order to avoid this false smoothing effect (Almeida *et al*, 1994, 1997, Soares and Almeida, 1995).

Traditional methods of imposing this zonal control consisted in estimating a point x, which belongs to a given phase, by using only data from this phase. The method proposed in this work, to estimate the internal properties with zonal control, accounts for the entire spatial sampling pattern (all phases) and for the spatial structure (variograms) of each phase. The zonal control technique basically consists in the two following fundamental steps:

i) Perform, over the entire area *A*, an estimation of the attributes of all phases based on all available data. The estimation consists in a generalisation of the multi-phase kriging algorithm to the estimation of attributes in a multi-phase set (Soares, 1992). The estimation area is delimited by the boundaries of the entire set of phases;

ii) Merge the estimated values with the morphology of the multi-phase set - fill these areas with the corresponding estimated values.

3.2.2. DEFINITION OF THE MULTI-PHASE SET

Consider a set of mutually exclusive categories *k* (rock types, lithoclasses, geological units, etc.) where an internal property *z(x)* is spatially dispersed in all categories and displays discontinuous transitions between them, giving rise to a zoning effect.

Defining the internal attribute *z(x)* as a random variable located in *x* in the studied area *A* (with a set of *K* phases, X_k, *k = 1,... K*), it is possible to construct the two following vector variables, $I_k(x)$ and $Y_k(x)$ (see Figure 3.1):

a) One indicator vector, according to the definition described above in section 2.1. Each spatial location *x* is coded for all phases *k = 1,… K* as a non-ordered indicator vector ($I_k(x)$, *k = 1, K*), where *K* represents the number of phases:

$$I_k(x) = \begin{cases} 1 & \text{if } x \text{ belongs to phase } X_k \\ 0 & \text{if } x \text{ belongs to phase } X_j \quad j \neq k \end{cases} \tag{3.1}$$

b) The content of *z(x)* inside each phase X_k: $Y_k(x) = I_k(x) \cdot z(x)$

$$Y_k(x) = \begin{cases} z(x) & \text{if } x \text{ belongs to phase } X_k \\ 0 & \text{if } x \text{ belongs to phase } X_j \quad j \neq k \end{cases} \tag{3.2}$$

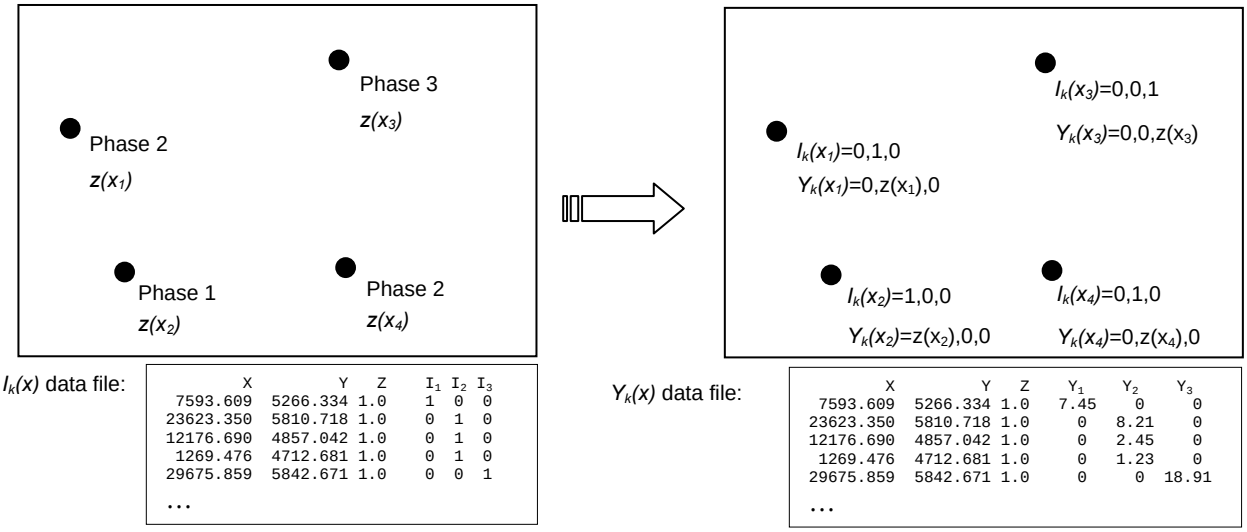

$I_k(x)$ data file:

X	Y	Z	I_1	I_2	I_3
7593.609	5266.334	1.0	1	0	0
23623.350	5810.718	1.0	0	1	0
12176.690	4857.042	1.0	0	1	0
1269.476	4712.681	1.0	0	1	0
29675.859	5842.671	1.0	0	0	1
…					

$Y_k(x)$ data file:

X	Y	Z	Y_1	Y_2	Y_3
7593.609	5266.334	1.0	7.45	0	0
23623.350	5810.718	1.0	0	8.21	0
12176.690	4857.042	1.0	0	2.45	0
1269.476	4712.681	1.0	0	1.23	0
29675.859	5842.671	1.0	0	0	18.91
…					

Figure 3.1 Illustration of the definition of the auxiliary variables in a multi-phase structure ($K = 3$).

For this auxiliary variable $Y_k(x)$ the following two first moments are defined by:

$$m_{Y_k} = E\{Y_k(x)\} = E\{z(x).I_k(x)\} \tag{3.3}$$

$$\text{var}_{Y_k} = E\{Y_k(x) - m_{Y_k}\}^2 = E\{z(x).I_k(x) - m_{Y_k}\}^2 \tag{3.4}$$

3.2.3. SPATIAL CONTINUITY MEASURES: COVARIANCE AND EXPERIMENTAL VARIOGRAMS

For the auxiliary variable $Y_k(x)$, $k = 1, \ldots K$, the non-centred covariance (a continuity measure of $z(x)$ inside each phase k) is defined by:

$$C_{Y_k}(h) = E\{Y_k(x).Y_k(x+h)\} = E\{z(x).I_k(x)\ .\ z(x+h).I_k(x+h)\} \tag{3.5}$$

and the corresponding variogram can be defined as follows:

$$\gamma_{Y_k}(h) = \frac{1}{2}E\{Y_k(x) - Y_k(x+h)\}^2 = \frac{1}{2}E\{(z(x).I_k(x)) - (z(x+h).I_k(x+h))\}^2 \tag{3.6}$$

In most situations the multi-phase set of phases is characterised by an insufficient number of experimental data to calculate or estimate individual covariances. In these situations, multi-phase covariance (a global continuity model) for the entire set of categories is the

appropriate tool to compute and estimate a continuity model. Thus, the multi-phase covariance of $Y_k(x)$ is calculated by:

$$C_Y(h) = E\left\{\sum_{k=1}^{K}\left[Y_k(x).Y_k(x+h)\right]\right\} =$$

$$= \sum_{k=1}^{K} E\left\{z_k(x).z_k(x+h).J_k(x,x+h)\right\} \qquad (3.7)$$

Using the above expression, $J_k(x, x+h)=I_k(x).I_k(x+h)$ is equal to *"1"* if both extremes of the vector h are in the same phase and *"0"* otherwise.

Given that $C_{Y_k}(h)$ is the covariance of $z(x)$ inside each phase X_k, the multi-phase covariance $C_Y(h)$ can be assumed to be a weighted average of the individual covariances of $z(x)$ inside each phase X_k:

$$C_Y(h) = \frac{1}{N(h)}\sum_{k=1}^{K} L_k(h).C_k(h) \qquad (3.8)$$

denoting by $L_k(h)$ the number of pairs of points inside each phase X_k and $N(h)$ the total number of pairs of points separated by h.

Lastly, the corresponding multi-phase variogram of $Y_k(x)$ can be defined by:

$$\gamma_Y(h) = \frac{1}{2}E\left\{\sum_{k=1}^{K}\left[Y_k(x) - Y_k(x+h)\right]^2\right\} =$$

$$= \frac{1}{2}\sum_{k=1}^{K} E\left\{\left(z_k(x).I_k(x)\right) - \left(z_k(x+h).I_k(x+h)\right)\right\}^2 \qquad (3.9)$$

and is directly estimated by:

$$\gamma_Y(h) = \frac{1}{2N(h)}\sum_{k=1}^{K}\sum_{i=1}^{N(h)}\left[Y_k(x_i) - Y_k(x_i+h)\right]^2 \qquad (3.10)$$

Calculation and modelling of the multi-phase covariances or variograms must account for the mixture of two or more different structures. This means that in several cases the multi-phase set can be characterised by more than one covariance, grouping a set of homologous phases (in terms of continuity).

3.2.4. SPATIAL INFERENCE OF ATTRIBUTES

At any spatial location x_0 inside area A, one can define the multi-phase kriging estimator of $Y(x_0)$ based on a set of n neighbourhood samples $z_i(x_\alpha)$:

$$\left[Y_k(x_0)\right]^* = \sum_{\alpha=1}^{n} \lambda_\alpha \; . \; Y_k(x_\alpha) \; = \sum_{\alpha=1}^{n} \lambda_\alpha \; (z_k(x_\alpha).I_K(x_\alpha)) \qquad (3.11)$$

with $k=1,\ldots K$ and $\alpha=1,\ldots n$

The set of weights λ_α are calculated by solving the corresponding ordinary kriging system written with multi-phase variogram or covariance models:

$$\begin{cases} \sum_{\alpha=1}^{n} \lambda_\alpha . C_Y(x_\alpha, x_\beta) + \mu = C_Y(x_\alpha, x_0) \\ ..... \qquad\qquad \text{with } \alpha, \beta = 1, \ldots n \\ \sum_{\alpha=1}^{n} \lambda_\alpha \; = 1 \end{cases} \qquad (3.12)$$

Thus, $\left[Y_K(x_0)\right]^*$ is the kriging estimator of the content of $z(x)$ inside each phase X_k in location x_0. The contribution of the values $z(x_\alpha)$ of other phases X_j, $j \neq k$ to the estimation is revealed only by the inclusion of the spatial location of these points in the weighting calculation when solving the kriging system.

Briefly, the zonal control of the estimation of $Y_k(x_0)$ with x_0 belonging to X_k in all area A must account for the neighbouring samples of x_0, $z(x_\alpha)$, $x_\alpha \in X_k$, and $z(x_\beta)$, $x_\beta \notin X_k$, and finally one global model of continuity - the multi-phase variogram - or a set of multi-phase variograms with similar continuity characteristics.

Since the estimator $\left[Y_K(x_0)\right]^*$ is based on a single multi-phase covariance, the estimation is performed just once for all phases X_k due to the independence between the kriging weights and the phases X_k. However, when dealing with different covariance models of groups of phases, the estimation procedure of $z(x)$ inside each multi-phase set is exactly the same as described above, but carried out in steps, according to the number of groups.

On the other hand, for any phase X_k the respective proportion in the location x_0, based on the multi-phase indicator variogram of $I_k(x)$, can be estimated as follows:

$$\left[I_k(x_0)\right]^* = \sum_{\alpha=1}^{n} \lambda_\alpha . I_k(x_\alpha) \tag{3.13}$$

It is important to emphasise that since a global model of covariance $C_I(h)$ is used, all kriging weights are independent of the phases X_k, which means that:

$$\lambda_\alpha(1) = \lambda_\alpha(2) = \ldots = \lambda_\alpha(K) = \lambda_\alpha$$

Finally, assuming the independence of variables $I_k(x)$ and $Y_k(x)$, the estimator of $z(x_0)$ in spatial location x_0 for each phase is given by:

$$z_k(x_0) = \begin{cases} \dfrac{\left[Y_k(x_0)\right]^*}{\left[I_k(x_0)\right]^*} & \text{if} \quad \left[I_k(x_0)\right]^* > 0 \\ 0 & \text{if} \quad \left[I_k(x_0)\right]^* = 0 \end{cases} \tag{3.14}$$

with $k = 1,\ldots K$.

After the calculation of $z_k(x_0)$ for all phases, the value $z(x_0)$ can be obtained by overlapping the morphology: if the point x_0 is allocated to a specific phase X_k then:

$$\left[z(x_0)\right]^* = \left[z_k(x_0)\right]^* \qquad \text{if} \quad x_0 \in X_k \tag{3.15}$$

The most important advantage of estimation with zonal control is that the spatial location of samples of all phases are taken into account whereas, in the classical procedure, only samples from the phase which x_0 (the point to be estimated) belongs to are taken into account.

The difference between these two procedures can be illustrated in the simple sampling examples sketched in Figure 3.2 a) and b). Following these figures, sampling points x_1, x_2 and x_3 and estimated point x_0 belong to phase A and x_4 belongs to phase B.

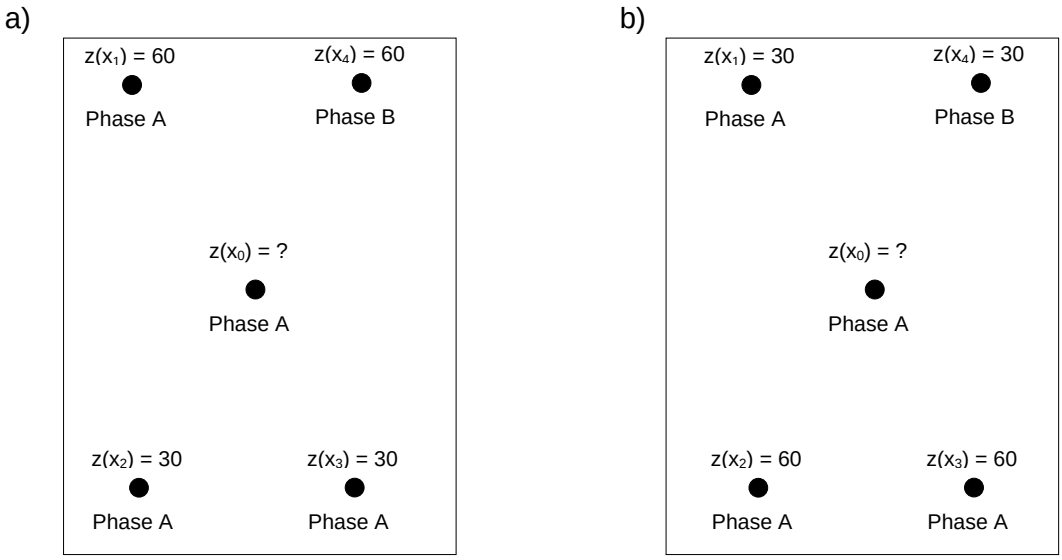

Figure 3.2 Sketch to illustrate zonal control estimation effects in two sampling situations.

For the sake of simplicity let us consider an isotropic variogram of $Z(x)$, $Y(x)$ and $I(x)$ and equal distances between x_1, x_2, x_3 and x_4 and x_0. The classical procedure gives for estimated value of $z(x_0)$ considering that x_0 belongs to phase A:

$$[\, Z_A(x_0) \,]^* = 0.50\, z(x_1) + 0.25\, z(x_2) + 0.25\, z(x_3) = 45$$

The estimation of x_0 using zonal control gives:

$$[\, Y_A(x_0) \,]^* = 0.25\, Y(x_1) + 0.25\, Y(x_2) + 0.25\, Y(x_3) + 0.25\, Y(x_4) = 30$$

$$[\, I(x_0) \,]^* = 0.25\, I(x_1) + 0.25\, I(x_2) + 0.25\, I(x_3) + 0.25\, I(x_4) = 0.75$$

Use of equation (3.14) gives:

$$[\, Z_A(x_0) \,]^* = 30 / 0.75 = 40$$

Following sampling scheme b), the classical procedure for the estimation of $z(x_0)$ gives:

$$[\, Z_A(x_0) \,]^* = 0.50\, z(x_1) + 0.25\, z(x_2) + 0.25\, z(x_3) = 45$$

Now, the estimation of x_0 using zonal control gives:

$$[\, Y_A(x_0) \,]^* = 0.25\, Y(x_1) + 0.25\, Y(x_2) + 0.25\, Y(x_3) + 0.25\, Y(x_4) = 37.5$$

$$[\, I(x_0) \,]^* = 0.25\, I(x_1) + 0.25\, I(x_2) + 0.25\, I(x_3) + 0.25\, I(x_4) = 0.75$$

Again, use of equation (3.14) gives in this case:

$$[\, Z_A(x_0) \,]^{*} = 37.5 / 0.75 = 50$$

In summary, estimation with zonal control does not consider $Z(x_1)$ as an isolated sample and reduces its weight in the estimation compared with the classical procedure, which, erroneously, does not consider the spatial location of $Z(x_4)$ (which belongs to phase B) and consequently overestimates the influence of $Z(x_1)$.

3.3 EXAMPLE OF POROSITY ESTIMATION USING A ZONAL CONTROL TECHNIQUE

The porosity of a rock is defined as the fraction of pore volume relative to the total volume of rock. Depending on the rock pattern at small scale, porosity can vary from 0% up to 25-30% or even more, in some areas of the reservoir (North, 1985). For example, shales usually have low porosity, in contrast to sandstone, which usually has the highest values.

Proper characterisation of porosity is an essential step in the construction of a petrophysical model: total oil reserves or oil-in-place depends on porosity (and also on permeability), and since non-porous rocks cannot accommodate fluids, they may act as barriers to flow. Usually a given rock type is characterised by a low range of porosity values, which justifies the use of estimation techniques for mapping this variable.

The objective of the present case study is accordingly to estimate porosity, which is a petrophysical variable dependent on lithoclass types. Porosity is an additive variable recorded along the wells through log devices (some wells are cored and logged simultaneously), and is estimated using the above-mentioned method of zonal control conditioned to the simulated morphology of the lithoclasses. The spatial transitions of porosity values between lithoclasses are sometimes not smooth, as can be seen in the sequence of values observed in the three wells (Figure 3.3) and in the univariate porosity statistics for each lithoclass (Figure 3.4).

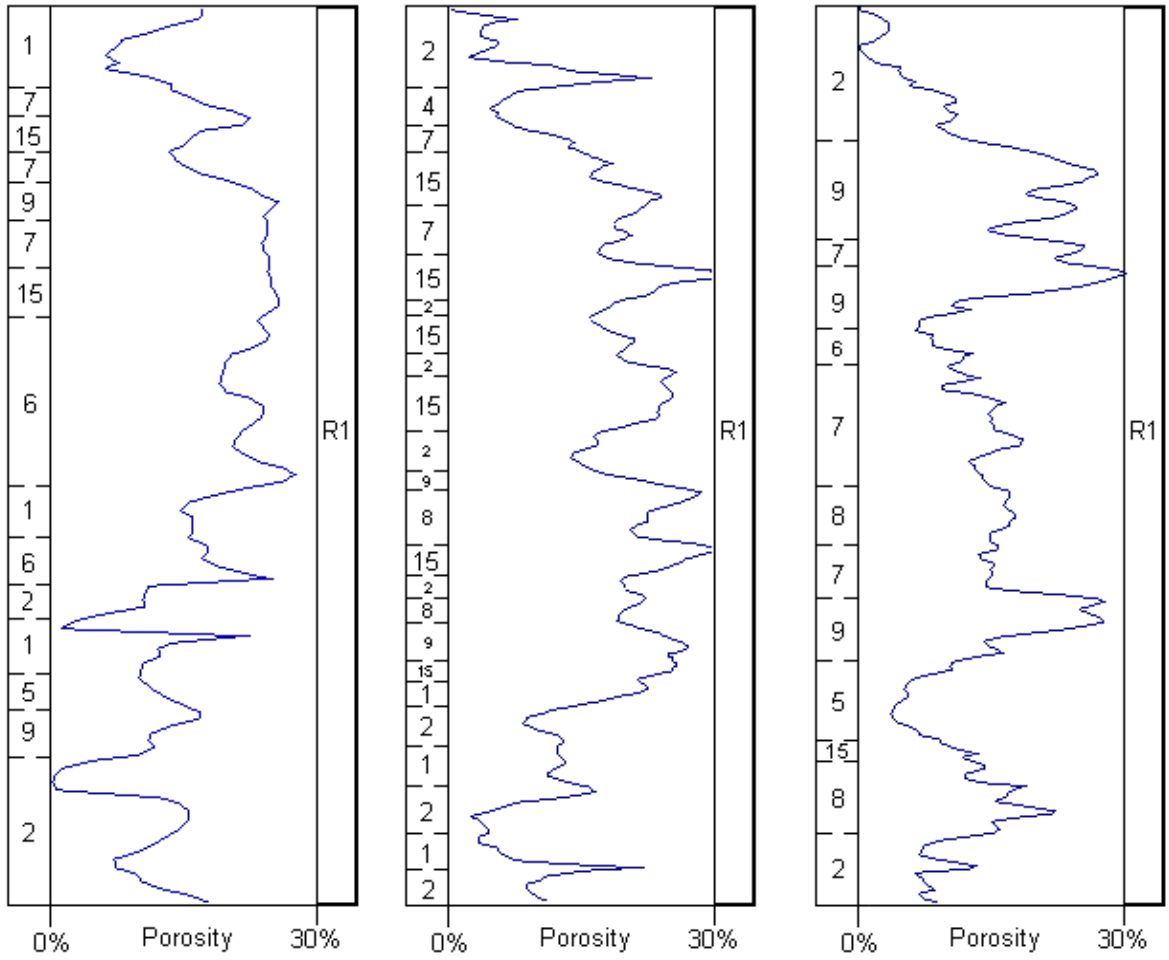

Figure 3.3 Sequence of porosity values and corresponding lithoclasses in three wells located in one upper layer.

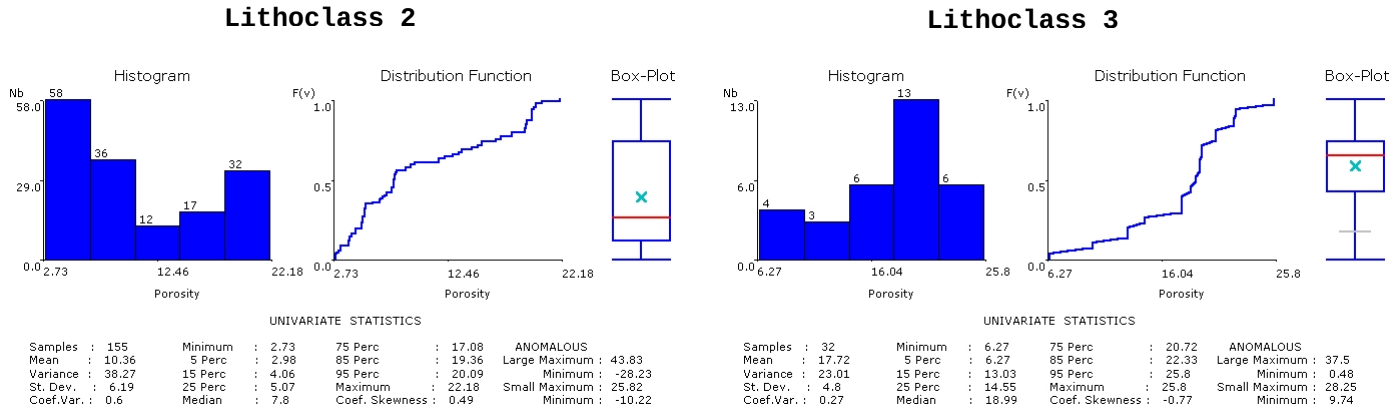

Figure 3.4 Univariate statistics for experimental values of porosity in one upper layer – layer 150, R1 - by lithoclasses: 2, 3, 4, 5, 6, 7, 8, 9 and 15.

Lithoclass 4

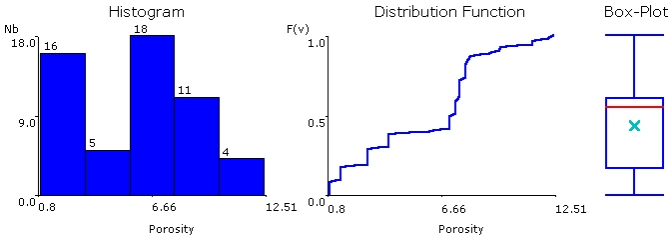

UNIVARIATE STATISTICS

Samples	54	Minimum	0.8	75 Perc	7.92	ANOMALOUS	
Mean	5.89	5 Perc	0.8	85 Perc	8.06	Large Maximum	22.74
Variance	10.58	15 Perc	1.34	95 Perc	11.45	Minimum	-8.28
St. Dev.	3.25	25 Perc	2.75	Maximum	12.51	Small Maximum	14.99
Coef.Var.	0.55	Median	7.23	Coef. Skewness	-0.1	Minimum	-0.52

Lithoclass 5

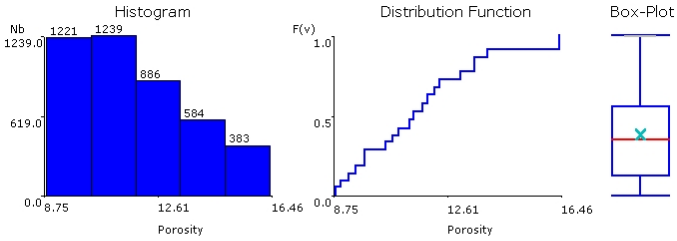

UNIVARIATE STATISTICS

Samples	4313	Minimum	8.75	75 Perc	13.06	ANOMALOUS	
Mean	11.68	5 Perc	8.91	85 Perc	13.53	Large Maximum	21.43
Variance	4.49	15 Perc	9.43	95 Perc	16.46	Minimum	1.45
St. Dev.	2.12	25 Perc	9.73	Maximum	16.46	Small Maximum	16.44
Coef.Var.	0.18	Median	11.44	Coef. Skewness	0.71	Minimum	6.45

Lithoclass 6

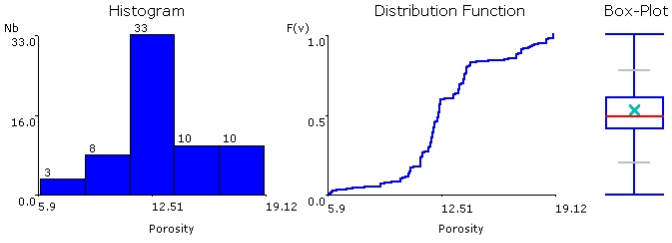

UNIVARIATE STATISTICS

Samples	64	Minimum	5.9	75 Perc	13.92	ANOMALOUS	
Mean	12.88	5 Perc	8.88	85 Perc	16.96	Large Maximum	20.01
Variance	8.1	15 Perc	10.69	95 Perc	18.7	Minimum	4.71
St. Dev.	2.85	25 Perc	11.37	Maximum	19.12	Small Maximum	16.19
Coef.Var.	0.22	Median	12.36	Coef. Skewness	0.24	Minimum	8.54

Lithoclass 7

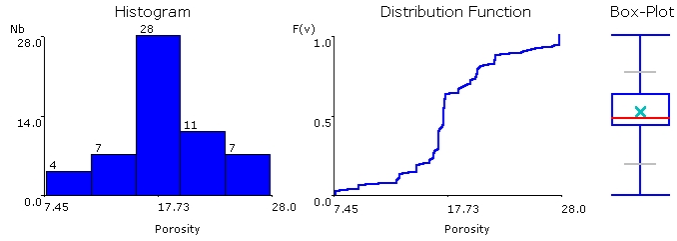

UNIVARIATE STATISTICS

Samples	57	Minimum	7.45	75 Perc	20.37	ANOMALOUS	
Mean	18.14	5 Perc	9.5	85 Perc	22.14	Large Maximum	29.12
Variance	21.22	15 Perc	14.85	95 Perc	28.0	Minimum	5.6
St. Dev.	4.61	25 Perc	16.45	Maximum	28.0	Small Maximum	23.24
Coef.Var.	0.25	Median	17.36	Coef. Skewness	0.22	Minimum	11.48

Lithoclass 8

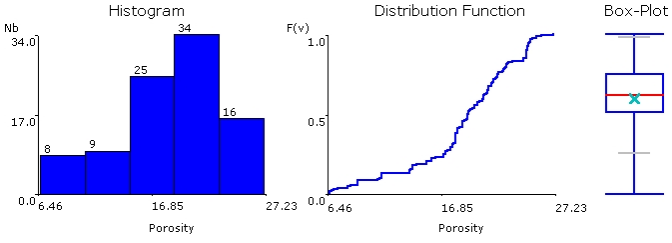

UNIVARIATE STATISTICS

Samples	92	Minimum	6.46	75 Perc	22.1	ANOMALOUS	
Mean	18.87	5 Perc	8.14	85 Perc	24.71	Large Maximum	34.26
Variance	24.11	15 Perc	13.83	95 Perc	25.11	Minimum	4.35
St. Dev.	4.91	25 Perc	17.12	Maximum	27.23	Small Maximum	26.78
Coef.Var.	0.26	Median	19.31	Coef. Skewness	-0.81	Minimum	11.83

Lithoclass 9

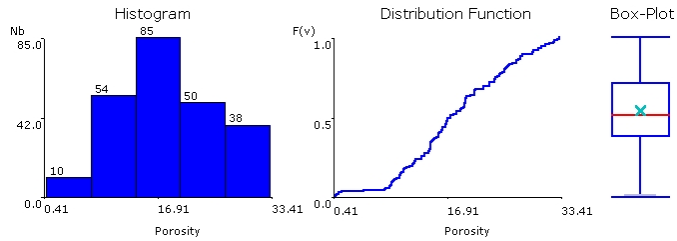

UNIVARIATE STATISTICS

Samples	237	Minimum	0.41	75 Perc	24.0	ANOMALOUS	
Mean	18.28	5 Perc	7.75	85 Perc	27.14	Large Maximum	50.37
Variance	58.38	15 Perc	10.09	95 Perc	31.43	Minimum	-15.63
St. Dev.	7.64	25 Perc	13.0	Maximum	33.41	Small Maximum	33.87
Coef.Var.	0.42	Median	17.37	Coef. Skewness	0.01	Minimum	0.87

Lithoclass 15

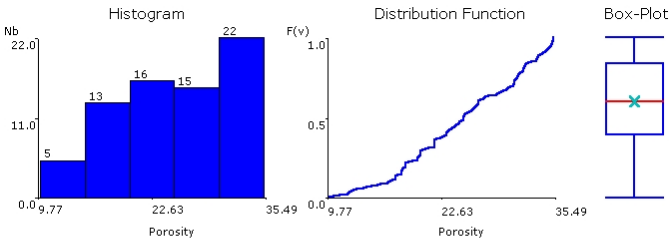

UNIVARIATE STATISTICS

Samples	71	Minimum	9.77	75 Perc	31.39	ANOMALOUS	
Mean	25.2	5 Perc	12.48	85 Perc	33.52	Large Maximum	59.72
Variance	46.94	15 Perc	17.97	95 Perc	35.3	Minimum	-9.28
St. Dev.	6.85	25 Perc	19.89	Maximum	35.49	Small Maximum	42.47
Coef.Var.	0.27	Median	25.22	Coef. Skewness	-0.22	Minimum	7.97

Figure 3.4(cont) Univariate statistics for experimental values of porosity in one upper layer – layer 150, R1 - by lithoclasses: 2, 3, 4, 5, 6, 7, 8, 9 and 15.

3.3.1. DEFINITIONS AND MULTI-PHASE VARIOGRAMS

The proposed methodology was applied to the entire field, and in this section detailed results for a selected layer - layer 150 - are shown. Using the porosity values $\phi(x)$ known in 19 wells, variables $Y_k(x)$ and $I_k(x)$ were constructed according to equations 3.1 and 3.2, using the porosity values and the lithoclass classification. Within the selected layer, 9 different lithoclasses were identified: 2, 3, 4, 5, 6, 7, 8, 9, and 15. Looking at the lithoclass simulation study (see section 2.5.2), two groups, one with four lithoclasses plus complementary areas, and the other with five lithoclasses, were identified corresponding to continuity models with 4000 metres and 500 metres of range respectively in the horizontal direction and both with 45 S.U. in the vertical direction.

In order to group the phases $Y_k(x)$ into homogeneous sets, individual multi-phase variograms were calculated for the horizontal direction. In Figure 3.5 a) through Figure 3.5 c) three experimental individual variograms corresponding to a continuous set (lithoclasses 4, 8 and 15) are represented. In Figure 3.6 a) through Figure 3.6 f) the erratic set (lithoclasses 2, 3, 5, 6, 7 and 9) is represented where it is not possible to identify spatial continuity evidence.

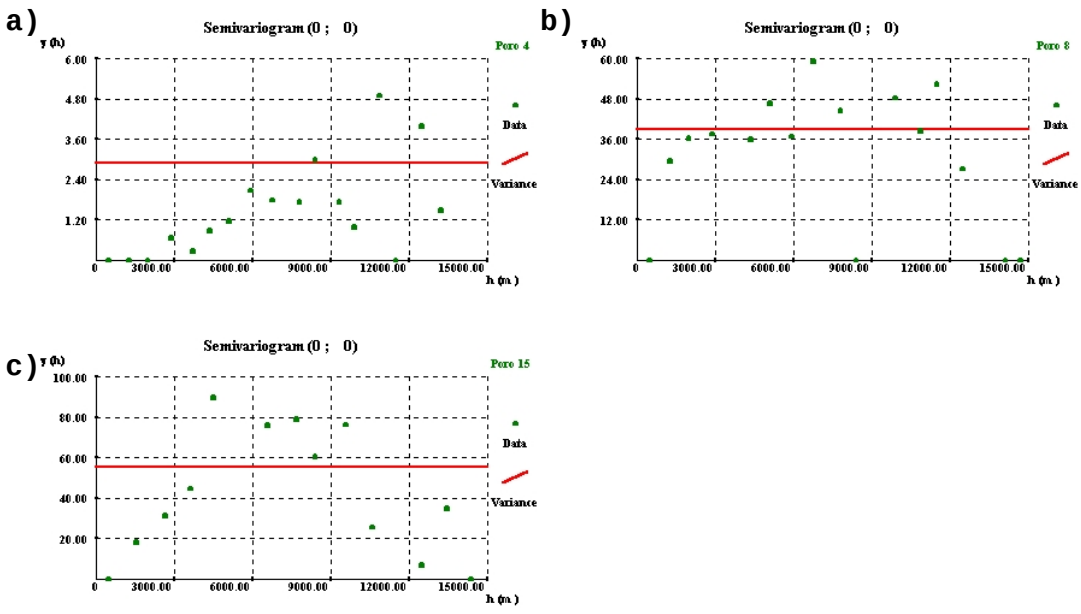

Figure 3.5 Experimental variograms of $Y_k(x)$ within lithoclasses classified as continuous: a) lithoclass 4; b) lithoclass 8; c) lithoclass 15.

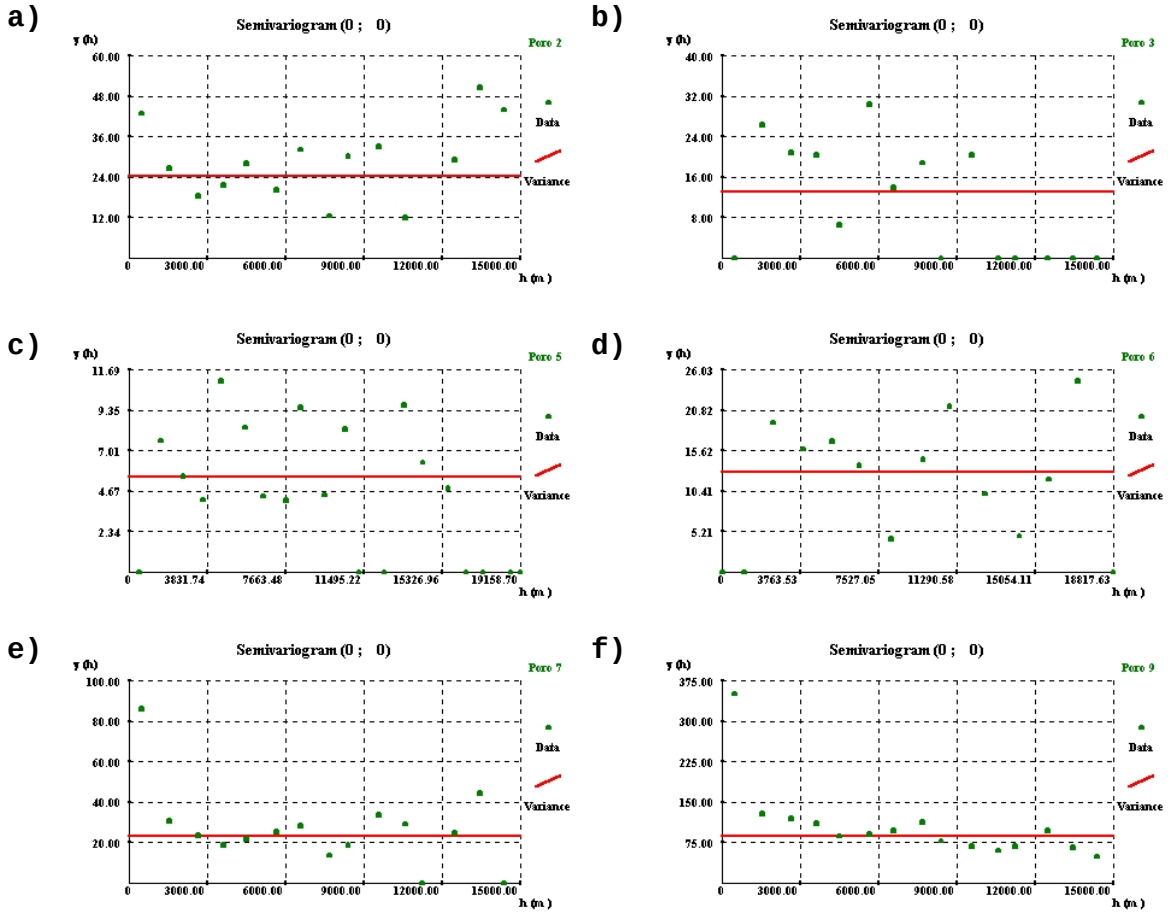

Figure 3.6 Experimental variograms of $Y_k(x)$ within lithoclasses classified as erratic: a) lithoclass 2; b) lithoclass 3; c) lithoclass 5; d) lithoclass 6; e) lithoclass 7; f) lithoclass 9.

In this particular layer, regarding variable $I_k(x)$, lithoclasses 4, 6, 8 and 15 are classified as continuous with an average range of 4000 metres and lithoclasses 2, 3, 5, 7, and 9 are classified as erratic. As can be observed, only the porosity from lithoclasses 4, 8 and 15 can be considered continuous. Lithoclass 2 is continuous, but the variability of porosity within this lithoclass is erratic. The entire set of erratic lithoclasses also displays low spatial continuity of porosity.

Multi-phase variograms of $Y_k(x)$ were calculated for both groups in the horizontal and vertical directions and are shown in Figure 3.7 and Figure 3.8: the horizontal multi-phase variogram for the continuous group was fitted with a spherical model with 4000 metres range and 40 S.U. in the vertical direction, while the non-continuous group or erratic group was fitted with a variogram displaying a range of 500 metres in the horizontal direction and 20 S.U. in the vertical direction. The horizontal range for the erratic group was adopted based on the reasons explained in section 2.5.2: this range corresponds to the smallest distance between wells and dimensions of the block for dynamic simulation.

Model: 97.6 Sph (a = 4000 m) **Model: 97.6 Sph (a = 40 S.U.)**

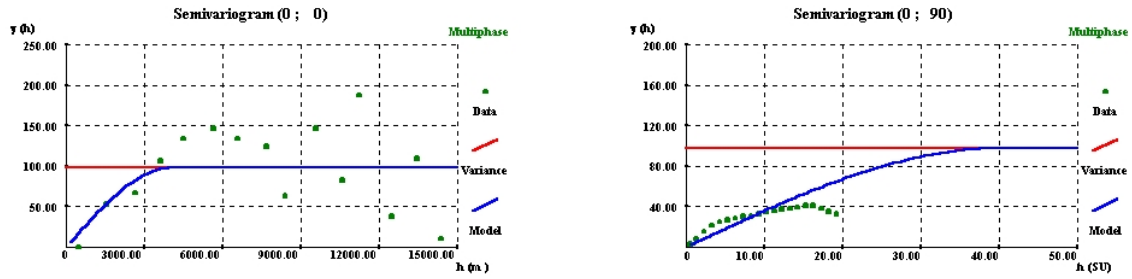

Figure 3.7 Experimental multi-phase variograms of the continuous set and theoretical model fitted.

Model: 166 Sph (a = 500 m) **Model: 166 Sph (a = 20 S.U.)**

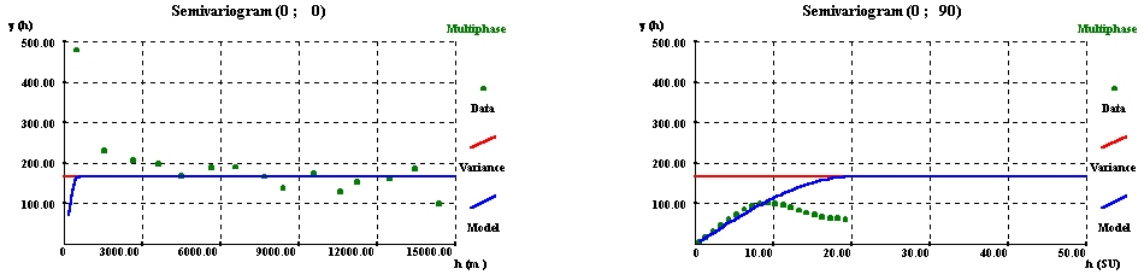

Figure 3.8 Experimental multi-phase variograms of the erratic set and theoretical model fitted.

3.3.2. KRIGING ESTIMATION WITH ZONAL CONTROL TECHNIQUE

The porosity was estimated with the zonal control methodology explained above based on two multi-phase variogram models corresponding to continuous and erratic groups of lithoclasses.

Finally, the estimated porosity values were merged with the stochastic images of lithoclasses (in this example, they came from sequential indicator simulation algorithm, see section 2.5) and the result consists of an estimated image of porosity conditioned to the simulated image of lithoclasses. In Figure 3.9 the estimated porosity values are displayed as well as the corresponding image of lithoclasses for a set of levels and sections from one intermediate layer. Since each grid node is previously classified as lithoclass *k*, the porosity distribution conditioned to the lithoclasses is finally obtained.

Simulated Lithoclasses ***Estimated Porosity***

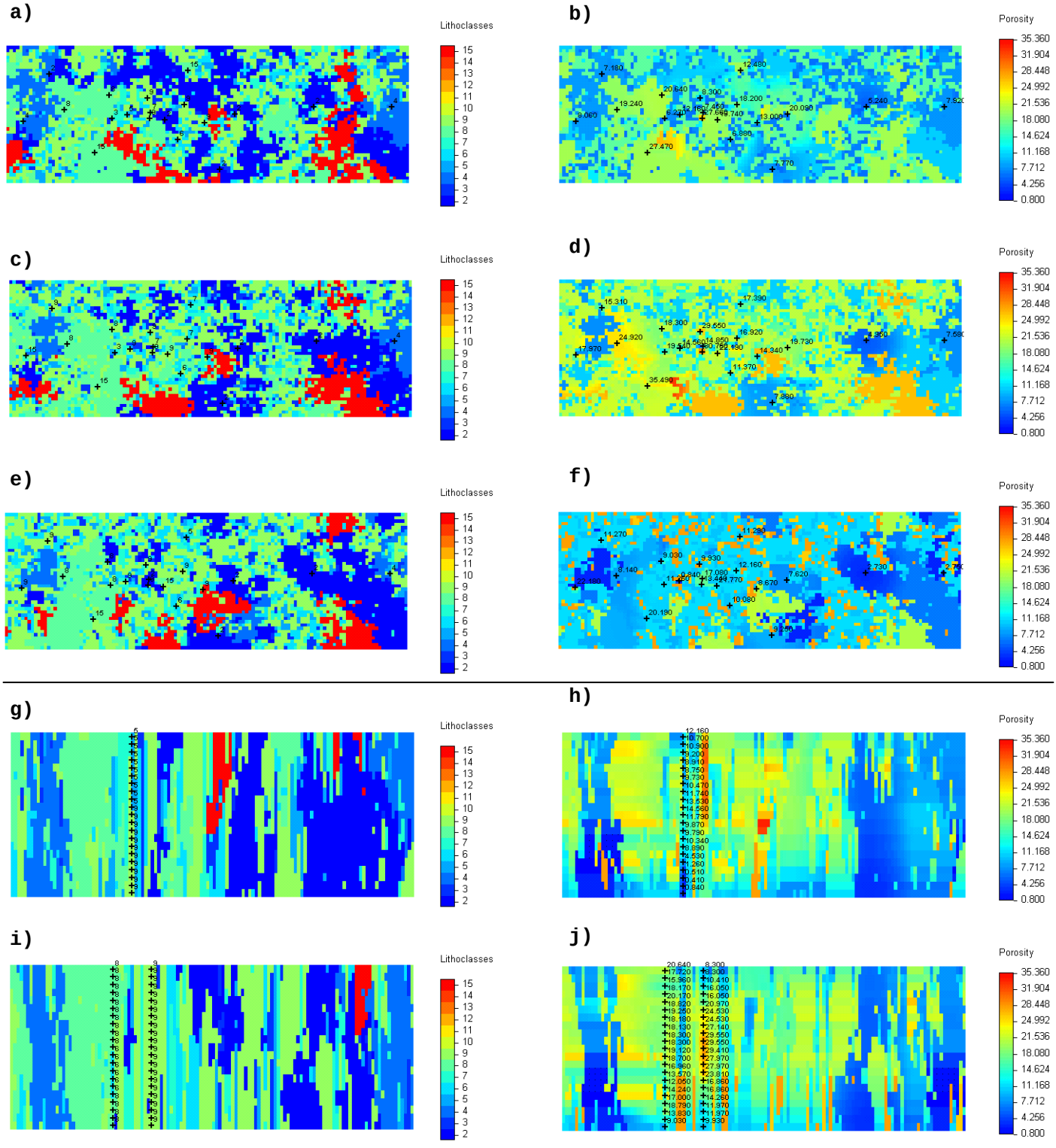

Figure 3.9 Illustration of 3 horizontal views and 2 sections from the generated stochastic images of lithoclasses using SIS with correction for local probabilities algorithm and corresponding estimated images of porosity using zonal control estimation.

Table 3.1 compares basic statistics from estimated porosity values and experimental data (after geometrical transformation) for the selected layer. In Figure 3.10, the univariate statistics for estimated values of porosity within the same layer are displayed.

Table 3.1 Univariate statistics of experimental and estimated values of porosity.

	Porosity: experimental data			Porosity: estimated values		
Lithoclass	# Samples	Mean (%)	Variance	# Samples	Mean (%)	Variance
2	154	10.36	38.27	21422	9.29	9.53
3	32	17.72	23.01	4269	19.79	29.51
4	54	5.89	10.58	7422	5.68	9.48
5	36	11.14	3.14	4313	11.68	4.49
6	65	12.87	8.10	8120	12.23	4.30
7	58	18.14	21.22	7762	21.16	36.43
8	92	18.86	24.11	13897	19.77	13.40
9	236	18.27	58.38	32350	18.80	9.66
15	71	25.33	45.78	9813	26.57	26.32
All	798	15.80	61.04	109368	16.31	47.99

As can be seen in the above table, estimated values display identical statistics, which can be considered the first validation of the proposed estimation method. In Figure 3.10, a set of sections of porosity values for the entire field using the above-described methodology is represented.

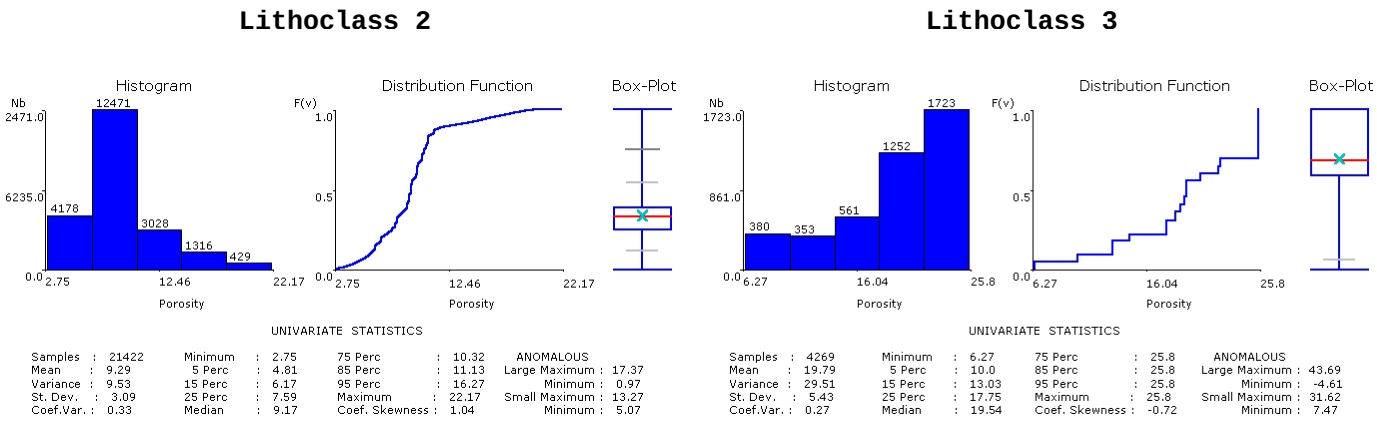

Figure 3.10 Univariate statistics for estimated values of porosity in one upper layer - layer 150, R1 - by lithoclasses: 2, 3, 4, 5, 6, 7, 8, 9 and 15.

Lithoclass 4

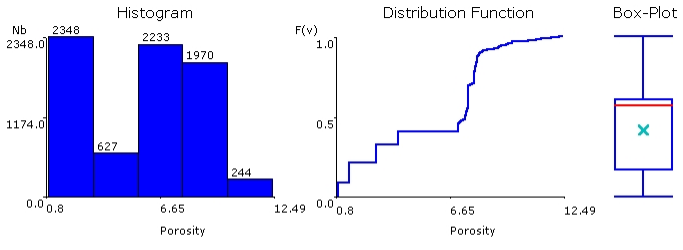

UNIVARIATE STATISTICS

Samples	7422	Minimum	0.8	75 Perc	7.92	ANOMALOUS	
Mean	5.68	5 Perc	0.8	85 Perc	8.05	Large Maximum	22.95
Variance	9.48	15 Perc	1.34	95 Perc	9.65	Minimum	-8.07
St. Dev.	3.08	25 Perc	2.75	Maximum	12.49	Small Maximum	15.2
Coef.Var.	0.54	Median	7.44	Coef. Skewness	-0.31	Minimum	-0.31

Lithoclass 5

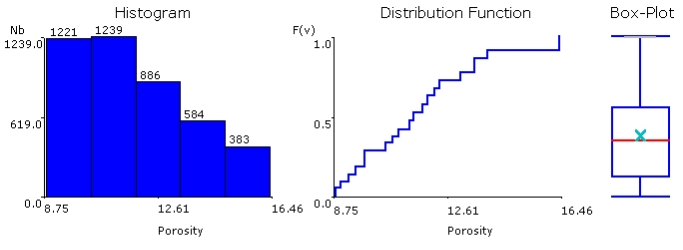

UNIVARIATE STATISTICS

Samples	4313	Minimum	8.75	75 Perc	13.06	ANOMALOUS	
Mean	11.68	5 Perc	8.91	85 Perc	13.53	Large Maximum	21.43
Variance	4.49	15 Perc	9.43	95 Perc	16.46	Minimum	1.45
St. Dev.	2.12	25 Perc	9.73	Maximum	16.46	Small Maximum	16.44
Coef.Var.	0.18	Median	11.44	Coef. Skewness	0.71	Minimum	6.45

Lithoclass 6

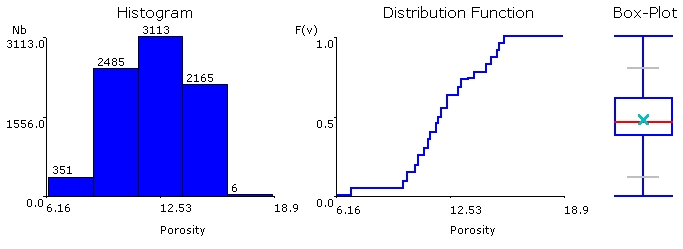

UNIVARIATE STATISTICS

Samples	8120	Minimum	6.16	75 Perc	13.93	ANOMALOUS	
Mean	12.23	5 Perc	9.88	85 Perc	14.88	Large Maximum	20.67
Variance	4.3	15 Perc	10.55	95 Perc	15.31	Minimum	3.39
St. Dev.	2.07	25 Perc	11.05	Maximum	18.9	Small Maximum	16.35
Coef.Var.	0.17	Median	12.03	Coef. Skewness	-0.27	Minimum	7.71

Lithoclass 7

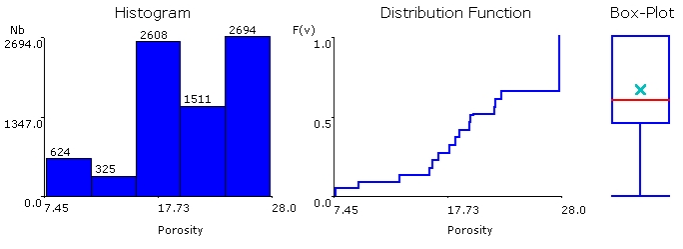

UNIVARIATE STATISTICS

Samples	7762	Minimum	7.45	75 Perc	28.0	ANOMALOUS	
Mean	21.16	5 Perc	9.5	85 Perc	28.0	Large Maximum	53.14
Variance	36.43	15 Perc	16.09	95 Perc	28.0	Minimum	-13.52
St. Dev.	6.04	25 Perc	16.89	Maximum	28.0	Small Maximum	36.48
Coef.Var.	0.29	Median	19.81	Coef. Skewness	-0.43	Minimum	3.15

Lithoclass 8

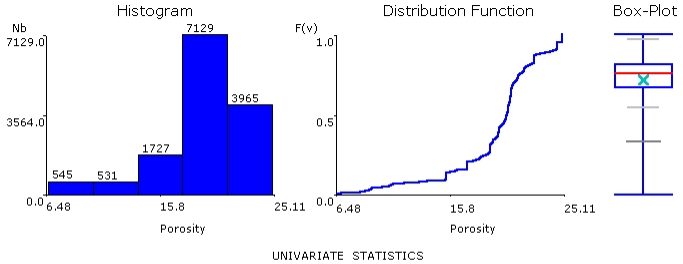

UNIVARIATE STATISTICS

Samples	13897	Minimum	6.48	75 Perc	21.64	ANOMALOUS	
Mean	19.77	5 Perc	10.84	85 Perc	22.84	Large Maximum	28.5
Variance	13.4	15 Perc	17.15	95 Perc	24.86	Minimum	12.62
St. Dev.	3.66	25 Perc	18.99	Maximum	25.11	Small Maximum	24.53
Coef.Var.	0.19	Median	20.56	Coef. Skewness	-1.26	Minimum	16.59

Lithoclass 9

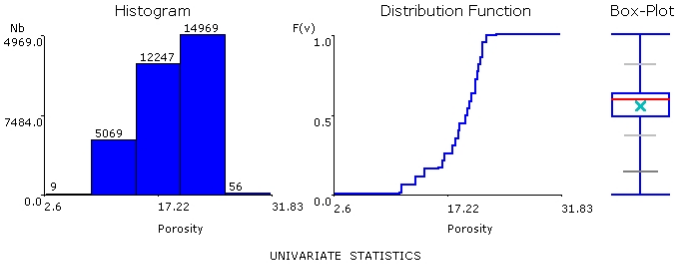

UNIVARIATE STATISTICS

Samples	32350	Minimum	2.6	75 Perc	21.11	ANOMALOUS	
Mean	18.8	5 Perc	11.21	85 Perc	21.56	Large Maximum	32.89
Variance	9.66	15 Perc	14.22	95 Perc	22.28	Minimum	6.88
St. Dev.	3.11	25 Perc	16.78	Maximum	31.83	Small Maximum	26.39
Coef.Var.	0.17	Median	19.89	Coef. Skewness	-0.99	Minimum	13.39

Lithoclass 15

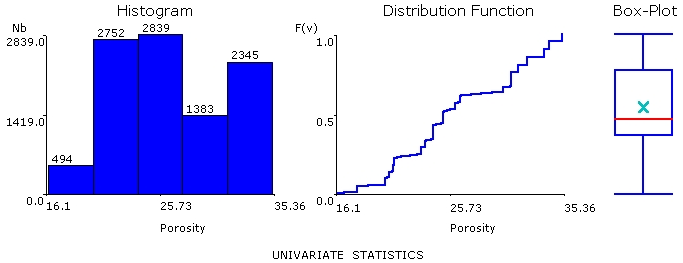

UNIVARIATE STATISTICS

Samples	9813	Minimum	16.1	75 Perc	30.99	ANOMALOUS	
Mean	26.57	5 Perc	19.88	85 Perc	32.35	Large Maximum	48.51
Variance	26.32	15 Perc	20.79	95 Perc	34.28	Minimum	1.8
St. Dev.	5.13	25 Perc	23.21	Maximum	35.36	Small Maximum	36.83
Coef.Var.	0.19	Median	25.16	Coef. Skewness	0.15	Minimum	13.48

Figure 3.10(cont) Univariate statistics for estimated values of porosity in one upper layer - layer 150, R1 - by lithoclasses: 2, 3, 4, 5, 6, 7, 8, 9 and 15.

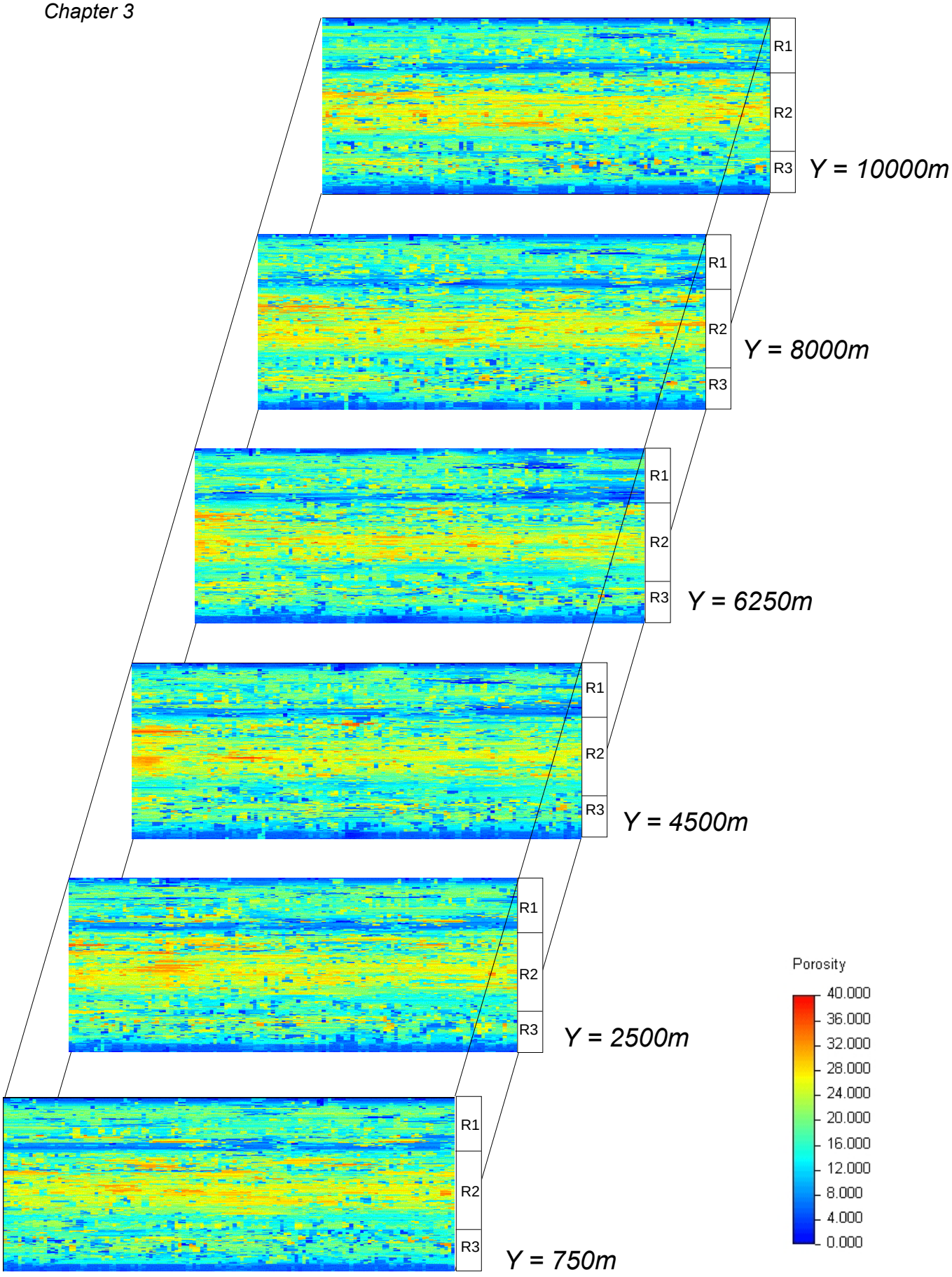

Figure 3.11 Cross sections for the entire field showing porosity estimation model using zonal control estimation based on a stochastic realization of lithoclasses produced with SIS with correction for local probabilities algorithm.

It is important to emphasise that this final image is intended to reproduce two aspects present in this particular field: the heterogeneity emerging from geological transitions, and the major continuity features evidenced by this particular variable within each lithoclass. Using this approach, it is clear that one estimated image of porosity (a smooth image) corresponds to each simulated image of the geology. Considering the classification of samples into homogeneous groups of lithoclasses, the smooth variability of the estimated values of porosity and the role of the extreme values are not particularly significant for the fluid flow movements. In this regard, the present approach can produce images that provide a realistic set of output scenarios for fluid flow simulation.

3.4 EXAMPLE OF CLASSES OF PERMEABILITY ESTIMATION USING ZONAL CONTROL TECHNIQUE

3.4.1. DEFINITION OF PERMEABILITY CLASSES

One of the most important features in flow simulation scenarios is the ability of fluids to move through the field. Fluid movements in a porous medium are governed and quantified by Darcy's Law (Crichlow, 1977, Dake, 1978). According to this law, fluid flow rates are dependent on fluid viscosity, pressure gradient and a local constant parameter named permeability. This constant is a direct measure of the ability of a fluid to move through a rock. Permeability is a characteristic of the rock, which depends on its small-scale internal features.

Permeability values can change quickly over short distances due to the geological heterogeneity of the field and to secondary geological processes like cementation or dolomitization. In an oil field it is possible to find wide ranges in permeability associated with layers (vertical zoning). Layers characterised by low permeability act as vertical barriers and can create isolated or compartmentalised areas. In the same way, spatial patterns of high and low permeability can create preferential areas for fluid flow circulation and no-flow areas.

Permeability is one of the most complex petrophysical variables involved in the characterisation of reservoirs. In reservoir engineering, the study of the relations between fluid flow movements and petrophysical properties is a major subject and these relations depend strongly on the existence of extreme values of permeability. As a matter of fact, preferential flow patterns in oil fields are highly conditioned by permeability values and possible connections between high permeability zones.

In this work, the spatial modelling of permeability accounted for two important characteristics:

- Permeability is a tensorial variable, since it depends on the direction of the fluid flow;
- Preferential flow patterns or barriers are strongly conditioned by the spatial location and connectivity of the highest and lowest permeability values within oil reservoirs.

In order to deal simultaneously with these two major properties, a formalism is proposed consisting in the treatment of permeability with probabilistic or non-parametric models (Da Costa e Silva *et al*, 1993, 1997). This kind of model ensures an appropriate representation of extreme values (both high and low permeability values) and overcomes the problem of the non-additive nature of permeability.

Combining zonal control methodology with an indicator formalism, the proposed methodology basically constitutes an extension of the zonal control method to estimate the morphology and permeability values corresponding to several classes of a histogram partition (Almeida *et al*, 1997). The proposed approach produces an image of the internal architecture of the permeability distribution within the entire field and has the following advantages:

- It uses all log derived permeability data recorded in the wells;
- It treats permeability as a categorical variable split into several classes, the extreme classes being the most significant for fluid flow models and production forecasting purposes. The advantage over methods like direct estimation using kriging is that the latter method attenuates the extreme values of the variable and gives a non-realistic representation of the field;
- The zonal control method is based on the estimation of indicator vectors and direct conditioning to experimental data via multi-phase kriging, which requires the inference of a global model of continuity (multi-phase covariance);
- Estimation of the permeability classes is independent of the characterisation of lithoclass morphology: at each grid node the probability of belonging to a specific range of permeability is calculated given that the grid node belongs to a specific lithoclass;
- Lastly, the 3D model of permeability is merged with the simulated images of lithoclasses to obtain a final distribution model of permeability.

As was stated in section 2, each lithoclass constitutes a geological entity, with specific characteristics in terms of porosity, permeability and saturation. At this stage, the basic assumption is that the variations of permeability within each geological unit are mainly controlled by rock type transitions. Estimation of permeability must thus account for the simulated morphology of lithoclasses.

3.4.2. EXTENSION OF ZONAL CONTROL TO ESTIMATE CLASSES OF PERMEABILITY

As permeability can not be considered an additive variable, estimation is performed on indicator variables corresponding to the classes in which it was divided. In each grid node, what is estimated is not the most probable permeability value (an average value) but the most probable class to which the grid node belongs based on the initial histogram and the defined classes.

The methodology used to estimate classes of permeability can be summarised in the following sequence of steps:

i) Definition of a set of *nc* contiguous permeability classes with cut-offs $z_{c_j}, j = 1,...nc+1$ that can properly represent the entire spread of permeability values, giving particular attention to extreme values and reflecting the major expected variations in the fluid flow movement;

ii) Denoting the permeability by *Z(x)* and based on the above division into classes, each point x_0 is coded by an indicator vector $P(x_0)$;

$$P_j(x_0) = \begin{cases} 1 & \text{if } z_{c_j} < Z(x_0) \leq z_{c_{j+1}} \\ & \text{with } j = 1, \ldots nc \\ 0 & \text{otherwise} \end{cases} \qquad (3.16)$$

At each point, an indicator vector is created with the value “1” corresponding to the existence of the class of the histogram of $Z(x_0)$ and (*nc*–1) “0” values, corresponding to the complementary classes. Within the framework of a probability model, $P_j(x_0)$ represents the probability of a point x_0 belonging to the class *j* of permeability.

iii) Construction of the two vectors, $I_k(x)$ and $Y_{k,j}(x)$:

$$I_k(x) = \begin{cases} 1 & \textit{if x belongs to phase } X_k \\ 0 & \textit{otherwise} \end{cases} \quad (3.17)$$

and

$$Y_{k,j}(x) = I_k(x).P_j(x) = \begin{cases} P_j(x) & \textit{if x belongs to phase } X_k \\ 0 & \textit{otherwise} \end{cases} \quad (3.18)$$

with $k = 1, \ldots K$ (number of phases) and $j=1,\ldots nc$ (number of classes).

For example, if a point x_0 belongs to phase X_1 and to the second permeability class then the indicator vector can be expressed as follows:

$$Y_{k,j}(x_0) = [0\ 1\ 0\ 0\ \ldots 0\ 0\ 0\ 0 \ldots 0\ 0\ 0\ 0\ \ldots]$$

or if a point x_1 belongs to phase X_3 and to the first permeability class then:

$$Y_{k,j}(x_1) = [0\ 0\ 0\ 0\ \ldots 0\ 0\ 0\ 0 \ldots 1\ 0\ 0\ 0\ \ldots]$$

iv) The estimation of permeability classes is performed according to the methodology described above in 3.2, and in the same way:

$$[P_{k,j}(x_0)]^* = \frac{[Y_{k,j}(x_0)]^*}{[I_K(x_0)]^*} \quad (3.19)$$

with $i = 1,\ldots K$ and $j = 1,\ldots nc$.

v) Transformation of the estimated probability values into indicator values, preserving the experimental proportions of each class in each category using the ranking selection criterion set out in section 2.4.1.2.

vi) The last step consists in merging the estimated permeability classes for all lithoclasses with the simulated maps of lithoclasses in order to obtain a unique map of permeability classes for each simulated map of lithoclasses.

3.4.3. CASE STUDY OF ESTIMATION OF PERMEABILITY CLASSES

The proposed methodology was applied to the entire field, using the permeability values $Z(x)$ known in 19 wells (log derived permeability), and results from one specific layer - layer 150 - are discussed again in more detail. Variables $Y_{k,j}(x)$ and $I_k(x)$ were constructed according to the above expressions (3.17 and 3.18). The permeability values were divided into 14 classes covering the entire range of each vertical unit. For the selected layer, the permeability range for each class and basic statistics (mean and median) are displayed in Table 3.2.

Table 3.2 Univariate statistics of the defined permeability classes for the selected layer.

Permeability class	Range (mD)	Frequency (#)	Mean (mD)	Median (mD)
1	[0.0; 0.1[	129	0.06	0.06
2	[0.1; 0.5[	117	0.28	0.28
3	[0.5; 1.0[	94	0.76	0.78
4	[1.0; 5.0[	207	2.41	2.27
5	[5.0; 10.0[	96	7.06	6.65
6	[10.0; 15.0[	30	12.55	12.51
7	[15.0; 25.0[	52	19.35	19.63
8	[25.0; 50.0[	38	35.47	34.82
9	[50.0; 80.0[	15	59.55	58.5
10	[80.0; 100.0[	8	85.59	86.53
11	[100.0; 130.0[	6	120.4	127.56
12	[130.0; 220.0[	11	169.32	180.34
13	[220.0; 375.0[	8	292.5	272.79
14	[375.0; 1168.0[1]]	2	467.05	467.05
All	[0.0; 1168.0]	798	14.35	1.66

Individual variograms of $Y_{k,j}(x)$ and $I_k(x)$ were calculated for both horizontal and vertical directions (variograms of $I_k(x)$ were calculated in above section). Due to the lack of samples, it was not possible to calculate individual variograms for all combinations of $Y_{k,j}(x)$, with $k=1, \ldots K$ and $j = 1, \ldots nc$. For this variable a variogram for each permeability class, grouping the entire set of lithoclasses, was calculated:

[1] Maximum value observed in unit R1

$$\gamma_{Y_j}(h) = \frac{1}{2}\sum_{k=1}^{K} E\left\{\left[Y_{k,j}(x) - Y_{k,j}(x+h)\right]^2\right\} \qquad (3.20)$$

with *j=1, …14* (number of permeability classes).

In Figure 3.12 and Figure 3.13 several individual variograms are displayed, reflecting two distinct situations: experimental variograms of $Y_{k,j}(x)$ evidencing continuity above 5000 metres, and erratic experimental variograms. Variograms of these two sets were grouped and multi-phase variograms were calculated for each set. The horizontal multi-phase variogram for the continuous group was fitted with an exponential model with a range of 5000 metres and 10 S.U. in the vertical direction (Figure 3.14). The erratic group was fitted with an exponential model with a range of 500 metres (small inter-well distances) in the horizontal direction and 4 S.U. in the vertical direction (Figure 3.15).

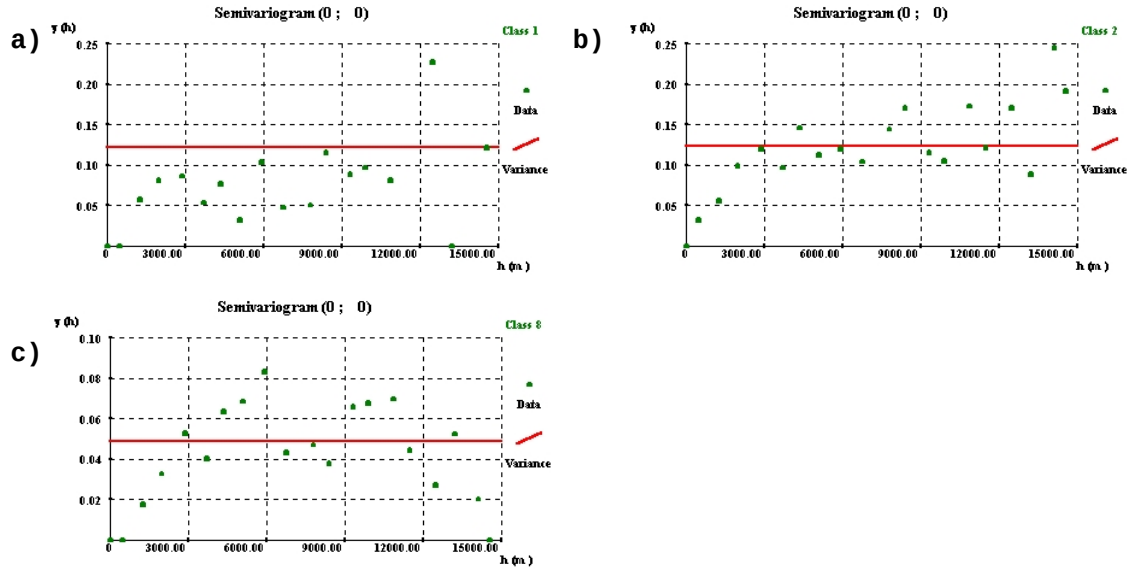

Figure 3.12 Experimental variograms for permeability classes classified as continuous: a) class 1; b) class 2; c) class 8.

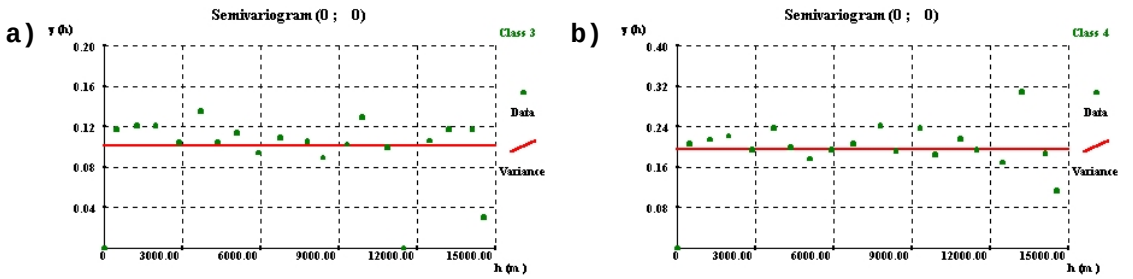

Figure 3.13 Experimental variograms for permeability classes classified as erratic: a) class 3; b) class 4; c) class 5; d) class 6; e) class 7; f) class 9; g) class 10; h) class 11; i) class 12; j) class 13; k) class 14.

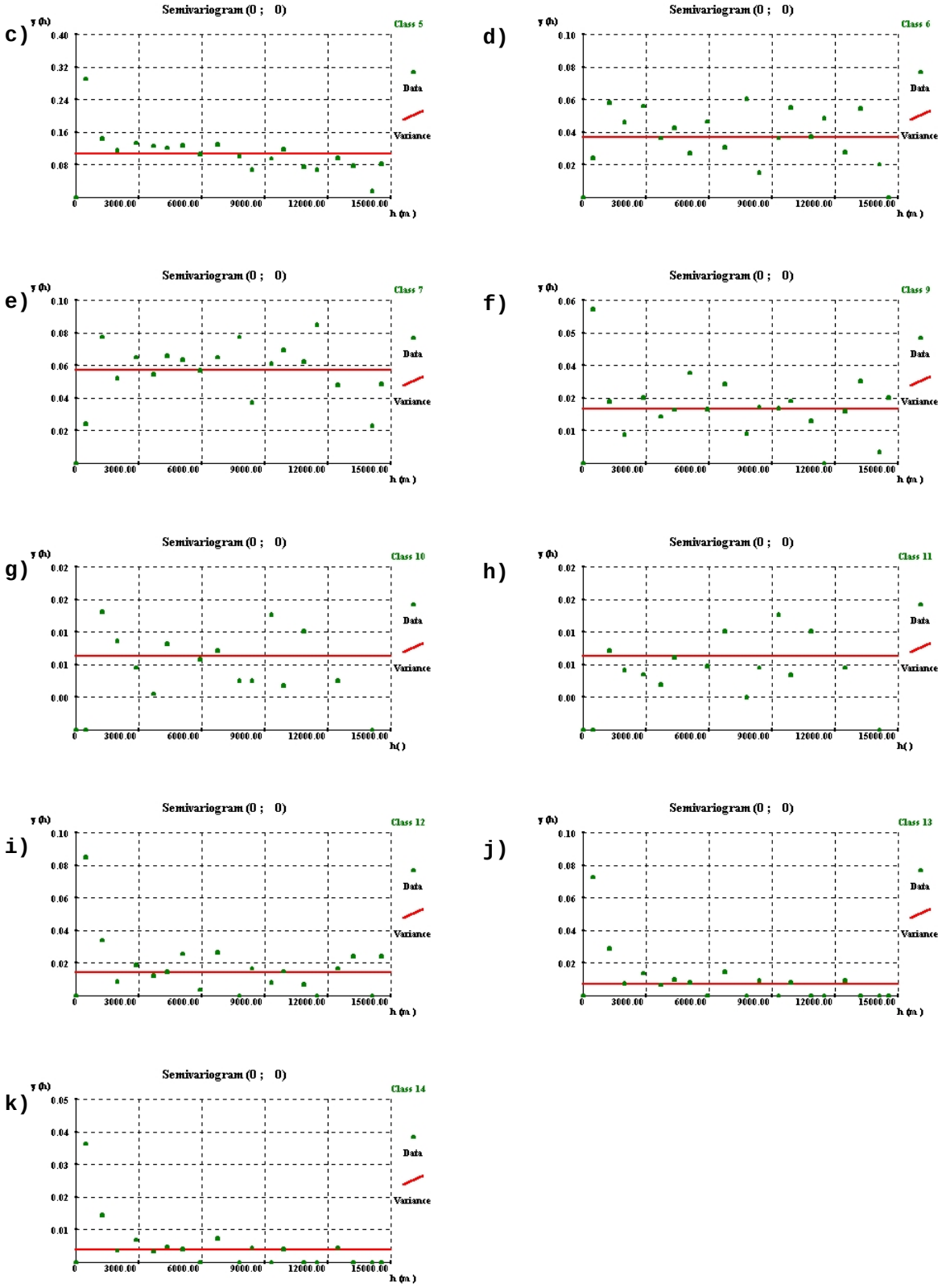

Figure 3.13(cont) Experimental variograms for permeability classes classified as erratic: a) class 3; b) class 4; c) class 5; d) class 6; e) class 7; f) class 9; g) class 10; h) class 11; i) class 12; j) class 13; k) class 14.

Model: 0.295 Exp (a = 5000 m)

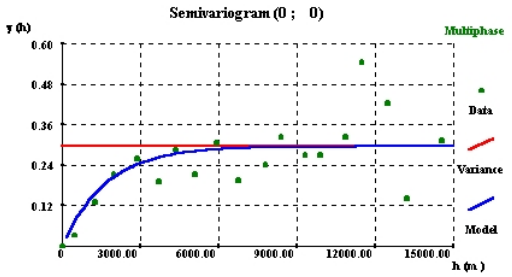

Model: 0.295 Exp (a = 10 S.U.)

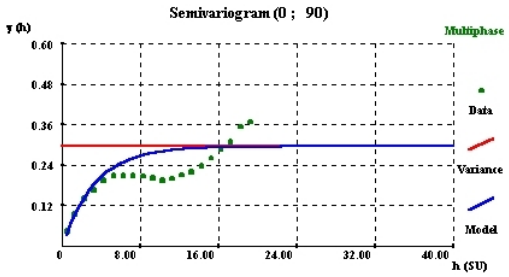

Figure 3.14 Experimental multi-phase variograms for the continuous group of classes of permeability in both horizontal and vertical directions.

Model: 0.559 Exp (a = 500 m)

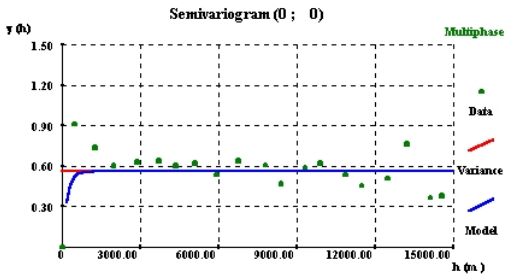

Model: 0.559 Exp (a = 4 S.U.)

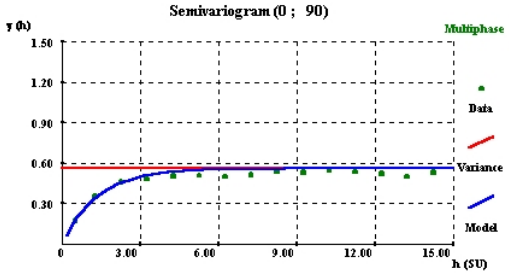

Figure 3.15 Experimental multi-phase variograms for the erratic group of classes of permeability in both horizontal and vertical directions.

The permeability was estimated with the zonal control methodology explained above. In this particular case, the morphology was established from previously simulated images of lithoclasses. Since each grid node is previously classified as lithoclass *k* by simulation, the final map of permeability classes is obtained by merging these two maps: simulated lithoclasses and permeability classes. In Figure 3.16 the estimated classes of permeability in a set of horizontal and vertical views of one layer and the corresponding images of lithoclasses are presented.

Table 3.3 and Table 3.4 compare basic statistics from estimated permeability classes and experimental data. As shown, the estimated values have approximate basic statistics, which validates the use of the proposed estimation method. The transformation of probability classes into categorical classes of permeability, using the morphological classification method described in section 2.4.1.2, makes the final image match exactly the original proportions of each experimental permeability class, which constitutes one of the most important advantages of this method.

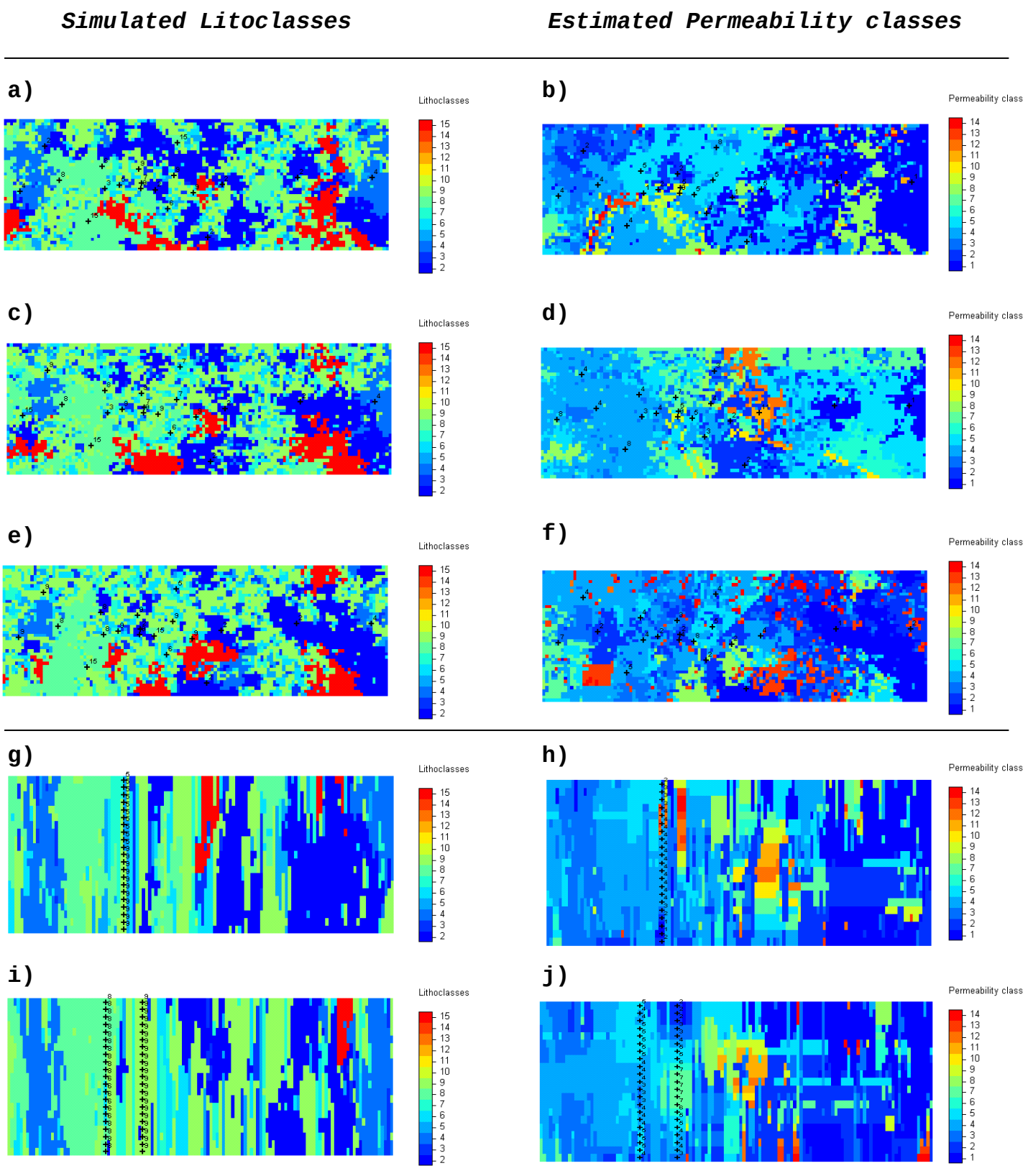

Figure 3.16 Illustration of 3 horizontal views and 2 sections from the generated stochastic images of lithoclasses using SIS with correction of local probabilities algorithm and corresponding estimated images of permeability classes using zonal control estimation.

Table 3.3 Univariate statistics of permeability classes for experimental data.

	Permeability classes													
Lithoclasses	***1***	***2***	***3***	***4***	***5***	***6***	***7***	***8***	***9***	***10***	***11***	***12***	***13***	***14***
2	0.045	0.041	0.018	0.026	0.031	0	0.010	0	0.005	0.005	0.005	0.006	0	0
3	0.026	0.003	0.005	0.006	0	0	0	0	0	0	0	0	0	0
4	0.046	0.015	0.004	0.004	0	0	0	0	0	0	0	0	0	0
5	0	0.010	0.013	0.024	0	0	0	0	0	0	0	0	0	0
6	0	0.021	0.033	0.026	0.001	0	0	0	0	0	0	0	0	0
7	0	0.006	0.015	0.029	0.015	0.004	0.005	0	0	0	0	0	0	0
8	0	0.005	0.001	0.073	0.036	0	0	0	0	0	0	0	0	0
9	0.026	0.045	0.032	0.070	0.028	0.026	0.030	0.010	0.007	0	0	0.007	0.010	0.002
15	0	0	0	0.002	0.008	0.008	0.020	0.038	0.006	0.005	0.002	0	0	0
All	0.143	0.146	0.121	0.260	0.119	0.038	0.065	0.048	0.018	0.010	0.007	0.013	0.010	0.002

Table 3.4 Univariate statistics of permeability classes for estimated probability values $P_{k,j}(x)$.

	Permeability classes													
Lithoclasses	***1***	***2***	***3***	***4***	***5***	***6***	***7***	***8***	***9***	***10***	***11***	***12***	***13***	***14***
2	0.027	0.042	0.007	0.028	0.049	0	0.018	0	0.008	0.007	0.003	0.003	0	0
3	0.020	0.011	0.004	0.006	0	0	0	0	0	0	0	0	0	0
4	0.052	0.013	0.001	0.003	0	0	0	0	0	0	0	0	0	0
5	0	0.008	0.011	0.026	0	0	0	0	0	0	0	0	0	0
6	0	0.021	0.029	0.030	0.001	0	0	0	0	0	0	0	0	0
7	0	0.001	0.007	0.040	0.015	0.003	0.004	0	0	0	0	0	0	0
8	0	0.001	0.001	0.079	0.033	0	0	0	0	0	0	0	0	0
9	0.038	0.016	0.038	0.134	0.001	0.013	0.013	0.002	0.002	0	0	0.013	0.026	0.003
15	0	0	0	0.001	0.007	0.004	0.027	0.033	0.004	0.010	0.003	0	0	0
All	0.137	0.113	0.098	0.347	0.106	0.020	0.062	0.035	0.014	0.017	0.006	0.016	0.026	0.003

Finally, to illustrate the applicability of this method to the entire field and to visualise the vertical permeability zoning, in Figure 3.17 the estimated classes of permeability in a set of vertical views for the entire field are presented.

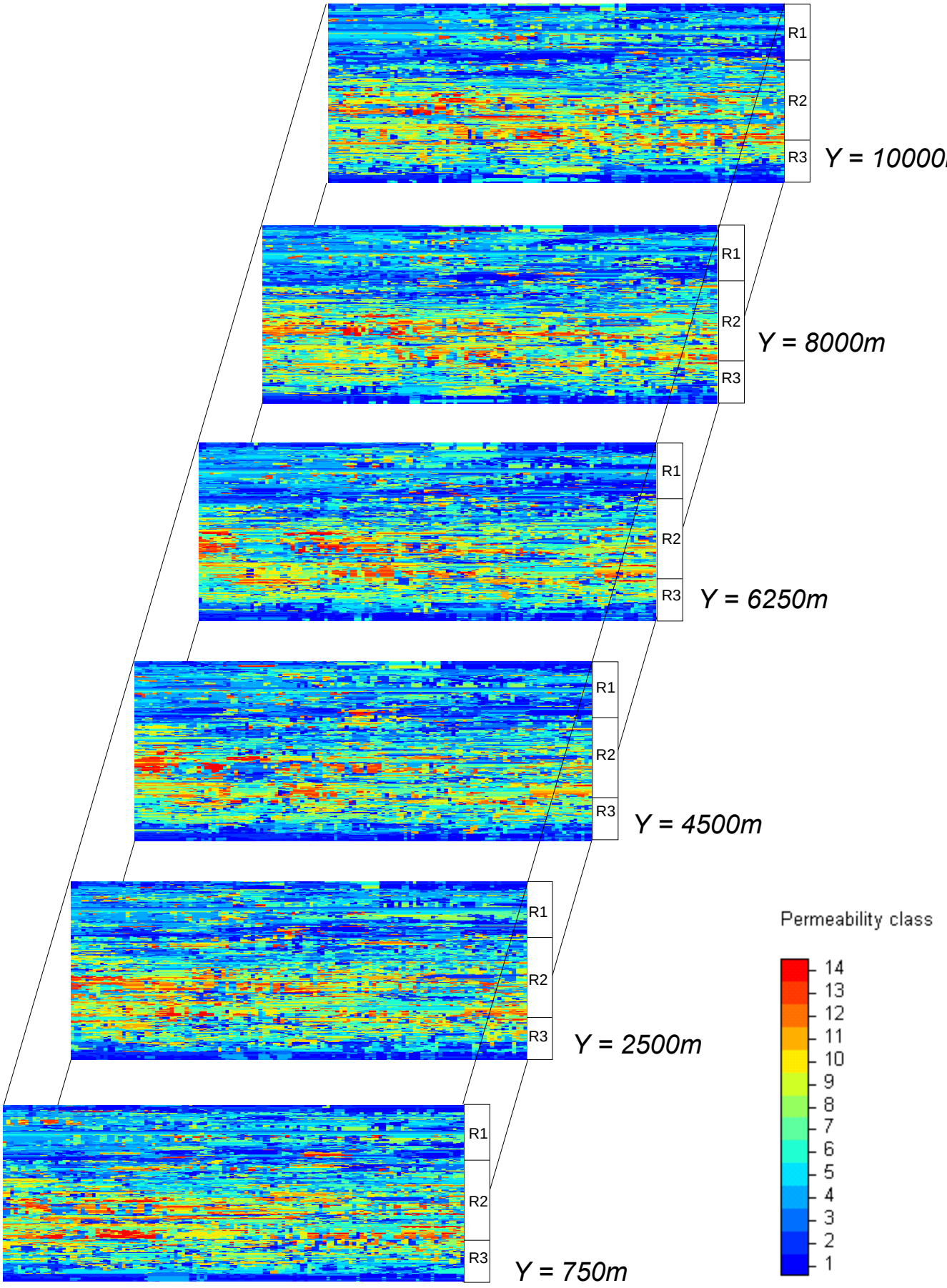

Figure 3.17 Cross sections for the entire field showing permeability class estimation model using zonal control estimation based on a stochastic realization of lithoclasses produced with SIS with correction for local probabilities algorithm.

3.5 WATER SATURATION MODELLING

3.5.1. POSITIONING THE PROBLEM

Unlike porosity and permeability, water saturation distribution is usually smoother even between different rock types. Gravity and capillary pressure control fluid distribution in porous media. Gravity acts as a density separator: low-density fluids tend to move to the upper zones of the reservoir. Capillary forces tend to counterbalance gravitational segregation and to move wetting fluids to areas where the non-wetting fluid is dominant, up to an equilibrium fluid balance. Usually, water is the wetting fluid relative to oil and gas and oil is the wetting fluid relative to gas. This process creates a natural segregation of fluids (water, oil and gas) (Dake, 1978, Archer and Wall, 1986). A typical distribution of fluids is sketched in Figure 3.18.

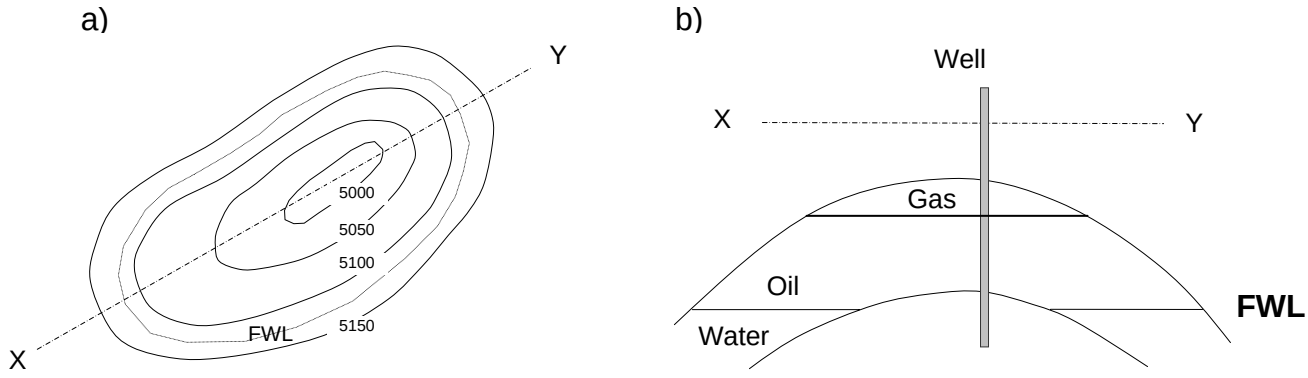

Figure 3.18 Typical distribution of fluids in an oil field: a) aerial view; b) cross-section.

In a rock formation, porous zones are conceptually similar to a tube system. Water will rise up a thin capillary tube in response to physical properties, such as surface tension, wettability of the tube to water and capillary pressure. Depending on the dimensions of the tube, water will rise higher or lower. Since water saturation is the ratio of water volume to the total fluid volume, it could range from 0 to 100%. However, in practice the lower limit is not 0% but tends asymptotically to a limit - irreducible water saturation - the residual water that is held by interfacial tension in the pores and that can not be displaced.

Typically the relation between capillary pressure and water saturation depends strongly on the permeability of the medium. For this reason, it is necessary to “normalise” all available data in order to establish a relation between saturation and capillary pressure. The best-

known correlation function applied universally in reservoir engineering is called the J-function and was proposed by Leverett (Archer and Wall, 1986). This expression relates water saturation and capillary pressure using the petrophysical properties of the rocks and the fluids:

$$J_{(S_W)} = \frac{P_c}{\sigma}\left(\frac{K}{\phi}\right)^{\frac{1}{2}} \tag{3.21}$$

where:

P_c - Capillary pressure

σ - Interfacial tension

K - Permeability

ϕ - Porosity

Initially the J-function was designed to establish a correlation between all the data involved. However, due to the dependence of the correlation on the formation characteristics, it is necessary to split all the data into several groups that represent the rock types involved and to draw a local correlation in order to reduce the scatter for each correlation.

In highly heterogeneous reservoirs, such as this one, modelling of the spatial distribution of water saturation is not an easy task. Geological heterogeneity and the complex mixture of rock types may introduce strong variations in capillary pressure and cause a non-continuous vertical distribution of water above the free water level (FWL). Also, in this oil field, the FWL surface is not flat, which reflects the impact of rock heterogeneity on capillary pressure variations.

Due to the small uncertainty that usually characterises the distribution of this variable, it is usual to construct water saturation models based on estimation methods. In fact, water saturation is not a petrophysical variable but a dynamic variable, which is mainly dependent on capillary pressure. Estimation models able to tackle this variable must take into account that this is a non-stationary variable that tends to 100% when capillary pressure decreases (with the depth to FWL).

To cope with this non-stationary variable, a simple estimation method by ordinary kriging is proposed. The first step of this method consists in performing a geometrical transformation of the vertical coordinate system in order to use the samples located at the same depth

above the FWL for estimation of the water saturation at each grid node. The main drawback to this estimate that may be pointed out is that porosity, permeability and rock types are not taken into account. In fact, in this particular oil field, due to the high heterogeneity of water saturation distribution, the correlation between J-function and water saturation is poor, even within rock types (Figure 3.19).

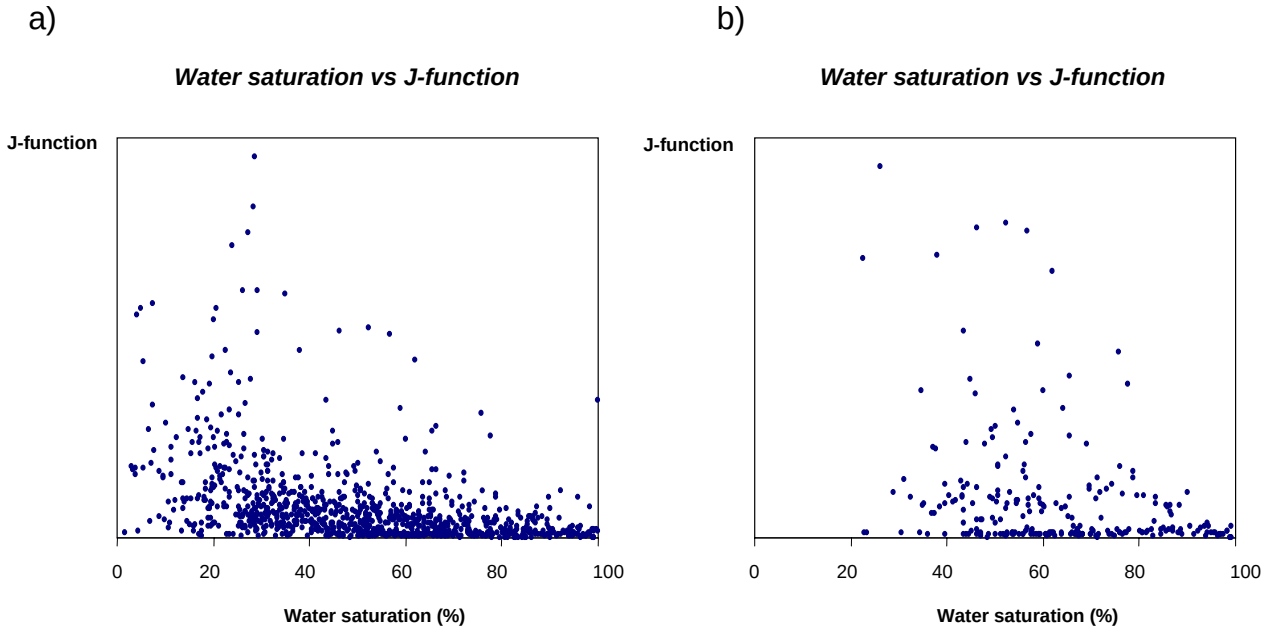

Figure 3.19 Scattergram representing correlation between water saturation and J-function for Upper unit R1: a) all rock types; b) mudstones.

Lastly, the main validation procedure of the water saturation model is to check it using a cross-validation test based on several wells.

3.5.2. GEOSTATISTICAL ESTIMATION BY ORDINARY KRIGING

The proposed methodology is based on a geostatistical estimation of water saturation values after geometrical transformation of the coordinate system. Several tests to find horizontal correlations showed the highest spatial correlation of water saturation measures when located at the same distance or height relative to free water level (FWL). Based on this single piece of evidence, it is proposed to model the water saturation using a new spatial referential in the vertical direction, with the origin in the FWL surface.

Another unusual factor related with the characterisation of water saturation is the presence of full water saturation in several areas at the top of this oil field. The presence of these areas at the top of the field is very difficult to explain and may derive from the geometry of several geological formations that act as preferential channels. The existence of these water geobodies (volumes with S_W = 100%) introduces a new problem in the estimation - kriging estimators tends to attenuate extreme values and if one estimates the entire field (above FWL) at one dash the volume of these zones is certainly underestimated.

In order to cope with the above considerations, the following procedure is proposed to create a 3D model of water saturation:

i) Geometrical transformation of the vertical coordinates of the well samples based on the heights to the FWL (see Figure 3.20);

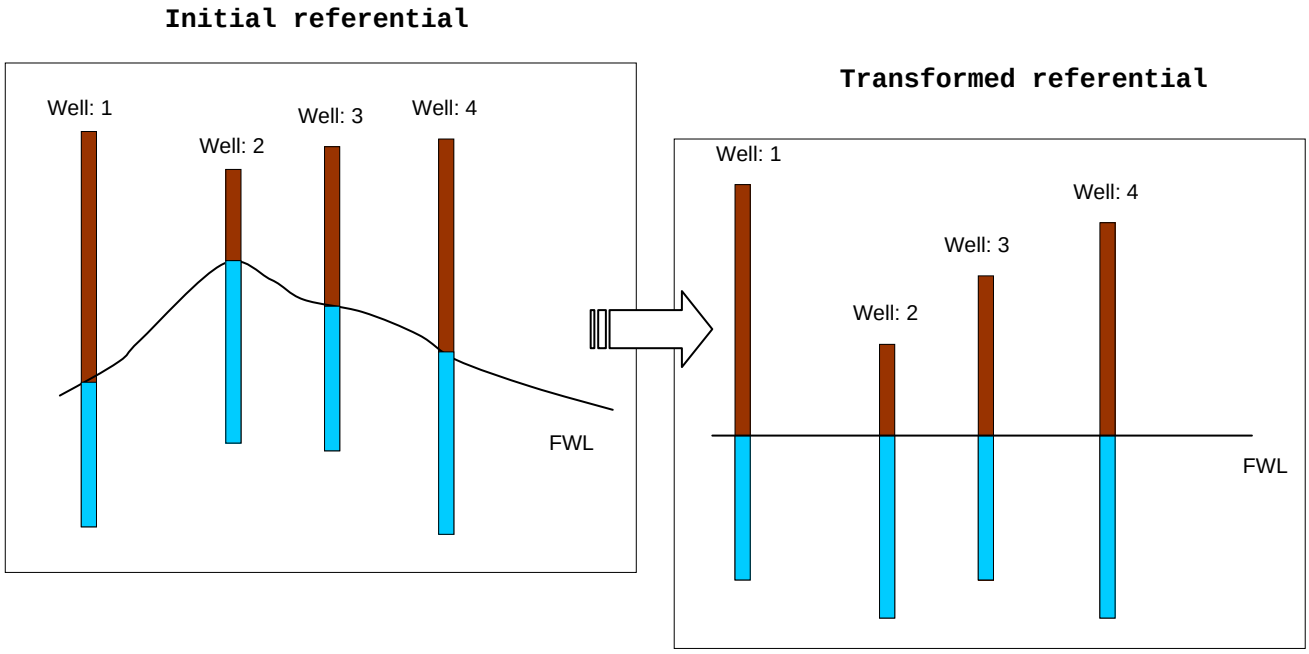

Figure 3.20 Illustration of the transformation of vertical coordinates according to the FWL.

ii) Estimation of the surface of free water level for the entire area of the field. Below this surface, water saturation is considered equal to 100%.

iii) Above the estimated free water level surface, estimation of the location and shape of the water geobodies using a simple indicator kriging approach. Using this approach, the maintenance of water geobody volumes is ensured in the same proportion as revealed by the experimental samples in wells. This step involves the generation of an indicator variable, the calculation of experimental indicator variograms in both

horizontal and vertical directions in the domain of the transformed referential, fitting a theoretical model, estimating probability maps and transforming the probability maps into indicator maps preserving the experimental proportions of these geobodies.

iv) For water saturation values below 100%, calculation of the experimental variograms in the domain of the transformed referential. Estimation by ordinary kriging of water saturation values in all the area A not fully filled by water (S_W < 100%, according to the areas delimited in the previous point) using the samples at the same depth as the free water level;

v) Finally, conversion of the transformed referential to the original geographic referential of the field.

3.5.3. ESTIMATION OF THE SURFACE OF FREE WATER LEVEL (FWL)

Usually, the FWL is an approximately flat surface for the entire field area; however, local variations in the FWL induced by geological heterogeneity and a complex mixture of rock types must be accounted for. The depths of the FWL observed in the wells suggest a very irregular surface that must be modelled first. This surface was estimated for the entire area of the field by kriging using the depths of the contacts observed in the wells and a global variogram model, which was a Gaussian model with a range of 4000 metres in the main direction of the field and 2000 metres in the perpendicular direction. The estimated map representing the FWL is illustrated in the Figure 3.21.

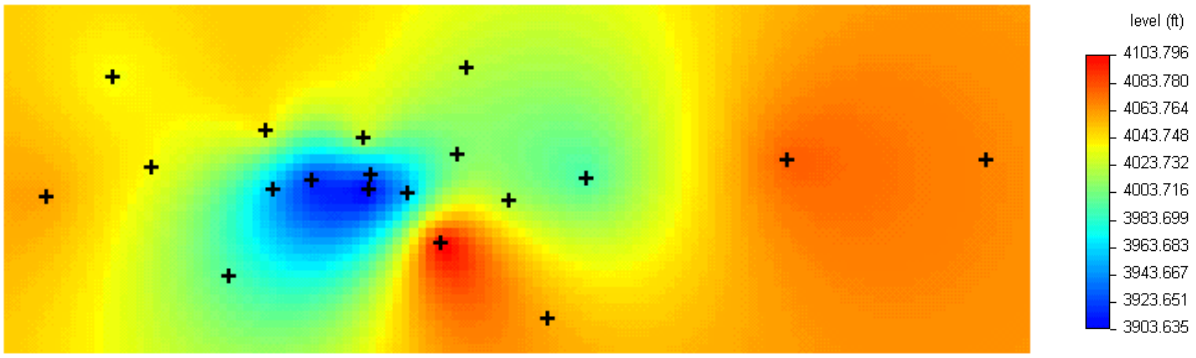

Figure 3.21 Illustration of the estimated FWL surface in the entire field area.

3.5.4. ESTIMATION OF THE SHAPE OF WATER GEOBODIES (S_W = 100%) LOCATED ABOVE THE FWL

The first step of the estimation procedure consists of separate estimation of the water geobodies (with 100% of water saturation) located above the FWL by using an indicator approach. Separate modelling of water saturation above the FWL allows us to deal with these local anomalies (S_W = 100%) and to treat the complementary area (S_W < 100%) in a more appropriate way. Any linear estimation with a mixture of these populations would lead to underestimation of the water zones.

To model these areas, the following indicator variable was defined:

$$I(x_o) = \begin{cases} 1 & \text{if} \quad S_W(x_0) = 100\% \\ 0 & \text{otherwise} \end{cases}$$

This indicator variable has the following statistics:

m_I = 0.084

σ^2_I = 0.077

Variograms of this indicator variable give the spatial continuity (or average measure) of these water geobodies and allows the most probable morphology of these zones to be estimated. Estimation at any grid node x_u of the field is provided by estimation of the following probability conditioned to a set of *n* neighbourhood experimental samples:

$$\text{Prob}\left\{ I(x_u) = 1 \mid I(x_\alpha), \alpha = 1,...n \right\}$$

This probability map is then transformed onto a binary map reproducing the shape of the water geobodies. The major advantage of this two-step approach is that the final classification step ensures that the percentage of water above the free water level is the same as measured from the experimental samples.

Figure 3.22 represents the experimental variograms of *I(x)* calculated for the entire field along the horizontal and vertical directions. In the horizontal direction, a spherical model with a range of 11000 metres was fitted in the main direction of the field and with a range of 5000 metres in the perpendicular direction. In the vertical direction a two-structure model (spherical model) was fitted with ranges of 8 and 30 feet respectively and sills of 0.035 and 0.025.

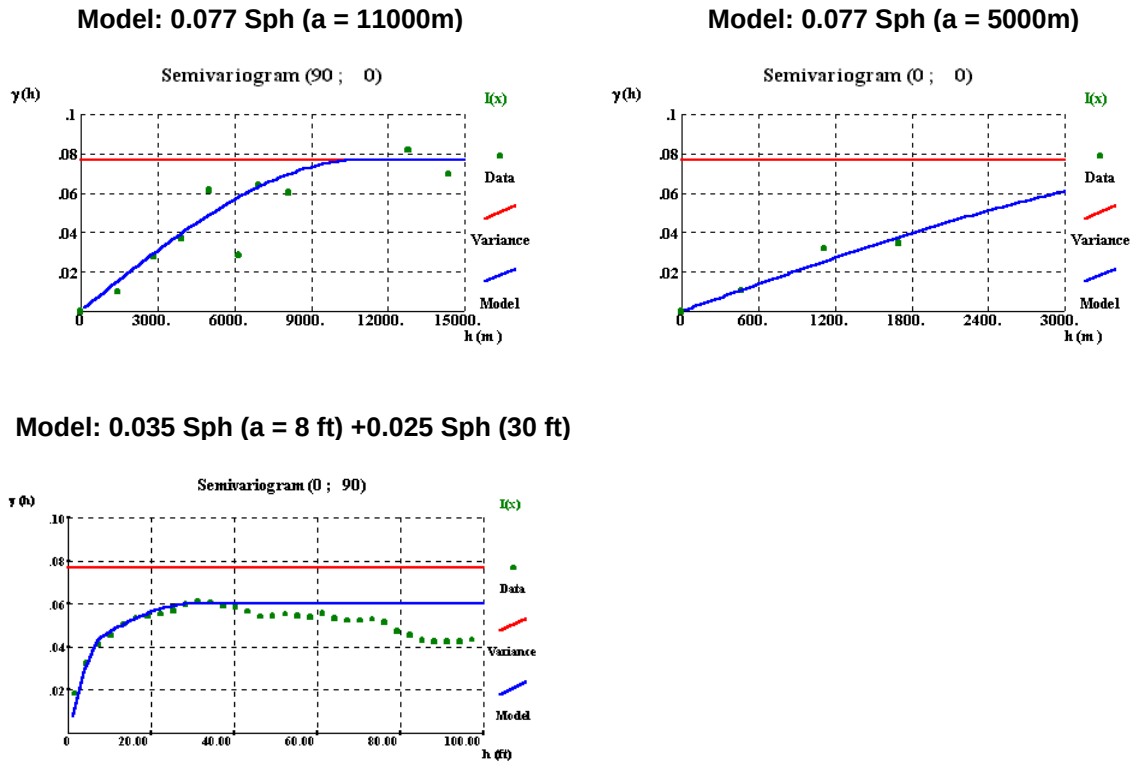

Figure 3.22 Experimental variograms of the *I(x)* in the transformed referential for the horizontal and vertical directions.

Figure 3.23 shows in cross-section the estimated water geobodies for the entire area above the FWL.

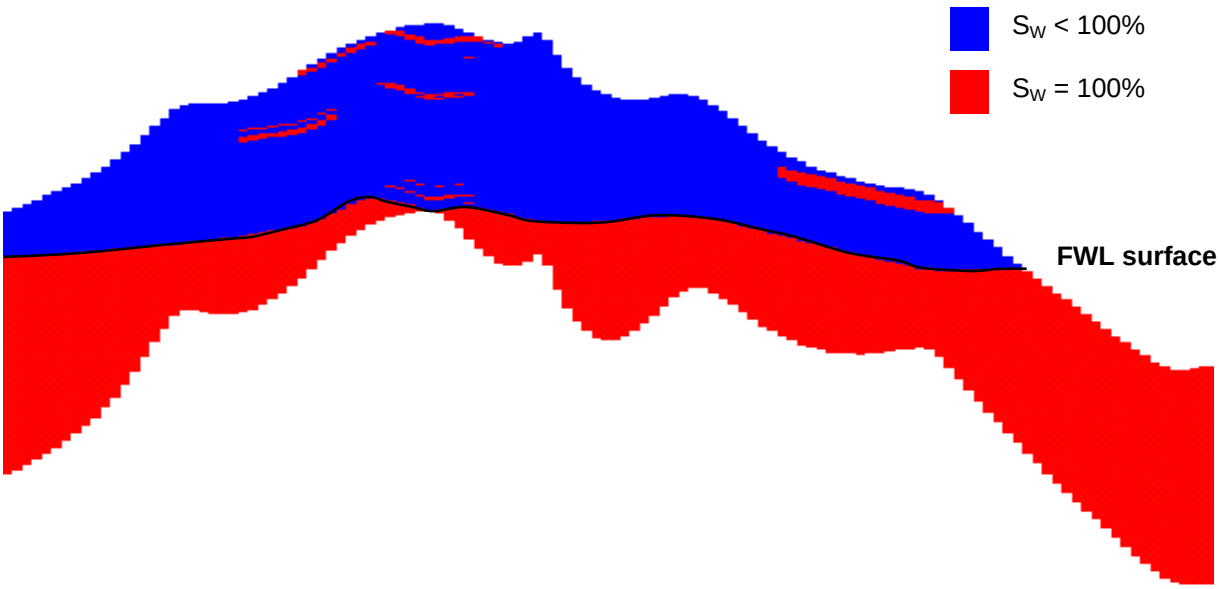

Figure 3.23 Illustration of water geobodies (S_W = 100%) in a cross-section of the entire field.

3.5.5. VARIOGRAM MODEL OF WATER SATURATION FOR THE REMAINING AREAS (S_W < 100%)

The highest spatial correlation of saturation values in the horizontal direction is observed between samples located at the same relative height above the FWL. As explained above, a single geometrical transformation of the vertical coordinates based on the heights to the FWL is the first step to calculate spatial continuity for the saturation, as revealed by experimental variograms.

After the transformation of all samples, analysis of the spatial continuity of saturation was conducted for the entire field. Experimental variograms were calculated using the sample values of S_W < 100% for all layers in the three main directions of the field and are represented in Figure 3.24. A high continuity structure was identified in the main horizontal direction of the field and was fitted using a spherical model with a range of 8000 metres. The perpendicular direction in the horizontal was fitted with a 3000 metres model and the vertical direction with two structures, with ranges 15 and 120 feet and sills of 275 and 62 respectively.

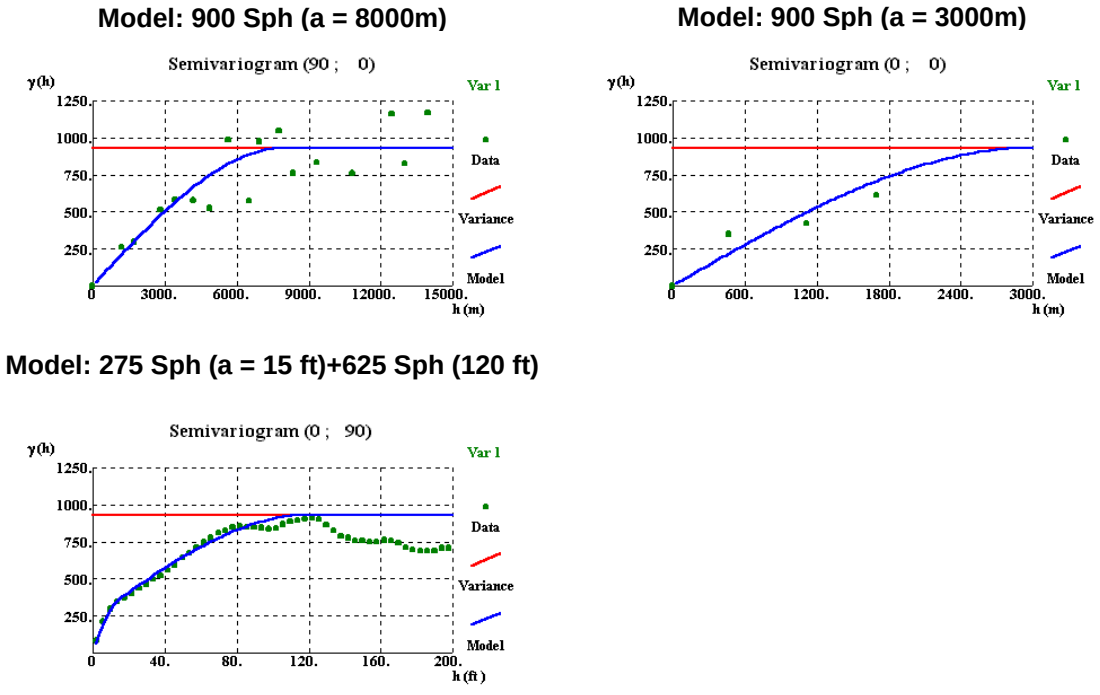

Figure 3.24 Experimental variograms of water saturation in the transformed referential and theoretical model fitted.

3.5.6. CROSS-VALIDATION TEST AND ESTIMATION OF WATER SATURATION FOR THE REMAINING AREAS (S_W < 100%)

In order to evaluate and validate the proposed method, a cross-validated test was performed that tested the ability of the model to reproduce the profile of water saturation in each well using only the remaining wells. In other words, water saturation is estimated in the location of each well, after removing it, based on the data of the remaining wells. Figure 3.25 a) through Figure 3.25 d) show the results of this cross-validation for a set of wells that could be considered very satisfactory considering the large distance between the wells used. The best matches between real and estimated S_W are verified in those wells located in the middle of the field (vertically) due to the considerable amount of surrounding information on the other wells. In general, the results of this cross-validation are very satisfactory and give us confidence to apply this model to the whole field and to cope with the complexity of the distribution of water saturation in this oil field and the non-stationarity shown by this variable.

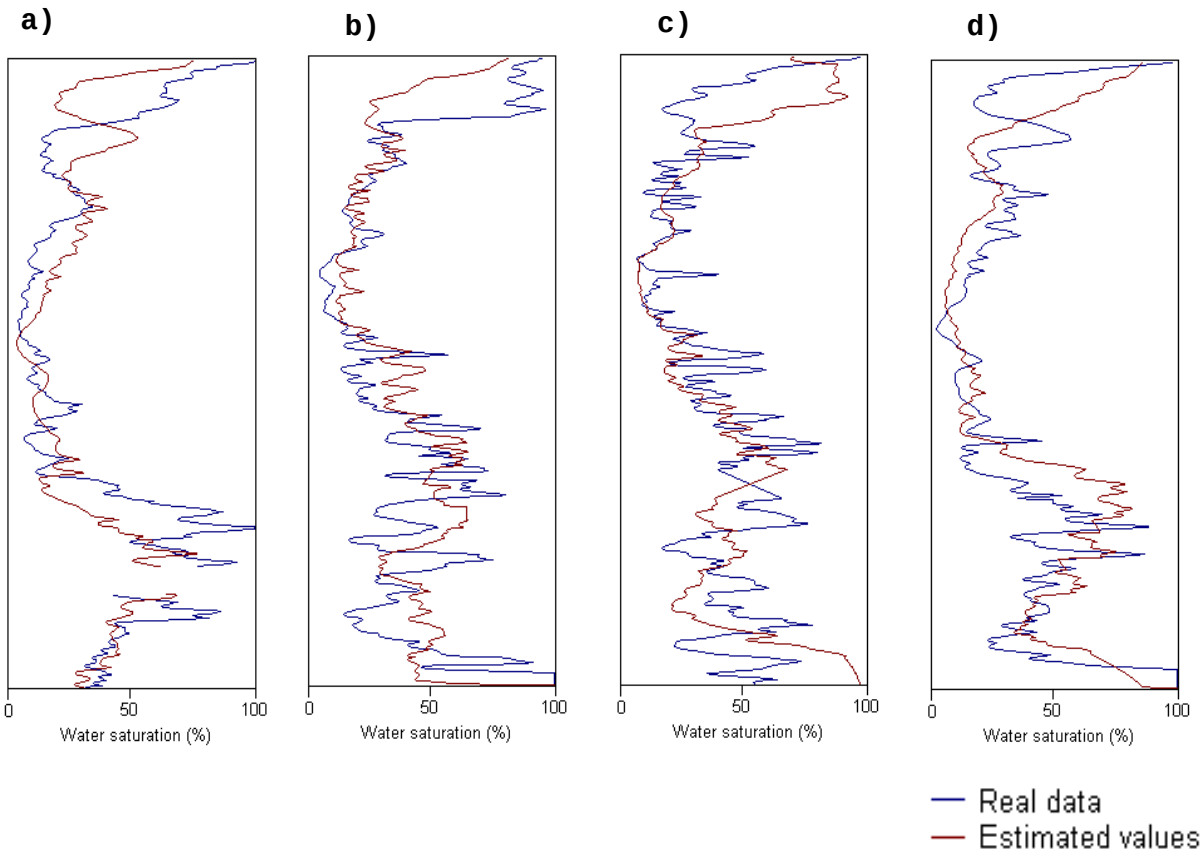

Figure 3.25 Results of the cross-validation test for four wells located in the middle area of the field.

In summary, two different estimates were made over the entire field: an estimate of water geobodies and an estimate of water saturation values. These two 3D maps must be merged and finally, back-transformed to the original geographic referential based on the estimated surface of FWL.

Complete results of the geostatistical water saturation model are shown in Figure 3.26 and Figure 3.27 in several levels and sections along the field.

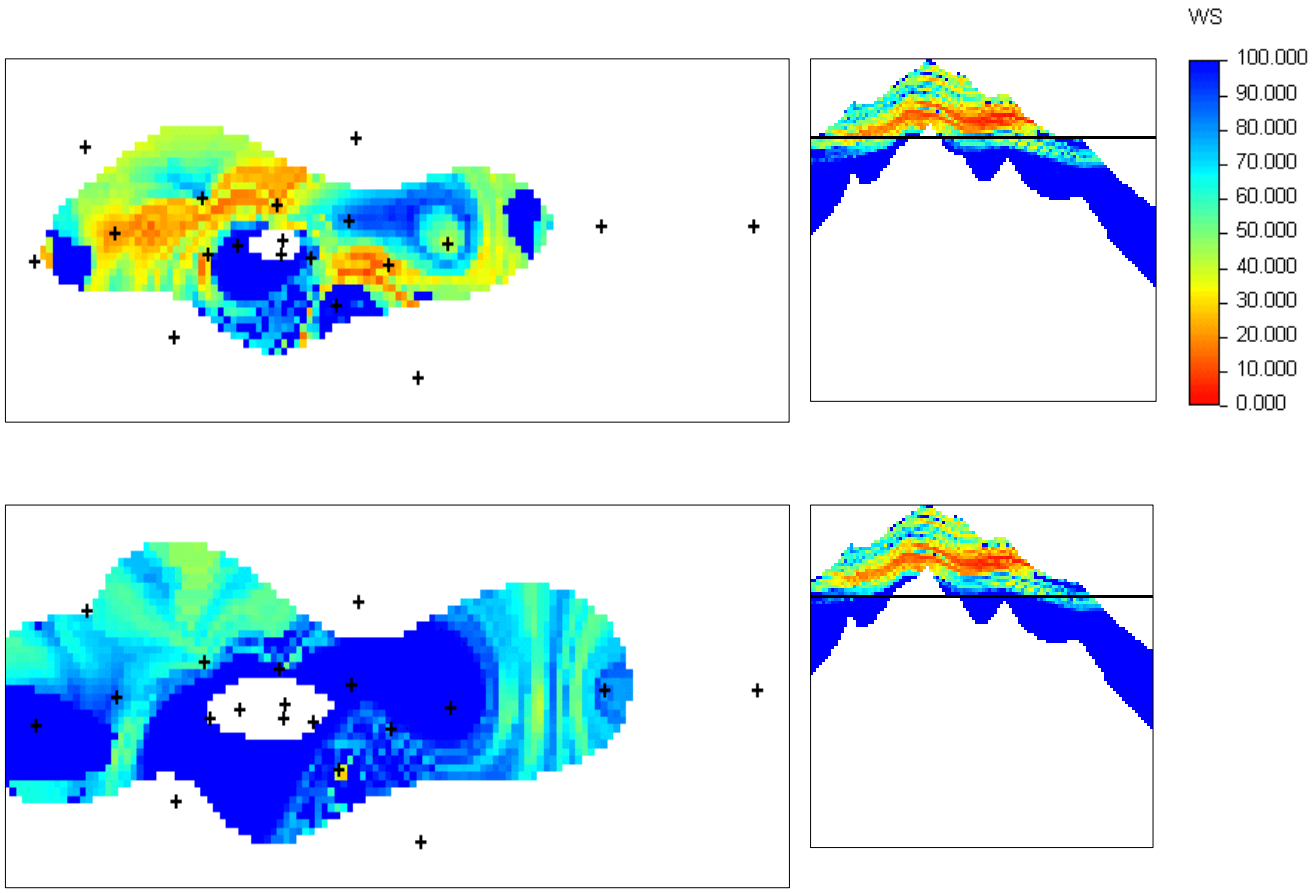

Figure 3.26 Horizontal distribution of the water saturation in two different levels.

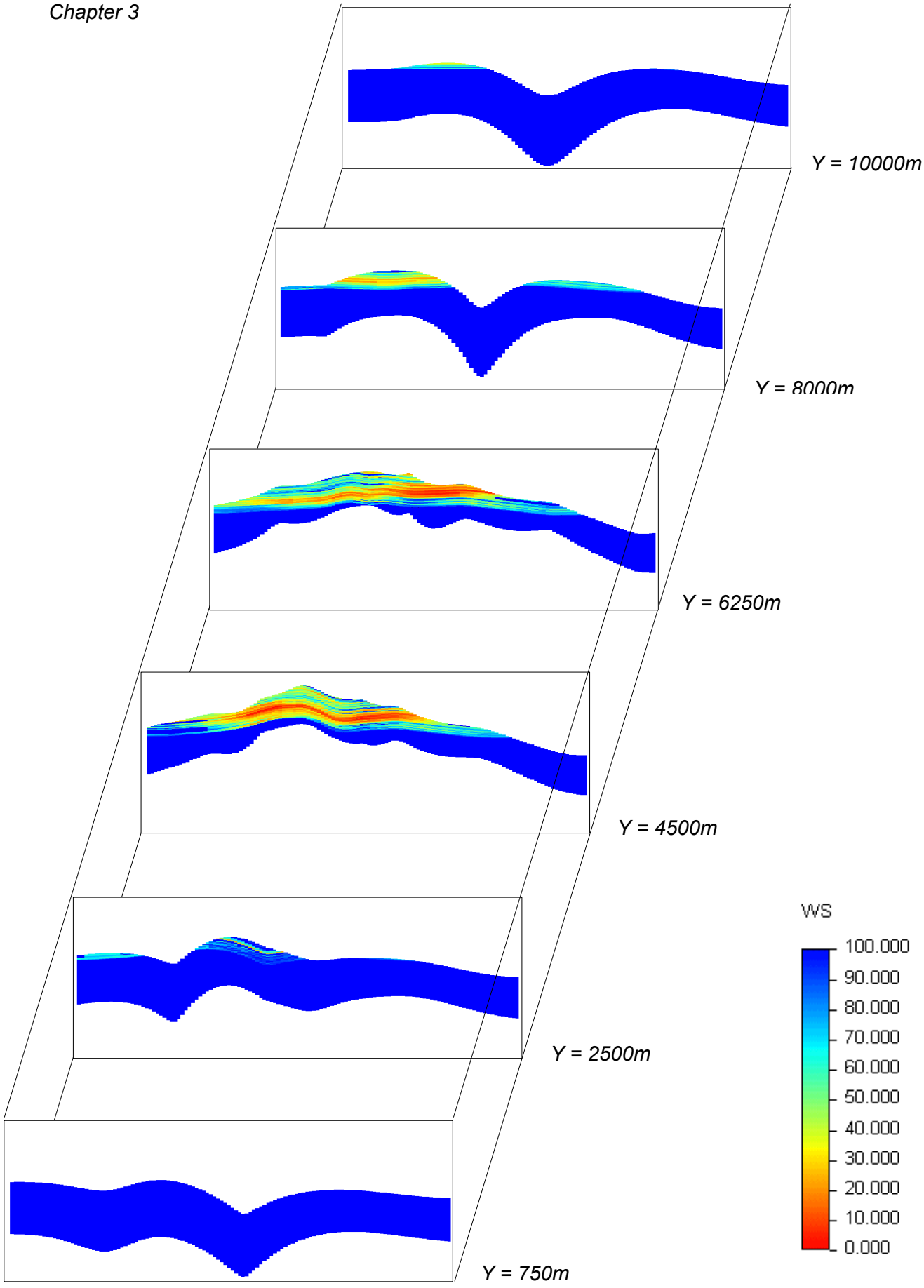

Figure 3.27 Cross-sections for the entire field showing the complete water saturation estimation model.

3.6 FINAL REMARKS

Each lithoclass consists of a geological entity with specific characteristics in terms of porosity, permeability and water saturation. The basic assumption at this stage is that the permeability and porosity variations within facies are mainly governed by rock type transitions. As a consequence the main objective at this stage was to obtain the average values of these petrophysical properties rather than their variability. This means that the objective was to estimate the average behaviour of porosity and permeability within the boundaries of each lithoclass and not to produce simulated images of these properties.

As described above, the stochastic model of porosity and permeability has accounted for the simulated reservoir images of lithoclasses (section 2). To estimate porosity and permeability we are taking into account the fact that our intention is to obtain images of average distribution of these properties rather than to obtain a set of equally probable scenarios. In the resulting images heterogeneity arises almost totally from the variability of the map of lithoclasses. The approach designed to fill these properties within the lithoclass images was denoted by zonal control estimation. This method should be used when petrophysical variables change sharply between rock types and when scarcity of data rules out calculation of cross-variograms or individual variograms for each lithoclass.

Estimating by using zonal control has certain clear advantages when the values of the variable to be estimated are different for each lithoclass and when there are sharp variations between lithoclasses. Thus, when a set of simulated images of lithoclasses is produced, this is the ideal method to fill the petrophysical variables in these images: a single estimate makes it possible to obtain images of this variable for each lithoclass. It is sufficient simply to merge the simulated lithoclass maps and estimated variable maps.

As permeability can not be considered an additive variable, estimation was performed on indicators corresponding to the classes into which they were divided. For this variable the objective was to estimate not the most probable value but the most probable class to which the grid node belongs. Permeability was estimated using prior division into classes. These classes were then estimated using the formalism of the indicator random variables. The approach presented here ensures that areas of high and low permeability are not under- or over-estimated, as might be expected if the values were estimated as such. In the same way, permeability values within the range of a class which does not exist in a lithoclass (within a specific layer) will not appear in the final image, as might happen if interpolation took into account the values of the variable. Also, this method is certainly more appropriate given that permeability is a non-additive variable. The filling-in of permeability values in the

maps of permeability classes may take different forms, such as using the median of each class calculated in each layer. Validation of this method may be carried out by observing the images of the models presented, which display clear vertical zoning of this reservoir in terms of porosity and permeability, as well as the coherence of the model.

Water saturation displays abnormal behaviour in this reservoir. There is a weak correlation with lithoclasses or rock types and with figures for porosity and permeability. Thus variations are mainly dependent on distance from the FWL. Another type of unusual behaviour displayed is the fact that there are areas with 100% water saturation at the top of the reservoir. It is therefore necessary to adapt the estimation method to the modelling of this particular behaviour variable, which is clearly not stationary and whose variation depends on distance from the FWL. Independent estimates of the areas with saturation equal to 100% using the indicator formalism avoids under-estimation of these areas and maintains a proportion equivalent to that shown by experimental data.

To create a 3D model of water saturation a single estimation method based on ordinary kriging is proposed. The basis of this proposed method is the use of a referential based on the surface FWL that proves to be the most appropriate to find horizontal correlation and selection of neighbourhood samples used to estimate each grid node (samples at the same depth to the FWL). This criterion used to select the set of conditioned samples copes with the non-stationary revealed by the water saturation. The final saturation model is independent of lithoclasses, porosity and permeability, and is characterised as an attenuated map of a variable which normally displays low variability, albeit with spatially anomalous behaviour.

4 CHARACTERISATION OF SPATIAL UNCERTAINTY OF UNDERSAMPLED VARIABLES

4.1. INTRODUCTION

When dealing with geostatistical models one of the most important challenges is to characterise the spatial uncertainty of petrophysical variables. Spatial uncertainty depends on the heterogeneity of the variable and in geostatistical models it is directly related to the number of samples, their spatial location and the continuity models of the variable. When multi-Gaussian models are used or the indicator formalism is applied to different thresholds, the resulting uncertainty is characterised by the cumulative distribution function obtained with the simulated images in each grid node. In other words, characterisation of uncertainty is merely local. However, in a large number of applications, notably in the area of reservoirs, we need to characterise the global uncertainty in the total area where the reservoir is defined, i.e., uncertainty associated with images is worked as a whole and not point by point. The use of geostatistical models thus enables us to characterise spatial uncertainty, which is modelled by generating a set of equally probable realisations or images of the studied variables in space - stochastic simulations (Deutsch and Journel, 1992, Goovaerts, 1997). These images can now be used to transfer functions, such as fluid flow simulators, that lead to a set of alternative and equally probable production responses, based on uncertainty provided by the entire set of grid nodes.

Preferential flow patterns and dynamic behaviour of the field are mostly conditioned by the permeability spatial pattern. Regarding this, the present section presents an approach towards creating simulated images of permeability distribution that combines all available permeability data: core data with horizontal measures of permeability, and log derived data. This approach combines sequential indicator simulation (SIS) and *p*-field simulation to produce spatial images of permeability values using these two data sources.

At this stage, a geological model showing the internal distribution of lithoclasses was produced using categorical simulation algorithms such as SIS. These images reproduce the heterogeneity observed between lithoclasses. The objective of this section is now to fill these lithoclasses by producing stochastic realisations of permeability values, conditioned to lithoclass morphology and incorporating the two sources of permeability data.

A more general objective of the proposed methodology is the spatial simulation of undersampled variables (Almeida and Guerreiro, 1997, Guerreiro *et al*, 1998). Permeability is usually measured in a few cores and is inferred for the remainder set using linear regressions with porosity (Archer and Wall, 1986) or exploring the non-linear relations between variables. Various non-linear regression models, like neural networks, may be applied based on the following methodological sequence: i) inference of a regression law between core permeability and log data at the few core data locations; ii) classification of remaining log data into permeability values according to the regression obtained in i). The results can be displayed as numerical values of permeability (soft data) or as a probability of belonging to a specific range of permeability. For example, deriving the permeability using probability neural networks (PNN) leads to each non-core data point being classified into a probability vector, which represents the probability of belonging to a set of continuous ranges of permeability (Pereira *et al*, 1995, L. Soares *et al*, 1996).

The proposed method is able to use two sources of permeability data with a different uncertainty attached (core permeability and log derived permeability - soft data), and can be summarised in the following main steps:

a) Definition of a set of classes to divide the entire range of permeability values. These permeability classes should have a consistent physical meaning;

b) For each data location, calculation (inference or classification) of the probability of belonging to each permeability class, for instance by using the PNN formalism;

c) Stochastic simulation of classes over the entire simulated area using a categorical simulation method (for instance, SIS with correction for local probabilities) conditioned to the simulated images of rock types;

d) Calculation of a conditional cumulative distribution function, ccdf, in each grid node, based on the simulated lithoclass and permeability class;

e) Generate n (n – number of realisations) probability fields $P(x)$ with uniform distribution reproducing the covariance model for permeability indicator values;

f) Simulation of the permeability values $z_s(x)$ on each grid node: draw a realisation from the local ccdf using the local value of the probability field $p(x)$.

This method was applied to characterisation of the permeability in this particular field, where the core permeability is undersampled relative to the entire set of wells.

The simulation of classes of permeability was performed for a single layer – layer 150 - and was based on 30 simulated images of lithoclasses, obtained using the SIS method (see section 2). In this case study, for each simulated image of lithoclasses three realisations of permeability are simulated. In total, 90 simulated images of permeability classes were produced. This large set of images certainly reproduces all of the heterogeneity that comes from the variability between lithoclasses and within each lithoclasses.

4.2. PROPOSED METHODOLOGICAL FRAMEWORK

Let us consider the variable $Z(x_\alpha), \alpha = 1,...P$ sampled at a restricted number of points *P* and the variable $Y(x_\alpha), \alpha = 1,...N$ known in all samples *N* >> *P*.

First of all, taking into account the range of values of *Z(x)*, a definition of a set of *nc* contiguous classes with thresholds $z_{c_j}, j = 1, n_c + 1$ is required. The selection criteria for these thresholds must take into account the number of data in each class, in particular the extreme values.

Dividing *Z(x)* in *nc* classes, for *N* sampled points, the probability of $Z(x_\alpha)$ belonging to each class $[z_{cl}, z_{cl+1}[$, conditioned to the known variable value $Y(x_\alpha)$ for *nc* classes in which the range of *Z(x)* was divided (conditional probabilities for all *nc* classes) is calculated as follows:

$$P_{Z_{cl}}(x_\alpha; cl) = prob\left\{ Z(x_\alpha) \in [z_{cl}, z_{cl+1}[\,|\, Y(x_\alpha) \right\} \quad with\ cl = 1, nc \tag{4.1}$$

Usually, this probability is computed based on a regression between variables *Z(x)* and *Y(x)* using the sub-set of samples *P* where the values of *Z(x)* and *Y(x)* are known, or using classification methods based on neural networks, particularly PNN. Based on the pre-defined permeability classes, each known point $Z(x_0)$ is coded by an indicator vector $P_{Z_{cl}}(x_0)$:

$$P_{z_{cl}}(x_0) = \begin{cases} 1 & if \quad z_{c_j} < Z(x_0) \le z_{c_{j+1}} \\ & \text{with } j = 1, n_c \\ 0 & otherwise \end{cases} \tag{4.2}$$

It is thus possible to classify all the samples with a probability of belonging to a specific class *cl* of the *Y(x)*:

$$P_{Zcl}(x_a; cl), a = 1, N \qquad cl = 1, nc \tag{4.3}$$

In a second step, the probability values $P_{Zcl}(x_u)$ are simulated for all grid nodes x_u within area A. The probability of each point x_u belonging to each permeability class can be interpreted as a categorical variable. Thus a stochastic simulation method like SIS or truncated Gaussian plus conditioning could be used (see section 2). In the present case study, SIS with correction for local probabilities was used to generate images of permeability classes conditioned to the proportions of the samples within each rock type.

The implementation of the proposed simulation algorithm for undersampled variables can be summarised in the following sequence of steps:

I) Statistical description of $P_{Zcl}(x_\alpha)$

Mean: proportion of each class *cl* in all area *A*:

$$m_{cl} = E\{P_{Zcl}(x_\alpha)\} \qquad cl=1, nc \tag{4.4}$$

Variance:

$$\text{var}_{cl} = \text{var}\{P_{Zcl}(x_\alpha)\} = E\{P_{Zcl}(x_\alpha) - m_{cl}\}^2 \qquad cl = 1, nc \tag{4.5}$$

II) Spatial continuity model of $P_{Zcl}(x_\alpha)$

In the same way, individual variograms can be defined for each class:

$$\gamma_{P_{cl}}(h) = E\{P_{Zcl}(x_\alpha) - P_{Zcl}(x_\alpha + h)\}^2 \tag{4.6}$$

and the corresponding multi-phase variogram, grouping sets of similar classes of the variable *Z(x)*:

$$\gamma_{P_Z}(h) = \sum_{cl=1}^{nc} \gamma_{Pcl} = \sum_{cl=1}^{nc} E\left\{ \left[P_{Zcl}(x_\alpha) - P_{Zcl}(x_\alpha + h) \right]^2 \right\} \tag{4.7}$$

The variogram of $\gamma_{P_Z}(h)$ represents a continuity measure of the whole set of the undersampled variable in all classes of the variable *Z(x)*.

III) Multi-phase simulation of permeability classes, conditioned to the simulated images of lithoclasses

The multi-phase sequential indicator simulation algorithm with correction for local probabilities described above in section 2 was used to produce stochastic images of permeability classes (Soares, 1998). This simulation method was modified in estimating the local conditional cumulative distribution function: the estimation of this local ccdf only takes into account the samples and grid nodes belonging to the same lithoclass. Instead of performing different simulated images of permeability classes (one for each lithoclass), and merging all the final maps (lithoclasses and permeability classes, one for each lithoclass) the original SIS program code was changed to perform a single simulation taking into account the geometry of lithoclasses:

a) Select at random a grid node x_u not yet simulated in area *A*. Identify the corresponding simulated lithoclass $k(x_u)$;

b) Build the local probability distribution of permeability classes. This entails estimating by kriging the probability of grid node x_u belonging to each class $\left[P_{Z_{cl}}(x_u)\right]^*$, cl=1,nc using the continuity model (4.7):

$$\left[P_{Z_{cl}}(x_u)\right]^* = \sum_{\alpha} \lambda_\alpha P_{Z_{cl}}(x_\alpha) \qquad (4.8)$$

The weights λ_α were calculated taking account only of the neighbouring samples that belong to the same lithoclass $k(x_u)$.

c) Correction of local probabilities, in order to impose the experimental proportions revealed by the samples within each lithoclass. These local deviations are independent for each lithoclass, and the correction in each grid node x_u takes into account only the deviation corresponding to the lithoclass $k(x_u)$. Thus, the goal of this independent correction is to minimise the differences between global probabilities shown by the samples and those of the simulated image in each lithoclass.

d) Calculation of the cumulative distribution function:

$$\left[F_{cl}(x_u)\right]^* = \sum_{i=1}^{cl} \left[P_{Z_i}(x_u)\right]^* \qquad (4.9)$$

e) Draw a random number *p* from a uniform distribution defined in the range [0; 1]. The grid node x_u will be allocated to class *cl* if:

$$x_u \in \text{class } cl \qquad if \qquad [F_{cl-1}(x_u)]^* < p <= [F_{cl}(x_u)]^*$$

f) Treat this simulated value as initial hard data and loop back to step a) until all grid nodes are simulated.

IV) Calculation of the cumulative distribution function for each grid node x_u

For each permeability class *cl* of each lithoclass, the global cumulative distribution function was inferred using only core permeability data.

$F_{cl,k}(x)$, *cl=1, nc* (*nc* is the number of permeability classes) and *k = 1, K* (*K* is the number of lithoclasses).

Thus, each global cumulative distribution function was allocated to the corresponding grid node x_u .

V) Finally, permeability values *Z(x)* are simulated at each grid node x_u using the *p*-field simulation approach

The cumulative distribution function corresponding to the class *cl* in each grid node x_u was calculated at each grid node x_u:

$$F_Z(x_u, c) = prob\{Z(x_u) < z \mid c = cl\}, \text{cl} = 1, \text{nc} \qquad (4.10)$$

Finally the simulated values of permeability $z_s(x_u)$ were generated from the local probability distribution functions $P_{Zcl}(x_\alpha)$ by using the *p*-field simulation approach (Srivastava, 1992, Froidevaux, 1993). A probability field *P(x)* is simulated for the entire area *A*, the simulated value of permeability $z_s(x_u)$ is equal to:

$$Z_s(x_u) = F_z^{-1}(x_u, c, p) \qquad \text{where} \qquad p = P(x_u) \qquad (4.11)$$

To generate a probability field *P(x)* over the entire area *A* it is assumed that the multi-phase variogram γ_{P_Z} is representative of the continuity of $F_z(x_u, c)$ within each class.

The use of this simulation method is particularly appropriate whenever two types of information co-exist with different sampling densities. In the case of this study, there are two variables with different characteristics indicating permeability. One is an indirect measure of

permeability - soft values - which is inferred from logs by multi-variable correlation and is available for all wells. The second variable is effective permeability, measured in a laboratory using cores, but this is characterised by low sampling density.

The main difference between this proposed method (which combines SIS and *p*-field) and running only a sequential simulation method is that the cumulative distribution function in each grid node is estimated independently of the simulation process. Thus, this process offers greater flexibility in combining densely sampled soft information with poor sampled hard information (Soares, 1995, Da Costa e Silva *et al*, 1996). In fact, when the *p*-field simulation approach is applied, each simulated image of lithoclasses and permeability classes acts as soft information and the permeability measured in cores acts as hard information. The cumulative distribution function at each grid node is estimated taking into account only the cumulative histograms of experimental core data.

4.3. EXAMPLE OF SPATIAL PERMEABILITY SIMULATION

4.3.1 AVAILABLE DATA

This methodology was applied to the studied field and results for a middle layer - layer 150 - are presented in more detail. As described above, the proposed approach for this field is a rock type based model. It starts by creating a stochastic model of the spatial distribution of lithoclasses (geological model) using categorical simulation algorithms and conditioning the generation of permeability and porosity values to the previous simulated images of lithoclasses. In the present section, the objective is to produce simulated images of permeability values, conditioned to the simulated images of lithoclasses. These images should incorporate all available sources of permeability data: core measures of permeability in the horizontal direction (accurate, but scarce) and log derived measures of permeability, available in all wells, 0.5 foot spaced (less accurate - soft variable).

Lack of accuracy in the acquisition and processing of the data can lead to a less representative reservoir model. This is a common problem with permeability data. Core measures are expensive and time-consuming and as a consequence the costs associated with this sampling task are always minimised. However, it is the permeability derived from core analysis that ensures high accuracy for reservoir characterisation.

In the selected layer, the proportion of cored wells to the entire set of samples is about 25%. In order to apply the proposed approach, the entire range of permeability was sub-divided

into 7 adjacent classes (μD): [0; 0.5[; [0.5; 5.0[; [5.0; 15.0[; [15.0; 50.0[; [50.0; 100.0[; [100.0; 220.0[and ≥ 220. All experimental samples are classified into an indicator vector based on the limits of these classes:

$$P_{Z\,cl}(x_\alpha) = \begin{cases} 1 & \text{if} \quad z_{cl} \le Z(x_\alpha) < z_{cl+1} \\ 0 & \text{otherwise} \end{cases} \tag{4.12}$$

Following the proposed methodology, cumulative histograms of permeability by lithoclass and permeability class are computed:

$F_{cl,k}(x)$, with *cl=1, 7* (number of permeability classes) and *k = 1, 9* (number of lithoclasses observed in the selected layer: 2,3,4,5,6,7,8,9, and 15)

To summarise, initial data is made up of:

- a set of 3D grids representing simulated images of lithoclasses for the whole of area *A*. In this study, these images were constructed using a SIS approach, see section 2;
- the probability of each sample (cored or not) belonging to each permeability class;
- cumulative histograms of permeability, by lithoclass and permeability class;
- core permeability data in cored samples.

For the studied layer, Table 4.1 shows the proportions of each lithoclass in all experimental data and in three simulated images. As is shown, all proportions calculated in the simulated images using the SIS simulation method with correction for local probabilities give a good match for the proportions of experimental data. In the selected layer, and based on the experimental variograms calculated for the horizontal direction, lithoclasses 2, 4, 8 and 15 were grouped and modelled together with a long-range - 4000 metres - multi-phase variogram (fitted by an exponential model). The complementary set of lithoclasses was classified as erratic in terms of spatial continuity. In the vertical direction these two groups of lithoclasses were modelled with exponential models with 25 S.U. and 15 S.U., respectively (see section 2).

Table 4.1 Proportion of each lithoclass in the experimental dataset and in three simulated images.

Lithoclass	Experimental data proportions	Realisations		
		#1	#2	#3
2	0.193	0.192	0.194	0.192
3	0.040	0.041	0.041	0.040
4	0.068	0.070	0.069	0.068
5	0.045	0.047	0.043	0.045
6	0.080	0.078	0.077	0.080
7	0.070	0.066	0.067	0.067
8	0.115	0.118	0.120	0.121
9	0.301	0.295	0.296	0.294
15	0.088	0.093	0.088	0.093

4.3.2 STOCHASTIC SIMULATION OF PERMEABILITY CLASSES CONDITIONED TO SIMULATED IMAGES OF LITHOCLASSES

In the selected layer, 124 x 42 x 21 points (total 109368) constitute the 3D grid. Again, spacing between nodes is 250 metres in the horizontal direction and 1 S.U. in the vertical direction.

Experimental omnidirectional variograms were calculated for each permeability class using the set of samples available for the selected layer. Classes 1 and 4 display a long-range variogram (about 4000 metres), unlike the complementary classes, which are more erratic. Thus, two multi-phase variograms were calculated, one grouping classes 1 and 4 and the other the complementary phases. For the continuous group of classes, the model fitted is an exponential model with 4000 metres range in the horizontal direction and 20 S.U. in the vertical direction. For the erratic group, an exponential model was fitted with 500 range (flow simulator block model) was fitted in the horizontal direction and 10 S.U. in the vertical direction. Figure 4.1 and Figure 4.2 show corresponding experimental omnidirectional variograms and theoretical models fitted.

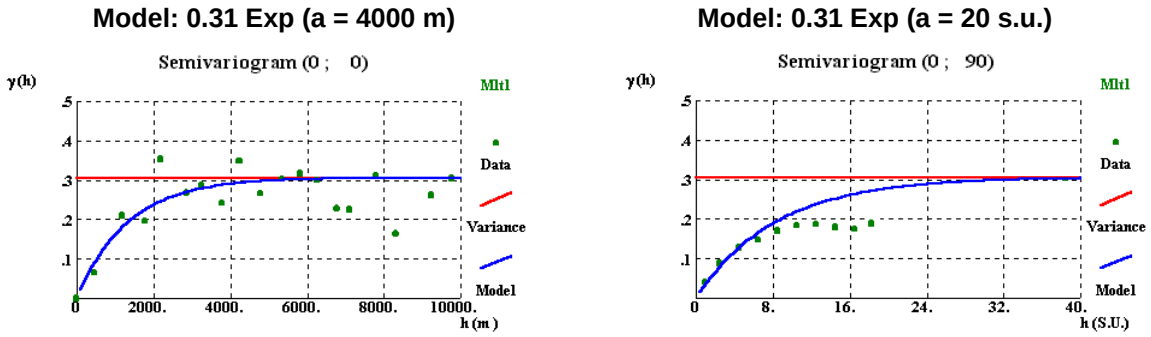

Figure 4.1 Experimental multi-phase variograms of the continuous set of permeability classes and theoretical models fitted: left) horizontal direction; right) vertical direction.

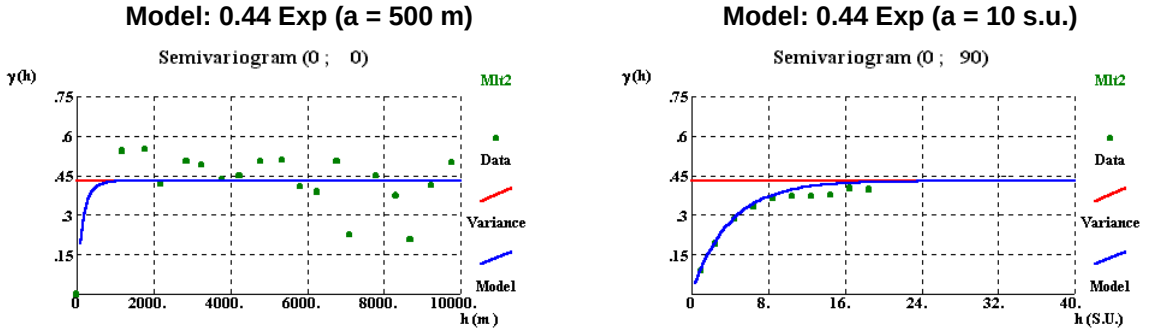

Figure 4.2 Experimental multi-phase variograms of the erratic set of permeability classes and theoretical models fitted: left) horizontal direction; right) vertical direction.

Permeability classes were simulated over the entire area *A* as categorical variables conditioned to the simulated images of lithoclasses. Instead of performing one independent simulation by lithoclass and merging the simulated images of permeability classes conditioned to the lithoclasses, the simulation was performed in a single step, after changing the original SIS code from GSLIB software (Deutsch and Journel, 1992). The advantage is the imposition of the proportions of the classes in the area occupied by each lithoclass. When a grid node x_u in area *A* is selected randomly, the lithoclass previously simulated in this grid node is identified. Thus, estimation of the probability of belonging to each permeability class follows a search strategy including only the samples and grid nodes that belong to the same lithoclass. Also, corrections for local probabilities are made taking into account the proportions shown by each permeability class in the simulated lithoclass. The result of the simulation consists of the allocation of each grid node x_u to one permeability class *cl*, in the case of the point x_u belonging to the *k* lithoclass: $\left[P_{Z_{cl}}(x_u)|k\right]^s$.

In Table 4.2, experimental marginal frequencies of each permeability class inside each lithoclass are displayed. In

Table 4.3 through Table 4.5, marginal frequencies of each permeability class inside each lithoclass corresponding to 3 different simulated images of permeability classes are displayed (values for each lithoclass were calculated for 100%). As can be observed, all experimental proportions are matched approximately in the simulated images. Figure 4.3 shows a set of simulated images of lithoclasses (left) and the corresponding simulated images of permeability classes (right).

Table 4.2 Experimental proportions $P_{Zcl}(x_\alpha)$ by lithoclass and permeability class (samples).

Lithoclass	1	2	3	4	5	6	7
2	0.449	0.227	0.162	0.052	0.052	0.058	0.000
3	0.719	0.281	0.000	0.000	0.000	0.000	0.000
4	0.889	0.111	0.000	0.000	0.000	0.000	0.000
5	0.222	0.778	0.000	0.000	0.000	0.000	0.000
6	0.261	0.723	0.016	0.000	0.000	0.000	0.000
7	0.086	0.586	0.259	0.069	0.000	0.000	0.000
8	0.044	0.641	0.315	0.000	0.000	0.000	0.000
9	0.242	0.344	0.186	0.136	0.025	0.025	0.042
15	0.000	0.128	0.169	0.548	0.127	0.028	0.000

Table 4.3 Simulated proportions $P_{Zcl}(x_\alpha)$ by lithoclass and permeability class (REALIZATION #1).

Lithoclass	1	2	3	4	5	6	7
2	0.444	0.253	0.150	0.064	0.043	0.046	0.000
3	0.624	0.376	0.000	0.000	0.000	0.000	0.000
4	0.824	0.176	0.000	0.000	0.000	0.000	0.000
5	0.268	0.732	0.000	0.000	0.000	0.000	0.000
6	0.289	0.630	0.081	0.000	0.000	0.000	0.000
7	0.193	0.501	0.217	0.089	0.000	0.000	0.000
8	0.119	0.580	0.301	0.000	0.000	0.000	0.000
9	0.276	0.358	0.169	0.116	0.026	0.022	0.032
15	0.000	0.126	0.152	0.581	0.112	0.029	0.000

Table 4.4 Simulated proportions $P_{Zcl}(x_\alpha)$ by lithoclass and permeability class (REALIZATION #2).

Lithoclass	**1**	**2**	**3**	**4**	**5**	**6**	**7**
2	0.439	0.256	0.148	0.065	0.040	0.051	0.000
3	0.614	0.386	0.000	0.000	0.000	0.000	0.000
4	0.825	0.175	0.000	0.000	0.000	0.000	0.000
5	0.281	0.719	0.000	0.000	0.000	0.000	0.000
6	0.292	0.623	0.084	0.000	0.000	0.000	0.000
7	0.201	0.495	0.210	0.095	0.000	0.000	0.000
8	0.123	0.578	0.299	0.000	0.000	0.000	0.000
9	0.271	0.359	0.175	0.114	0.025	0.023	0.033
15	0.000	0.136	0.147	0.576	0.113	0.028	0.000

Table 4.5 Simulated proportions $P_{Zcl}(x_\alpha)$ by lithoclass and permeability class (REALIZATION #3).

Lithoclass	**1**	**2**	**3**	**4**	**5**	**6**	**7**
2	0.442	0.251	0.154	0.061	0.040	0.051	0.000
3	0.627	0.373	0.000	0.000	0.000	0.000	0.000
4	0.829	0.171	0.000	0.000	0.000	0.000	0.000
5	0.270	0.730	0.000	0.000	0.000	0.000	0.000
6	0.283	0.633	0.084	0.000	0.000	0.000	0.000
7	0.196	0.488	0.222	0.093	0.000	0.000	0.000
8	0.127	0.583	0.290	0.000	0.000	0.000	0.000
9	0.274	0.353	0.172	0.117	0.027	0.025	0.031
15	0.000	0.141	0.143	0.576	0.112	0.028	0.000

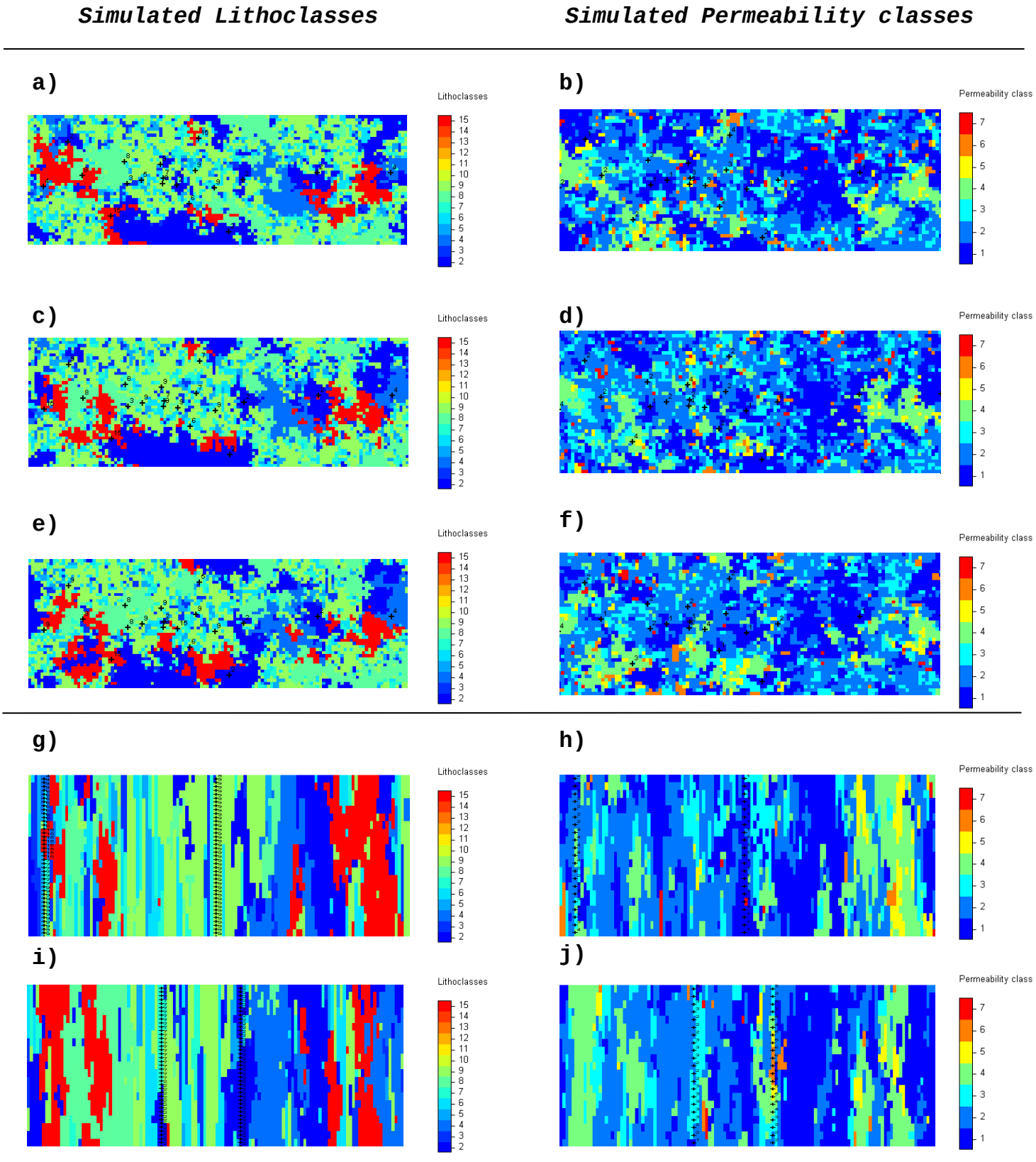

Figure 4.3 Illustration of 3 horizontal views and 2 cross-sections from the generated stochastic images of lithoclasses using SIS algorithm and corresponding simulated images of permeability classes.

4.3.3 TRANSFORMATION OF IMAGES OF PERMEABILITY CLASSES INTO NUMERICAL IMAGES OF PERMEABILITY

The final step of the proposed methodology consists of transforming permeability classes (categorical maps) into numerical values of permeability. The aim of this step is to simulate probability values based on the local ccdf by using the *p*-field simulation approach. Thus, for the field area *A*, 9 plus 9 independent probability fields were simulated $\left[p_k(x_u)\right]^s$ (one by lithoclass and for the continuous and erratic sets) using the permeability classes ($P_{Z_{cl}}$) variogram model (see Figure 4.1 and Figure 4.2). Simulation of a probability field with uniform distribution can be obtained via a sequential Gaussian simulation. After ranking the entire set of Gaussian values in increasing order, each grid node is transformed according to the following relation: p_i / N, where p_i is the position order of the node x_u in rank vector and N represents the total number of grid nodes.

Finally, in each point x_u a permeability value $Z_S(x_u)$ is drawn with the local ccdf and the simulated probability field $\left[p_k(x_u)\right]^s$:

$$z_s(x_u) = F^{-1}(x_u, z, p(x_u)) \tag{4.13}$$

An additional step is required to ensure a match between the simulated permeability maps and the core data samples. For this purpose, the experimental values of permeability were directly allocated to the nearest grid node. This single step guarantees that the simulated values match the core data samples.

The practical application of this final step - the transformation of permeability classes into permeability values using the probability field values - is presented in the flow chart in Figure 4.4.

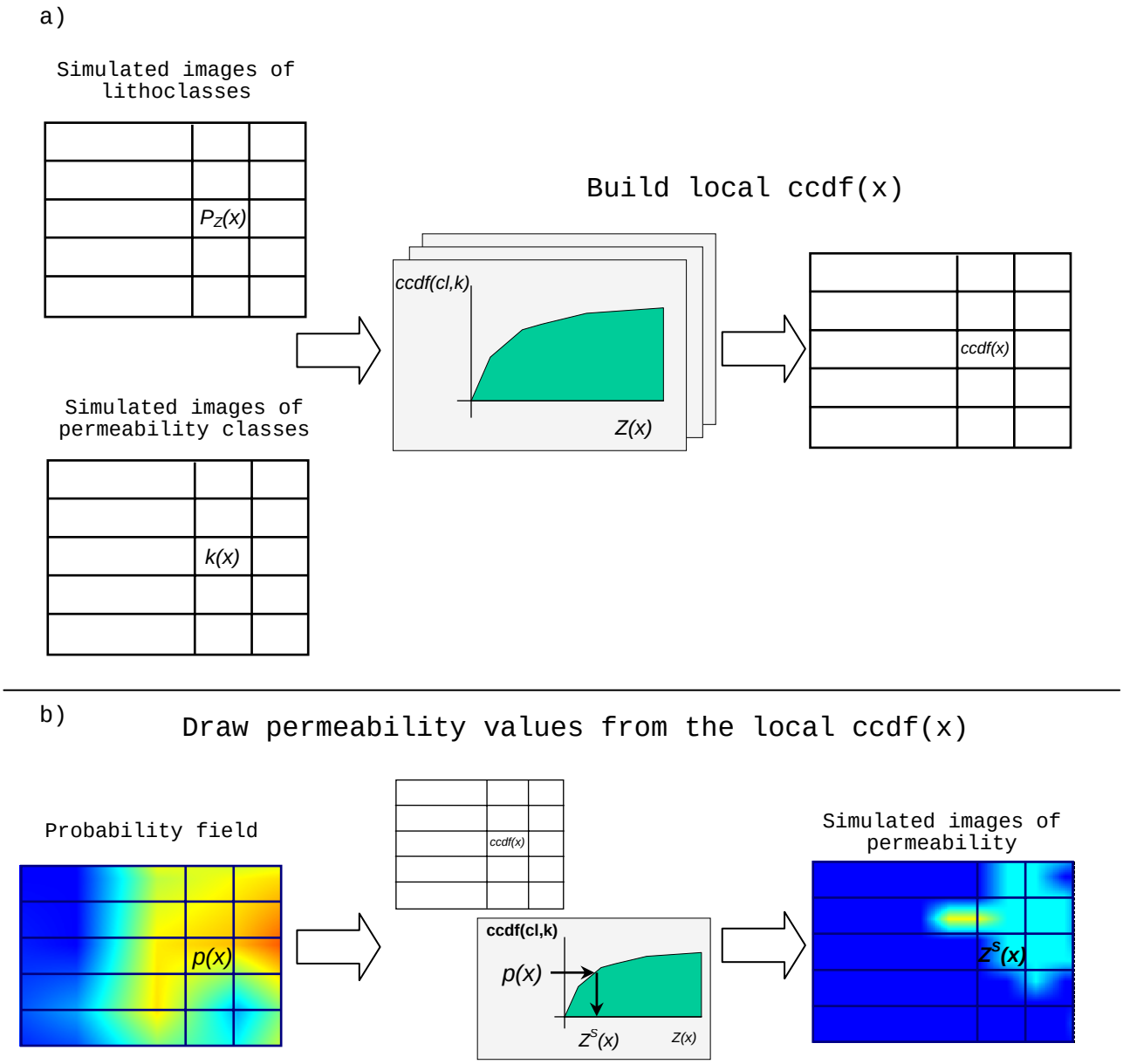

Figure 4.4 Flow chart representing: a) building local ccdf(x) for the entire grid area; b) drawing permeability values from the local ccdf(x), using a probability field and a Monte Carlo approach.

4.3.4 VALIDATION OF RESULTS

Figure 4.5 shows a sequence of cross-sections representing one realisation of permeability values.

In Figure 4.5 the basic statistics of *z(x)* (each one by lithoclass) for the samples (left images) and for one simulated realisation of permeability (right image) are displayed. As the figures show, the match between the two types of data is excellent. This means that the methodology used is an appropriate tool to describe heterogeneous reservoirs like this carbonate field which involve dealing with under-sampled variables like permeability.

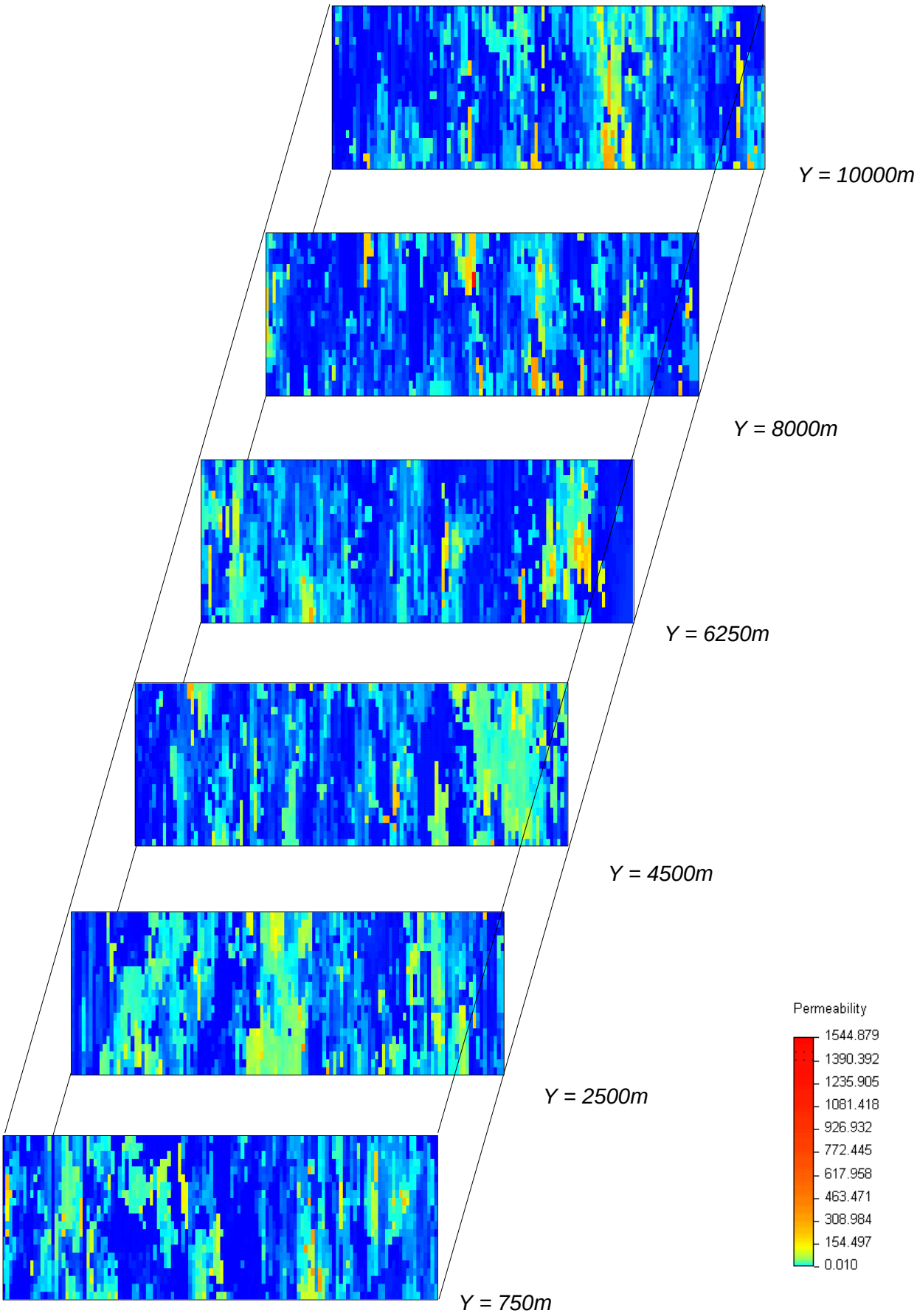

Figure 4.5 Cross-sections for the selected layer showing the vertical distribution of permeability values.

Lithoclass 2

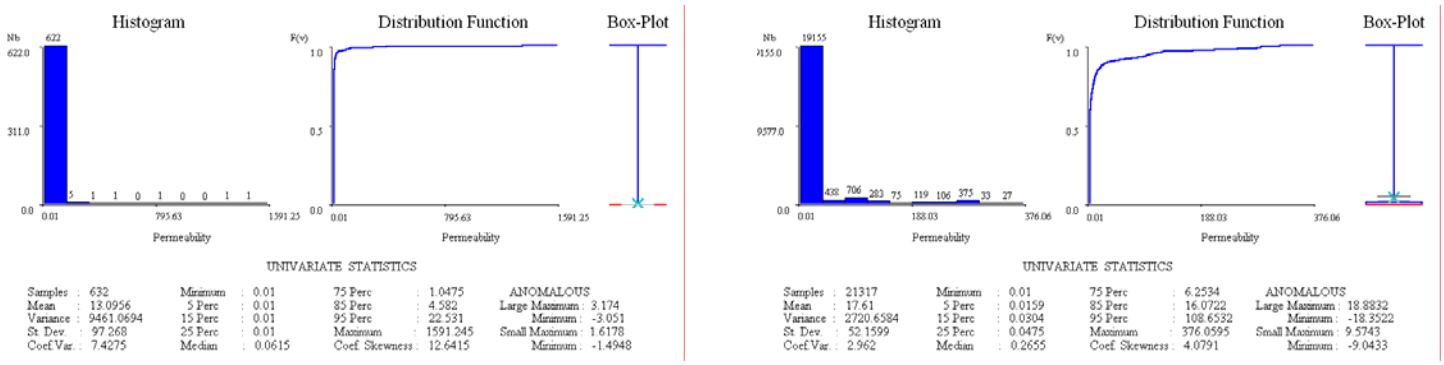

Lithoclass 3

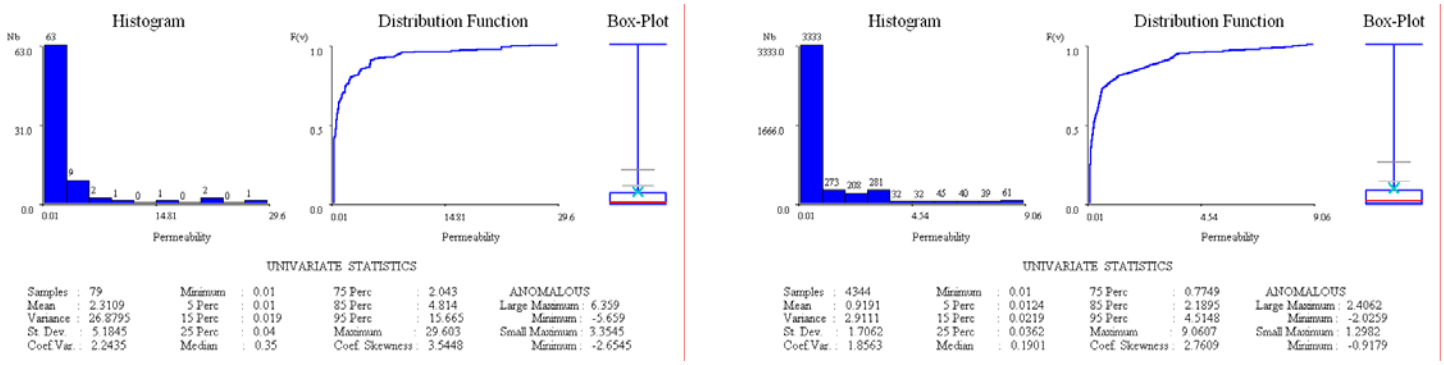

Lithoclass 4

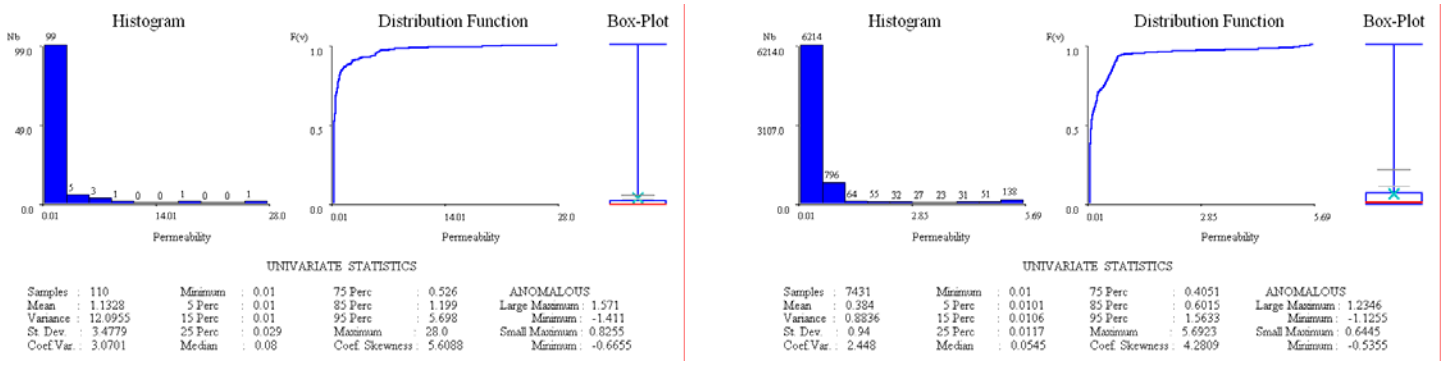

Lithoclass 5

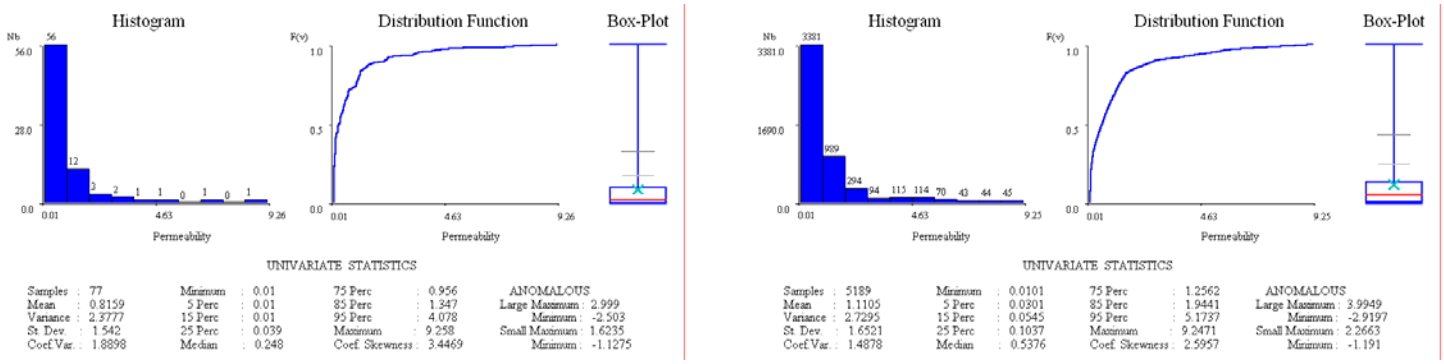

Figure 4.6 Univariate statistics illustrating distribution of permeability by lithoclass: left) core data; right) simulated values.

Lithoclass 6

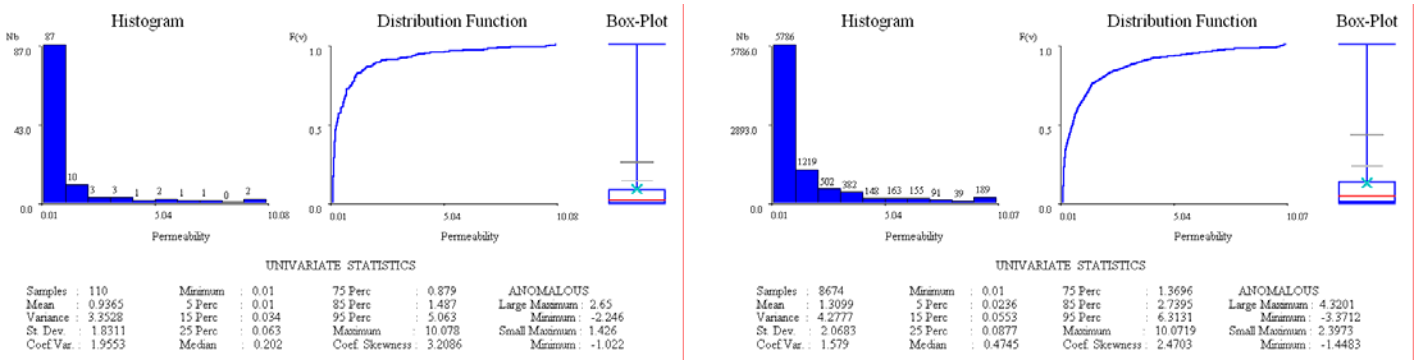

Lithoclass 7

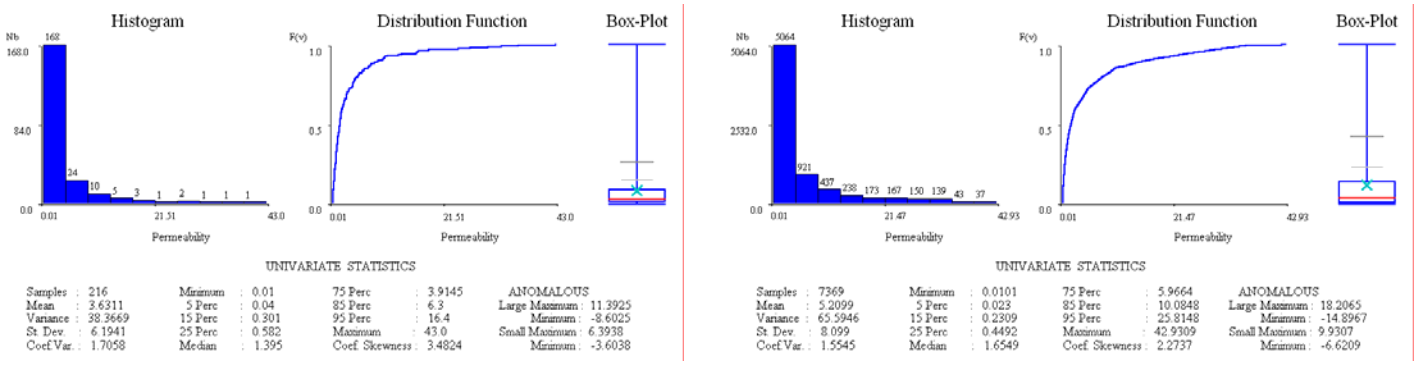

Lithoclass 8

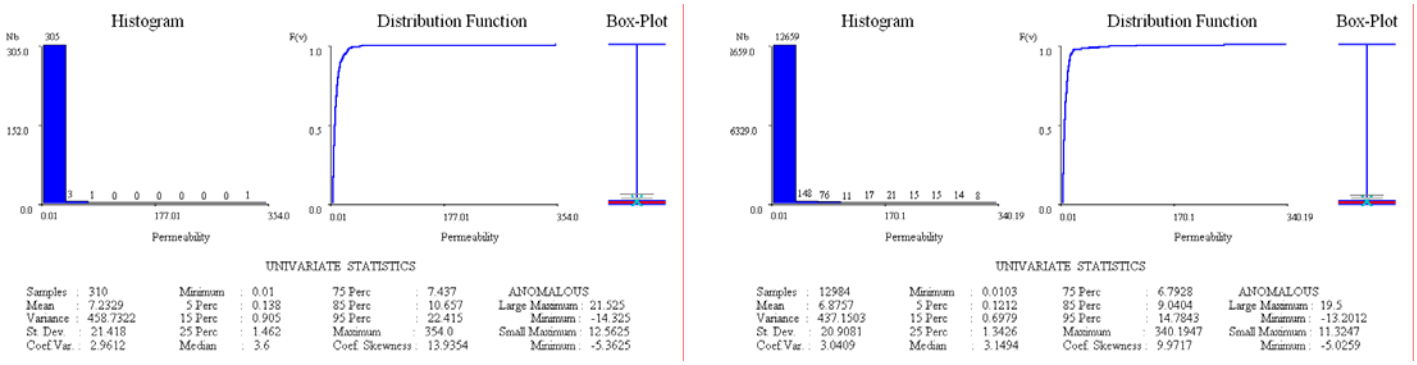

Lithoclass 9

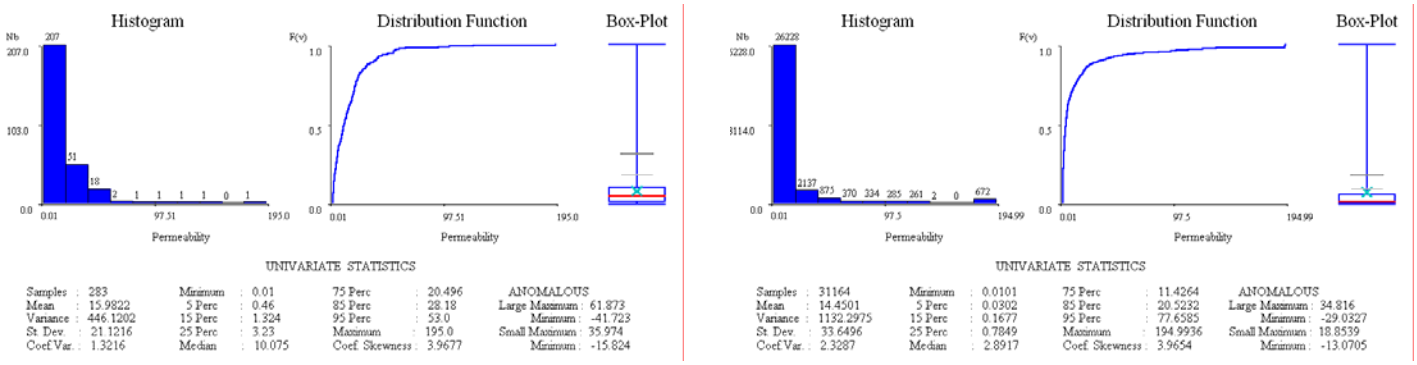

Figure 4.6(cont) Univariate statistics illustrating distribution of permeability by lithoclass: left) core data; right) simulated values.

Lithoclass 15

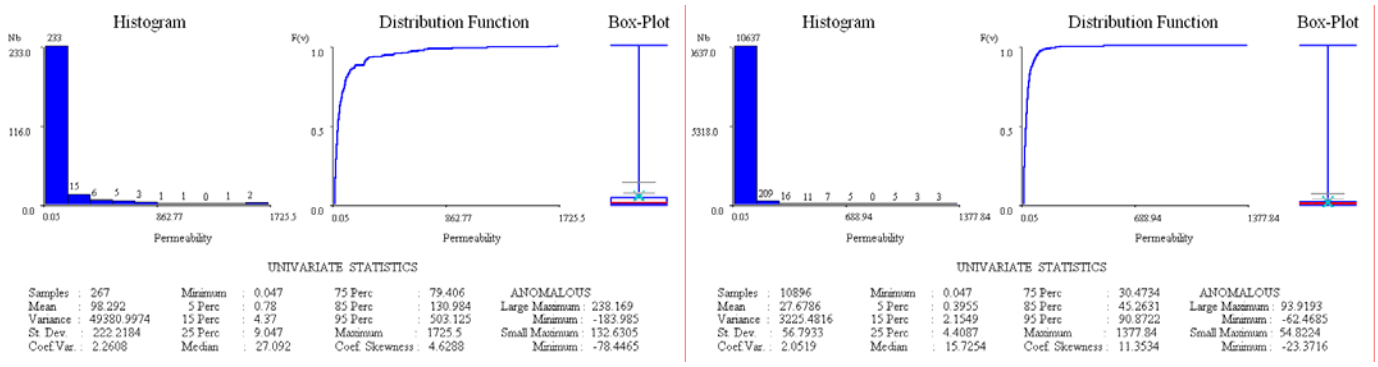

Figure 4.6(cont) Univariate statistics illustrating distribution of permeability by lithoclass: left) core data; right) simulated values.

Finally, to evaluate the contribution of the conditioning effect of the samples on the different images involved in the sequence presented in this section (initial images of lithoclasses, filling of simulation of permeability classes and filling of permeability values), an entropy analysis through these different images is performed. Thus the entropy measurement was calculated (expressions 2.32 and 2.33, see section 2.5) for the set of simulated lithoclass images and for the set of permeability classes images. As has already been stated, this is a measure (varying between 0 and 1) of the variability of sets of images that represent a categorical variable. Figure 4.7 contains illustrated images of entropy with reference to a level selected from layer 150 for the lithoclass images and for the corresponding image of permeability classes.

In the entropy image related to the simulated images of lithoclass, there is a gradual increase in variability, which is smooth around some wells and sharp around others. These differences in variability transitions depend on the type of lithoclass sampled in the well and the respective continuity model: there is a significant increase in variability around wells of erratic lithoclasses.

Regarding the entropy of the simulated images of permeability classes, there is a significant increase in variability around wells of continuous lithoclasses due to the fact that there are erratically distributed permeability classes in continuous lithoclasses. Overall, the entropy measurement is lower in the images of permeability classes, due to the concentration of permeability values in two classes (1 and 2), one of which is classified spatially as continuous.

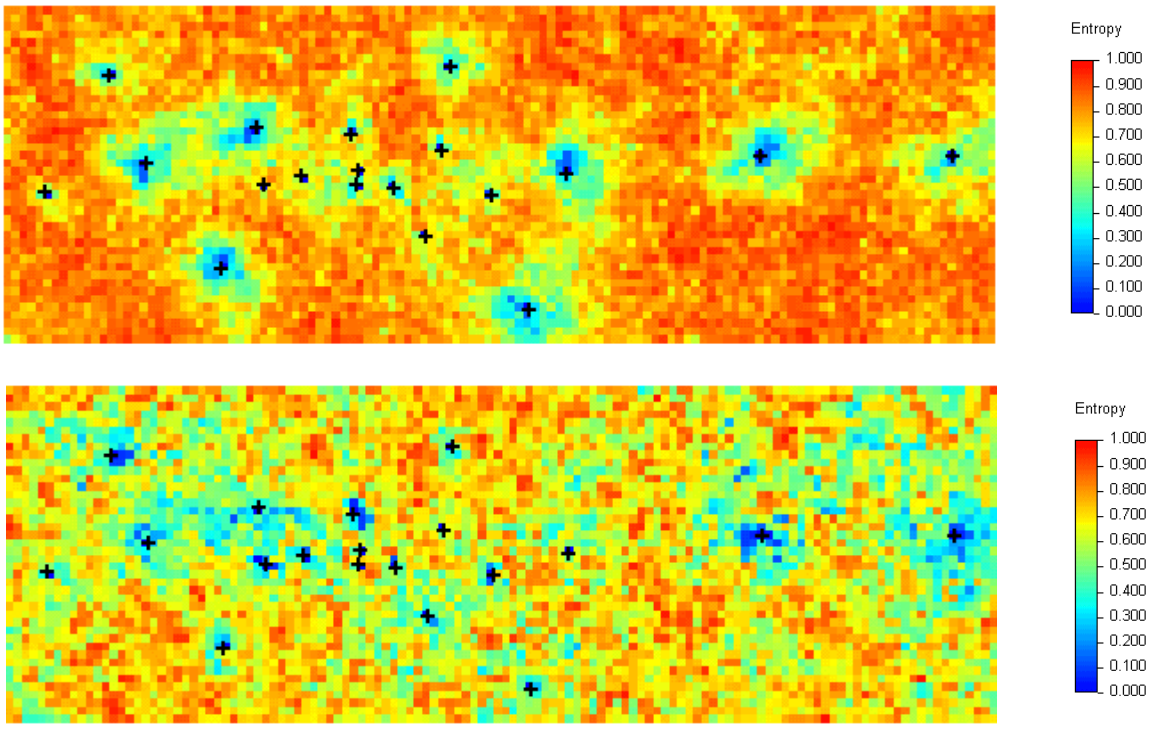

Figure 4.7 Upper image: entropy distribution on level 1 of the lithoclass image set; Lower image: entropy distribution on level 1 of the permeability class image set.

In order to be able to check whether the number of simulations was considered sufficient (30 lithoclass simulations and 90 permeability classes simulations – 3 for each lithoclass image), entropies were calculated taken at each point of the whole grid of points for different sets of realisations, varying between 2 and the total number of realisations. These results are represented graphically in Figure 4.8. Observing the graphs, it can be seen that the number of simulations may be considered sufficient given that the rate of increase of total entropy diminishes greatly as the number of realisations considered increases.

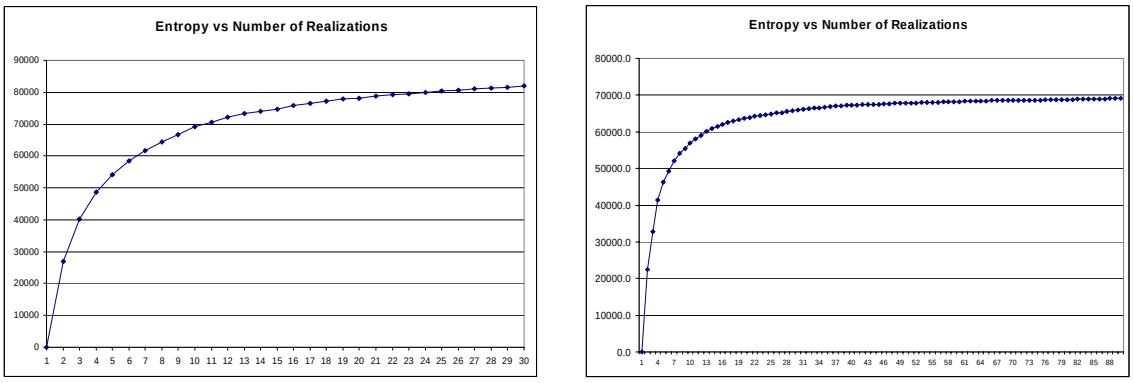

Figure 4.8 Left: variability of the sum of the entropy with increasing number of realisations for stochastic images of lithoclasses; Right: variability of the sum of the entropy with increasing number of realisations for stochastic images of permeability classes.

For the simulated images of permeability, the variance of values at each grid node was used as a measure of the variability of the images. The variance obtained varies from 0 (in the sample locations) to approximately 688. Figure 4.9 shows images of the variance relating to a selected level of layer 150 for the image of permeability figures. Figure 4.10 shows the total variances for all simulated nodes for different sets of realisations. Based on these figures, it can also be observed that that the number of realisations may be considered satisfactory given that the increase in variability stabilises. It should also be pointed out that the criterion used was based on the sum of local measures of entropy or on local variances to measure the variability of a set of simulated images. It should therefore be borne in mind that the use of this criterion is based on local measures of the variability of simulated values at each node of the grid and not on the variability of the whole set.

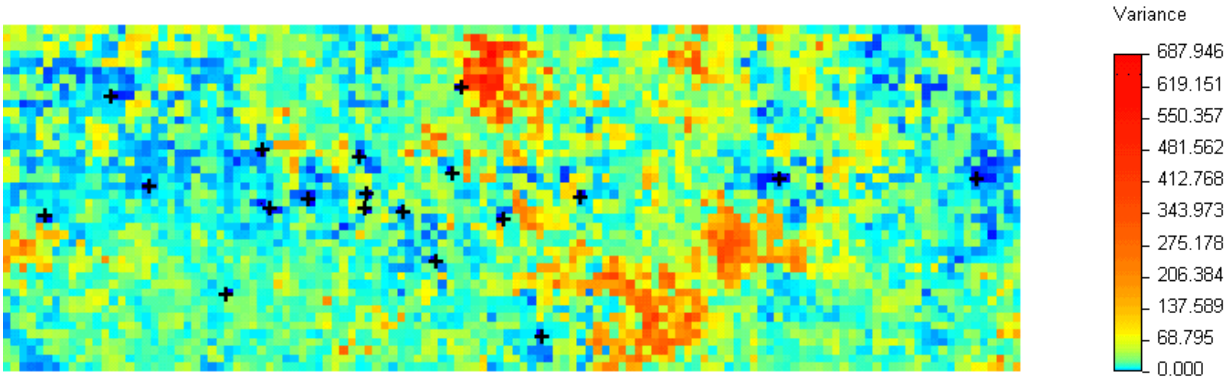

Figure 4.9 Variance distribution on level 1 for the entire set of 90 simulated images of permeability values.

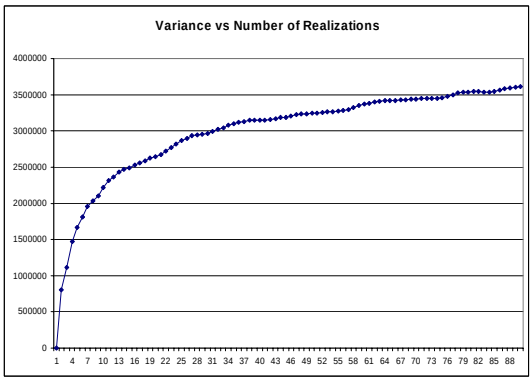

Figure 4.10 Variability of the sum of the variance with increasing number of realisations for the stochastic images of permeability values.

4.4. FINAL REMARKS

This case study illustrates a methodology for the characterisation of under-sampled variables, which is a common situation in most oil reservoirs, regarding permeability data. Permeability is usually estimated by correlation based on a small amount of core data and detailed log measurements. The method described in this section is able to produce simulated images of permeability combining core data (more accurate) and additional soft data (less accurate). The advantage of this proposed method consists in the ability to integrate two types of information that carry different levels of accuracy.

The permeability simulation must reflect the high level of heterogeneity usually associated with this variable and must preserve the extreme values. Great care was taken in the permeability simulation in view of the complexity involved in the methodology. It is important that the variability shown in the permeability core histogram is preserved and reproduced through the stochastic model. As the dynamic simulator must be fed with numerical values of petrophysical properties, such as permeability, it was necessary to develop a process for transforming the permeability classes into data values. This process accounts for the heterogeneity of permeability values found in the field, preserving the spatial structure and, perhaps most importantly, it reproduces the extreme values. In a field like the one presented in the case study, where the permeability is either very low or very high, it is important that the stochastic model reproduces the patterns of high and low fluids flow paths.

5 RESERVOIR INTERFACE DESCRIPTION/RESERVOIR FLUID FLOW SIMULATION

5.1. SCREENING OF DIFFERENT STOCHASTIC REALIZATIONS: GEOBODY ANALYSIS

In reservoirs for which only a small amount of information exists, the range of geostatistical techniques for producing conditional simulations can be used to generate several equally probable realisations of the internal distribution of rock types and properties. This set of images honours the data points, basic statistics and continuity models, and is a tool to quantify uncertainties in forecasting studies associated with reservoir fluid flow performance and depletion. Geostatistical models based on simulation techniques have been devised to account for small-scale variability, ensuring adequate representation of extreme values. Each realisation is unique, because the random component influence is proportional to the distance between wells and inversely proportional to the spatial continuity revealed by the variogram tool. In areas where well spacing decreases and spatial correlation increases, the different stochastic realisations become more alike. Furthermore, the presence of geological heterogeneities conditions the drainage mechanism of oil and affects fluid flow. For example, low permeability geobodies act as barriers to fluid flow, unlike high permeability connections, which are preferential fluid flow channels.

Following the use of geostatistical stochastic simulations to generate equally probable reservoir descriptions, the set of output images of permeability, porosity and fluid saturation conditioned to lithoclass morphology constitutes the main input datasets for the fluid flow simulators. The importance of having different realisations for this particular complex reservoir is that they provide an assessment of uncertainty in space. Comparison between realisations helps us to identify critical uncertainties and perform risk analysis, and constitutes a guideline for future steps on data gathering programmes (Da Costa e Silva, 1992). The final objective is to obtain the range of uncertainty of the parameters that can affect reservoir performance. To transform the uncertainty of the simulated images into reservoir performance forecasting one needs to run the fluid flow simulator using the entire range of images. In order to process all simulated images in a fluid flow simulator, even after a change of scale, a previous selection of the more representative stochastic images is proposed.

In this approach, the selection of a few images is based on the extreme behaviour of internal characteristics (permeability) of the reservoir. The basic tool to classify all the simulated

images is a measure of the continuity and connexity of geobodies of high and low permeability. The application of this screening tool can be summarised in the following steps:

i) Define a threshold, the permeability being classified as high if it is above the threshold, otherwise it is considered low or medium. To provide better screening between realisations, the threshold should correspond to a value that creates a considerable volume of high and low permeability areas;

Thus, for the entire set of simulated images:

ii) Transform all permeability images into binary images, using the threshold defined above;

iii) Identify of all geobodies in the binary image and calculate the volumes of all individual geobodies;

iv) Represent on a single histogram the frequency of different volume geobodies for each realisation;

v) Visually select the extreme situations: the realisation with highest percentage of high volume geobodies; the realisation with highest frequency of low volume geobodies.

The main drawback of the proposed selection algorithm is that the spatial location of the wells is not taken into account. In other words, a classification based on the volumes of individual geobodies does not take into account the location of these same geobodies. Another approach derived from this is to calculate the volume of high or low permeability areas that contact a specific well or set of wells and comparison of volumes between simulations. A major feature of these tools is that the scanning of each realisation is performed in 3D space, which enables for a detailed and complete analysis of continuity characteristics.

To illustrate the performance of the proposed measuring tools, 90 simulated images of permeability produced using the simulation methodology for undersampled variables were used and compared (see section 5). The threshold used to define high permeability geobodies was 15mD, corresponding to the 0.85 percentile. Otherwise, to define low permeability geobodies, the threshold used was 0.1mD, corresponding to the 0.2 percentile. In Figure 5.1, the histogram of the geobodies volume is shown.

High permeability geobodies

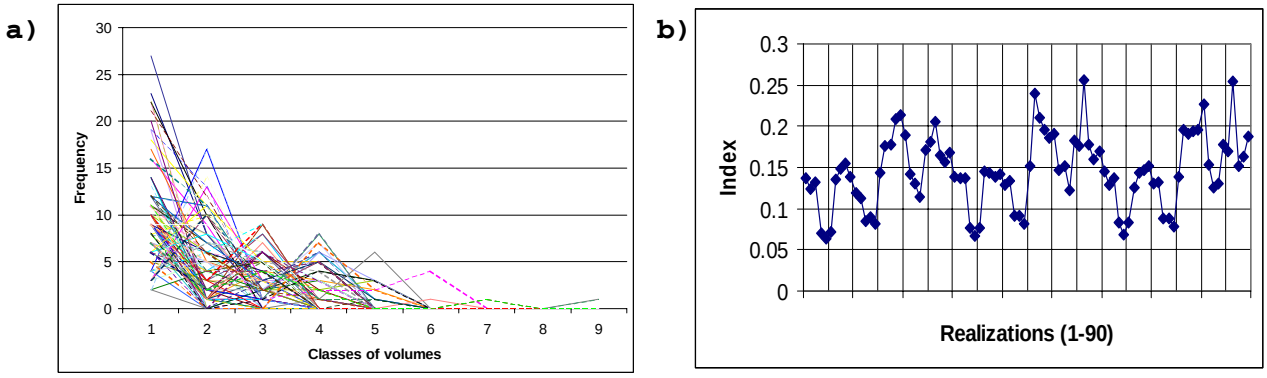

Figure 5.1 a) Histogram of volumes for geobodies of high permeability for the set of realisations; b) Representation of the index volume of geobodies (high permeability) for the set of realisations.

To produce this histogram, data from the first class corresponding to the smallest geobody volumes was removed because this class has a very high frequency for all simulations (over than 1500 occurrences compared with the second class, between 2 and 27 occurrences) and this difference of occurrences would undoubtedly mask the analysis.

To summarise each of these lines into a value which can be compared to others, an index based on the frequency of each class weighted by volume was computed for each realisation #*r* using the expression:

$$Index_{\#r} = \frac{\sum_{i=2}^{n} \lambda_i f_i}{\sum_{i=2}^{n} \lambda_i}$$

where *n* is the number of classes of volumes, f_i is the number of occurrences of geobodies with class of volume *i*, and λ_i represents the weight of class of volume *i* - ($\lambda_i = i - 1$) in this application.

The results are given in Figure 5.1 b). Looking at this chart, it is easy to select low and high continuity realisations or even middle situations based on the defined criteria.

In Figure 5.2 a) the histogram of the volume of low permeability geobodies is displayed. In Figure 5.2 b) the corresponding representation of the index based on the frequency of each class weighted by volume is also displayed. Extreme and middle situations based on the defined criteria can be easily selected.

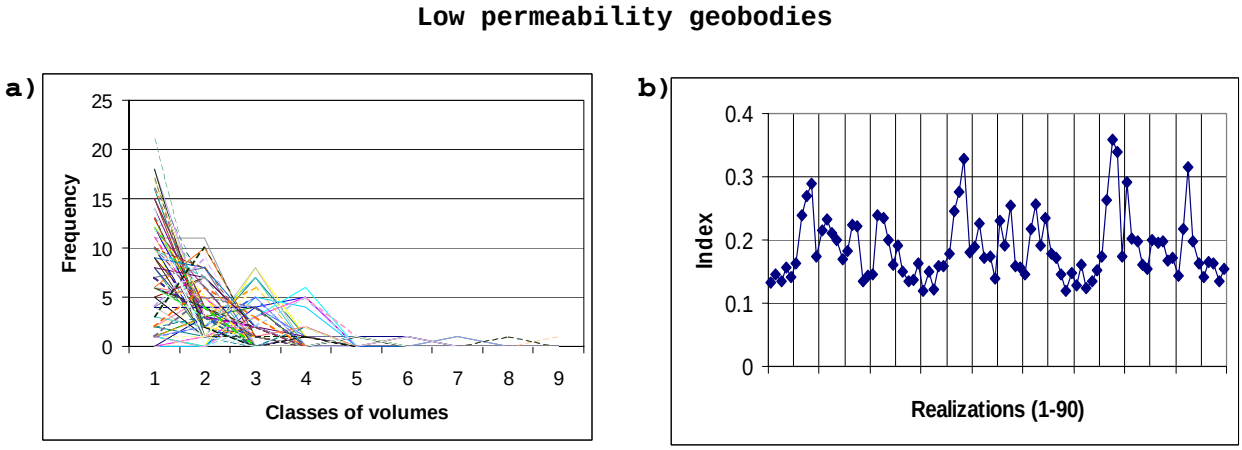

Figure 5.2 a) Histogram of volumes for geobodies of low permeability for the set of realisations; b) Representation of the index volume of geobodies (low permeability) for the set of realisations.

The second objective is to rank the realisations based on a measure of volumes of high permeability that contact a set of wells. For illustrative purposes, the selection includes 11 wells located in the middle of the field (see Figure 2.12 through Figure 2.16). Figure 5.3 represents the number of blocks (volumes) of high and low permeability that contact the selected central wells.

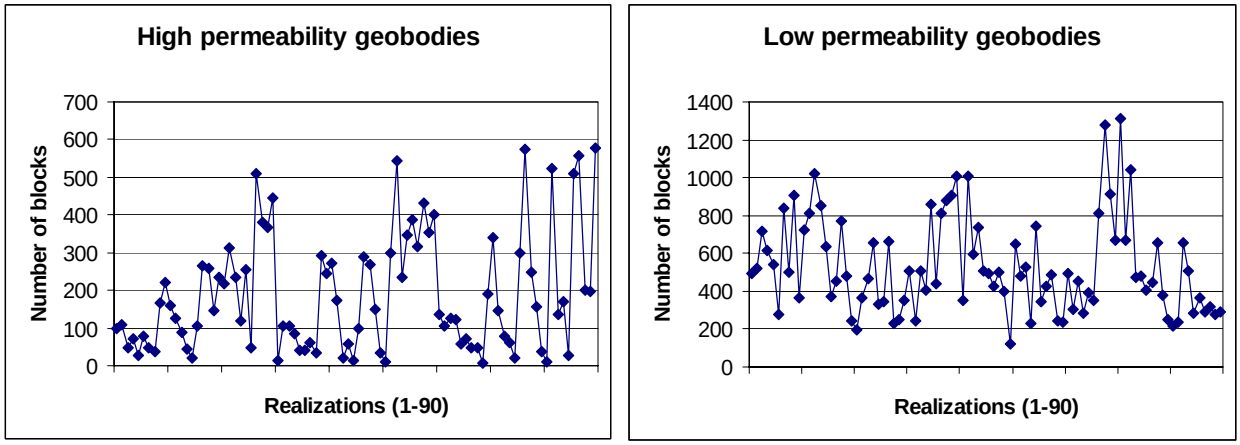

Figure 5.3 Volumes of geobodies that contact the selected 11 central wells: left: high permeability geobodies; right: low permeability geobodies.

Following this representation, the realisations were ranked by the defined criteria. The main problem consists in the selection of a few realisations (for example, two or three) that are representative of the field based on multi-selection criteria. Another difficulty is the assumption that the criterion used to rank the simulations is appropriate for the required purpose. However, it is important to note that the main objective at this stage is to use a simple classification to rank the simulations before upscaling, ensuring that the flow

simulations enable us to pick the most representative scenarios of extreme behaviours in terms of fluid flow.

5.2. UPSCALING OF PROPERTIES

5.2.1 INTRODUCTION

In the present work a conditional and iterative approach of upscaling of permeability is proposed based on the formulation of mass balance equations and Darcy's Law (Archer and Wall, 1986). In the classic approach, the effective permeability in a particular set of blocks is derived from the application of a pressure gradient between two opposite boundaries and the imposition of a no-flow condition in the others. Based on the pressure solver technique, the idea is to improve the quality of upscaling by including in the calculation of the equivalent permeability of each large-scale block (macroblock) the influence of the permeability values in the set of neighboring small-scale blocks (microblocks) as well as the interdependence between the scale-up values of previously transformed macroblocks (Gomez-Hernandez and Journel, 1990, 1994, Almeida *et al*, 1996). These concepts led to the proposed interactive method: in each iteration corresponding to the upscaling of one macroblock, the solutions are ranked according to a criterion based on a flow test and expressed in one objective function. In the second step, the macroblock corresponding to the minimum value of the objective function is selected. The process continues until all blocks are scaled up. This method guarantees that the solutions are successively conditioned to initial permeability values and/or to scale-up values obtained in previous iterations.

The performance of this method is illustrated (in comparison with the classic approach) by comparing the waterflood shape in a flow test using two opposite wells located in the small-scale blocks and the large-scale blocks using the flow simulator ECLIPSE 100.

5.2.2 THE PROBLEM OF UPSCALING PERMEABILITY

The use of geostatistical simulation methods (*e.g.* sequential Gaussian simulation and sequential indicator simulation) in oil reservoirs to describe the petrophysical properties between wells (namely lithofacies, permeability and porosity), leads to equally probable images of the spatial distribution of these properties (Journel and Alabert, 1988, Journel and Gomez-Hernandez, 1994, Da Costa e Silva *et al*, 1993). Each of these images contains several hundred thousand values and constitutes a valuable tool in interpretation of the morphological and petrophysical structure of the reservoir. For instance, the studied

reservoir illustrated in this work was sub-divided into 4 million small-scale blocks. Each set of values is also used as input into dynamic simulation studies, which determine the flow between adjacent wells.

Running flow simulations on computers is a complex task and consequently the operations tend to be slow, which restricts the number of blocks and layers that can be used simultaneously. These restrictions that in most cases the scale of the simulated blocks must be changed, in order to come up with just one value for a set of adjacent blocks with a particular fixed geometry. The solution lies in the use of a correct scale-up or upscaling (or grossing up) technique coupled with a preliminary dynamic assessment and validation of the model.

Since the permeability in a porous medium is a non-additive variable with tensor characteristics, calculation of one equivalent value for a set of blocks can not be performed using any type of averages (with exceptions for very simple geometrical configurations). Also, of all petrophysical properties, permeability makes the greatest contribution to formulation of the equations associated with fluid flow in porous media, namely Darcy's Law.

Several methodologies have been proposed for calculating the equivalent permeability, which are more or less complex depending on the simplifications imposed on the upscaling, the geometry of the grid, and the heterogeneity of the field. The question of upscaling has been approached from several standpoints, such as using techniques based on the stream tube concept (Haldorsen and Lake, 1982), study of tortuosity in porous media - application of the renormalisation technique (King, 1989, Abu-Elbashar, 1990), use of means of power *n*, or the formulation of the equations of mass transfer based on mass balance and Darcy's Law (Gomez-Hernandez and Journel, 1990, Rummy, 1990, Malick and Hewett, 1994).

Consider the following example, which illustrates the applicability of techniques based on different averages and renormalization: for a set of blocks in a serial sequence (1 by 1 by n), the equivalent permeability in the longitudinal direction is given by the harmonic mean; for the same set of blocks in the perpendicular direction the equivalent permeability is given by the arithmetic mean of permeability values. Using renormalization, it is possible to calculate the equivalent permeability (the two orthogonal components of the permeability tensor K_x and K_y) for a set of blocks based on a geometry of 2 by 2, or with simplifications for other 2D geometry (this implies recursive calculations). But considering a set of 2 by 2 by *n* blocks, calculation of the equivalent permeability for each orthogonal direction cannot be done using a single mean or combination of means. Thus, more complex upscaling methods based on the formulation of transfer equations between blocks when a pressure gradient is applied

can be considered. The solutions provided by these methods are the set of pressures in each block, which leads to the computation of the equivalent permeability, according to Darcy's Law.

In the present work a new technique of upscaling is proposed derived from these formulations. The objective is to improve the quality of upscaling by including in the calculation of the equivalent permeability of each large-scale block (macroblock) the influence of the permeability values in the set of neighbouring small-scale blocks (microblocks). The application of this principle has led to an iterative method. Each iteration corresponds to the upscaling of one macroblock and the derived solutions are successively conditioned to initial permeability values and/or scale-up values obtained in previous iterations.

The performance of this method is compared with the classic approach, corresponding to the formulation of the system of equations for each macroblock, when considered separately.

In this case study, one flow test was performed to evaluate the performance of the proposed method. This test consists in the evaluation of the performance over the entire grid and is a comparison of the shape of the waterflood in a flow test using two opposite wells located in the small-scale blocks and the large-scale blocks and using the flow simulator ECLIPSE 100.

5.2.3 CALCULATION OF EFFECTIVE PERMEABILITY USING THE PRESSURE SOLVER TECHNIQUE

Figure 5.4 represents a partial set of microblocks extracted from reservoir grid blocks, each with dimensions Δx, Δy and Δz, and a known permeability value on each grid block.

Given that permeability is a tensorial variable, in each block orthogonal components are assumed to be known. In this case, the same value is allocated to the three components of the permeability tensor $K_x = K_y = K_z = K$.

For simplification, consider this explanation of upscaling using the pressure solver technique in two dimensions. The objective is to calculate the effective components of permeability for each macroblock (set of n_x by n_y microblocks), respectively K_x and K_y (Figure 5.4), that summarise the initial isotropic values.

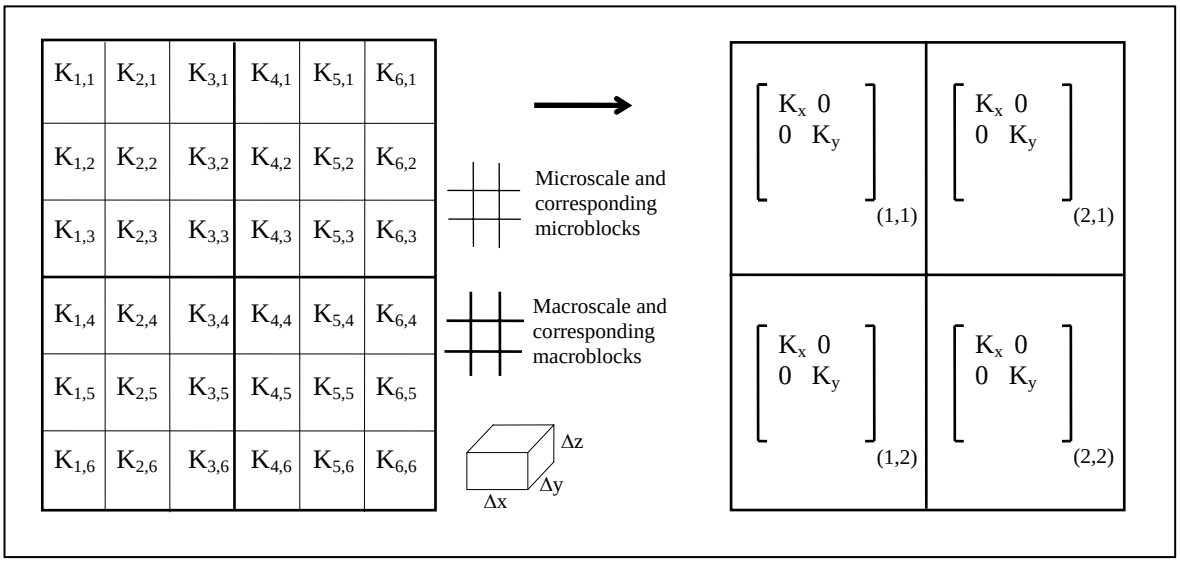

Figure 5.4 Upscaling of permeability: representation of microblocks and corresponding macroblocks.

In each set of microblocks that corresponds to a macroblock, two flow situations are created (Figure 5.5), parallel to the axes of the block coordinates, and derived from a pressure gradient imposed under no-flow boundary conditions. Boundary conditions are imposed to ensure that the system of equation resulting from the application of mass balance and Darcy's Law can be solved. To calculate the component K_x of equivalent permeability, a flow is simulated parallel to the X direction, under the following conditions:

i) Blocks belonging to the first column have a constant pressure, P_{inp};

ii) Blocks belonging to column n_x have a pressure lower than P_{inp} ; P_{out} results from the application of a pressure gradient equal to P_{inp}-P_{out};

iii) Blocks in boundaries have null transmissivity, *i.e.* no flow in the Y direction.

Consider the flow Q of an incompressible fluid; the equations for the microblock of indices *(i,j)*, resulting from the mass balance due to steady-state conditions are:

$$(Q_{x_{i+\frac{1}{2},j}} - Q_{x_{i-\frac{1}{2},j}}) + (Q_{y_{i,j+\frac{1}{2}}} - Q_{y_{i,j-\frac{1}{2}}}) = 0 \qquad (5.1)$$

where indices *(i+1/2, j)*, *(i-1/2, j)*, *(i,j-1/2)* and *(i,j+1/2)* represent respectively the interface of the block *(i, j)* with its neighbouring blocks, namely *(i+1,j)*, *(i-1,j)*, *(i,j+1)* and *(i,j-1)*.

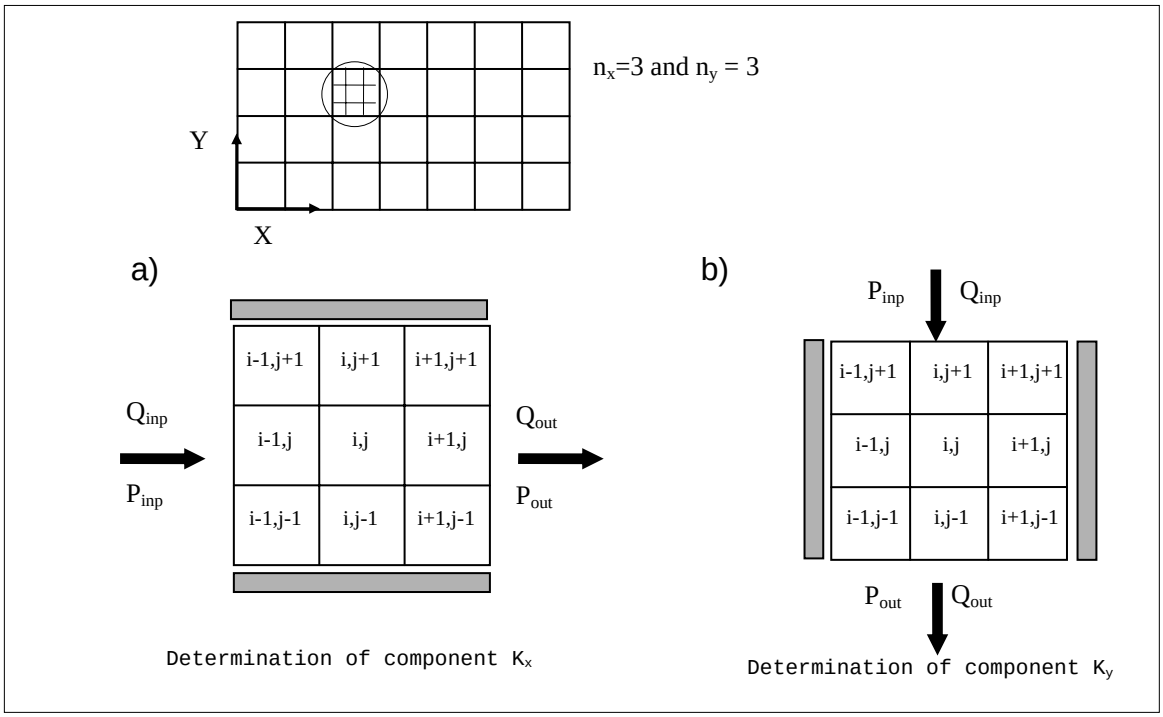

Figure 5.5 Two-flow design conditions for the determination of the effective permeability for each macroblock aggregating a set of 3 by 3 microblocks.

Suppose that only a single fluid is considered and the flow is under Darcy's Law conditions:

$$Q_x = \frac{-K_x \Delta y \Delta z}{\mu} \frac{dP}{dx} \quad \text{and} \quad Q_y = \frac{-K_y \Delta x \Delta z}{\mu} \frac{dP}{dy} \tag{5.2}$$

where μ represents the viscosity of the fluid.

This equations yields:

$$Q_{x_{i-\frac{1}{2},j}} = -\frac{K_{x_{i-\frac{1}{2},j}} \Delta y \Delta z}{\mu} \frac{(P_{i-1,j} - P_{i,j})}{\Delta x} \quad Q_{x_{i+\frac{1}{2},j}} = -\frac{K_{x_{i+\frac{1}{2},j}} \Delta y \Delta z}{\mu} \frac{(P_{i,j} - P_{i+1,j})}{\Delta x} \tag{5.3}$$

$$Q_{y_{i,j-\frac{1}{2}}} = -\frac{K_{y_{i,j-\frac{1}{2}}} \Delta x \Delta z}{\mu} \frac{(P_{i,j-1} - P_{i,j})}{\Delta y} \quad Q_{y_{i,j+\frac{1}{2}}} = -\frac{K_{y_{i,j+\frac{1}{2}}} \Delta x \Delta z}{\mu} \frac{(P_{i,j} - P_{i,j+1})}{\Delta y} \tag{5.4}$$

where $K_{x_{i-1/2,j}}$ and $K_{x_{i+1/2,j}}$ represent respectively the permeability in the interface between the blocks *(i-1,j)* with *(i,j)* and *(i,j)* with *(i+1,j)*; $K_{y_{i,j-1/2}}$ and $K_{y_{i,j+1/2}}$ represent respectively the mean permeability in the interface between the blocks *(i,j-1)* with *(i,j)* and *(i,j)* with *(i,j+1)*. These permeability values in the interface between the blocks can be estimated using the harmonic average of each two adjacent blocks:

$$K_{x_{i-\frac{1}{2},j}} \cong 2\frac{K_{x_{i-1,j}}.K_{x_{i,j}}}{K_{x_{i-1,j}}+K_{x_{i,j}}} \qquad K_{x_{i+\frac{1}{2},j}} \cong 2\frac{K_{x_{i,j}}.K_{x_{i+1,j}}}{K_{x_{i,j}}+K_{x_{i+1,j}}} \tag{5.5}$$

$$K_{y_{i,j-\frac{1}{2}}} \cong 2\frac{K_{y_{i,j-1}}.K_{y_{i,j}}}{K_{y_{i,j-1}}+K_{y_{i,j}}} \qquad K_{y_{i,j+\frac{1}{2}}} \cong 2\frac{K_{y_{i,j}}.K_{y_{i,j+1}}}{K_{y_{i,j}}+K_{y_{i,j+1}}} \tag{5.6}$$

Arranging equations (5.1) through (5.4) gives:

$$\begin{aligned}&\frac{\Delta y\Delta z}{\Delta x}\left[K_{x_{i+\frac{1}{2},j}}(P_{i,j}-P_{i+1,j})-K_{x_{i-\frac{1}{2},j}}(P_{i-1,j}-P_{i,j})\right]+\\&\frac{\Delta x\Delta z}{\Delta y}\left[K_{y_{i,j+\frac{1}{2}}}(P_{i,j}-P_{i,j+1})-K_{y_{i,j-\frac{1}{2},}}(P_{i,j-1}-P_{i,j})\right]=0\end{aligned} \tag{5.7}$$

This expression (5.7) is simplified when multiplied by $(\frac{\Delta x\Delta y}{\Delta z})$, which gives the equation:

$$\begin{aligned}&\Delta y^2\left[K_{x_{i+\frac{1}{2},j}}P_{i+1,j}-K_{x_{i-\frac{1}{2},j}}P_{i-1,j}+(K_{x_{i+\frac{1}{2},j}}+K_{x_{i-\frac{1}{2},j}}).P_{i,j}\right]+\\&\Delta x^2\left[K_{y_{i,j+\frac{1}{2}}}P_{i,j+1}-K_{y_{i,j-\frac{1}{2}}}P_{i,j-1}+(K_{y_{i,j+\frac{1}{2}}}+K_{y_{i,j-\frac{1}{2}}}).P_{i,j}\right]=0\end{aligned} \tag{5.8}$$

The formulation of this mass balance equation for all blocks leads to one $n_x.n_y$ system of equations (one equation for each block) in this general form:

$$A_{i,j}P_{i,j}-B_{i,j}P_{i-1,j}-C_{i,j}P_{i+1,j}-D_{i,j}P_{i,j-1}-E_{i,j}P_{i,j+1}=0 \tag{5.9}$$

This equation system can be solved using iterative techniques. For example, in Matax and Dalton (1990, pp. 146-151) several common iterative methods used in the solution of this particular type of equation system are described. The approach used in this case study (and implemented FORTRAN-77 code, Almeida[b], 1996) is based on point relaxation. In each iteration, for the block *i,j* a new pressure value is calculated, using the following expression:

$$P^{k+1}{}_{i,j} = P^{k}{}_{i,j} + \omega\,(R^{k}{}_{i,j} / A_{i,j}) \tag{5.10}$$

where:

ω is the relaxation parameter, with an optimal value (which leads to a smaller number of iterations) between 1 and 2. In our example, after some attempts and comparisons based on the number of final iterations, the value 1.8 was used,

and

$$R^{k}{}_{i,j} = -A_{i,j}P^{k}{}_{i,j} + B_{i,j}P^{k+1}{}_{i-1,j} + C_{i,j}P^{k}{}_{i+1,j} + D_{i,j}P^{k+1}{}_{i,j-1} + E_{i,j}P^{k}{}_{i,j+1} \tag{5.11}$$

The solutions of this system of equations are the pressure values $P_{i,j}$ in the centre of each block (*i,j*), conditioned to the boundary conditions imposed by the flow.

Taking the flow in the X direction to obtain the permeability tensor component in the same direction, and making use of the Darcy's Law and mass balance, leads to the following:

$$Q_{inp} = -\frac{\Delta y \Delta z}{\Delta x}\sum_{j=1}^{ny}\left[K_{x_{1+\frac{1}{2},j}}(P_{2,j} - P_{inp})\right] \tag{5.12}$$

and:

$$Q_{out} = -\frac{\Delta y \Delta z}{\Delta x}\sum_{j=1}^{ny}\left[K_{x_{nx-\frac{1}{2},j}}(P_{out} - P_{nx-1,j})\right] \tag{5.13}$$

Given that $Q_{inp} = Q_{out}$, using expressions (5.2) and (5.12) or (5.13):

$$-\frac{\Delta y \Delta z}{\Delta x}\sum_{j=1}^{ny}\left[K_{x_{1+\frac{1}{2},j}}(P_{2,j} - P_{inp})\right] = -\frac{ny\Delta y \Delta z}{(nx-1)\Delta x}K_x(P_{out} - P_{inp}) \tag{5.14}$$

which leads finally to:

$$K_x = \frac{\sum_{j=1}^{ny}\left[K_{x_{1+\frac{1}{2},j}}(P_{2,j} - P_{inp})\right]}{\frac{ny}{(nx-1)}(P_{out} - P_{inp})} \tag{5.15}$$

Similarly, taking a flow parallel to the Y direction, one has the solution:

$$K_y = \frac{\sum_{i=1}^{nx}\left[K_{y_{i,1+\frac{1}{2}}}(P_{i,2} - P_{inp})\right]}{\frac{nx}{(ny-1)}(P_{out} - P_{inp})} \tag{5.16}$$

5.2.4 IMPROVEMENT OF THE PRESSURE SOLVER TECHNIQUE FOR A CONDITIONAL UPSCALING APPROACH OF PERMEABILITY

In the previous chapter the calculation of the equivalent components of the permeability tensors is illustrated based on the pressure solver technique, K_x and K_y using expressions (5.15) and (5.16) respectively. This approach assumes a flow parallel to the coordinate axis with no-flow boundary conditions to solve the equation system. The upscaling of different blocks is considered independently of each other. Thus the permeability and consequent flow in the neighbourhood of a given block are not taken into account. The permeability values in neighbouring blocks and sets may result in different flow patterns from the assumed orthogonal X and Y directions.

In this study a new approach is proposed based on one iterative and optimal calculation of the tensor permeability components for each macroblock; these are conditioned to the permeability values of the neighbouring microblocks and to the values that result from this upscaling approach in previous iterations.

This proposed algorithm can be summarised in the following steps (Figure 5.6):

1) For each set of microblocks to come up with one value, calculate a variability measure, for instance the range of values.

2) Rank these values in increasing order.

3) For the first selected set of microblocks, the effective permeability (tensor components K_x and K_y) is calculated using the pressure solver approach described above. Each of these components is the solution of the system of equations resulting from the mass balance in a flow test as illustrated in Figure 5.7 a), which in this particular case, shows the determination of the component K_x.

In the first stage, the amount of flow Q^1_{inp} that occurs in the conditions illustrated in Figure **5.7** a) is calculated. This flow is calculated taking the pressure calculated in the centre of each microblock (assuming steady-state flow conditions) resulting from a pressure gradient to be equal to (P_{inp}-P_{out}) applied to the blocks of both extremities and corresponding transmissivities in the interface between these microblocks. The pressure on the centre of each microblock is calculated by solving a system of equations similar to the (5.9). In this system of equations, null transmissivity between microblocks (to come up with one value) in the Y direction is imposed to ensure a single solution in the calculation of equivalent K_x.

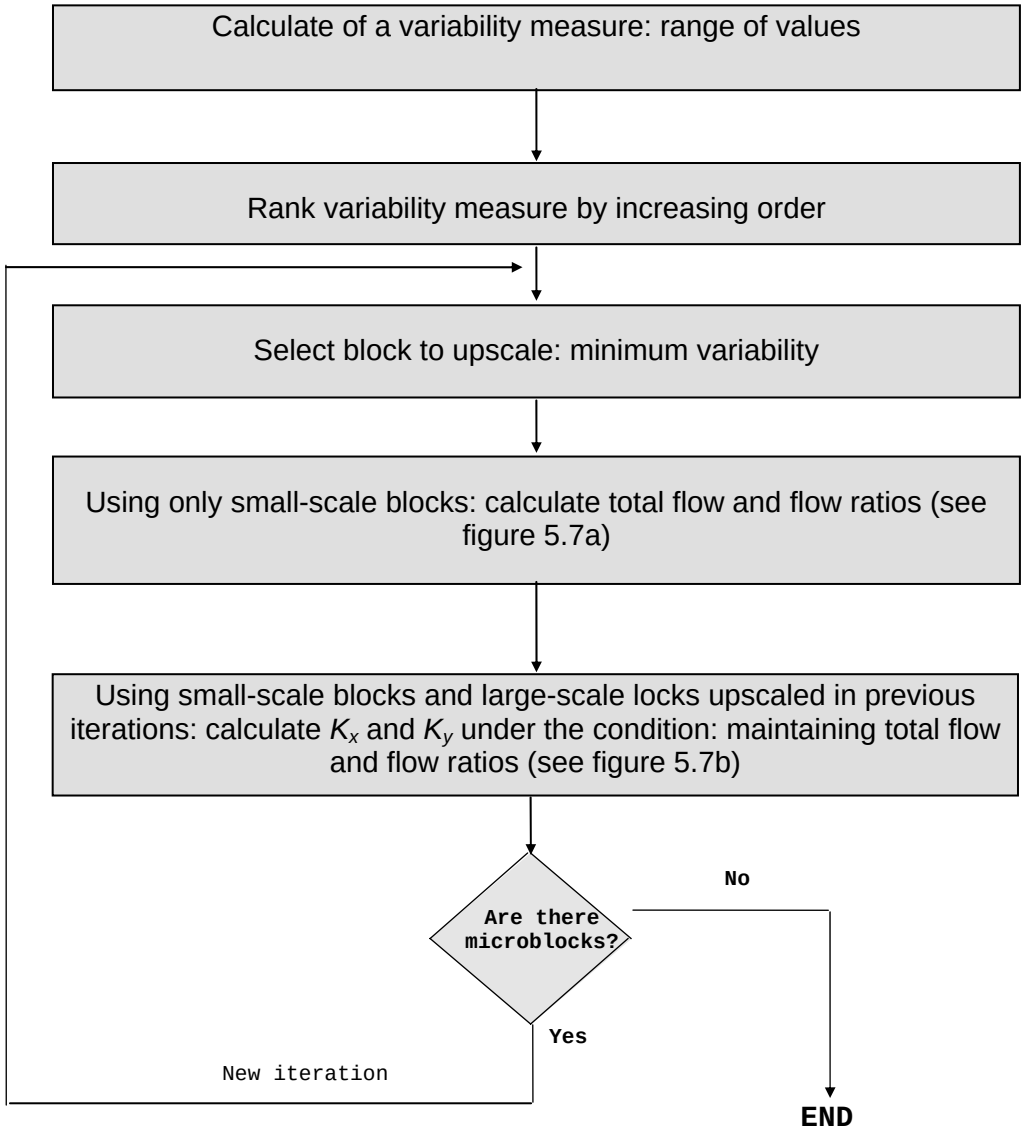

Figure 5.6 Steps of the proposed conditional upscaling approach.

Given the calculated values of pressure in all microblocks $P_{i,j}$ and transmissivities in the interface of blocks $K_{x_{i+\frac{1}{2},j}}$, the flow Q^1_{inp} is computed using this expression:

$$Q^1_{inp} = \sum_{j=1}^{ny}\left(\frac{K_{x_{1+\frac{1}{2},j}}\Delta y\Delta z}{\mu}\frac{(P_{1,j}-P_{2,j})}{\Delta x}\right) = \sum_{j=1}^{ny}\left(\frac{K_{x_{2+\frac{1}{2},j}}\Delta y\Delta z}{\mu}\frac{(P_{2,j}-P_{3,j})}{\Delta x}\right) = \ldots$$

In the second stage, the value K_x equivalent is calculated to be assigned to the macroblock (see example illustrated in Figure 5.7 b), with the condition Q^2_{inp}=Q^1_{inp}, when the same pressure gradient is applied.

Determination of equivalent permeability K_x based on the condition $Q^1_{inp} = Q^2_{inp}$

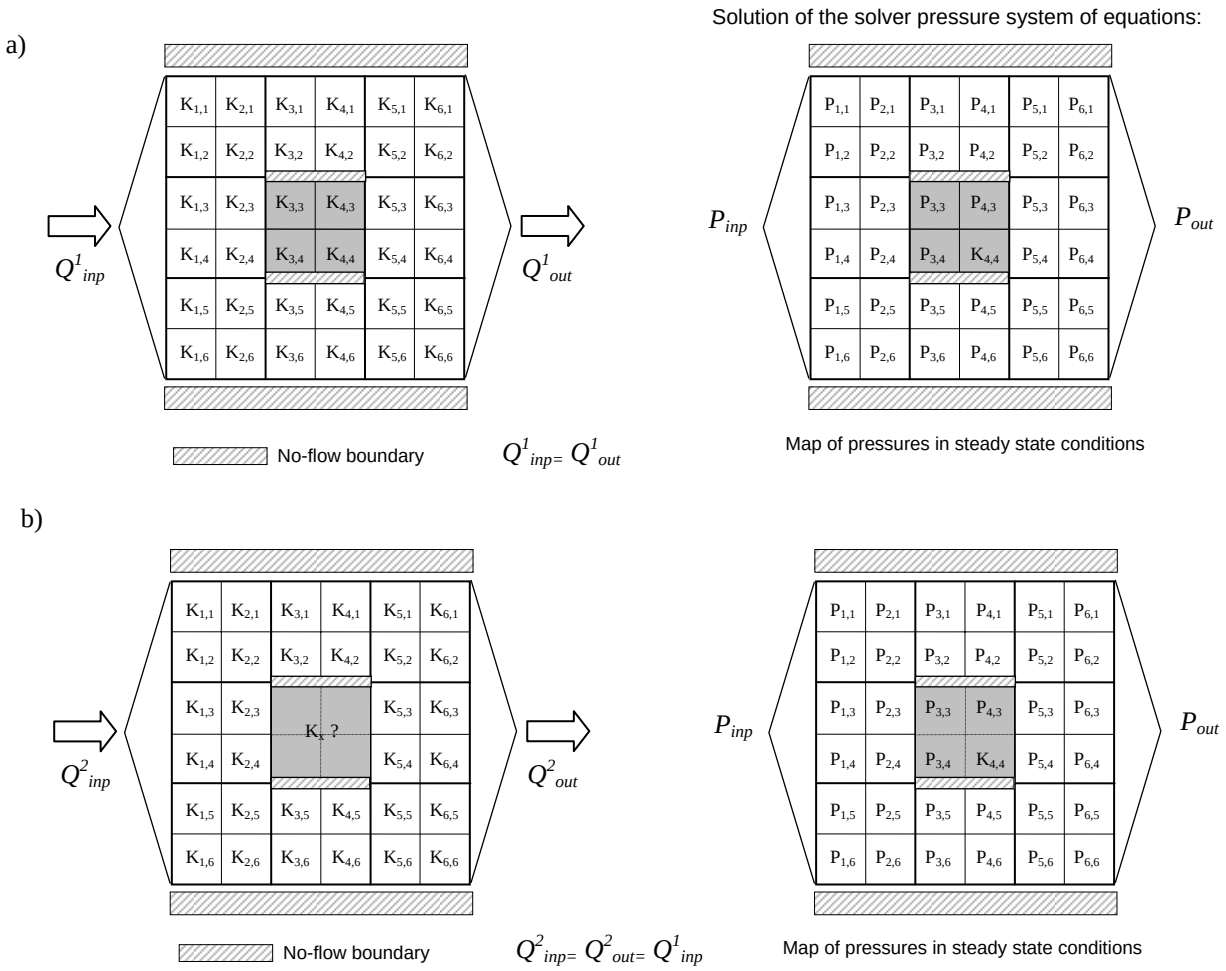

Figure 5.7 Flow test for the formulation of the system of equations in order to calculate the equivalent permeability K_x: a) first stage: calculation of the flow Q^1_{inp} ; b) second stage: calculation of the equivalent permeability K_x based on the condition $Q^2_{inp}=Q^1_{inp}$, when the same pressure gradient is applied.

Following this sketch, if a given permeability K'_x is greater than K_x, this means that:

$$Q^2_{inp} = f(K'_x) > Q^2_{inp}(K_x) \qquad (5.17)$$

This condition suggests that the calculation of K_x can be performed iteratively using a suitable optimisation procedure.

The calculation of K_y follows a similar scheme, in this case generating a flow parallel to Y and imposing a no-flow boundary condition on the X direction.

4) Test if microblock exist. If there are more small blocks, return to step 3, which means triggering a new iteration. The process continues until all small blocks are upscaled.

During this upscaling process, the calculation of the equivalent permeability components K_x and K_y takes into account the upscaled blocks given by previous iterations. Figure 5.8 illustrates the flow scheme used to calculate the K_x and K_y in one iteration step of the upscaling procedure by using microblocks together with macroblocks already upscaled in previous steps.

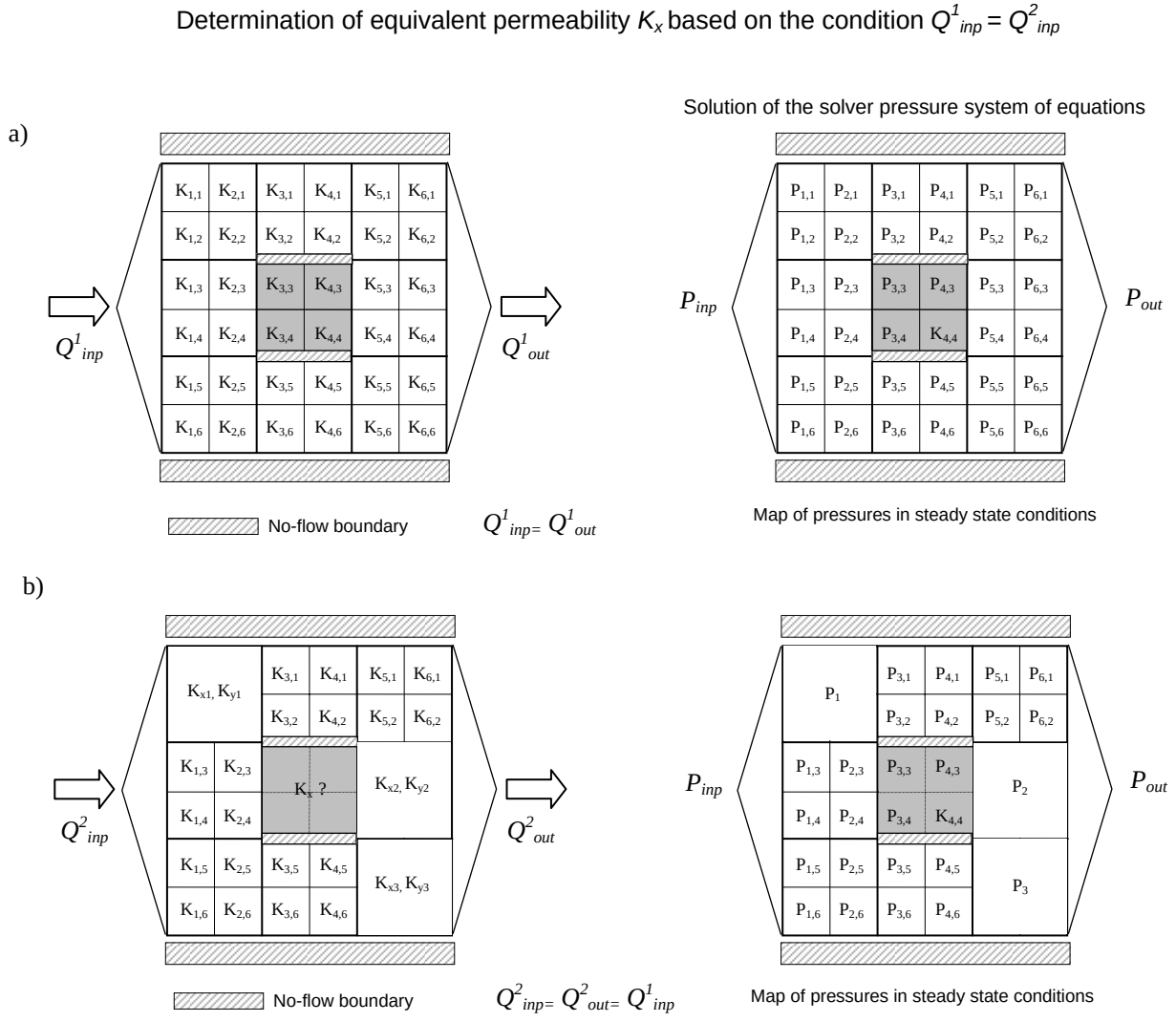

Figure 5.8 Calculation of flow ratios and equivalent permeability in one step of upscaling.

5.3. VALIDATION OF THE PROPOSED UPSCALING METHODS FOR PERMEABILITY

To evaluate the quality of the upscaling a single test is proposed that consists in the observation of the waterflood front advance in a flow simulation using the simulation package ECLIPSE 100. This dynamic simulation test involves comparison of the shape of a waterflood front when a full set of blocks is submitted to injection of water.

The first part of the test consists of a dynamic flow test, using initial microblock geometry and two wells: one is used to inject water and the other, in the opposite corner, is used to produce oil, assuming initial pressure, water saturation, and porosity constant for all microblocks. Time steps of reports and total simulation time were chosen in order to observe the advance of the waterflood front over the entire field and when water arrives at the producing well. The second part of the test consists of a similar dynamic flow test, at using this time the upscaled macroblock geometry and corresponding permeability components K_x and K_y. Thus, for the same time period of simulation the waterflood front advance was compared in both situations (after and before upscaling), particularly in critical regions, where the amount of heterogeneity in permeability values leads to a more irregular and winding flow.

The initial permeability map is obtained by stochastic simulation, see section 5. This test was conducted for a selected level of the entire 3D model. In this set of values (120 by 40 by 1 blocks) it is possible to observe some spatial heterogeneity of the values, and more or less tortuous connections of the highest and lowest values (Figure 5.11, upper image).

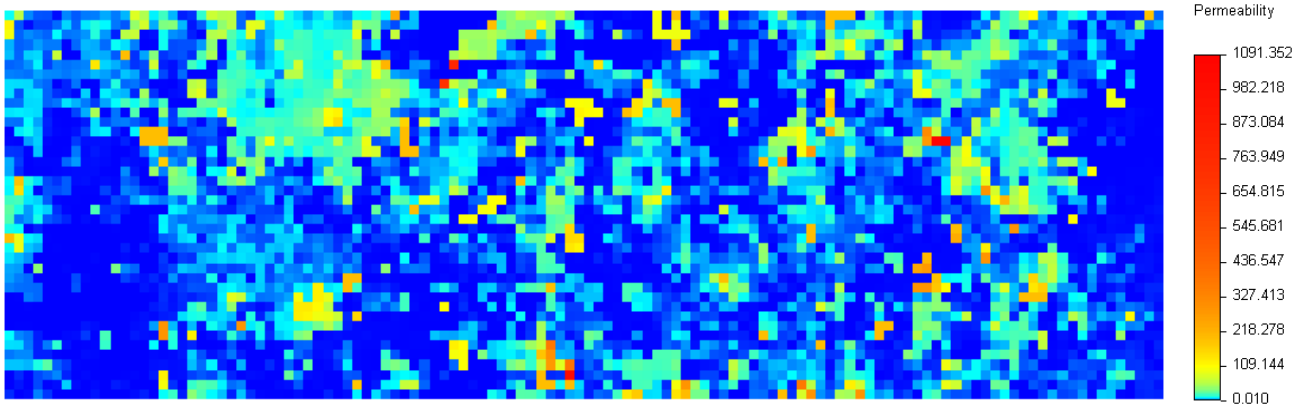

Figure 5.9 Initial permeability map.

In this example the performance of the proposed approach is illustrated when applied to the upscaling of 2 by 2 blocks and 4 by 4 sets of blocks using the proposed test.

- **2 by 2 single upscaling grid**

The upscaling of 2 by 2 grid nodes was conducted using a set of 4 neighbouring microblocks to condition the solution.

For illustrative purposes only, the permeability components K_x and K_y resulting from the conditional upscaling approach are illustrated in Figure 5.10.

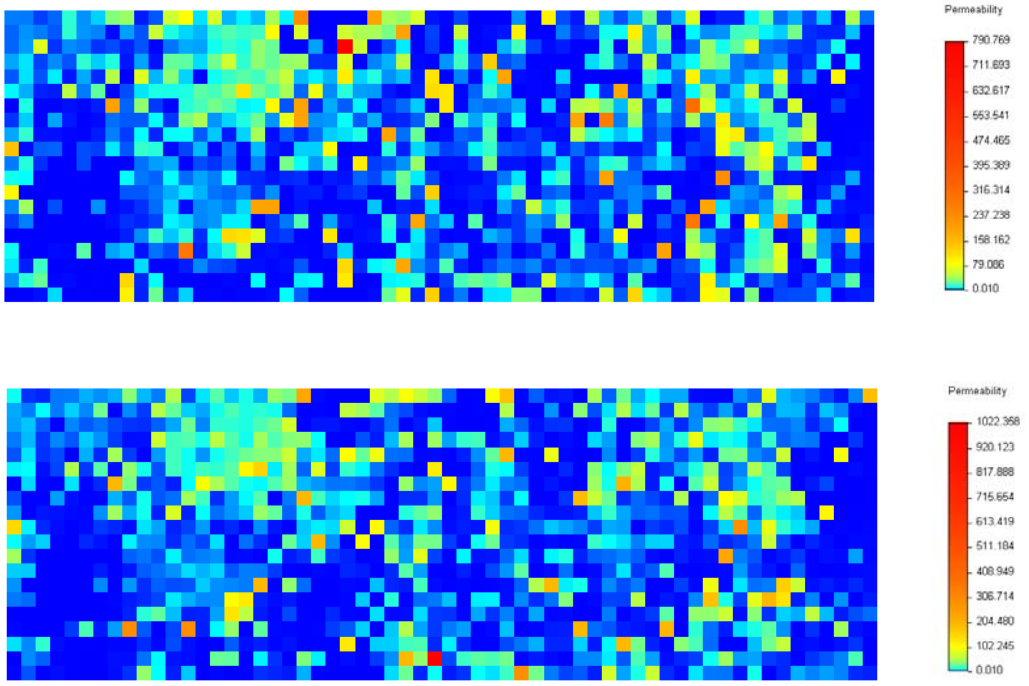

Figure 5.10 Equivalent permeability components K_x and K_y resulting from a conditional upscaling approach.

Relative to this grid, the results of the advance of the waterflood front are illustrated in a sequence of 3 time steps, Figure 5.11 through Figure 5.13. Following this sequence of images an improved match of the waterflood front is observed when the permeability values coming from the conditional proposed approach are considered. These improvements are highlighted in the selected images of the waterfront advance.

Looking at Figure 5.13, a slight retardation of the waterfront near the produced well is observed when the permeability values coming from the non-conditional approach are considered. Again, results from this dynamic study show that the conditional approach produces large-scale permeability maps that attenuate the differences between flow movements at both scales.

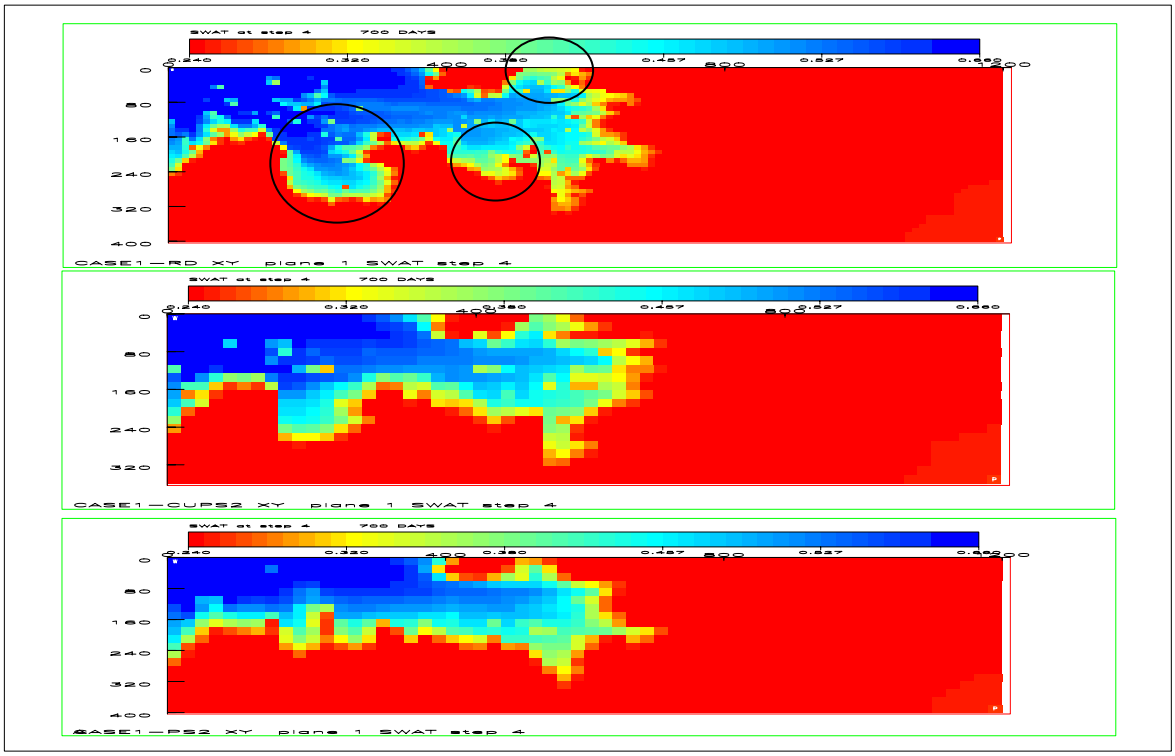

Figure 5.11 Waterflood front advance in a first time step (2 by 2 upscaling grid): upper image - flow simulation using initial microblocks; central image - flow simulation using permeability values from the conditional approach; lower image - flow simulation using permeability values from the non-conditional approach.

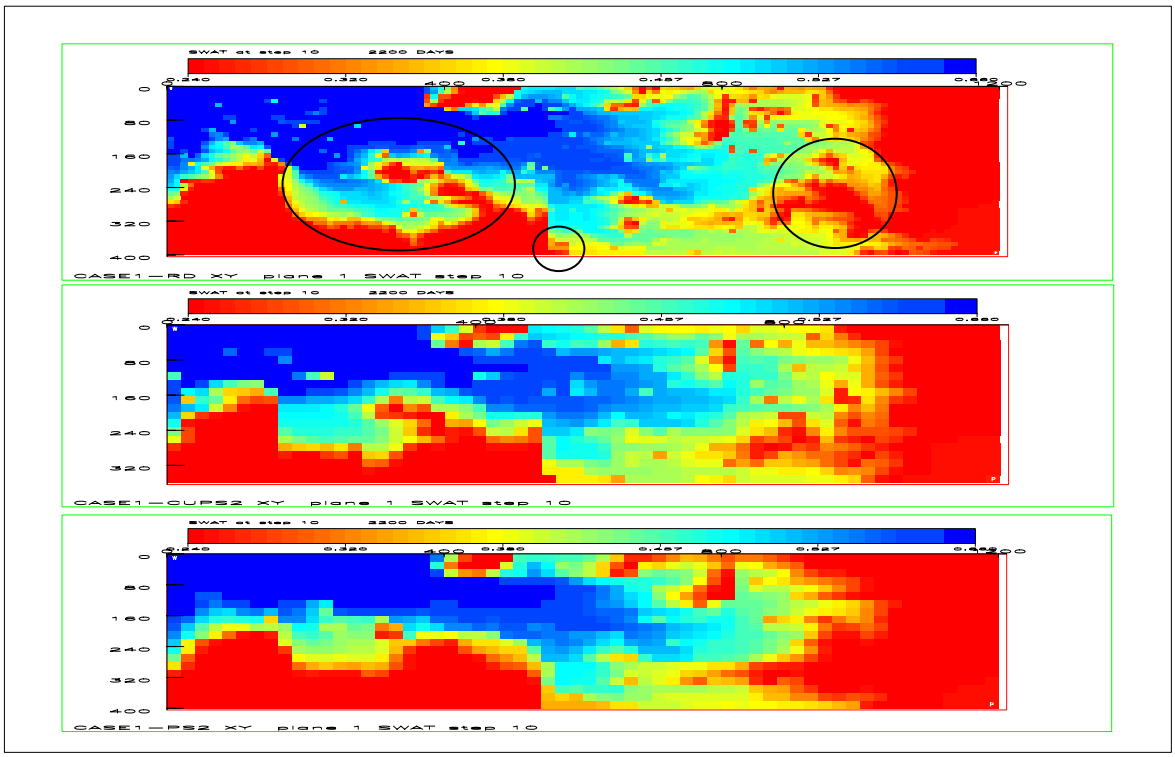

Figure 5.12 Waterflood front advance in a second time step (2 by 2 upscaling grid): upper image - flow simulation using initial microblocks; central image - flow simulation using permeability values from the conditional approach; lower image - flow simulation using permeability values from the non-conditional approach.

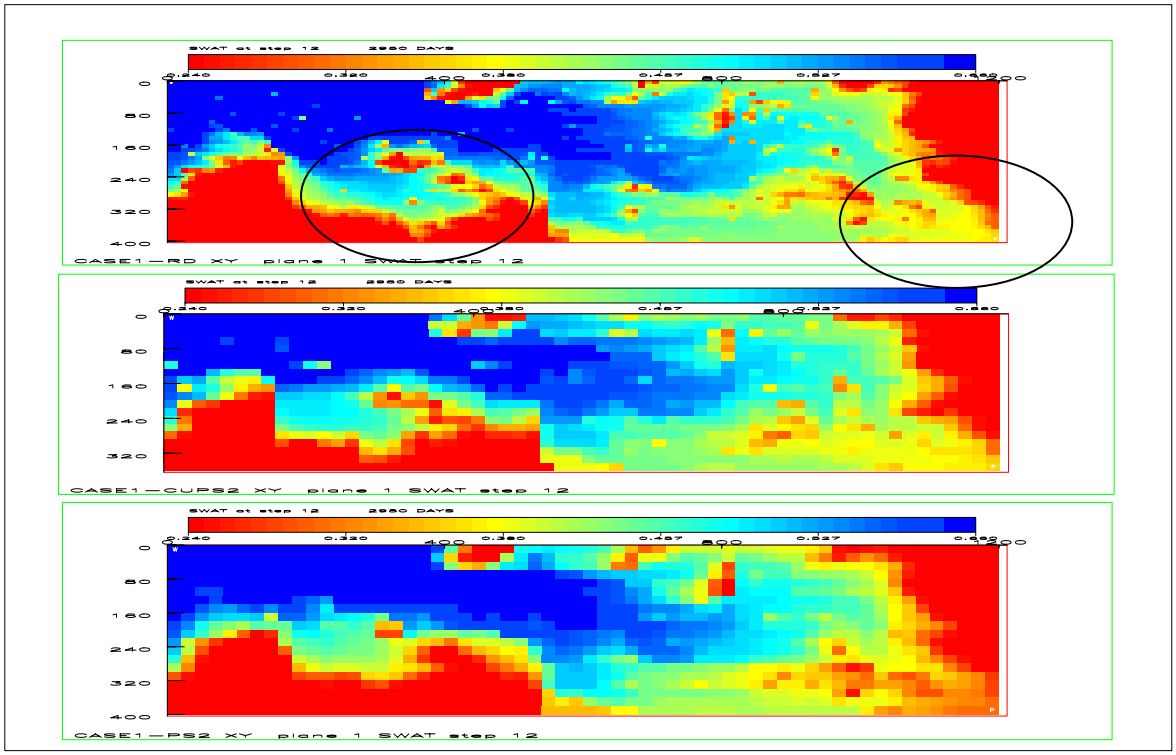

Figure 5.13 Waterflood front advance in a third time step (2 by 2 upscaling grid): upper image - flow simulation using initial microblocks; central image – flow simulation using permeability values from the conditional approach; lower image - flow simulation using permeability values from the non-conditional approach.

- **4 by 4 single upscaling grid**

Relative to this grid, the upscaled permeability values and results of the different tests can be seen in the sequence of Figure 5.14 through Figure 5.16.

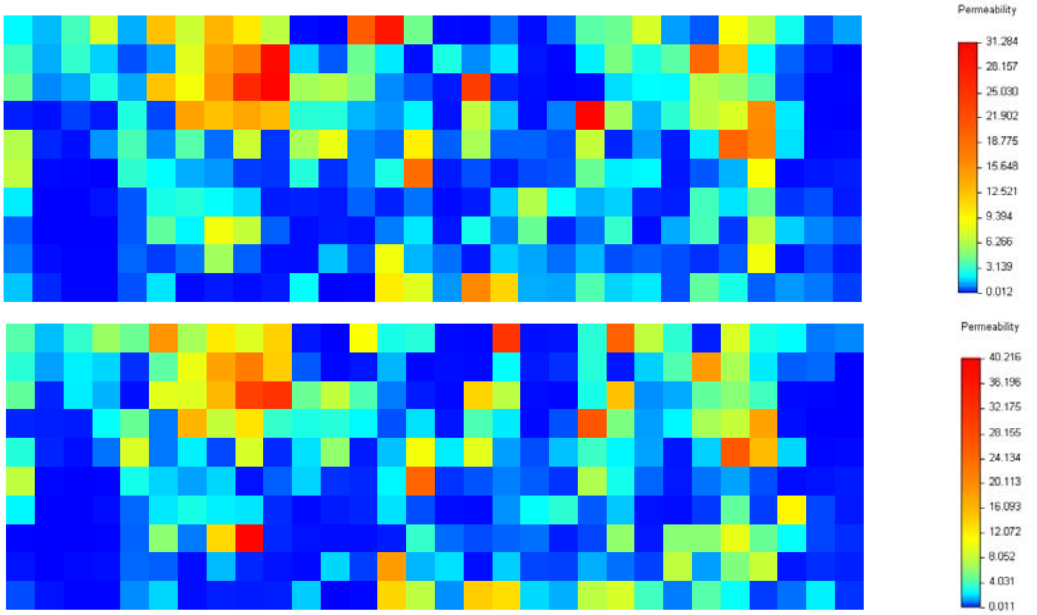

Figure 5.14 Equivalent permeability components K_x and K_y resulting from a conditional upscaling approach.

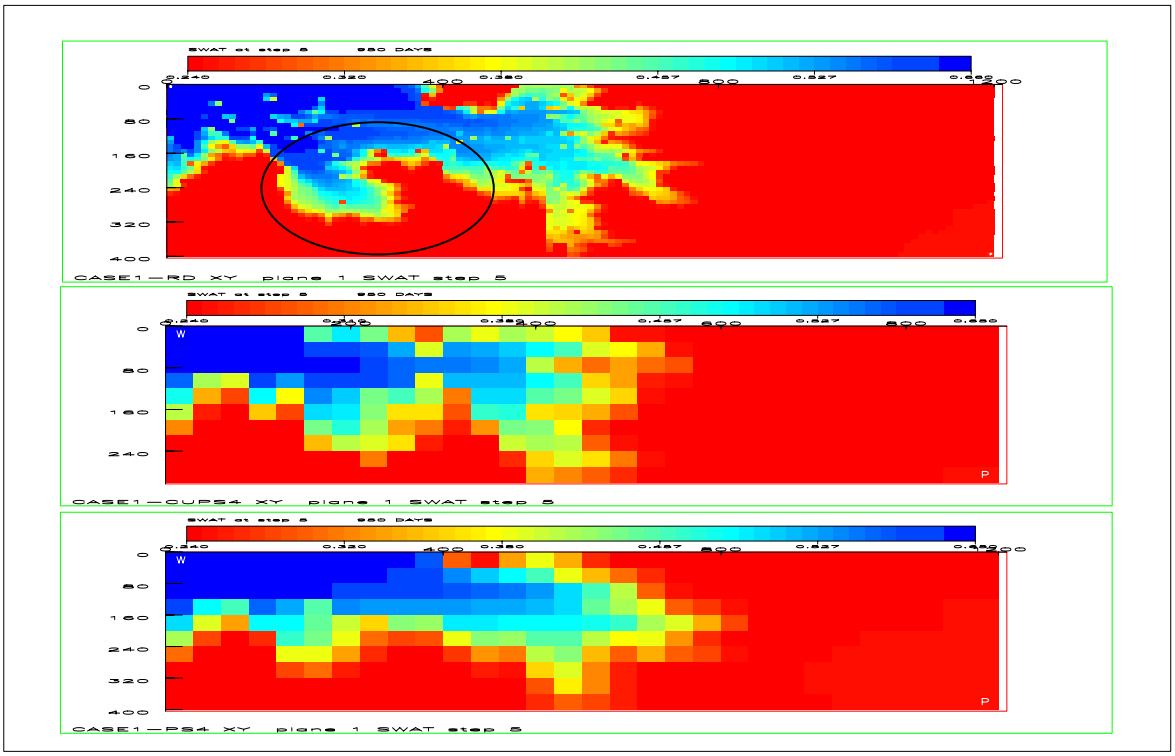

Figure 5.15 Waterflood front advance in a first time step (4 by 4 upscaling grid): upper image - flow simulation using initial microblocks; central image - flow simulation using permeability values from the conditional approach; lower image - flow simulation using permeability values from the non-conditional approach.

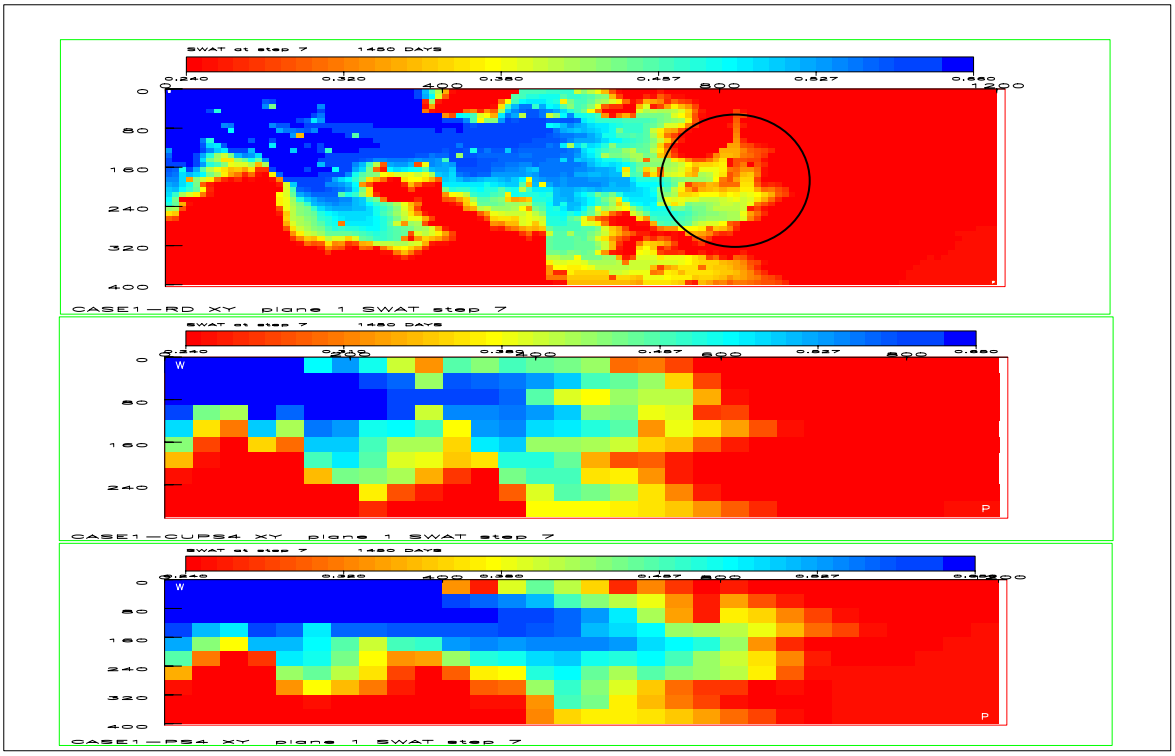

Figure 5.16 Waterflood front advance in a second time step (4 by 4 upscaling grid): upper image - flow simulation using initial microblocks; central image - flow simulation using permeability values from the conditional approach; lower image - flow simulation using permeability values from the non-conditional approach.

The upscaling of 4 by 4 grid nodes was conducted using a set of 8 neighbouring microblocks to condition the solution.

Again, looking at the results from this dynamic study it is possible to conclude that the conditional approach produces large-scale permeability maps that attenuate the differences between flow movements at both scales.

5.4. FINAL REMARKS

The selection of a particular upscaling methodology should be related to the major or minor heterogeneities of the initial permeability values and the number of blocks to be aggregated and represented by one value. If the set of values is homogeneous the conventional pressure solver approach with isolated sets of blocks provides a good solution. For heterogeneous block grids this study shows that the use of a more elaborate method increases the quality of the reproduction of the flow shape in tests with the simulation package.

With these results it is possible to conclude that the reproduction of the flow shape over the upscaled blocks is more accurate when using the proposed conditional methodology of upscaling. This improvement is evident in both upscaled grids used, 2 by 2 and 4 by 4. In Figure 5.11 through Figure 5.13 and Figure 5.15 and Figure 5.16 the advantage of using this type of upscaling versus the conventional pressure solver is demonstrated.

This approach can easily be generalised to three-dimensional grids. It is necessary to emphasise that all tests in this case study are performed in two dimensions to simplify the presentation. The disadvantage of this method is that it is extremely time-consuming, especially when using three-dimensional grids. One possible way to avoid this problem is to combine this method with the simple pressure solver approach. Thus, in small heterogeneous sets of blocks, upscaling could be performed successfully using the simple pressure solver. Otherwise, in more heterogeneous sets of blocks, the optimisation method proposed should be used.

6 CONCLUSIONS

At this final stage it is useful to emphasise the main steps of the proposed methodology for the spatial characterisation of heterogeneous reservoirs. Regarding this, the following paragraphs synthesise the new developments and the main remarks concerning to the proposed set of methods.

This integrated methodology of characterisation is based on a multi-step approach and encompasses the construction of a geological model of lithoclasses, a petrophysical model, constrained to the previous geological model, and the interface between geostatistical models and the input to the fluid flow simulator. The geological model of lithoclasses is intended to reproduce the heterogeneity observed between lithoclasses. The conditional petrophysical model is responsible for displaying the heterogeneity within each lithoclass, rather than between lithoclasses.

This multi-step methodology was implemented and adapted to the particular specifications of the reservoir studied - a highly heterogeneous carbonate reservoir.

The simulation of lithoclasses was performed using alternative methods of simulation of categorical variables that enable a comparative study to be performed. Regarding this comparative study, it is important to highlight the following points:

a) All approaches used generate sets of equally probable images of lithoclasses that reproduces spatial continuity models, the proportions of each lithoclass and experimental data. However, each of them produces typical spatial patterns of lithoclass distribution, which were compared exhaustively.

b) The theoretical background of all simulation approaches implemented in the characterisation of the spatial geometry of lithoclasses is based on the multi-phase concept. This concept and the corresponding multi-phase continuity measure tool, proved throughout along this study to be one of the most suitable to characterise the spatial continuity of categorical variables (for example, lithologies or rock types) rather than the usual alternative methods.

c) The improvement of correction for local probabilities in SIS shows accurate reproduction of the proportions of each lithoclass in the final simulated images, maintaining the reproduction of the variograms.

The characterisation of petrophysical properties was conducted following the estimation of the properties of porosity, permeability and water saturation. Permeability, due to its particular characteristics, was also modelled using stochastic simulation.

a) Regarding porosity and permeability, estimation models were built using zonal control estimation (with ordinary kriging) taking into account the previously generated images of lithoclasses.

b) One of the most important advantages of estimation with zonal control is that the spatial location of samples of all phases are accounted for while, in the classical procedure, only samples from the phase which x_0 (point to be estimated) belongs to are taken into account.

c) Given that permeability is a variable which displays a tensorial nature and strong variability in space, it was always coded in different classes and treated as a multi-phase set (or categorical set) in the general framework of the stochastic model.

d) The resulting stochastic model of permeability enables the occurrence of extreme values of permeability to be handled and mapped, which is of great importance in modelling fluid flows in the reservoir, since low and high permeability values define flow barriers and preferential paths.

e) Estimation of water saturation must take into account the physical rules that condition its spatial distribution and variability, rather than the distribution of lithoclasses. The construction of a 3D model of water saturation was performed by ordinary kriging estimation. The basis of this method is the use of a spatial referential based on the surface free water level (FWL) that proves to be the most suitable to find the horizontal correlation and to select the neighbouring samples used to estimate each grid node (samples at the same depth from the FWL).

f) Permeability is a variable that mainly conditions the preferential flow patterns and dynamic behaviour of the field, and consequently the characterisation of its spatial uncertainty is a key point of the study. Regarding this, a combined approach is presented able to produce several equally probable simulated images of permeability. Major advantages of this approach are the combination of two types of information with different sampling densities, the integration of the undersampled variable (in this particular permeability) using a probabilistic formalism, and the reproduction of continuity models and histograms by the simulated images.

Due to the difficulty of using all simulated images in flow simulation studies, it is important to rank the set of images based on some criteria easily and rapidly implemented criterion that will select the more representative stochastic images. Concerning permeability realisations, this study illustrates the application of one simple classification tool based on measure of volumes of geobodies of high and low permeability and their connectivity with selected wells.

Finally, this characterisation study presents a new technique of permeability upscaling derived from pressure solver methods. The objective is to improve the quality of upscaling by including in the calculation of the equivalent permeability the influence of permeability values in neighbouring blocks. This work illustrates that this method produces coarse images that more accurately reproduce the patterns of flow observed at small scale.

Finally, it is important to point out that all stochastic methods presented in this work belong to a more general set of geostatistics methods that are currently used in numerous applications of earth and environmental sciences. Thus, the methods presented here are not exclusively for application to reservoirs, but can be generalised to many different applications.

7 REFERENCES

Aarts, E. and J. Korst, 1989, *Simulated Annealing and Boltzmann Machines*, John Wiley & Sons, New York.

Abramovitz, M. and I. A. Stegum, editors. 1972. *Handbook of Mathematical Functions: with Formulas, Graphs, and Mathematical Tables*, 9th (revised) printing. Diver, New York. 1046 p.

Abu-Elbashar. 1990. *Characterisation and modelling of layered discontinuous reservoirs for waterflood predictions*. Master science dissertation, Imperial College University, London, 253 p.

Almeida, J., A. Soares and R. Reynaud. 1993. "Modelling the Shape of Several Marble Types in a Quarry", *Proceedings of the XXIV International Symposium APCOM*, Montreal, vol. 3: 452-459.

Almeida, J., A. Soares, A. C. Mariano and A. Albuquerque. 1994. Zonal control of reserves estimation of a diamond alluvial deposit. In *Proceedings of the Berg-and-Dal Conference on Mining Geostatistics*, South Africa.

Almeida, J., A. Soares, M. J. Pereira and S. Daltaban. 1996. Upscaling of permeability: implementation of a conditional approach to improve the performance in flow simulation. In *Proceedings of the 1st European 3D Reservoir Modelling Conference*, *SPE paper* #35490.

Almeida[a], J. 1996. Pós-processamento de imagens por Simulated Annealing: Aplicação à caracterização espacial de litoclasses e canais, *CMRP #8*, Instituto Superior Técnico, Lisboa, 20p.

Almeida[b], J. 1996. Manual técnico e de utilização do software CUPS V1.0: Upscaling condicional de permeabilidade numa malha regular de blocos, *CMRP #19*, Instituto Superior Técnico, Lisboa, 23p.

Almeida, J. and L. Guerreiro. 1997. Simulação estocástica de variáveis sub-amostradas. IV Siminário Interno CMRP/EXPRO.

Almeida, J., A. Soares and A. Albuquerque. 1997. Zonal control to estimate classes of histograms: application to a diamond alluvial deposit. In E.Y. Baafi and N.A. Schofield, editors, *Geostatistics Wollongong'96*, Kluwer Academic Pub., Dordrecht, 2: 658-669.

Archer, J. S. and C. G. Wall. 1986. *Petroleum engineering - principles and pratice*, Ed. Graham & Trotman, Alden Press, Oxford, 362 p.

Craft, B. C. and M. F. Hawkins. 1959. *Applied Petroleum Reservoir Engineering*, Prentice-Hall, Inc. New Jersey, 437p.

Crichlow, H. B., 1977, *Modern Reservoir Engineering: a Simulation Approach*, Prentice-Hall, 354p.

Da Costa e Silva, A. J. 1984. *Characterisation of reservoir heterogeneities at different scales*, MSc Thesis, Imperial College University, London.

Da Costa e Silva, A. J., A. Soares, J. Almeida and J. Carvalho. 1991. Geostatistical simulation of the geometry of a shale/limestone sequence in an oil field. *SPE paper* #26233.

Da Costa e Silva, A. J. 1992. *Desenvolvimento de modelos estocásticos aplicados à descrição e caracterização de reservatórios petrolíferos*, Tese de Doutoramento, Instituto Superior Técnico, Universidade Técnica de Lisboa, Lisboa, 653 p.

Da Costa e Silva, A. J., H. G. Pereira, A. Soares, J. Almeida and A. Guterres. 1993 A new approach for permeability classes simulation in undersampled oil reservoirs, *Geostatistics* TROIA'92, Ed. Soares, A., Kluwer Pub., 339-350.

Da Costa e Silva, A. J. and A. Soares. 1994. Stochastic modelling of a complex and heterogeneous carbonate oil reservoir, *Proceedings of the 6th ADIPEC – Abu Dhabi International Petroleum Exhibition & Conference*, (*ADSPE* #116): 17-25.

Da Costa e Silva, A. J., L. Ramos, R. Guerra, J. Rodrigues, A. Soares and E. Pires. 1996. Use of seismic to improve reservoir characterization, *SPE paper* #35484.

Da Costa e Silva, A. J., A. Soares, J. Almeida, L. Ramos and J. Carvalho. 1997. A multi-step approach for modelling oil reservoir lithologies and petrophysical attributes based on the integration of geostatistics and geology, In E.Y. Baafi and N.A. Schofield, editors, *Geostatistics Wollongong'96*, Kluwer Academic Pub., Dordrecht, 1: 327-338.

Dake, L. P. 1978. *Fundamentals of reservoir engineering*, Developments in Petroleum Science, nº 8, Elsevier, Science, 443 p.

Daly, C. and G. W. Verly. 1994. Geostatistics and data integration, In R. Dimitrakopoulos (ed), *Geostatistics for the Next Century*, Kluwer Academic Pub., Dordrecht, pages 94-107.

Deutsch, C. V. and A. G. Journel. 1992. *GSLIB: Geostatistical software library and user's guide*, Oxford University Press, New York, 340 p.

Deutsch, C. V. 1994. Algorithmically-defined random function models, In R. Dimitrakopoulos, editor, *Geostatistics for the Next Century*, Kluwer Academic Pub., Dordrecht, pages 422-435.

Deutsch, C. V. and P. W. Cockerham. 1994. Practical considerations in the application of simulated annealing to stochastic simulation, *Mathematical Geology*, 26(1), pages 67-82.

Deutsch, C. V. 1996. Challenges in reservoir forecasting, *Mathematical Geology*, 28(7): 829-841.

Deutsch, C. V. and L. Wang. 1996. Hierarchical object-based stochastic modelling of fluvial reservoirs, *Mathematical Geology*, 28(7), pages 857-880.

Dowd, P. 1979. The conditional simulation of regionalized variables, *In* Técnica, 1º Seminário de Geomatemática, 225-234.

Farmer, C., 1992, *Numerical rocks*, In P. King editor, *The Mathematical Generation of Reservoir Geology*, Oxford.

Froidevaux, R. 1993. Probability field simulation, In A. Soares (ed), Geostatistics Troia'92, Kluwer Academic Pub., Dordrecht, 1, pages 73-84.

Gatlin, C. 1960. *Petroleum Engineering: Drilling and Well Completion*, Englewood Cliffs, Prentice-Hall, Inc. New Jersey, 341 p.

Gomez-Hernandez, J. and A. G. Journel. 1990. Stochastic characterisation of grid-block permeabilities: from point values to block tensors, 2nd European Conference on the Mathematics of Oil Recovery, D. Guérillot, O. Guillon (Editors), Paris, pages 83-90.

Gomez-Hernandez, J. and A. G. Journel. 1994. Stochastic characterisation of grid-block permeability, In *Report 7*, *Stanford Center for Reservoir Forecasting*, Stanford, CA.

Goovaerts, P. 1994. Prediction and stochastic modelling of facies types using classification algorithms and simulated annealing, In *Report 7*, *Stanford Center for Reservoir Forecasting*, Stanford, CA.

Goovaerts, P. 1996. Stochastic simulation of categorical variables using a classification algorithm and simulated annealing, *Mathematical Geology*, 28(7), 909-921.

Goovaerts, P. 1997. *Geostatistics for natural resources evaluation*. Oxford University Press, New York, 483 p.

Guerreiro L., J. Almeida and A. Soares. 1998. "Permeability Simulation in Poor Sampling Conditions", SPE paper #49451, *Proceedings of the 8th Abu Dhabi International Petroleum Exhibition and Conference*, Abu Dhabi.

Haldorsen, H. and L. W. Lake. 1982. A new approach to shale management in field scale simulation models, SPE 57th Technical Conference, (September 1982), New Orleans.

Haldorsen, H., P. Brand and C. Macdonald, 1988, Review of the stochastic nature of reservoirs, In S. Edwards and P. King, editors, *Mathematics in Oil Production*, pages 109-209, Clarendon Press.

Isaaks, E. H. and R. M. Srivastava. 1989. *Applied geostatistics*, Oxford University Press, New York, 561 p.

Journel, A. G. 1977. *Geostatistique Miniere*. Centre de Geostatistique de Fontainebleau, 705p.

Journel, A. G. and C. J. Huijbregts. 1978. *Mining geostatistics*. Academic Press, New York, 600 p.

Journel, A. G. and E. H. Isaaks. 1984. Conditional indicator simulation: Application to a Saskatchewan uranium deposit, *Mathematical Geology*, 16(7): 685-718.

Journel, A. G. and F. G. Alabert. 1988. Focusing on spatial connectivity of extreme-valued attributes: stochastic indicator models of reservoir heterogeneities, *SPE paper* #18324.

Journel, A. G. and F. G. Alabert. 1989. Non Gaussian data expansion in the earth sciences, Terra Nova, Vol.1: 123-134.

Journel, A. G. and J. Gomez-Hernandez. 1989. Stochastic imaging of the Wilmington clastic sequence. *SPE paper* #19857.

Journel, A. G. 1989. *Fundamentals of geostatistics in five lessons*. In *Short Course in Geology*, 8:1-33.

Journel, A. G. and D. Posa. 1990. Characteristic behavior and order relations for indicator variograms. *Mathematical Geology*, 22(8): 1011-1025.

King, P. R. 1989. The use of renormalization for calculating effective permeability transport in porous media, *Kluwer Academic Press*, pages 37-58.

Luis, J. and J. Almeida. 1997. Stochastic characterisation of fluvial and channels. In E.Y. Baafi and N.A. Schofield, editors, *Geostatistics Wollongong'96*, Kluwer Academic Pub., Dordrecht, 1: 477-488.

Malick, K. M. and T. A. Hewett. 1994. Boundary effects in the successive renormalization of absolute permeability, In *Report 7*, *Stanford Center for Reservoir Forecasting*, Stanford, CA.

Matheron, G., H. Beucher, C. de Fouquet, A. Gali, D. Guerillot and C. Ravenne. 1987. Conditional Simulation of the Geometry of fluvio-deltaic reservoirs. *SPE paper* #16753.

Mattax, C.C. and R.L. Dalton. 1990. *Reservoir simulation*, SPE 1, 173 p.

North, F. K. 1985. *Petroleum geology*, Chapman & Hall, 631 p.

Omre, H., K. Solna and H. Tjelmeland, 1990, Calcite cementation description and production consequences, SPE paper #20607.

Pereira, H. G., A. J. Da Costa e Silva, A. Soares, L. Ribeiro and J. Carvalho. 1990. Improving Reservoir Description by Using Geostatistical and Multivariate Data Analysis Techniques, *Mathematical Geology*, 22(8), pages 879-913.

Pereira, M. J., L. Cortez and F. Durão. 1995. Application of neural networks for oil reservoir characterisation: classification of lithoclasses and permeability classes, *CMRP #7*, Instituto Superior Técnico, Lisboa, 20p.

Perez, V. S. and A. G. Journel. 1990. Stochastic simulation of lithofacies for reservoir characterisation, In *Report 3*, *Stanford Center for Reservoir Forecasting*, Stanford, CA.

Ripley, B. 1987. *Stochastic Simulation*. John Wiley & Sons, New York.

Rodrigues, A., J. Almeida, A. Soares. 1998. *Manual de Utilização do geoMS*, CMRP/IST.

Rumhy, M. H. 1990. *A Conditional Kriging Approach for Ascribing Permeability Distribution in Porous Media*, Doctoral dissertation, Imperial College University, London, 203p.

Sen, M.K., Gupta, A.D., Stoffa, P.L., Lake, L.W., Pope, G.A. 1992. Stochastic Reservoir Modeling Using Simulated Annealing and Genetic Algorithm, *SPE paper* #24754.

Soares, A. 1990. Geostatistical estimation of orebody geometry: morphological kriging. *Mathematical Geology*, 22(7): 787-802.

Soares, A. 1992. Geostatistical estimation of multi-phase structures. *Mathematical Geology*, 24(2): 149-160.

Soares, A. 1995. Simulação estocástica de redes densas de informação secundária. *CMRP #10*, Instituto Superior Técnico, Lisboa, 20p.

Soares, A. and J. Almeida. 1995. Zonal control of geostatistical simulation, *CMRP #1*, Instituto Superior Técnico, Lisboa, 20p.

Soares, A. and A. Brusco. 1997. Simulation of naturally fracturated reservoirs, In E.Y. Baafi and N.A. Schofield, editors, *Geostatistics Wollongong'96*, Kluwer Academic Pub., Dordrecht, 1: 433-442.

Soares, A. 1998. Sequential indicator simulation with correction for local probabilities. *Mathematical Geology*, 30(6): 761-765.

Soares, L., T. Ribeiro, F. Alves and M. J. Pereira. 1996. Determination of horizontal permeability through a probability neural network approach, In *Proceedings of the 7th Abu Dhabi International Petroleum Exhibition and Conference*, *SPE paper* #36266.

Sousa, A. J. 1983. Simulação de funções aleatórias estacionárias, *Encontros sobre métodos quantitativos aplicados às variáveis regionalizadas*, INIC: 65-171.

Srivastava, R. M. 1992. Reservoir characterisation with probability field simulation, In *SPE Annual Conference and Exhibition, Washington, D.C., paper* #24753, pages 927-938, Washington, D. C., Society of Petroleum Engineers.

Srivastava, R. M. 1994. An overview of stochastic methods for reservoir characterisation, In *Stochastic Modelling and Geostatistics, Practical Applications and Case Histories*, J. Yarus and R. Chambers, editors, American Association of Petroleum Geologists.